Theoretical Studies of Solvation and Catalysis: Clusters as Chemical Nano-reactors

Tao-Nhân V. Nguyen

A Thesis

In

The Department

Of

Chemistry and Biochemistry

Presented in Partial Fulfillment of the Requirements
For the Degree of Doctor of Philosophy at
Concordia University
Montreal, Quebec, Canada

September 2005

Your file Votre référence
ISBN: 0-494-09951-8
Our file Notre référence
ISBN: 0-494-09951-8

ABSTRACT

Theoretical Studies of Solvation and Catalysis: Clusters as Chemical Nano-reactors

Tao-Nhân Nguyen, Ph. D.
Concordia University, 2005

In this work, computational studies of clusters were performed to understand solvent effects on chemical reactivity (Part A), and assess their potential use as micro-reactors to catalyze reactions not usually possible (Part B).

In Part A, a comparative investigation of the structural and energetic properties of ions and ion pairs in polar solvent clusters of acetonitrile, ammonia and water is undertaken by means of Monte Carlo simulations with custom-built model potentials. Quantum chemistry calculations demonstrate the presence of nonlinear hydrogen-bonded $I^-(CH_3CN)_2$ isomers, which leads to a reinterpretation of previous experimental work. In addition, our work has some implications for the strong solvent selectivity observed experimentally for the NaI photoionization in polar clusters. Equilibrium constant calculations of the NaI ion pair in clusters suggest that the lack of large ionized product fragments observed experimentally in acetonitrile is not due to solvent-induced charge separation (as suggested previously in analogy with water clusters), but could be attributed either to differential solvation effects or to solvent evaporation on the ionized state. On the other hand, the lack of large product signal in $NaI(NH_3)_n$ multi-photon ionization experiments might be connected to the low evaporation temperature of

ammonia, which may prevent production of large parent ground-state $NaI(NH_3)_n$ clusters, and result in massive solvent evaporation on the excited states.

In Part B, the dynamics of energy transfer in $(O_2)_n$ cluster-surface scattering is characterized by means of classical molecular dynamics simulations, providing insights for several experiments, such as the cluster-catalyzed oxidation of a silicon surface. Simulations of the cluster scattering process reveals that the oxidation mechanism cannot occur through molecular dissociation nor by direct molecular reaction. Molecular dynamics simulations of $(O_2)_n$ cluster-surface scattering, along with high-level quantum chemistry calculations of the $(O_2)_2$ cluster model, suggested a novel "ladder climbing" mechanism, involving curve-crossing and spin orbit coupling, for the efficient mechanically-induced formation of highly reactive singlet O_2 molecules. Such a process may also be responsible for the presence of a "dark channel" in the enhanced vibrational relaxation of highly excited O_2 molecules, and shows that the Born-Oppenheimer approximation breaks down in the “chemistry with a hammer”.

ACKNOWLEDGMENTS

I would like to take this opportunity to thank Dr. G. H. Peslherbe for the chance to work in his laboratory and for his guidance throughout the course of this research, as well as Dr. H. Vach who collaborated on the "chemistry with a hammer" project.

I wish to thank Dr. M. A. Lawrence and Dr. P. H. Bird for being on my research committee and for their helpful suggestions during the course of my research.

I am grateful to all the students and postdocs who work in our laboratory, in particular to Q. K. Timerghazin, G. Dolgonos and D. M. Koch for their constant help and support.

I also wish to acknowledge the financial support of Concordia University. Calculations were performed at the Centre for Research in Molecular Modeling (CERMM), the Western Canada Research Grid (WestGrid), the French National Computer Center (IDRIS) and the computer center of Ecole Polytechnique (DSI).

To my family.

TABLE OF CONTENTS

PART B – CLUSTERS IN CATALYSIS STUDIES

LIST OF FIGURES

LIST OF TABLES

CONTRIBUTIONS OF AUTHORS

Chapter A2: "Microsolvation of alkali and halide ions in acetonitrile clusters"
T.N. Nguyen: research work and manuscript preparation.
G. H. Peslherbe: project supervisor.

Chapter A3: "Asymmetric solvation revisited: the importance of hydrogen bonding in iodide-acetonitrile clusters"
Q. K. Timerghazin: completed research work and manuscript preparation.
T. N. Nguyen: early research work.
G. H. Peslherbe: project supervisor.

Chapter A4: "Microsolvation of the sodium iodide ion pair in acetonitrile clusters: a theoretical study"
T. N. Nguyen: research work and manuscript preparation.
S. R. Hughes: early research work.
G. H. Peslherbe: project supervisor.

Chapter A5: "Microsolvation of alkali and halide ions and ions pairs in ammonia clusters"
T. N. Nguyen: research work and manuscript preparation.
M. Harpham: early research work.
B. M. Ladanyi and G. H. Peslherbe: project supervisors.

Chapter B2: "Molecular dissociation and vibrational excitation in the surface scattering of $(N_2)_n$ and $(O_2)_n$ clusters"
T. N. Nguyen: research work and manuscript preparation.
D. M. Koch: provided computer simulation and data analysis programs.
H. Vach: collaborator.
G. H. Peslherbe: project supervisor.

Chapter B3: "Non-adiabatic ladder climbing in molecular collisions"
H. Vach: manuscript preparation.
T. N. Nguyen: research work.
G. H. Peslherbe: project supervisor.

Chapter B4: "Mechanically-Induced Generation of Highly Reactive Excited-State Oxygen Molecules in Clusters
T. N. Nguyen: research work and manuscript preparation.
Q. K. Timerghazin: research work.
H. Vach: collaborator.
G. H. Peslherbe: project supervisor.

GENERAL INTRODUCTION

Clusters are defined as an aggregated state of matter, in which the individual constituents are held together by forces that are typically weak compared to those involved in chemical bonding.[1] Often, they can be viewed as finite-size "pieces" of condensed-phase matter. Nowadays, many types of clusters can be synthesized and research has focused on several classes of such systems. For instance, extensive effort has been devoted to carbon clusters, metal and semiconductor systems, rare-gas and van der Waals systems, as well as clusters composed of hydrogen-bonded molecules.[2]

The area of cluster research originates from the mid-nineteenth century when the first studies of colloids, aerosols, and nucleation phenomena were reported.[3] While cluster research underwent a slow development in the early part of the twentyth century,[4] a resurgence of interest occured several decades ago, when well-defined clusters generated by supersonic expansions could be investigated using mass spectrometry.[5] From that point on, combinations of beams for cluster generation and mass spectrometry for detection and selection prompted a plethora of studies.[6] By the early 1970s, cluster science started to be considered as a field of research of its own, as new methods were developed for synthesizing clusters of variable size[7] and various laser spectroscopic techniques[8] could be employed for probing cluster properties.

Nowadays, neutral clusters are usually formed by supersonic expansion techniques, which facilitates cooling processes and concomitant association steps related to their growth.[6] The expansion cools the gas well below its condensation temperature, and pressure control allows interruption of the condensation process at any point, generating clusters of different size.[9] Clusters can be generated in conditions well suited

for high-resolution spectroscopy, and numerous methods have been developed for this purpose.[10] Ionic clusters have been successfully synthesized using electrospray techniques,[11] although related thermal vaporization methods have also been employed to produce clusters of neutral species from liquids.[12] In the case of metal and semiconductor clusters, laser vaporization and use of condensation sources have been especially valuable as methods for cluster production.[13]

In the last two decades, progress in experimental techniques was accompanied by a steady increase in computational power, which made possible a direct comparison of the results of molecular modeling and experimental studies. Both approaches can provide structural, thermodynamic and spectroscopic properties, and even dynamic properties of small clusters in the gas phase. From both experimental and theoretical points of views, the limited number of degrees of freedom is of great advantage, such that high-resolution experiments and accurate theoretical calculations are possible. Furthermore, theoretical studies proved to be essential for the interpretation of increasingly complex experimental results, and such interplay between theory and experiment induced an explosive growth of the research field.[6]

In terms of fundamental knowledge, cluster studies provide a molecular-level characterization of molecular interactions and chemical reaction dynamics. These small aggregates typically display a behavior that significantly differs from those of the solid, liquid, or gas phases, and as such, clusters are often considered as a new state of matter. In particular, their small size implies that not only a large fraction of their constituents lie on the surface, but also quantum effects imposed by size-dependent constraints can be determining.[14] For instance, studies of clusters were employed to investigate nucleation

phenomena, including the formation of highly dispersed media having a large surface-to-volume ratio, e.g., aerocolloids, ultrafine particles, and nanoscale materials.[15,16]

The ability to vary the number of atoms or molecules in a cluster allows us to monitor how its various structural and dynamical properties evolve with size, and comparative investigations of properties of gaseous and related condensed-phase systems has been part of an overriding theme of many studies.[1,17] Although considerable progress has been made in many different areas of the field, the point where cluster properties can be directly connected to that of the corresponding bulk limit has not been reached yet, and much work remains to be accomplished. For instance, some elementary questions related to the nature of clusters as an intermediate form of matter remain unanswered, such as whether or not they can be characterized as liquids or solids, and if so, what is the nature of the associated phase transitions.[7,8,18]

In addition to providing insights on the nature of microscopic molecular interactions, cluster studies can provide information on basic mechanisms of reactions within clusters. As such, the unique properties of the cluster state can be exploited for the investigation of a multitude of fundamental processes, such as solvation[2,19,20] and photochemistry.[21,22] Two broad classes of cluster studies have been designed. The first group involves chemical reactions within the cluster environment, which allow, for instance, the study of solvation effects on reactivity. Indeed, investigations of intracluster interactions can provide insights on the structure and bonding of complexes in solution, and on solvent effects on reactivity. In addition, it is also possible to control chemical reactions by selective solvation of reactants, as the solvent affects the properties of the solvated species. This leads to the concept of solvation control of reactivity, a topic which

we will purse in the first part of the thesis. In the second group of studies, one typically seeks to induce new reactions by clustering reactants together. For instance, impacting or colliding clusters at high velocities can lead to extreme conditions of internal pressure and temperature that result in efficient cluster catalysis. This leads to the concept of the "chemistry with a hammer", which employs molecular clusters as a new class of reactants.

PART A

CLUSTERS IN SOLVATION STUDIES

CHAPTER A1
Introduction to Cluster Solvation Control of Reactivity

The fact that chemical reactions may differ in the gas, bulk and cluster phase has long been a challenging problem in the field of chemical physics.[14,20,23] One typical application is the study of the ubiquitous solvation effects on the physical and chemical properties of systems, along with that on their reactivity.[2,6,19,24] For instance, hydration of biomolecules was found to affect strongly their chemical properties.[25] Furthermore, solvent effects on some chemical reactions have been shown to depend strongly on the solvent.[6,16,17,26] More generally, solvent effects may be classified as (i) altering the nature of the reaction sites, (ii) affecting the reaction thermodynamics (exothermicity or exoergicity) , (iii) affecting the reaction kinetic properties (energy of activation), and (iv) effects due to caging by the cluster molecules.[6]

In cluster solvation studies, comparative investigations at various degrees of cluster aggregation reveal the evolution of the system properties and reactivity as a function of the degree of solvation, possibly providing insight into the differences observed in the gaseous and condensed phases. The course of a chemical reaction depends on the mechanisms of energy transfer and dissipation from the reaction site, which neighboring solvent molecules were shown to perturb.[6,17] For instance, transient configurations reached by the solvent can induce low energy barrier situations, making possible reactions that would not occur in gas phase. Further perturbations may be induced through caging effects which keep dissociating molecules in relatively close proximity for long periods of time. A mathematical formulation of the solvent reorganization free energy during a reaction has been provided by Marcus, which allowed

calculation of activation barriers and reaction free energy changes in solvated environments.[27] This theory first provided an explanation for the varying rate constants measured for electron transfer reactions, and was then proven invaluable in the interpretation of many chemical processes.[28] Marcus was awarded the Nobel prize in Chemistry (1992) in part for this seminal work on electron transfer reactions.[29]

Electron-transfer reactions are among the most ubiquitous and elementary of all chemical processes, with a wide range of implications for many areas of chemistry, physics and biology.[30] As electron-transfer processes in natural environments are quite complex, cluster science allows investigation of elementary aspects of this process in simplified model systems, free from the complicating or competing processes found in natural environments. In particular, photoinduced electron-transfer reactions provide detailed information on the structure of neutral and ionic clusters, as well as on energy transfer processes, photodepletion and photodissociation dynamics, which fueled a continued interest in determining the molecular-scale details of the initial electron-transfer step. Early studies on photodissociation and photoexcitation studies focused on simple systems, such as rare-gas dimers and trimers,[31] and then attention moved onto larger rare-gas cluster ion systems.[32] A wide variety of other small cluster ions have also been investigated, many of which are likely to be relevant for atmospheric chemistry.[33]

From the recent advances in generating laser pulses of subpicosecond duration arose the field of femtochemistry, pioneered by the Zewail group.[34] Many breakthroughs in this emerging field have been reported over the past decade,[35] and Zewail was awarded the Nobel Price in Chemistry in part for his innovative work in 1999.[36] Real-time observation of chemical reactions became possible via femtosecond pump-probe

techniques, and the evolution of the system could be monitored along the reaction path, from reactants to transition states, and then products. In typical photodissociation experiments, an electron-transfer process is initiated by a femtosecond pulse and the reaction progress is followed with a femtosecond probe pulse.[37,38] Experimental results indicate that the electron transfer process and the subsequent reaction dynamics are strongly correlated to the structural properties of the complex, and in particular to its degree of solvation.[37] Thus, the time resolution and coherence provided by femtosecond laser pulses also allows for the observation of the evolution of cluster properties going from the gas to the liquid phase, providing important insights on solvation processes.

In this work, we investigate the solubility of salts in solvents at the microscopic level, by focusing on the properties of the prototype NaI embedded in solvent clusters. A salt of iodine was selected because iodine is an ideal electron-acceptor molecule for studying electron-transfer processes.[39] In addition, the photodissociation dynamics of NaI has been well characterized.[40] Our theoretical studies aim at understanding the differing experimental results reported for the multi-photon ionization of NaI in clusters of water, acetonitrile, and ammonia.[26] Because $NaI(H_2O)_n$ clusters have already been studied,[41,42] we focus here on the properties of NaI in clusters of acetonitrile and ammonia, which will allow a comparison of various solvent effects on cluster properties. We employ standard methods of statistical mechanics to generate representative ensembles of ion-$(solvent)_n$ and ion pair-$(solvent)_n$ clusters, which require the development of classical model potentials to describe molecular interactions within the cluster.

As the first part of this work (Chapter A2), we present an early model potential for acetonitrile clusters, geared towards a proper description of the CH_3CN-CH_3CN, Na^+-

CH_3CN and I^--CH_3CN interactions, based on ab initio calculations for small clusters and available experimental data. We focus on the properties of $Na^+(CH_3CN)_n$ and $I^-(CH_3CN)_n$ clusters, but also investigate those of $Cs^+(CH_3CN)_n$ clusters, in order to gain some insight into the influence of ionic size and charge on cluster properties. Finally, comparison with analogous water clusters is made to clarify solvent effects on clusters properties.

The second part of this work (Chapter A3) deals with the investigation of hydrogen bonding in acetonitrile clusters. Acetonitrile is not known as a hydrogen-bonding solvent, yet in the course of the investigation of small acetonitrile clusters with first-principle methods, we discovered the possible existence of low-energy hydrogen-bonded $I^-(CH_3CN)_2$ complexes. We thus report an in-depth investigation of hydrogen-bonding in $I^-(CH_3CN)_2$ as a prototype for $I^-(CH_3CN)_n$ clusters and show how a combination of theory and experiment may help provide insight into cluster structure and energetics. [43-46]

In the third part of this work (Chapter A4), we develop an improved model potential for $NaI(CH_3CN)_n$ clusters, as our earlier model potential based on ion-solvent properties (cf. Chapter A2) failed to properly reproduce some subtle features of the $NaI(CH_3CN)_n$ complexes. Particular attention was paid to the modeling of $I^-(CH_3CN)_n$ hydrogen-bonding interactions, and the NaI-(CH_3CN) interaction. Following a brief study of ion-$(acetonitrile)_n$ clusters, we turn our attention towards $NaI(CH_3CN)_n$ structural and thermodynamic properties, along with possible implications for NaI multi-photon ionization in clusters.[26]

In the fourth part of this work (Chapter A5), in order to complete our investigation of the solvent-selective behavior of NaI multi-photon ionization in clusters, we turn our attention to the analogous ion-$(ammonia)_n$ and ion pair-$(ammonia)_n$ clusters. Again, we

found it necessary to develop a new model potential for both ion-solvent and solvent-solvent interactions, based on properties of small ammonia clusters obtained from ab initio calculations and experiment. Particular interest was paid to the influence of cluster temperature, and the possible implications for NaI multi-photon ionization in clusters. Finally, a comparison of the structural and thermodynamic properties of NaI ion pairs in ammonia, acetonitrile and water clusters is made to provide further insight into the role of solvation in preparing specific reactants and ultimately controlling chemical reactions.

CHAPTER A2
Microsolvation of Alkali and Halide Ions in Acetonitrile Clusters

A2.I. INTRODUCTION

Since a large fraction of chemical reactions occurs in solution, considerable attention has been paid to the influence of solvent on the physical and chemical properties of species.[47] By that token, experimental and theoretical studies of clusters – an intermediate state of matter between the condensed and gas phases - are very valuable for gaining insight into such fundamental processes such as the role of microsolvation in chemical reactions.[48] Over the past decade, an increasing number of cluster types have been investigated,[17] due to the development of experimental techniques for generating such species and observing their properties.[49] For example, studies of simple ionic clusters have provided detailed information about the cluster structures, thermodynamics and spectroscopic properties.[50-56] Of particular interest is the investigation of the properties of clusters of increasing size in order to determine at which point cluster properties would converge to bulk phase values.[57,58] A number of experimental and theoretical studies have been reported about the solvation of ion pairs in clusters.[26,41,42,57-64] Salt ion pairs such as NaI in polar solvent clusters are of particular interest to us. The NaI system has been a prototype system for the study of photodissociation dynamics involving curve crossing of covalent and ionic states.[65,66] Briefly, NaI photoexcitation results in transient trapping in an excited state well that arises from the avoided crossing between ionic and covalent states, together with a decay of the excited state population into atomic products via nonadiabatic transitions.[67,68] In typical femtosecond pump-probe experiments, the excited state population can be time-resolved by ionization of the

trapped excited NaI to a probe state and collection of the dissociation products with a mass spectrometer.[26,68] Our early theoretical work on $NaI(H_2O)$ clusters[69] showed how the presence of solvent affects the nonadiabatic dynamics of the photodissociation process, and prompted experimental multi-photon ionization studies of NaI ion pairs in polar solvent clusters of water, acetonitrile and ammonia.[26,61,62] In these experiments, a very clear solvent-selective behavior was observed in the distribution of the detected $Na^+(solvent)_n$ product ions.[26] For instance, clusters of size up to n~50 have been observed experimentally with water, but no clusters larger than size 10 and 7 have been observed with ammonia and acetonitrile, respectively.

In previous theoretical work, we also investigated the structure and thermodynamics of NaI ion pairs in aqueous clusters.[41,42] We found that NaI ion pairs are actually stable with respect to complete ground-state dissociation, even in very large water clusters, but that solvent-separated ion pairs become rapidly predominant over contact ion pairs with increasing cluster size. Model electronic structure calculations showed that solvent-separated ion pairs have a much reduced oscillator strength and may not possess optically accessible excited states akin to that of gas-phase NaI.[42] Our findings are consistent with the fact that products of $NaI(H_2O)_n$ cluster multi-photon ionization of size n>50 were not observed experimentally, as the larger solvent-separated-ion-pair parent clusters may just not be photochemically active. Interestingly enough, we also found that the structure of ion pairs in water clusters could be relatively simply related to that of the individual ions in water clusters.[41] Of particular importance in this case is the now well-known "hydrophobic" character of the iodide ion in aqueous

clusters,[55,70] which may explain why NaI ion pairs are "dragged" to the surface of small water clusters.[41]

We are now turning our attention to acetonitrile and ammonia clusters in order to understand the experimental differences observed for the various solvents.[26] The first step involves the development and validation of model potentials for Monte Carlo simulations of the structure and thermodynamics of NaI ion pairs in clusters. While we defer our work on ammonia clusters to a separate publication,[71] in this work, we derive model potentials for simulations of acetonitrile clusters, and validate the potentials by comparing the results of ionic cluster simulations with available experimental thermochemical data. Model potentials for acetonitrile simulations have been proposed in previous work,[51,72-74] but none of them seemed to be completely adequate for our cluster simulations. We naturally focus on $Na^+(CH_3CN)_n$ and $I^-(CH_3CN)_n$ clusters, but also investigate $Cs^+(CH_3CN)_n$ clusters for comparison. Since the Cs^+ ion is a monovalent cation like Na^+ but of a size similar to that of I^-, this may help untangle the role of ion size and charge in determining the structure of ionic clusters. The photodissociation of CsI in solvent clusters is also being investigated experimentally, and theoretical studies akin to our previous work[42,69] on NaI in water clusters might be needed for that system. Finally, a key point of this work is to compare the structural properties of ion-acetonitrile clusters to those of aqueous clusters.[75] Despite being both highly polar solvents, acetonitrile and water differ significantly, due to very different molecular sizes and molecular dipole moments, and the propensity of water to form relatively strong hydrogen bonds. Since the latter plays a major role in determining the surface structure of $I^-(H_2O)_n$ clusters, we will pay particular attention to the structure of $I^-(CH_3CN)_n$ clusters.

The outline of this chapter is as follows. The simulation procedure is briefly presented in Sec. A2.II. The thermodynamic and structural properties of the ion-acetonitrile clusters resulting from the simulations are presented and discussed in Sec. A2.III., where they are compared and contrasted to previous findings for ion-water clusters. Concluding remarks follow in Sec. A2.IV.

A2.II. COMPUTATIONAL PROCEDURE

A2.II.A. Monte Carlo Simulations

Metropolis Monte Carlo simulations[76] are used to investigate the thermodynamic and structural properties of $Na^+(CH_3CN)_n$, $Cs^+(CH_3CN)_n$, and $I^-(CH_3CN)_n$ clusters at 300K. We follow the procedure developed in previous work,[41] where independent simulations are carried out for clusters of various sizes. A given number n of CH_3CN molecules is placed around a fixed ion and canonical ensembles are generated as Markov chains of cluster configurations.[77] We employ the random-walk method[64] to generate a new trial solvent configuration by randomly translating one acetonitrile molecule in each Cartesian direction and rotating it about its standard Euler angles θ, ψ, and φ.[78] Since each random walk involves the six degrees of freedom of only one acetonitrile molecule, the length of the Markov chain is naturally increased with cluster size. Only sampled configurations for which all acetonitrile molecules have changed position are stored for structural analysis. Finally, the clusters are periodically heated and cooled with a smooth temperature schedule in order to sample all possible local minima.[79]

In contrast to liquid simulations,[78] no potential truncation is necessary and no periodic boundary conditions are imposed in cluster simulations. However, complications

arise from the fact that acetonitrile molecules may undergo evaporation at room temperature,[80] which results in a reduction of the size of the cluster being simulated.[81] Since our goal is to obtain a well-defined equilibrium ensemble of clusters of a given size, each Markov chain containing clusters that have undergone solvent evaporation is excluded from the final conformational sampling (in practice, acetonitrile is considered as evaporated from the cluster when it is farther than 20 Å from the ion). This is formally equivalent to adding a stepfunction to the configurational integral, so as not to take into account clusters which are not of the appropriate size.[82,83] Each run entails about 10^6 steps of equilibration, followed by an equivalent number of steps for data collection. The range of displacement for translational and rotational motion were chosen so as to obtain acceptance ratios between 40 and 60%. This typically corresponds to a displacement range of 0.25 Å for translation, and 25°, 0.25 and 25° for φ, cos θ, and ψ, respectively.

Cluster enthalpies are computed from the average energies <V> of the canonical ensembles of configurations as

$$\Delta H_n = \Delta U + \Delta(PV) = < V > + nRT, \qquad \text{(A2.1)}$$

where n is the number of solvent molecules in the cluster,[84] and stepwise binding enthalpies are simply obtained as

$$\Delta H_{n,n-1} = \Delta H_{n-1} - \Delta H_n. \qquad \text{(A2.2)}$$

Structural properties of the clusters are analyzed in terms of a distance-dependent coordination number $N_{coord}(r)$, and its derivative, which is the normalized radial probability distribution function

$$P(r) = \frac{dN_{coord}(r)}{dr} = n\frac{4\pi r^2 g(r)}{\int_0^\infty 4\pi r^2 g(r)dr} \quad . \tag{A2.3}$$

It should be noted that $P(r)$ differs from the radial distribution functions $g(r)$ used in liquid structure theory[78] by a factor $4\pi r^2$, and it actually represents spatial relative probabilities. The probabilities are normalized so that integral distributions equal the number of solvent molecules present in the cluster.

A1.II.B. Model Potentials

Early model potentials for acetonitrile did not explicitly include hydrogen atoms [72] or employ a very simple empirical potential function.[73] We tested a more recently proposed potential,[51] which includes Coulombic, distributed polarizability and repulsion-dispersion terms, but the model seems to underestimate solvent polarization effects in the presence of ions.[85] Another model was parameterized for pure acetonitrile[74] and sodium-acetonitrile[86] liquid simulations, based on ab initio calculations that do not take into account zero-point energy corrections for the acetonitrile-acetonitrile binding energy. Further, the sodium-acetonitrile polarization interactions were added to the potential function in an *ad hoc* fashion.[86] Hence, we have opted to develop a new model potential function describing both solvent-solvent interactions and ion-solvent interactions for simulating alkali and halide ions in acetonitrile clusters.

In our simulations, we employ rigid acetonitrile molecules and the interaction energy between various monomers (including the ion) consists of Coulombic, many-body polarization and repulsion-dispersion contributions,

$$V = V_{Coul} + V_{pol} + V_{rep-disp}. \tag{A2.4}$$

The Coulombic part,

$$V_{Coul} = \sum_i \sum_j \frac{q_i . q_j}{|\mathbf{r}_i - \mathbf{r}_j|}, \tag{A2.5}$$

simply represents the interactions between the fractional charges q_i on each atomic site (at position $\mathbf{r}_i$) of the monomers. The ion and each acetonitrile molecule carries an isotropic polarizable site (that is located on the middle carbon for CH_3CN) with a polarizability α_i and an induced dipole moment $\boldsymbol{\mu}_i$. The polarization contribution is expressed as[87]

$$V_{pol} = -\frac{1}{2} \sum_i \mathbf{E}_i^{\circ} . \boldsymbol{\mu}_i , \tag{A2.6}$$

where the electric field $\mathbf{E}_i^{\circ}$ due to the permanent charges of the other monomers is given by

$$\mathbf{E}_i^{\circ} = \frac{\sum_j q_j . \mathbf{r}_j}{|\mathbf{r}_i - \mathbf{r}_j|^3}, \tag{A2.7}$$

and the induced dipole moments are calculated from

$$\boldsymbol{\mu}_i = \alpha_i . \mathbf{E}_i = \alpha_i \left[\mathbf{E}_i^{\circ} + \sum_{j \neq i} T_{ij} . \boldsymbol{\mu}_j \right] \tag{A2.8}$$

in a self-consistent iterative procedure. T_{ij} in Eq. (A2.8) is the dipole tensor.[87] The polarizable sites included in the induced dipole problem of Eqs. (A2.6) to (A2.8) account for mutual polarization of the solvent molecules and the solute ion. In cluster simulations, the low dimensionality of the problem allows one to solve the set of linear equations in Eq. (A2.8) in matrix form.[88] In the present work, the induced dipoles are solved by LU decomposition and backsubstitution.[77] Finally, short-range repulsion and dispersion

interactions are modeled via Lennard-Jones potentials with well depth ε_{ij} and size parameter σ_{ij} between all atoms.

$$V_{rep-disp} = \sum_{i,j} 4\varepsilon_{ij}\left[\left(\frac{\sigma_{ij}}{r_{ij}}\right)^{12} - \left(\frac{\sigma_{ij}}{r_{ij}}\right)^{6}\right]. \qquad \text{(A2.9)}$$

First-principles quantum chemistry calculations provide the basis for the parameterization of our model potentials. Accordingly, we now turn our attention to ab initio calculations for small clusters.

A1.II.C. Ab Initio Calculations

Ground-state properties of $(CH_3CN)_{1\text{-}2}$, $Na^+(CH_3CN)_{1\text{-}4}$, $Cs^+(CH_3CN)_{1\text{-}3}$, and $I^-(CH_3CN)_{1\text{-}2}$ clusters were calculated with the quantum chemistry packages GAMESS[89] and Gaussian98.[90] Cluster structures were first optimized with acetonitrile molecules constrained to the isolated molecule geometry. The intramolecular coordinates were subsequently allowed to relax before a frequency calculation was performed in order to characterize the stationary points and obtain harmonic zero-point energies. This procedure allows estimation of the energy gain associated with monomer geometry relaxation in clusters, and to estimate the extent of the error introduced in our model potential by employing rigid solvent molecules. A number of model chemistries were tested, including Hartree-Fock (HF),[91] second-order Møller-Plesset (MP2),[91] and Becke 3 Lee-Yang-Parr (B3LYP) theories,[92,93] together with standard 6-31G(d) and 6-311+G(d) basis sets.[91] Stuttgart-Dresden-Bonn quasi-relativistic effective core potentials (ECP) and valence basis sets[94] with additional polarization functions were employed for the I^- and Cs^+ ions, and an all-electron 6-311+G(d) basis set recently reported for iodine was also used for comparison.[95] As will become evident in the following, we found that, overall,

the MP2/6-311+G(d) model chemistry is quite reliable, with the advantage of being computationally feasible for larger clusters. Energetics of the smaller clusters were also evaluated at the coupled cluster with single, double and linearized triple excitations [CCSD(T)] level of theory with a 6-311+G(2df,pd) basis set,[96] using the MP2/6-311+G(d) cluster geometries.

The cluster minimum energy structures obtained from ab initio calculations are shown in Fig. A2.1, and the results of the calculations are collected in Table A2.1 for a number of small clusters. Remarkably, the MP2/6-311+G(d) model chemistry reproduces the experimental CH_3CN geometry, which is essentially the same in the liquid phase[97] and in the gas phase, and the computed dipole moment compares very well to its experimental counterpart of 3.92 D.[98] This inspires confidence in this level of ab initio quantum chemistry. We are reporting geometric parameters in Table A2.1 for the clusters *after* monomer geometry relaxation to illustrate the effect of constraining monomer geometries to their experimental values. The latter is obviously not significant. In general, the C-H bonds are shortened by only 0.01 Å, relative to the isolated acetonitrile molecule, and the C-N bond lengthens by only 0.01 Å in $I^-(CH_3CN)_n$ clusters. Properties such as binding energies or charge distributions are actually not affected by monomer geometry constraints. The molecular dipole moments of individual monomers can be evaluated from the ESP charge distribution[99] of the supermolecule, and they are also listed in Table A2.1.

Binding energies (D_0) are calculated via the supermolecule approach, including zero-point energy corrections and a correction for basis set superposition error (BSSE) estimated with the Counterpoise method.[100]

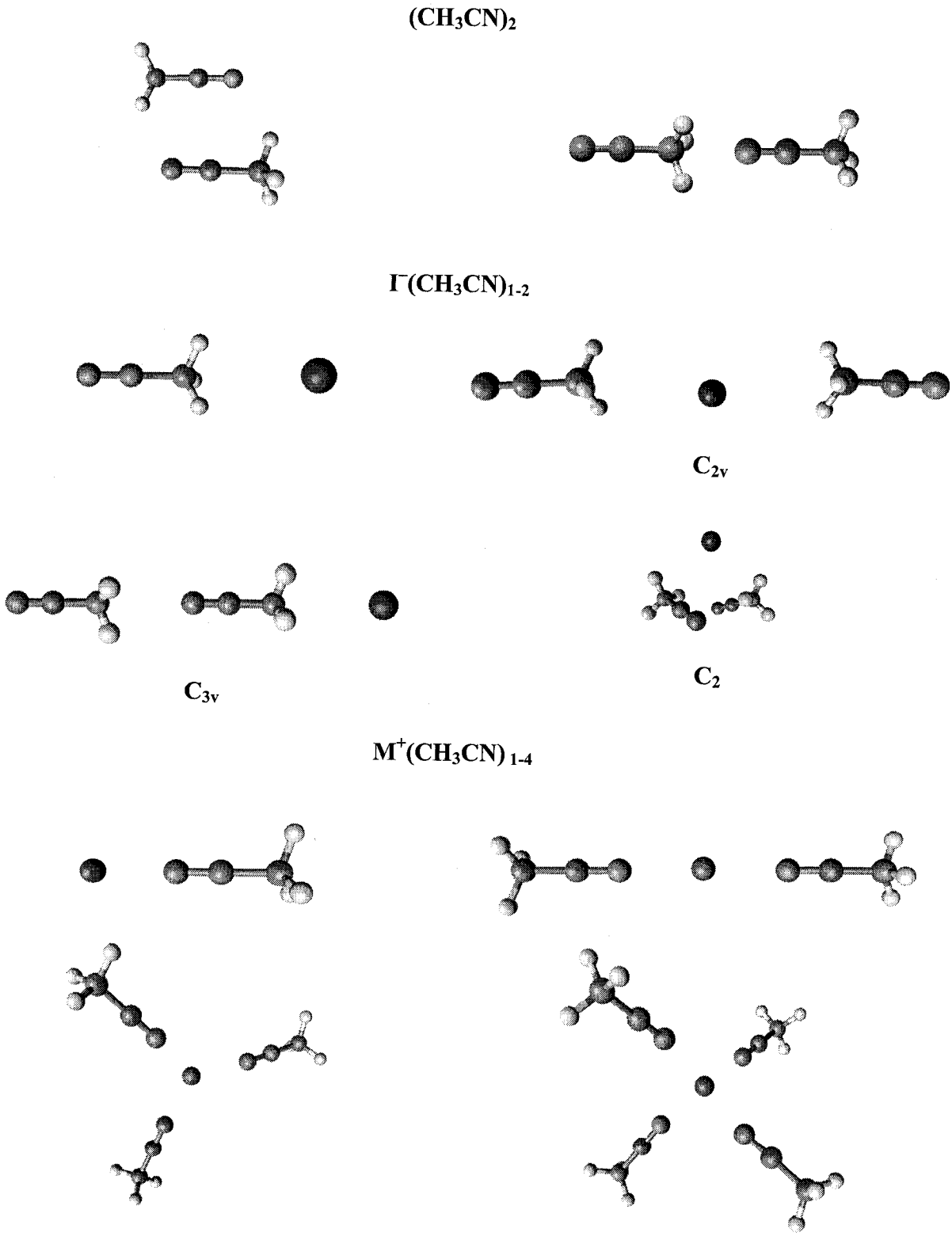

Fig. A2.1. Minimum energy structures of $(CH_3CN)_2$, $M^+(CH_3CN)_{1-4}$ [M=Cs,Na] and $I^-(CH_3CN)_{1-2}$ clusters predicted by the MP2/6-311+G(d) model chemistry.

The zero-point energy correction is based on the MP2/6-311+G(d) harmonic frequencies. Monomer relaxation in the Counterpoise calculations is not an issue here, since we constrain the acetonitrile molecules to the isolated molecule geometries in all calculations but for frequencies. Also, since the Counterpoise method tends to overestimate the BSSE,[101] we report binding energies with and without BSSE corrections. It is obvious from Table A2.1 that the zero-point energy and BSSE corrections to the binding energy amount to at most 2 kcal/mol for all clusters considered, except for $I^-(CH_3CN)_n$ clusters. Experimental binding enthalpies are listed in Table A2.1 for comparison and perspective; they may be good estimates of the binding energies, if enthalpies are not strongly temperature-dependent (assuming a rare gas relationship, stepwise room-temperature binding enthalpies might only differ by RT=0.6 kcal/mol from binding energies).

Previous calculations[102,103] of the potential energy surface for $(CH_3CN)_2$ have demonstrated the existence of two stable isomers for pure acetonitrile dimers (shown in Fig. A2.1), one with anti-parallel dipoles, and the other with linear head-to-tail dipoles, a finding that is supported by experimental evidence.[104] The binding energy of the linear local minimum (1.8 kcal/mol) was reported to be about half of that for the anti-parallel dimer configuration (3.7 kcal/mol).[102] Our MP2/6-311+G(d) calculations are consistent with these findings. The linear local minimum has C_{3V} symmetry, with the hydrogen atoms in an eclipsed configuration; the molecules are separated by a distance $r_{N\text{-}C}$=3.26 Å, and the presence of the nitrogen atom in the vicinity of the other acetonitrile molecule slightly increases that molecule's C-C_M-H bending angle (by 0.5°) in the relaxed structure.

Table A2.1. Properties of small pure-solvent and ionic clusters.[a]

	Geometric parameters					$D_e^{n,n-1}$ [b] (no BSSE)	$D_0^{n,n-1}$ [b] (no BSSE)	$D_0^{n,n-1}$ [b]	$\Delta H_{n,n-1}$ [c]	μ_{CH_3CN} [d]
				$(CH_3CN)_n$						
	$R_{C\text{-}C_M}$ [e]	$R_{C_M\text{-}H}$	$R_{C\text{-}N}$	$R_{C\text{-}C}$ [f]	$R_{N\text{-}H}$ [g]					
(CH_3CN)	1.46	1.10	1.17							3.9
$(CH_3CN)_2$ C_{2h}	1.46	1.09	1.17	3.35	2.55	6.4 (6.0)	5.7 (5.3)	4.3 (4.7)		4.2, 4.2
$(CH_3CN)_2$ C_{3v}	1.46	1.09	1.17			3.0 (3.2)	2.8 (2.9)	2.2 (2.5)		4.3, 4.0
				$Na^+(CH_3CN)_n$						
	$R_{C\text{-}C_M}$	$R_{C_M\text{-}H}$	$R_{C\text{-}N}$	$R_{Na\text{-}N}$						
$Na^+(CH_3CN)$	1.46	1.09	1.17	2.31		30.7 (31.1)	30.0 (30.4)	29.3 (29.5)		5.4
$Na^+(CH_3CN)_2$	1.46	1.09	1.17	2.34		26.7	26.1	25.1	24.4 ± 0.3 [h]	4.9
$Na^+(CH_3CN)_3$	1.46	1.09	1.17	2.38		20.3	19.8	19.1	20.6 ± 0.5	4.8
$Na^+(CH_3CN)_4$	1.46	1.09	1.17	2.41		16.2	15.5	14.2	14.9 ± 0.2	4.7

a. All properties are calculated with the MP2/6-311+G(d) model chemistry, except for the numbers in parenthesis which are CCSD(T)/6-311+G(2df,pd)//MP2/6-311+G(d) values. SDD effective core potentials (ECP) are used as indicated, all other results are obtained from all-electron calculations. Internuclear distances are in angstroms (Å) and binding energies in kcal/mol.

b. Stepwise binding energies for clusters of size n. D_e is the classical binding energy while D_0 is the zero-point-energy-corrected binding energy. Values are corrected for BSSE unless indicated otherwise.

c. Experimental stepwise binding enthalpy in kcal/mol.

d. Dipole moment of acetonitrile molecule(s) in Debye (D), calculated from ESP charge distributions.

e. C_M is the methyl carbon.

f. Distance between the central carbons of the acetonitrile molecules.

g. Distance between the nitrogen atom of a molecule and the hydrogen in the symmetry plane of the other molecule.

h. Taken from Ref. [105].

	Geometric parameters				$D_e^{n,n-1}$ [b] (no BSSE)	$D_0^{n,n-1}$ [b] (no BSSE)	$D_0^{n,n-1}$ [b]	$\Delta H_{n,n-1}$ [c]	μ_{CH_3CN} [d]
$Cs^+(CH_3CN)_n$ [ECP]									
	$R_{C\text{-}C_M}$	$R_{C_M\text{-}H}$	$R_{C\text{-}N}$	$R_{Cs\text{-}N}$					
$Cs^+(CH_3CN)$	1.46	1.09	1.17	3.17	17.4 (19.2)	17.0 (18.8)	16.5 (18.1)	19.2 ± 0.1[i]	4.7
$Cs^+(CH_3CN)_2$	1.46	1.09	1.17	3.22	15.5	15.2	13.0	16.7 ± 0.1	4.7
$Cs^+(CH_3CN)_3$	1.46	1.09	1.17	3.22	13.5	13.4	12.7	14.3 ± 0.1	4.6
$I^-(CH_3CN)_n$									
	$R_{C\text{-}C_M}$	$R_{C_M\text{-}H}$	$R_{C\text{-}N}$	$R_{C_M\text{-}I}$					
$I^-(CH_3CN)$	1.46	1.09	1.18	3.70	11.5 (10.9)	11.4 (10.9)	9.9 (10.5)	11.0 ± 0.2[j]	5.0
$I^-(CH_3CN)_2$ C_{3v}	1.46	1.09	1.18	3.65, 9.43	6.2	6.2	5.4		5.0, 5.0
$I^-(CH_3CN)_2$ C_2	1.46	1.09	1.18	3.95	11.1	10.1	7.2	10.4 ± 0.2[j]	5.0
$I^-(CH_3CN)_2$ C_{2v}	1.46	1.09	1.18	3.95	10.0	9.8	9.0		4.7
$I^-(CH_3CN)_n$ [ECP]									
	$R_{C\text{-}C_M}$	$R_{C_M\text{-}H}$	$R_{C\text{-}N}$	$R_{C_M\text{-}I}$					
$I^-(CH_3CN)$	1.46	1.09	1.18	3.76	12.4 (11.1)	12.0 (10.6)	8.4 (10.1)	11.0 ± 0.2[j]	5.7
$I^-(CH_3CN)_2$ C_{3v}	1.46	1.09	1.18	3.71, 9.50	6.5	6.1	5.2		4.6, 4.4
$I^-(CH_3CN)_2$ C_2	1.46	1.09	1.18	3.94	9.9	8.9	6.2	10.4 ± 0.2[j]	5.2

i. Taken from Ref. [106].
j. Taken from Ref. [105].

The anti-parallel configuration has C_{2h} symmetry, with the molecular axes in the σ_h symmetry plane and the hydrogen atoms in this plane pointing toward the nitrogen atom of the other molecule, and the central carbons are separated by 3.35 Å, which incidentally corresponds to the interchain spacing reported in the liquid phase.[106] Because of a slight bending of the C_M-C-N axis (179.3°) in the relaxed structure, the monomers lose their C_{3V} symmetry, but the energy gained by allowing this slight deformation is only 0.2 kcal/mol. The binding energies obtained in this work for both dimer structures are in good qualitative agreement with those previously reported,[102] but our calculations predict slightly larger binding energies, i.e. 2.2 kcal/mol for the C_{3V} linear dimer and 4.3 kcal/mol for the C_{2h} anti-parallel configuration with MP2/6-311+G(d). Higher-level CCSD(T)/6-311+G(2df,pd)//MP2/6-311+G(d) calculations also support larger binding energies for the acetonitrile dimers. Finally, we note that the mutual polarization of the acetonitrile molecules in the dimer is not negligible, and increases the dipole moments of the acetonitrile molecules by ~10%.

Previous ab initio calculations at the HF level with a double-zeta-quality valence basis set[52] predicted stable high-symmetry structures for $Na^+(CH_3CN)_n$ clusters, with the ion aligned in the acetonitrile molecular axis (on the nitrogen side). The structures obtained in the present work for small $Na^+(CH_3CN)_n$ clusters are in good agreement with this finding, and the cluster structures (shown in Fig. A2.1) are found to be linear, trigonal planar, and tetrahedral for n=2, 3 and 4, respectively. The sodium ion is found to lie between 2.3 Å and 2.4 Å from the acetonitrile nitrogen, with a separation increasing with cluster size. This distance is slightly larger than the separation observed in previous work,[52,107] which arises from inclusion of electronic correlation in our calculations. For

clusters sizes 2 to 4, the MP2/6-311+G(d) binding energies are within *ca.* 1 kcal/mol of the available experimental binding enthalpies. This is quite an improvement over previous results,[52] which deviated from experimental values by 5 kcal/mol, again because of the lack of electronic correlation. Finally, we note that increasing the size of the basis set and using a higher level of theory only improve the binding energy of $Na^+(CH_3CN)$ by 0.2 kcal/mol.

To our knowledge, no prior calculations have been reported for cesium-acetonitrile complexes. The minimum energy structures of $Cs^+(CH_3CN)_n$ clusters are similar to those obtained for sodium clusters. It should be noted that the $Cs^+(CH_3CN)_2$ minimum energy structure is found to be linear, and not slightly bent like that of $Cs^+(H_2O)_2$.[108] The ion-nitrogen distance increases from 2.34 Å in $Na^+(CH_3CN)_n$ to 3.17 Å in $Cs^+(CH_3CN)_n$ clusters. Structural similarities can be attributed to the fact that both Cs^+ and Na^+ are monovalent ions, giving rise to similar electrostatic interactions with acetonitrile molecules, and not surprisingly, electrostatic interactions seem to govern the determination of the cluster structure. However, because of the larger size and more diffuse positive charge of Cs^+, the ion-molecule interactions are weaker. This results, not only in larger ion-molecule equilibrium distances, but also in smaller binding energies for $Cs^+(CH_3CN)_n$ clusters relative to those for $Na^+(CH_3CN)_n$. For instance, the CCSD(T)/6-311+G(2df,pd)//MP2/6-311+G(d) binding energy is 29.5 kcal/mol for $Na^+(CH_3CN)$, while it is only 18.1 kcal/mol for $Cs^+(CH_3CN)$. If the latter number is in good agreement with the experimental $Cs^+(CH_3CN)$ binding enthalpy, in general the MP2/6-311+G(d) binding energies seem to deviate from experimental binding enthalpies significantly more

for $Cs^+(CH_3CN)_n$ clusters than for $Na^+(CH_3CN)_n$. This could be due to a poorer description of the ion-solvent interactions due to the ECP treatment of the cesium ion.

We now turn our attention to small iodide-acetonitrile complexes. The optimized geometry of the $I^-(CH_3CN)$ cluster has the ion in the C_{3v} axis, but obviously on the methyl side of acetonitrile.[109] The strong electrostatic attraction between the hydrogen atoms of acetonitrile and the ion cause a slight distortion of the C-C_M-H angle (by 1°) in the relaxed $I^-(CH_3CN)$ structure. The all-electron MP2/6-311+G(d) binding energies for $I^-(CH_3CN)$, with and without BBSE correction, bracket the experimental number for the cluster binding enthalpy, and high-level CSSD(T) calculations seem to perform remarkably well. The binding energies obtained with ECPs, with and without BSSE correction, also bracket the experimental number, but they deviate from the latter more significantly. Despite the similar size of the ions, the binding energy of $I^-(CH_3CN)$ is less than that of $Cs^+(CH_3CN)$, because of the weaker interaction of acetonitrile with negative ions. The latter is due to the diffuse distribution of the positive pole of the dipole over the H atoms of the molecule, while interactions with cations via the charge-concentrated negative nitrogen are much stronger.

For $I^-(CH_3CN)_2$, three isomers which lie close in energy were identified.[110] According to the MP2/6-311+G(d) calculations reported here, the most stable structure has a C_{2v} quasi-linear configuration ($\alpha_{CM\text{-}I\text{-}CM}$=168°), with the methyl groups in eclipsed configuration. The second isomer corresponds to a C_{3v} structure, higher in energy by 3 to 4 kcal/mol, with the acetonitrile molecules aligned on one side of the ion and the iodide ion along the acetonitrile molecular axis. The last isomer has C_2 symmetry, with the acetonitrile molecules oriented in a perpendicular fashion, and results from a combination

of hydrogen bonding of acetonitrile to the ion and ion-dipole interactions.[110] The latter isomer has a calculated binding energy comparable to that of the C_{2v} isomer, especially before inclusion of the approximate BSSE correction. We note that the results are obviously very sensitive to the choice of model chemistry and the treatment of BSSE, and a more comprehensive study of the actual nature of the $I^-(CH_3CN)_2$ structure is reported elsewhere.[110] We also note that previous studies[56] of $Br^-(CH_3CN)_n$ clusters employing density functional theory showed comparable results but with some additional structures involving hydrogen bonding. A full discussion of anionic-acetonitrile clusters and the sensitivity of the results to the model chemistry employed will also be given somewhere else.[111]

Finally, the magnitude of the ESP charge of the ions in the ionic clusters (not listed) is *ca.* ±0.98e, which demonstrates very little electron transfer between the ion and the solvent molecules. This provides support for a model potential primarily based on electrostatics and employing unit point charges for the ions. We note from the molecular dipole moments listed in Table A2.1 that the CH_3CN polarity increases significantly from its gas-phase value when placed in the vicinity of another solvent molecule or an ion. For example, the acetonitrile dipole moment increases by 0.3 D in the presence of another solvent molecule and by 1.0 to 1.5 D in the presence of an ion.

A1.II.D. Parameterization of Model Potentials

The parameters for our model potential include point charges (q_i), polarizabilities (α_i), and Lennard-Jones terms (ε_{ij},σ_{ij}). All parameters are derived on the basis of ab initio data, with the exception of polarizabilities, and are listed in Table A2.2.

Table A2.2. Model potential parameters[a]

	Atomic point charges						
	N	C	C_M	H	Na	I	Cs
q_i	-0.49	0.48	-0.56	0.19	1.00	-1.00	1.00
	Molecular and ionic polarizabilities						
	CH_3CN		Na^+		I^-		Cs^+
α_I	4.5		0.2		5.3		3.1
	Solvent-solvent Lennard-Jones parameters						
	N-N	C-N	H-N	C-C	H-C	H-H	
ε_{ij}	50	30	50	3	40	40	
σ_{ij}	3.50	3.60	2.70	3.80	2.80	1.90	
	Ion-solvent Lennard-Jones parameters						
	Na^+-N	Na^+-C	Na^+-H	Cs^+-N	Cs^+-C	Cs^+-H	I^--N	I^--C	I^--H
ε_{ij}	50	500	50	800	750	700	40	857	34
σ_{ij}	3.00	3.40	2.30	3.20	4.30	3.30	4.52	3.20	3.95

a. Point charges (q_i) in fractions of e, polarizabilities (α_i) in $Å^3$, Lennard-Jones parameters ε_{ij} in cal/mol and σ_{ij} in Å.

As discussed in the previous section, the ab initio data was obtained for pure-solvent and ionic clusters where the acetonitrile molecule is typically constrained to the isolated molecule geometry, since our model potential employs rigid solvent molecules with that geometry. We did ensure that monomer geometry relaxation had very little impact on the ab initio predictions of such properties such as cluster geometries, binding energies and electric properties. The fractional atomic charges for acetonitrile are assigned on the basis of the MP2/6-311+G(d) ESP charge distribution, which is obtained by fitting the electrostatic potential over a large grid of points,[112] while the ions simply carry a positive or negative unit charge. Polarizabilities are notoriously difficult to determine accurately with quantum chemistry, and thus the polarizabilities associated with the ionic and molecular polarizable sites are taken from gas-phase experimental data.[113,114] Finally, the Lennard-Jones parameters (σ_{ij},ε_{ij}) are adjusted[115] to fit the $(CH_3CN)_2$, the $Na^+(CH_3CN)_{1\text{-}2}$, the $Cs^+(CH_3CN)_{1\text{-}2}$ and the $I^-(CH_3CN)_{1\text{-}2}$ calculated

geometries and binding energies.[116] Attention is also paid to the dipole moments of acetonitrile in clusters, which primarily depend on the cluster geometry. The fitting procedure was performed with a non-linear-least-squares program based on the Marquardt-Levenberg algorithm.[77]

Inspection of Table A2.3 shows that structural properties for $(CH_3CN)_2$, $Na^+(CH_3CN)_{1-4}$, $Cs^+(CH_3CN)_{1-3}$, and $I^-(CH_3CN)$ determined with our model potentials agree well with their ab initio counterpart.

Table A2.3. Properties of small clusters predicted by the model potential[a]

	R_{C-C}	R_{N-H} [b]	$R_{Cation-N}$	R_{I-C_M}	$D_0^{n,n-1}$ [c]	μ_{CH_3CN} [d]
$(CH_3CN)_2$	3.35	2.57			4.7	4.3
			$Na^+(CH_3CN)_n$			
$Na^+(CH_3CN)$			2.30		29.3	5.6
$Na^+(CH_3CN)_2$			2.33		25.9	5.4
$Na^+(CH_3CN)_3$			2.35		20.7	5.2
$Na^+(CH_3CN)_4$			2.38		16.2	4.9
			$Cs^+(CH_3CN)_n$			
$Cs^+(CH_3CN)$			3.15		18.6	5.1
$Cs^+(CH_3CN)_2$			3.17		16.4	4.9
$Cs^+(CH_3CN)_3$			3.19		14.4	4.8
			$I^-(CH_3CN)_n$			
$I^-(CH_3CN)$				3.68	10.5	4.7
$I^-(CH_3CN)_2$ C_{3v}				3.65/8.83	5.3	4.9/4.3
$I^-(CH_3CN)_2$ C_2				3.61	8.6	4.7
$I^-(CH_3CN)_2$ C_{2v}				3.73	9.7	4.6

a. Internuclear distances in Å.
b. Distance between the nitrogen atom of a molecule and the hydrogen in the symmetry plane of the other molecule in Å.
c. Stepwise binding energy in kcal/mol.
d. Molecular dipole moment of acetonitrile in D.

For instance, bond lengths are reproduced within 3 % for all clusters. This is an indication of the reliability of the model potential for reproducing cluster geometries. Not

surprisingly, energetic properties such as stepwise binding energies are less accurately reproduced with simple model potentials, when compared to the ab initio data, and the difference between the two increases with cluster size. However, the model binding energies are still within ~2 kcal/mol of the quantum chemistry values, which may be the error bar that one can assign to the ab initio results in the first place. Finally, the CH_3CN dipole moments seem to be reproduced almost quantitatively with the simple induction model of our potential. This model is, to our knowledge, the first one to succesfully reproduce a significant increase of the CH_3CN polarity from its gas-phase value when placed in the vicinity of another solvent molecule or an ion, as discussed earlier. For example, the acetonitrile dipole moment increases by 0.4 D in the presence of another solvent molecule and by 1.0 to 1.7 D in the presence of an ion.

A2.III. RESULTS AND DISCUSSION

A2.III.A. Thermodynamic Properties

The stepwise binding enthalpies obtained from room-temperature Monte Carlo simulations are listed in Table A2.4. Comparison with the experimental stepwise binding enthalpies for small clusters suggests that our model potentials are adequate for describing many-body interactions in the larger clusters. The largest deviations of the stepwise binding enthalpy are 1.3 kcal/mol, 1.3 kcal/mol, and 0.9 kcal/mol for $Na^+(CH_3CN)_n$, $Cs^+(CH_3CN)_n$ and $I^-(CH_3CN)_n$ clusters, respectively. To our knowledge, the $Na^+(CH_3CN)$ binding enthalpy has not been measured experimentally, and the results of our simulations suggest that we can predict this number to be 29 kcal/mol with some degree of confidence.

Table A2.4. Stepwise binding enthalpies $\Delta H_{n,n-1}$

	$Na^+(CH_3CN)_n$		$Cs^+(CH_3CN)_n$		$I^-(CH_3CN)_n$	
n	Calculated [a]	Expt. [b]	Calculated [a]	Expt. [c]	Calculated [a]	Expt. [d]
1	28.8		19.1	19.2	9.8	11.0
2	25.2	24.4	16.9	16.7	8.9	10.4
3	20.1	20.6	14.7	14.3	7.7	9.2
4	15.3	14.9	12.4	12.1	6.5	7.8
5	11.4	12.7	9.6	10.9	6.2	7.1

a. Stepwise binding enthalpies obtained from room-temperature Monte Carlo simulations.
b. Taken from Ref. [105].
c. Taken from Ref. [107].
d. Taken from Ref. [117].

The calculated binding enthalpies are displayed as a function of cluster size in Fig. A2.2. One might expect the stepwise binding enthalpy to reach a plateau converging to the liquid-phase enthalpy of vaporization. This is illustrated in the top panel of Fig. A2.2, where the reduced binding enthalpies, i.e. the binding enthalpies per solvent molecule $\Delta H_n / n$, are shown as a function of cluster size n. The reduced binding enthalpy is closely related to the average amount of heat necessary to vaporize one acetonitrile molecule from the cluster. We note that all curves seem to converge to the liquid-phase acetonitrile heat of vaporization, ΔH_{vap}=7.9 kcal/mol.[118] For example, the deviations observed are respectively 1.4 kcal/mol, 2.8 kcal/mol and 1.7 kcal/mol for $Na^+(CH_3CN)_{36}$, $Cs^+(CH_3CN)_{36}$ and $I^-(CH_3CN)_{36}$ clusters, respectively. Moreover, the reduced binding enthalpies are smaller than the experimental heat of vaporization at medium cluster size such as n=36. This can be attributed either to the limits of our model potentials or to cluster edge effects.

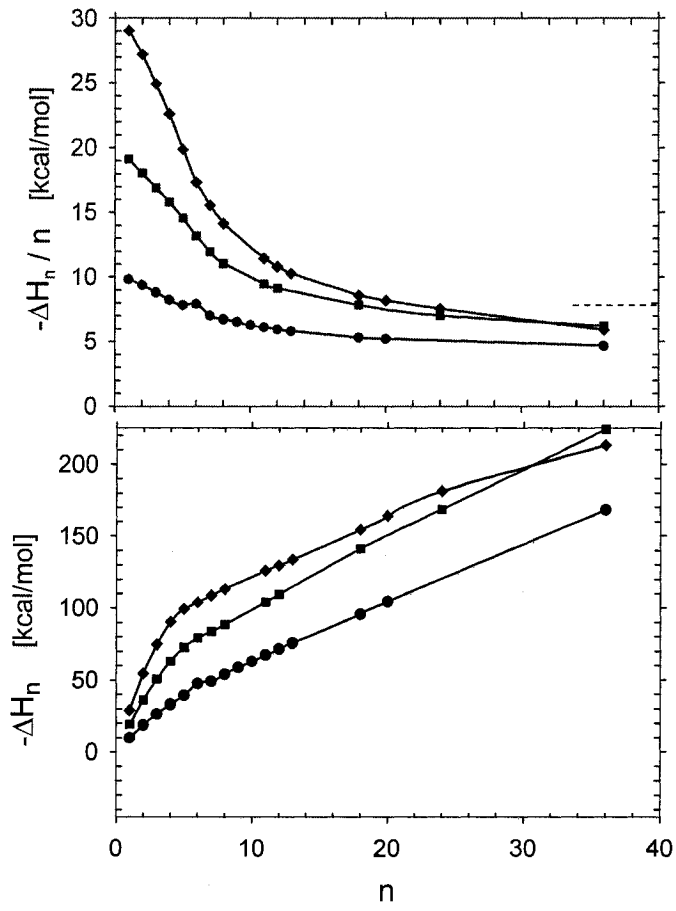

Fig. A2.2. Binding enthalpies ΔH_n from room-temperature Monte Carlo simulations for $Na^+(CH_3CN)_n$ [diamonds], $Cs^+(CH_3CN)_n$ [squares] and $I^-(CH_3CN)_n$ [circles] as a function of cluster size. The top panel displays reduced binding enthalpies $\Delta H_n / n$. The dashed line in the top panel is the acetonitrile experimental heat of vaporization.

The calculation of the actual heat of vaporization of bulk acetonitrile predicted by our model potentials is left for future work,[119] and it is unclear at this stage whether our model potentials will produce a heat of vaporization in quantitative agreement with experiment. However, cluster edge effects may provide a more likely explanation. On the surface of ionic clusters, there is a deficiency of acetonitrile molecules relative to the bulk liquid situation, which results in less solvation energy for the surface solvent molecules

and leads to an underestimation of the reduced binding enthalpy. These findings, as well as the very slow convergence of binding enthalpies to their bulk counterpart with cluster size, are consistent with earlier predictions of the liquid drop model.[120]

Finally, the bottom panel of Fig. A2.2 illustrates the fact that stepwise binding enthalpies (i.e. the slopes of the curves in the bottom panel of Fig A2.2) decrease with increasing cluster size. As the number of acetonitrile molecules increases, the relative importance of the stronger ion-acetonitrile interactions becomes less significant. Moreover, the decrease observed for smaller ions is faster than that for larger ones, which may reflect the ability of smaller ions to complete solvation shells more rapidly. As a matter of fact, we observe two clearly distinct regimes for cation-acetonitrile clusters that we can actually relate to the cluster structural properties: binding enthalpies first increase very fast up to n=6 for $Na^+(CH_3CN)_n$ and n=7 for $Cs^+(CH_3CN)_n$ clusters, corresponding to strong ion-acetonitrile interactions for the molecules close to the ion; then the binding enthalpy increase seems to slow down considerably, because of weaker contributions from solvent molecules further away from the ion. Similar features can be found for $I^-(CH_3CN)_n$ clusters, but they are not as pronounced, because of a less well-defined solvation shell structure. As we shall see shortly, binding enthalpies are closely related to the structure of ionic clusters. Accordingly, we now turn our attention to the structural properties of the clusters.

A2.III.B. Structural Properties

Fig. A2.3 shows some representative structures of $Na^+(CH_3CN)_n$, $Cs^+(CH_3CN)_n$ and $I^-(CH_3CN)_n$ clusters obtained from room-temperature simulations, for cluster sizes n=12 and 36. The coordination of acetonitrile to ions is naturally via the nitrogen for

cations and the methyl hydrogens for iodide, and the corresponding cluster radial probability distributions are shown in Figs. A2.4 and A2.5. As can be seen immediately from Fig. A2.3, the Na^+, Cs^+ and I^- ions all appear to reside inside the solvent cluster. This interior solvation is a result of the stabilization gained by fully solvating the ion, which seems to overcome the loss of free energy associated with disrupting the solvent structure.[106] In other words, the ion-solvent interactions seem to prevail over solvent-solvent interactions in determining the structure of ionic acetonitrile clusters.

Inspection of Fig. A2.4 reveals that both $Na^+(CH_3CN)_n$ and $Cs^+(CH_3CN)_n$ clusters exhibit a very clear solvation shell structure, identified by sharp, distinct peaks in the probability distributions. The size of the first coordination sphere of $Na^+(CH_3CN)_n$ clusters is *ca.* 6, which happens to be the same as that computed for the liquid phase with another model potential.[86] We note that, even though the model potentials employed are different,[119] it is not uncommon to find similar coordination numbers for the first solvation shell of ions in both cluster and liquid simulations.[50,54] Since Cs^+ is a larger and more diffuse positive ion than Na^+, the lower binding energy and larger ion-acetonitrile equilibrium distance result in cesium cluster structural properties with broadened peaks in the probability distributions relative to those for sodium clusters. Because of the larger ion-acetonitrile equilibrium distance in $Cs^+(CH_3CN)_n$, solvent steric effects are less significant and the size of the first coordination sphere for $Cs^+(CH_3CN)_n$ clusters increases to 7, compared to that of $Na^+(CH_3CN)_n$ clusters.

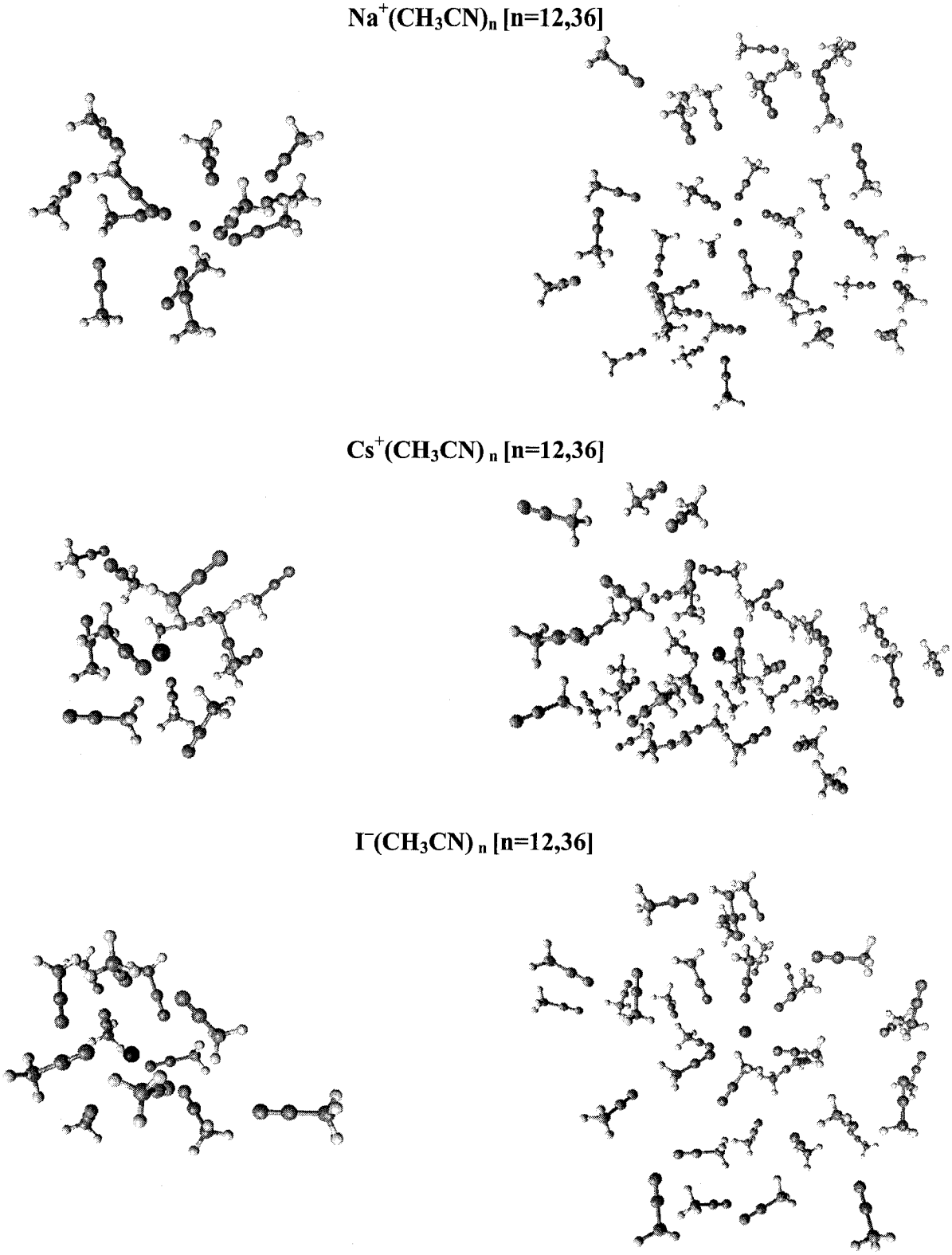

Fig. A2.3. Representative structures of room-temperature $Na^+(CH_3CN)_n$, $Cs^+(CH_3CN)_n$ and $I^-(CH_3CN)_n$ clusters [n=12 and 36] obtained from Monte Carlo simulations employing model potentials.

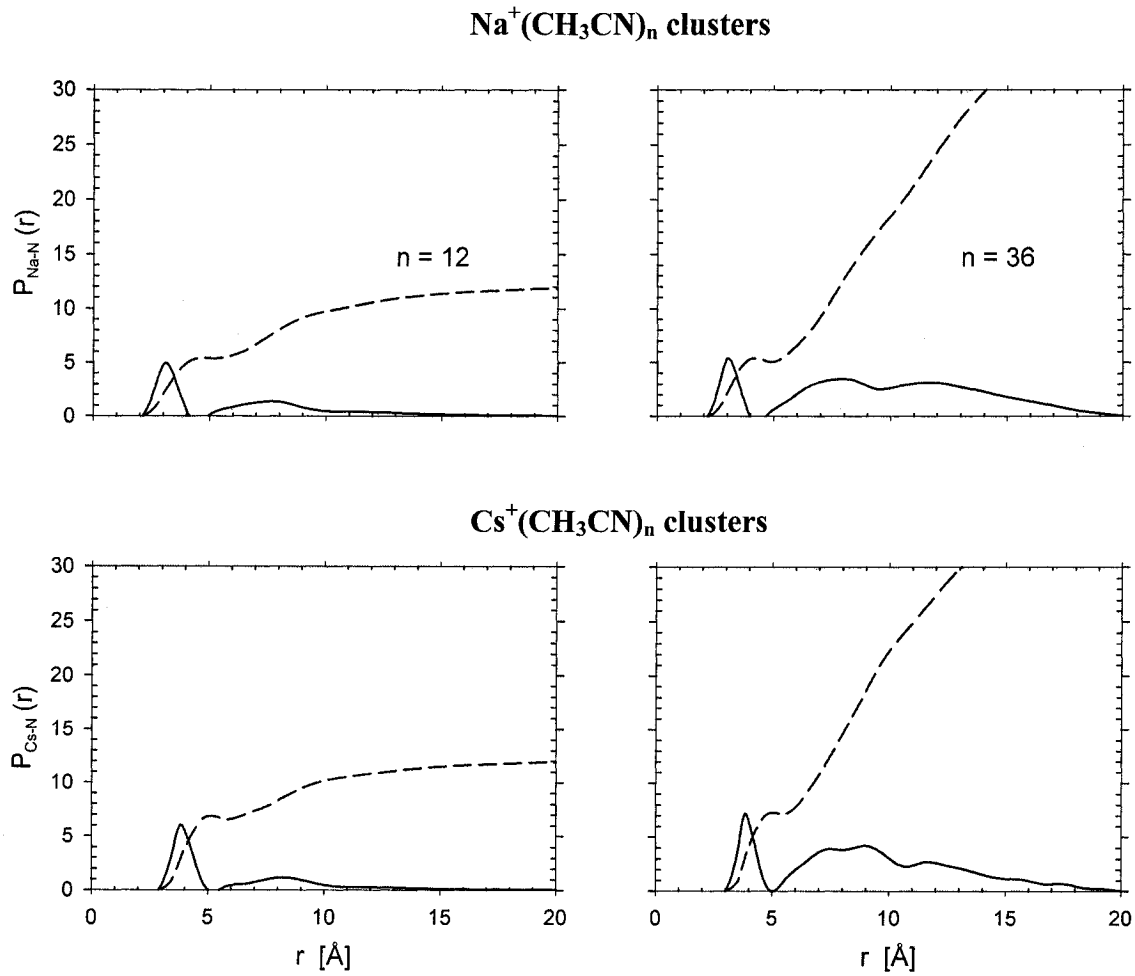

Fig. A2.4. Structural properties of $Na^+(CH_3CN)_n$ [top panel] and $Cs^+(CH_3CN)_n$ [bottom panel] obtained from Monte Carlo simulations. Solid curves are radial probability distribution functions $P(r)$, while dashed curves are the distance-dependent coordination number $N_{coord}(r)$, i.e. the integral of $P(r)$.

In cationic clusters, the high dipole moment of acetonitrile is fully effective towards solvation of the cations via strong interactions of the metal with the charge concentrated negative nitrogen. On the other hand, because of weaker anion-solvent interactions, via the diffuse charge distribution spread over the hydrogens of acetonitrile, very broad radial probability distributions are observed for $I^-(CH_3CN)_n$ clusters in Fig. A2.5. The spacing between the first two peaks in the ion-hydrogen $P_{H\text{-}I}(r)$ probability distributions roughly

corresponds to the distance between two hydrogens in acetonitrile. Interestingly enough, the solvation shell structure is not immediately evident from the $P_{H\text{-}I}(r)$ probability distributions. However, when one plots the ion-methyl carbon $P_{I\text{-}CM}(r)$ probability distributions (bottom panel of Fig. A2.5), it becomes evident that $I^-(CH_3CN)_n$ clusters adopt an interior solvation shell structure. The peaks in the $P_{H\text{-}I}(r)$ probability distributions in fact correspond to averages over three possible acetonitrile hydrogens interacting with the ion. Whenever one hydrogen is directly coordinated to the ion, the other two are likely to be further away from the ion. As a result of averaging over all hydrogen-iodide distances, multiple peaks appear in the $P_{H\text{-}I}(r)$ probability distribution even though the clusters have a clearly defined shell structure.

The marked differences observed in the solvation of positive and negative ions are a direct consequence of the nature of the charge distribution of the dipolar solvent molecule. The results for iodide-acetonitrile clusters are also in contrast with results with other solvents such as water, where only one hydrogen per solvent molecule would point towards the ion and the first solvation shell would be represented by a single peak in the ion-hydrogen radial probability distribution. Accordingly, we now turn our attention to a comparison between ion-acetonitrile and ion-water clusters.

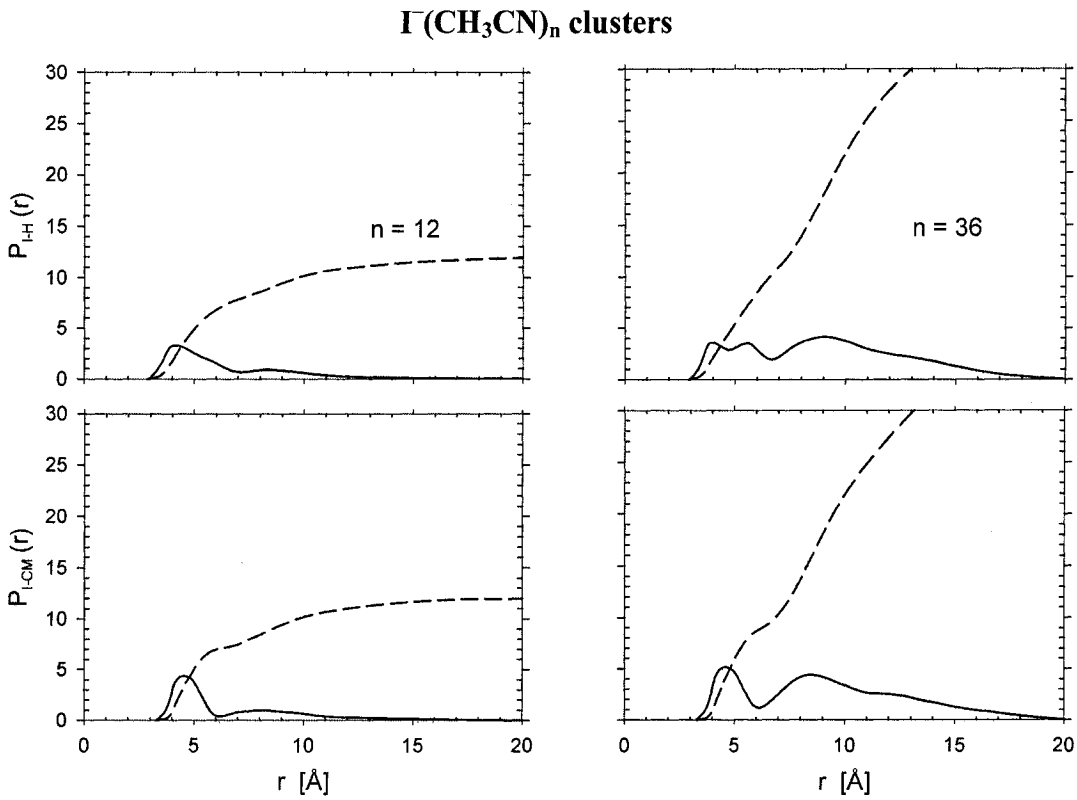

Fig. A2.5. Structural properties of $I^-(CH_3CN)_n$ clusters obtained from Monte Carlo simulations. The top panel shows the ion to hydrogen distance $P_{I\text{-}H}$ (r) probability distribution, and the bottom panel the ion to methyl carbon distance $P_{I\text{-}CM}$ (r) probability distribution. Solid curves are radial probability distribution functions $P(r)$, while dashed curves are the distance-dependent coordination number $N_{coord}(r)$, i.e. the integral of $P(r)$.

A2.III.C. Comparison with Aqueous Clusters

Inspection of the iodide-acetonitrile cluster radial probability distributions show that, unlike water, solvent molecules in large acetonitrile clusters are not clearly structured at room temperature. In general, the weak bonding of the solvent molecules and the dipole-dipole nature of the solvent-solvent interactions produce solvent clusters where orientation of any given molecule is correlated only with those of its immediate neighbors, a finding that was observed in high-pressure mass spectroscopy studies of

pure clusters.[97,98] On the other hand, it is well known that the water network is well organized in clusters such as $Na^+(H_2O)_n$ and $I^-(H_2O)_n$ clusters, because of relatively strong hydrogen-bonding interactions between water molecules.[41] Another major difference between acetonitrile and water is the solvent molecular size, which causes a significant increase in the ion-molecule distances in clusters, and results in much weaker interactions between the ions and more distant solvent molecules, in the second solvation shell for example.

In both $Na^+(CH_3CN)_n$ and $Na^+(H_2O)_n$ clusters, the strong sodium-solvent interactions overcome solvent-solvent interactions, and the ion is thus located inside the solvent cluster. Despite the difference in the solvent molecular size, both $Na^+(CH_3CN)_n$ and $Na^+(H_2O)_n$ clusters have a first-solvation-shell coordination number of 6.[41] The ion also tends to reside in the interior of the solvent cluster for $I^-(CH_3CN)_n$, in sharp contrast with the situation of $I^-(H_2O)_n$ clusters, where the ion-solvent interactions are not strong enough to allow the ion to disrupt the water network, and consequently, the ion tends to remain at the surface of the cluster up to relatively large cluster sizes.[55,70] This feature is very well illustrated by the large ion-solvent-center-of-mass (r_{cm}) distances and the nonuniform distributions of the angle θ between solvent molecules, the ion and the solvent center of mass observed for $I^-(H_2O)_n$ clusters.[41] Obviously, when the distribution of solvent molecules is not spherically symmetric around the ion, the solvent center of mass is displaced from the ion, and the angular distribution differs significantly from a $\sin\theta$ function.

Again because of the very different solvent molecular size, ionic clusters of the same size *n* will have different physical sizes. For example, $Na^+(H_2O)_{20}$ and $I^-(H_2O)_{20}$

clusters have an approximate radius of 5 Å, while their acetonitrile counterparts have a radius of 9 Å. For this reason and for purpose of comparison between various solvents, we decided to focus on the distributions of ion-solvent-center-of-mass distances relative to the cluster radius (r'_{cm}). Shown in Fig. A2.6 are such distributions for sodium and iodide ions in water and acetonitrile clusters.

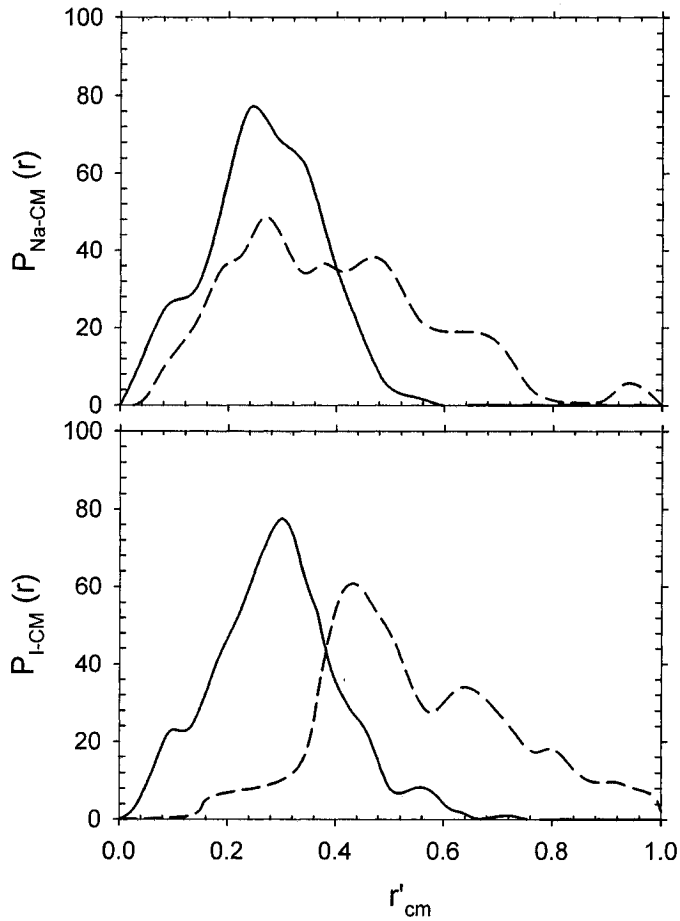

Fig. A2.6. Probability distributions of the scaled ion-solvent-center-of-mass distance r'_{cm} (see text) for ion-acetonitrile clusters (solid curve) and ion-water clusters (dashed curve). The top panel displays results for $Na^+(CH_3CN)_n$ and $Na^+(H_2O)_n$, and the bottom panel those for $I^-(CH_3CN)_n$ and $I^-(H_2O)_n$.

It is immediately evident that $Na^+(CH_3CN)_n$ and $Na^+(H_2O)_n$ clusters have a very similar *interior* solvation structure, while that of $I^-(CH_3CN)_n$ and $I^-(H_2O)_n$ clusters differ significantly, i.e. $I^-(CH_3CN)_n$ have interior structures and $I^-(H_2O)_n$ have surface structures. Further support for this fact is provided by the distributions of the angle θ between solvent molecules, the ion and the solvent center of mass shown in Fig. A2.7.

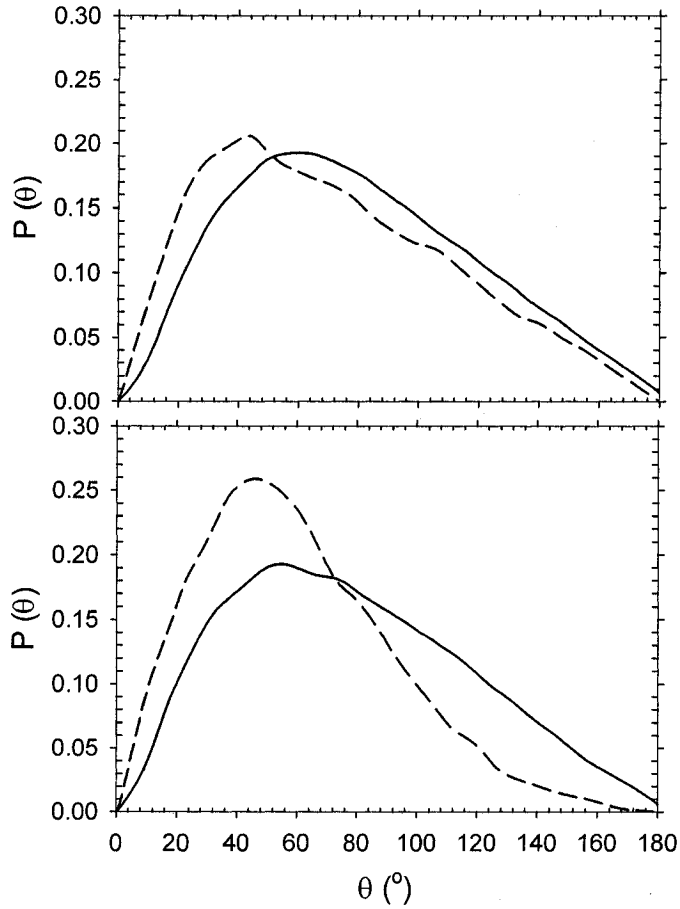

Fig. A2.7. Angular probability distributions for ion-acetonitrile clusters (solid curve) and ion-water clusters (dashed curve). The angle θ is that between an individual solvent molecule, the ion and the solvent cluster center of mass, as described in Ref. [41]. The top panel displays results for $Na^+(CH_3CN)_n$ and $Na^+(H_2O)_n$, and the bottom panel those for $I^-(CH_3CN)_n$ and $I^-(H_2O)_n$.

While there is a clear deficiency of water molecules on the ion side directly opposite to the solvent center of mass, indicative of surface solvation, the angular distribution for acetonitrile clusters is fairly isotropic. This, again, illustrates the importance of the polar nature of the solvent, where strong ion-dipole interactions with acetonitrile (μ_{CH3CN}=3.92 D *vs.* μ_{H2O}=1.85 D) combined with the absence of strong solvent-solvent interactions (such as hydrogen bonding in water) favors the interior solvation of ions at the expense of disrupting the solvent network.

A2.IV. CONCLUDING REMARKS

We have investigated the structural and thermodynamic properties of $Na^+(CH_3CN)_n$, $Cs^+(CH_3CN)_n$ and $I^-(CH_3CN)_n$ clusters by means of room-temperature Monte Carlo simulations. An intermolecular model potential has been parameterized that adequately reproduces the small cluster solvent binding energies and structural properties derived from quantum chemistry calculations. One of the remarkably novel features of these model potentials is that they also reproduce the significant increase of the polarity of solvent molecules in the presence of ions (and other solvent molecules) that is observed in quantum chemistry calculations.

The rather successful comparison of the stepwise binding enthalpies obtained from our Monte Carlo simulations with available experimental data suggests that our model potentials are adequate for describing many-body interactions in the clusters. The computed stepwise binding enthalpies for large clusters, which are not accessible experimentally, reach a plateau, slowly converging to the liquid-phase acetonitrile heat of vaporization. The very slow convergence of binding enthalpies to the bulk counterpart

with cluster size, is consistent with earlier predictions of the liquid drop model.[120] Changes in the evolution of the binding enthalpies of ion-acetonitrile clusters with cluster size seem to reflect the completion of ionic solvation shells, a finding that is less pronounced for iodide-acetonitrile clusters. Binding energies are closely related to the solvation structure of ionic clusters, and differences in the evolution of binding energies with cluster size for anionic and cationic clusters are closely linked to differences in cluster structural properties.

All ion-acetonitrile clusters are found to exhibit an interior solvation structure. Cationic clusters are found to have a very clear solvation shell structure, with sharp peaks in the radial probability distributions. The first solvation shell of $Na^+(CH_3CN)_n$ clusters, like that of $Na^+(H_2O)_n$ clusters, contains 6 solvent molecules. Weaker ion-solvent interactions cause broadening of the peaks in the radial probability distributions of $Cs^+(CH_3CN)_n$ clusters, accompanied by an increase of the first-shell coordination number to 7. In $I^-(CH_3CN)_n$ clusters, we still observe interior solvation, even though the peaks in the probability distributions appear broader than for cation-acetonitrile clusters, and the coordination number for the first solvation shell equals 9. The interior solvation of $I^-(CH_3CN)_n$ clusters is in sharp contrast to the surface solvation of $I^-(H_2O)_n$ clusters, where the "hydrophobic" iodide tends to sit at the surface of the water network, because ion-solvent interactions are not strong enough to disrupt the stable solvent network. The situation is obviously much different for acetonitrile, and this may result in very different structural and thermodynamic properties of $NaI(CH_3CN)_n$ clusters, which in turn may explain why some aspects of their photodissociation dynamics seem to differ significantly from that of $NaI(H_2O)_n$ clusters.[26]

CHAPTER A3
Asymmetric Solvation Revisited: The Importance of Hydrogen Bonding in Iodide-Acetonitrile Clusters

Small anion – solvent clusters have been the subject of intense experimental and theoretical studies because of their significance in understanding solvation phenomena at the microscopic level.[121] Of particular interest are the structure, energetics, and photochemistry of the clusters of halide anions with polar solvent molecules. Investigations by Johnson and co-workers[43-45,122] of photoelectron spectra and electronic absorption spectra revealed the existence of dipole-bound excited states of small iodide-solvent clusters with organic solvents acetonitrile, acetone, nitromethane, and methyl iodide. These states are thought to be precursors of the well-known bulk charge-transfer-to-solvent (CTTS) states,[123] in which the excited electron is stabilized by the collective action of polar solvent molecules. Moreover, relaxation of the excited clusters leads to ejection of a neutral iodine atom and release of a negatively charged solvent cluster.

Iodide-acetonitrile clusters have been studied experimentally in great detail.[44,104] Photoelectron and absorption spectra suggested the existence of two isomers for $I^-(CH_3CN)_2$ clusters. The possible structures that were postulated for these isomers have acetonitrile molecules either on both sides of the iodide anion (symmetric solvation) or aligned on the same side of the ion (asymmetric solvation).[44,75] The structures are expected to have D_{3d} and C_{3v} symmetry, respectively (cf. Fig. A3.1). Upon relaxation, the photoexcited cluster with $\boldsymbol{D_{3d}}$ symmetry is unlikely to yield a negatively charged acetonitrile dimer, but rather CH_3CN and CH_3CN^- fragments.[44]

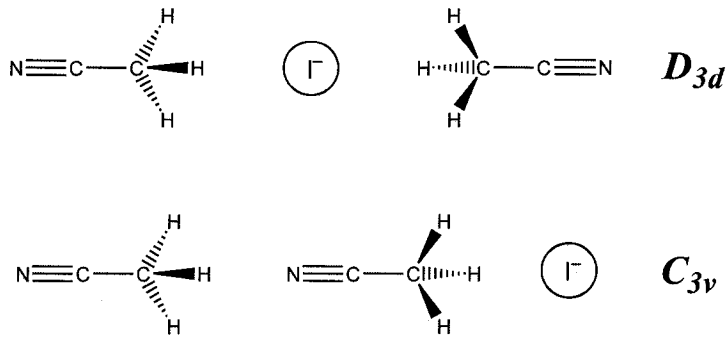

Fig. A3.1. Structural representation of the postulated $I^-(CH_3CN)_2$ isomers

The other, higher-energy, linear structure with C_{3v} symmetry was then assumed to be responsible for the formation of the $(CH_3CN)_2^-$ anion observed in experiments, which incidentally might also be linear. The excess electron could be stripped off the anionic dimer, supposedly forming a linear, higher-energy, neutral acetonitrile dimer that had not been observed before.[44,104] In previous experimental work,[124] the only $(CH_3CN)_2$ isomer that was isolated had the acetonitrile molecules in antiparallel orientation. It thus appears that asymmetric solvation in $I^-(CH_3CN)_2$ could be exploited to generate new cluster species, an avenue that remains to be confirmed from a theoretical point of view. We have recently engaged in theoretical studies of $I^-(CH_3CN)_n$ clusters,[109] and in this communication, we report preliminary ab initio calculations of the structures, energetics, and excitation energies of $I^-(CH_3CN)_2$ clusters.

Equilibrium geometries of clusters were optimized at the second-order Møller-Plesset (MP2) perturbation theory level of theory using Stuttgart-Dresden-Bonn quasi-relativistic ECP46MWB effective core potentials (ECP) and a standard ECP46MWB basis set[94] augmented by diffuse and polarization functions[95] for iodine, and a standard 6-311++G(df,p) basis set[90,91] for the other atoms. Geometry optimization of the "classical" symmetric and asymmetric clusters showed that the actual minimum energy structures,

shown in Fig. A3.2a and A3.2b, *do not* possess exact D_{3d} and C_{3v} symmetry, respectively, as previously postulated on the basis of ion-dipole interaction arguments. Instead, the cluster minimum energy conformations are slightly *distorted* from D_{3d} and C_{3v} symmetry. In the symmetric cluster structure, the iodine atom is shifted from the CH_3CN–CH_3CN axis and the acetonitrile CH_3 groups are eclipsed. In the asymmetric cluster structure, the CH_3CN molecule next to the iodine atom appears to be tilted from the ideal cluster C_3 symmetry axis. Besides the two isomers previously postulated, we also found a third structure, shown in Fig. A3.2c, which can also be considered a case of asymmetric solvation, since both acetonitrile molecules reside on one side of the anion. Acetonitrile dipoles in this structure are aligned in perpendicular fashion, leading to C_2 symmetry for the whole cluster structure.

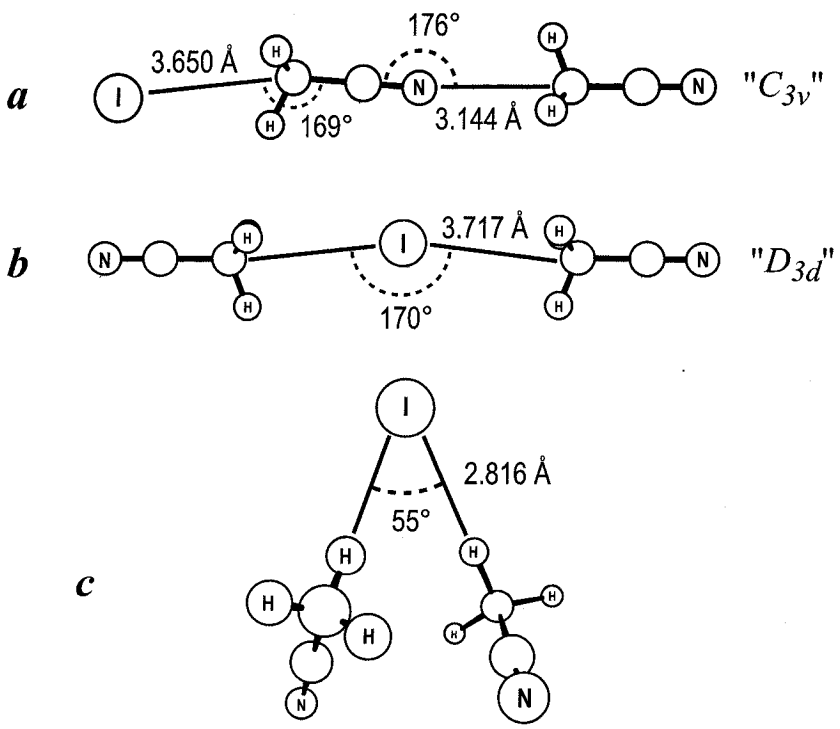

Fig. A3.2. $I^-(CH_3CN)_2$ cluster structures optimized at the MP2 level of theory.

To study the relative stability of these three structures, we performed single-point calculations at the coupled cluster level of theory with single, double and perturbative triple excitations [CCSD(T)]. Cluster binding energies were corrected for zero-point energy and basis set superposition error (BSSE) using the standard counterpoise (CP) approximation.[100] According to our results, which are collected in Table A3.1, the "classical" asymmetric structure is the least stable one, with binding energies of 17.7 and 15.0 kcal/mol, before and after inclusion of BSSE correction, respectively. The other two isomers – the "classical" symmetric and the new asymmetric structures – have binding energies about 3–4 kcal/mol higher. Out of these two structures, the new found asymmetric structure is predicted to be the most stable according to binding energies before BSSE correction, but the full CP correction reverses the order of stability, predicting the "classical" symmetric structure to be more stable by 1.7 kcal/mol. It should be mentioned here that the CP method has been repeatedly argued to yield crude estimates of the BSSE.[125] Furthermore, BSSE correction for many-body systems is a bit more ambiguous than for dimers, as the CP correction for these systems can be defined in several ways (site-site, pair-wise additive, and hierarchical CP methods).[126] Some authors claim that including only *half* of the CP correction yields more reliable results.[127] With this approach, the binding energies of both structures are within 1 kcal/mol, and those values are actually much closer to the experimental value of 21.8 ± 0.9 kcal/mol[128] than those obtained with the full CP correction. Moreover, the CP correction was evaluated here with CCSD(T) single-point calculations, whereas a more rigorous procedure might involve CP-corrected optimizations, since BSSE is known to distort intermolecular

potential energy surfaces.[129] With the aforementioned considerations about the CP correction for binding energies, we can conclude that, at the relatively high level of theory considered here, it is impossible to determine with certanity which of the two isomers is the most stable. However, both structures are obviously close in energy, both are definitely more stable than the "classical" asymmetric structure, and both are likely to exist at the temperature involved in the experiments.

Table A3.1. Binding energies (kcal/mol) for the $I^-(CH_3CN)_2$ isomers calculated with the CCSD(T)/ 6-311++G(df,p),ECP46MWB++(df)// MP2 model chemistry

	D_e[a]	D_0[b]		
		No BSSE	Full BSSE	½ BSSE
Symmetric cluster	21.7	21.6	18.4	20.0
Asymmetric cluster	17.9	17.7	15.0	16.3
H-bonded cluster	22.8	21.9	16.7	19.3

[a] Classical binding energies
[b] ZPE corrected binding energies estimated using MP2 vibrational frequencies

In postulating cluster structures with C_{3v} and D_{3d} symmetry for $I^-(CH_3CN)_2$, the interaction of the iodide anion with acetonitrile molecules was considered solely in terms of ion-dipole interactions.[122] Clearly, this simple model can not account for the distortions from ideal symmetry in the "classical" isomer structures, and fails to predict the existence of the third isomer. In the latter structure, CH_3CN molecules are oriented towards the I^- ion via the C–H bonds of methyl groups – which suggests the possible role of hydrogen bonding in the existence of this isomer. Indeed, Atoms-In-Molecule analysis[130] of the electronic density within the cluster shows the existence of bond critical points between hydrogen atoms and the iodine atom, with electronic density ρ and Laplacian of electronic density $\nabla^2\rho$ values characteristic[130] of hydrogen bonding (0.014

e/a_0^3 and 0.030 e/a_0^5, respectively). Similar hydrogen-bonding type interactions appear for the distorted "classical" asymmetric cluster: the iodide ion is closer to one of the hydrogen atoms, with which it forms a weak hydrogen bond. Therefore the distortion from C_{3v} symmetry seems to be due to a subtle interplay between ion-dipole interactions and hydrogen bonding – the distorted structures are lower in energy than the linear ones by no more than *ca.* 0.1 kcal/mol at the MP2 level of theory. Because hydrogen bonding obviously plays a crucial role in the existence and stability of the third isomer, we now refer to this isomer as the H-bonded cluster for convenience (Fig. A3.2c), while the "classical" structures will be called asymmetric (Fig. A3.2a) and symmetric (Fig. A3.2b) clusters respectively. A detailed investigation of the bonding in iodide-acetonitrile clusters, using Atoms-In-Molecule and Natural Bond Orbitals (NBO) analyses, will be discussed elsewhere.[131]

We now turn our attention to the photochemistry of the $I^-(CH_3CN)_2$ clusters. In order to evaluate electronic excitation energies, we used time-dependent density functional theory[132] (TD-DFT) with the B3LYP hybrid functional.[93] The TD-DFT method was shown to be an efficient tool for investigating CTTS phenomena in small anionic clusters.[109,133] As discussed previously,[109] the experimentally observed CTTS absorption band of $I^-(S)_n$ clusters (S = H_2O, CH_3CN) corresponds to transitions to the lowest three excited states which involve electronic excitation form the three 5*p* orbitals of iodide. These excited states lie very close in energy, i.e. within 0.1 eV.[109] For $I^-(CH_3CN)$, the vertical excitation energies calculated by TD-DFT (hν=3.33–3.39 eV) are shifted by *ca.* 0.3 eV from the bare iodide experimental ionization potential.[109] When compared to that of $I^-(CH_3CN)$, the calculated vertical excitation energy of the

asymmetric cluster drops by *ca.* 0.5 eV, but for the symmetric and H-bonded clusters, it goes up by *ca.* 0.3 eV, as seen from Table A3.2.

Table A3.2. Vertical excitation energies (eV) in $I^-(CH_3CN)_2$ clusters calculated with the TD-DFT B3LYP method

Transition	Asymmetric solvation	Symmetric solvation	H-bonded	Experiment
$\tilde{A} \leftarrow \tilde{X}$	2.80	3.57	3.64	
$\tilde{B} \leftarrow \tilde{X}$	2.80	3.57	3.67	3.85, 4.05
$\tilde{C} \leftarrow \tilde{X}$	2.84	3.64	3.75	

Experimentally, the vertical excitation energy shifts from the bare iodide ionization potential by *ca.* 0.5 eV per solvent molecule. Our results therefore suggest that, of the three possible isomers of $I^-(CH_3CN)_2$ found in this work, the two involved in the actual experiments[44] are the symmetric and H-bonded isomers: the "classical" asymmetric structure not only lies much higher in energy than the other two isomers and is thus not likely to be present at the temperature of experiments, but the calculated vertical excitation energy for this isomer is in serious contradiction with experimental trends. Although TD-DFT B3LYP calculations clearly underestimate vertical excitation energies for CTTS transitions, the general trend in vertical excitation energies observed experimentally[44,45] as a function of cluster size is reproduced in our calculations, i.e. the vertical excitation energies shift from the bare iodide ionization potential by *ca.* 0.3 eV per solvent molecule, as opposed to experimental shifts of 0.5 eV. We also note that subsequent relaxation of the photoexcited H-bonded clusters, with formation of a new

$(CH_3CN)_2^-$ anion – where the acetonitrile molecules are oriented in perpendicular fashion, is consistent with the experimental observation of negatively charged solvent dimers. A detailed investigation of the relaxation of photoexcited $I^-(CH_3CN)_2$ and of the resulting $(CH_3CN)_2^-$ anions will be reported elsewhere.[131]

In conclusion, the present calculations show that hydrogen bonding is extremely important for iodide-acetonitrile clusters, first causing a slight distortion of the C_{3v} and D_{3d} structures postulated earlier in insightful interpretations of experimental data, and more importantly, giving rise to a third, hydrogen-bonded cluster isomer. The importance of hydrogen bonding in halide-water clusters has been recognized before.[134] Obviously, hydrogen bonding could play a similar role for clusters with other halide anions and/or other solvents (*e.g.* acetone, nitromethane, etc.). As a matter of fact, smaller halide anions hydrogen-bind almost linearly to acetonitrile.[111,135] In the case of $I^-(CH_3CN)_2$, hydrogen bonding is responsible for the existence of cluster structures that could not be predicted solely on the basis of ion-dipole interactions. The calculated binding energies and CTTS transition energies suggest that the cluster structures involved in actual experiments are the H-bonded (Fig. A3.2c) and "classical" symmetric structures (Fig. A3.2a). While very accurate calculations of the potential energy surfaces, ionization potentials and excitation energies of $I^-(CH_3CN)_n$ [n=1–3] clusters are underway,[131] we also note that the $I^-(CH_3CN)_2$ cluster structures have very distinct infrared spectral signatures,[131] which are being probed experimentally.[136]

CHAPTER A4
Microsolvation of the Sodium Iodide Ion Pair in Acetonitrile Clusters: a Theoretical Study

A4.I. INTRODUCTION

A number of studies have been reported in the literature regarding the solvation of ions in clusters,[44,51,81,83,104,137,138] but only a few have focused on the solvation of ion pairs in clusters.[58,59,139] A good candidate system to investigate solvation phenomena is the NaI ion pair in polar solvent clusters. This system has served as a prototype for cluster photochemistry,[66] and has allowed exploration of the effects of solvent on the dynamics of such fundamental chemical reactions as electron transfer.[140] In brief, photoexcitation results in the transient trapping of gas-phase NaI in an excited-state well that arises from the avoided crossing between ionic and covalent states, coupled to a decay of the excited-state population into atomic products via nonadiabatic transitions.[67,68] In femtosecond pump-probe experiments, the excited-state population can be monitored by ionization of the trapped, excited NaI to a probe state, and collection of the dissociation products with a mass spectrometer.[26,68] Early theoretical work indicated that radiative deactivation to the ground ionic state would follow photoexcitation of the NaI ion pair in a weakly polar solvent, but that more interesting photodissociation dynamics may occur in small clusters.[141] Previous theoretical work on $NaI(H_2O)_n$ clusters[69] has shown that the presence of solvent greatly affects the nonadiabatic dynamics of the photodissociation process. Subsequent experimental studies of NaI ion pairs in polar solvent clusters of water, acetonitrile and ammonia[26,61,142] have shown a very clear, solvent-selective, behavior in the distribution of the detected $Na^+(solvent)_n$

product ions.[26] More specifically, clusters up to size 50 have been observed experimentally with water, but no clusters larger than size 9 and 6 have been observed with ammonia and acetonitrile, respectively, in multi-photon ionization experiments.

Our previous work has focused on the structural and thermodynamic properties of NaI ion pairs in water clusters,[41,42] along with their implications for multi-photon ionization experiments. It was found that NaI ion pairs are quite stable with respect to complete ground-state dissociation to ionic clusters, even at large solvent cluster sizes. Two thermodynamically stable forms of the cluster ion pairs, namely "contact" ion pairs (CIP) and solvent-separated ion pairs (SSIP), were identified. Model quantum chemistry calculations[42] showed that the calculated oscillator strength for the isolated NaI transition from the ground to first excited-state decreases drastically with increasing interatomic distance. In addition, the presence of a polar solvent molecule in the middle of the ion pair causes both the transition dipole moment and oscillator strength to decrease significantly, compared to the isolated NaI case, a finding that has recently been confirmed for $NaCl(H_2O)_n$ clusters.[143] As the cluster size increases, a progressively larger fraction of ground-state NaI exists as SSIPs, which are not photoexcitable according to our model calculations. This is consistent with the experimental observation[26,61,142] that laser photoexcitation produces $Na^+(H_2O)_n$ cluster products of size no larger than ~n=50, implying that large $NaI(H_2O)_n$ clusters are not photoexcitable despite their stability towards ground-state dissociation. Interestingly, the structure of ion pairs in water clusters could be tied to that of the individual ions in water clusters.[41] Of particular interest is the "hydrophobic" nature of the iodide ion in aqueous clusters,[55,70] which seems to govern surface-solvated NaI ion pair structures at small cluster sizes.[41]

In order to possibly elucidate the experimental differences observed in the products of NaI-solvent cluster multi-photon ionization with different solvents,[26] we turn our attention to the structural and thermodynamic properties of $NaI(CH_3CN)_n$ clusters. Despite being a highly polar solvent, acetonitrile differs from water with respect to molecular size, the magnitude of the dipole moment and its lack of propensity to form hydrogen bonds. Monte Carlo simulations have been employed to investigate cluster structural properties, paying particular attention to CIP and SSIP structures, and the stability of the ion pair is investigated via computations of the Potential of Mean Force (PMF) and related equilibrium constants.[144] Of paramount importance for these simulations are the development and validation of model potentials capable of adequately describing the intermolecular interactions between the NaI ion pair and solvent molecules in clusters. Accordingly, we have developed model potentials parameterized on the basis of quantum chemistry calculations for small clusters, and the model validation is achieved by comparing the results obtained from simulations with these potentials to experimental, thermochemical data for ionic clusters such as $Na^+(CH_3CN)_n$ and $I^-(CH_3CN)_n$. We note that a number of model potentials for simulating acetonitrile have been proposed in previous work,[51,72-74] but none of them seemed to be completely adequate for our cluster simulations.

The outline of this chapter is as follows. Following a description of the simulation procedure in Sec. A4.II, the thermodynamic and structural properties from simulations of ion-acetonitrile clusters will be presented and discussed in Sec. A4.III, and present results will be compared to available experimental data for validation of the model potentials. This will be followed by a presentation and discussion of simulation results for

$NaI(CH_3CN)_n$ clusters in section A4.IV. Again, particular focus will be placed on cluster thermodynamics and structures. The present findings will then be compared and contrasted with those for $NaI(H_2O)_n$ clusters and possible implications for cluster photodissociation dynamics will be outlined. Concluding remarks follow in Sec. A4.V.

A4.II. COMPUTATIONAL PROCEDURE

A4.IIA. Model Potentials

The model potentials employed in the cluster simulations consist of classical solvent-solvent and solute-solvent intermolecular potentials, and NaI solute potentials derived from semiempirical quantum chemistry. A number of acetonitrile model potentials can be found in the literature, but they were found to neglect or improperly account for polarization interactions.[72,74,81,86] Gregoire *et al.*[62] reported a model capable of reproducing ion-acetonitrile and acetonitrile-acetonitrile dimer structures, but failed to reproduce the $NaI(CH_3CN)$ and $I^-(CH_3CN)_2$ minimum energy structures, as discussed in section A4.IV.B. Our previous model potential[145] which included explicit polarization, was capable of describing most features of solvent-solvent interactions and ion-solvent interactions for alkali and halide ions in acetonitrile clusters. However, it failed to reproduce hydrogen-bonded structures predicted for $I^-(CH_3CN)_n$ clusters by quantum chemistry,[146] a finding that is not too surprising since no directional hydrogen-bonded term was included in the potential analytical form. As recently reported,[110,111] hydrogen bonding plays a significant role in halide ion-acetonitrile interactions and it should be accounted for in order to appropriately describe the structural features of microsolvated complexes containing halide ions and acetonitrile. In addition to this shortcoming, our

early model potential also appears inadequate for modeling ion-pair solvent clusters, predicting the existence of a number of unrealistic structures that mainly arise because of the oversimplistic, single-site molecular polarizability of the model. These shortcomings have prompted us to develop a new model potential, with an improved treatment of polarization and repulsion-dispersion interactions.

Our new model employs rigid acetonitrile molecules fixed at their experimental gas-phase geometry as in previous work. The interaction energy between solvent molecules, and between solvent molecules and ions, consists of Coulombic, many-body polarization and repulsion-dispersion contributions,

$$V = V_{Coul} + V_{pol} + V_{rep-disp} \tag{A4.1}$$

The Coulombic part,

$$V_{Coul} = \sum_i \sum_{j<i} \frac{q_i \cdot q_j}{|\mathbf{r}_i - \mathbf{r}_j|} \tag{A4.2}$$

represents the interactions between the fractional charges q_i on each atomic or ionic site (at position $\mathbf{r}_i$) of the monomers. Associated with each ion and solvent molecule are polarizability sites α_i and induced dipole moments μ_i. One polarizable site is placed on each of the ions, while 3 sites are located on the N, C, and methyl C (C_M) atoms for each acetonitrile molecule. The polarization contribution is expressed as[87]

$$V_{pol} = -\frac{1}{2} \sum_i \mathbf{E}_i^o \cdot \boldsymbol{\mu}_i \tag{A4.3}$$

where the electric field $\mathbf{E}_i^o$ due to the permanent charges of other monomers is given by

$$\mathbf{E}_i^o = \frac{\sum_j q_j \cdot \mathbf{r}_j}{|\mathbf{r}_i - \mathbf{r}_j|^3} \tag{A4.4}$$

and the induced dipole moments are calculated from

$$\boldsymbol{\mu}_i = \alpha_i . \mathbf{E}_i = \alpha_i \left[\mathbf{E}_i^o + \sum_{j \neq i} T_{ij} . \boldsymbol{\mu}_j \right] \tag{A4.5}$$

where T_{ij} in Eq. (A4.5) is the dipole tensor.[87] Because of mutual polarization, the set of induced dipoles $\boldsymbol{\mu}_i$ is obtained in a self-consistent fashion by solving the set of linear equations of Eq. (A4.5) with LU decomposition and backsubstitution.[77] Finally, short-range repulsion-dispersion interactions between all atoms are modeled via modified generalized Lennard-Jones potentials[147] of the form

$$V_{rep-disp} = \left(\sum_{i,j} A_{ij} r_{ij}^{-12} + B_{ij} r_{ij}^{-8} + C_{ij} r_{ij}^{-6} \right) \left(1 + D_{ij} \cos E_{ij} \varphi \right) \tag{A4.6}$$

The last term in Eq. (A4.6) is a directionality term included to account for hydrogen bonding between the acetonitrile molecule and the halide ion, with φ the angle between the halide ion, a hydrogen atom and the methyl carbon of acetonitrile. We note that such a hydrogen-bonded term was not found to be necessary in simulations of iodide in water[41] or ammonia clusters.[148]

The NaI ion pair model potential has been reported in earlier publications,[41,42,69,141] to which the reader is referred to for details. Briefly, the potential energy expression contains Coulombic, polarization, and core-core repulsion terms

$$V_{solute} = V_{Coulomb} + V_{pol} + V_{core-core} \tag{A4.7}$$

The Coulombic and polarization interactions are described by potential terms of Eqs. (A4.2) and (A4.3) discussed earlier, respectively. The core-core potential is represented by an exponentially repulsive Born-Mayer potential[42]

$$V_{core-core} = Ae^{-Br} \tag{A4.8}$$

parameterized to reproduce ground-state NaI potential curves determined from either experiment[149] or high level quantum chemistry calculations[150] (A=70810 kcal/mol, and B=0.326 $Å^{-1}$). Since the effective polarizability of ions is affected by the presence of other species, the ion polarizabilities are attenuated with decreasing internuclear separations via a smooth switching function, in order to reproduce the calculated NaI dipole moment.[69] We note that this model potential allows ions and solvent molecules to polarize each other. First-principles quantum chemistry calculations provide the basis for the parameterization of the model potentials. Accordingly, we now turn our attention to quantum chemistry calculations for small clusters.

A4.II.B. Quantum Chemistry Calculations

Ground-state properties of $(CH_3CN)_{1-2}$, $Na^+(CH_3CN)_{1-4}$, and $I^-(CH_3CN)_{1-2}$ clusters were taken from our previous work,[110,145] and properties of $NaI(CH_3CN)$ were evaluated in this work. Geometry optimizations and frequency calculations were performed with the Gaussian 98 quantum chemistry package[90] at the second-order Møller-Plesset (MP2)[91] level of theory with a 6-311+G(d) all-electrons basis set.[91,95] It is worth noting that this model chemistry is well suited for characterizing weak, hydrogen-bonded complexes.[111] As in previous work, cluster geometries were first optimized with rigid acetonitrile molecules in their experimental, gas-phase geometry, and cluster geometries were further optimized with all coordinates relaxed, while conserving symmetry group constraints in order to locate true minimum energy structures. This procedure allowed us to confirm that monomer geometry relaxation in clusters is insignificant, hence justifying the use of rigid solvent molecules for our model potential.[151] A frequency calculation followed in order to characterize the stationary points and obtain harmonic zero-point energies.

Single-point energy calculations were also performed for selected clusters with the coupled cluster method with single, double and linearized triple excitations [CCSD(T)] and the 6-311+G(2df,pd) basis set for MP2 optimized geometries.[145] The minimum energy structures of the solvent dimer and ion-solvent clusters are shown in Fig. A4.1, along with stationary points for $NaI(CH_3CN)$.

Binding energies (D_e) are calculated via the supermolecule approach, and corrections for zero-point energy (ZPE) are included to obtain D_o. The ZPE correction is calculated from harmonic frequencies. $D_{o/BSSE}$ was obtained by including a correction for basis set superposition error (BSSE) which was estimated with the site-site Counterpoise method.[100,152] The structural and energetic properties of all complexes predicted by quantum chemistry calculations are collected in Table A4.1, along with molecular dipole moments of the individual monomers evaluated from the Electrostatic Potential (ESP) charge distributions[99] of the supermolecule. Typically, the ZPE and BSSE corrections to the binding energy are in the range of 1-2 kcal/mol, except for $I^-(CH_3CN)_2$, where the BSSE correction is of the order of 3 kcal/mol.

Our quantum chemistry calculations predict three stationary points, shown in Fig. A4.1, for the $NaI(CH_3CN)$ complex. The first isomer features acetonitrile and NaI dipoles aligned in an anti-parallel fashion, and is thus referred to the "antiparallel C_s $NaI(CH_3CN)$". In the other two isomers, named "C_s $NaI(CH_3CN)$" and "C_{3v} $NaI(CH_3CN)$" the NaI ion pair is located on either side of the acetonitrile molecule, and aligned with the molecular main axis.

$(CH_3CN)_2$

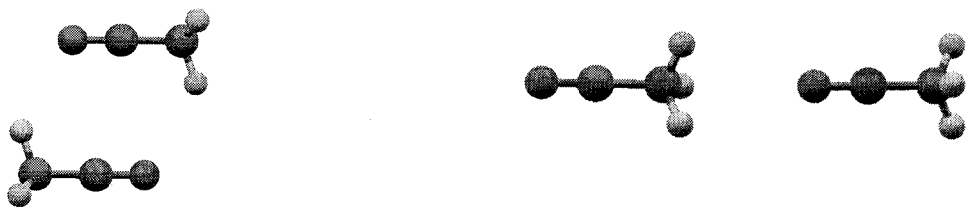

$I^-(CH_3CN)_{1-2}$

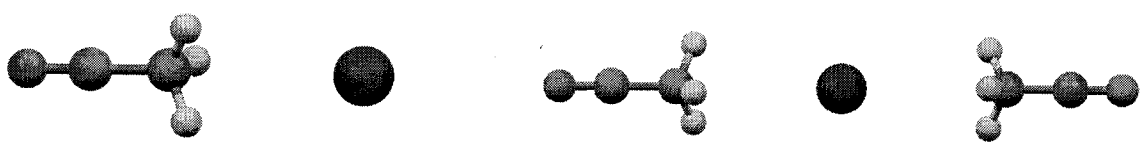

C_{2v}

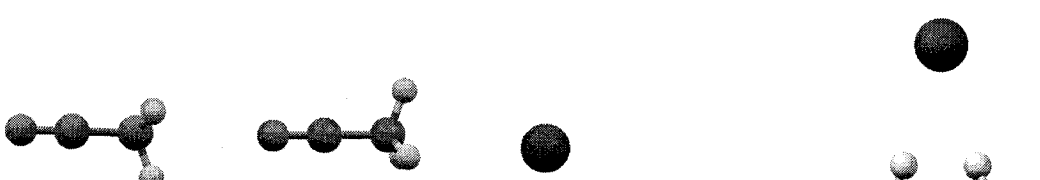

C_{3v}

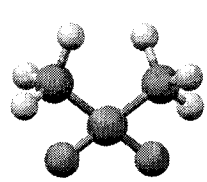

C_2

$M^+(CH_3CN)_{1-4}$

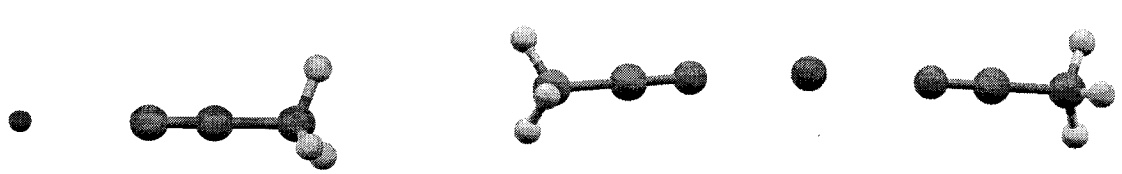

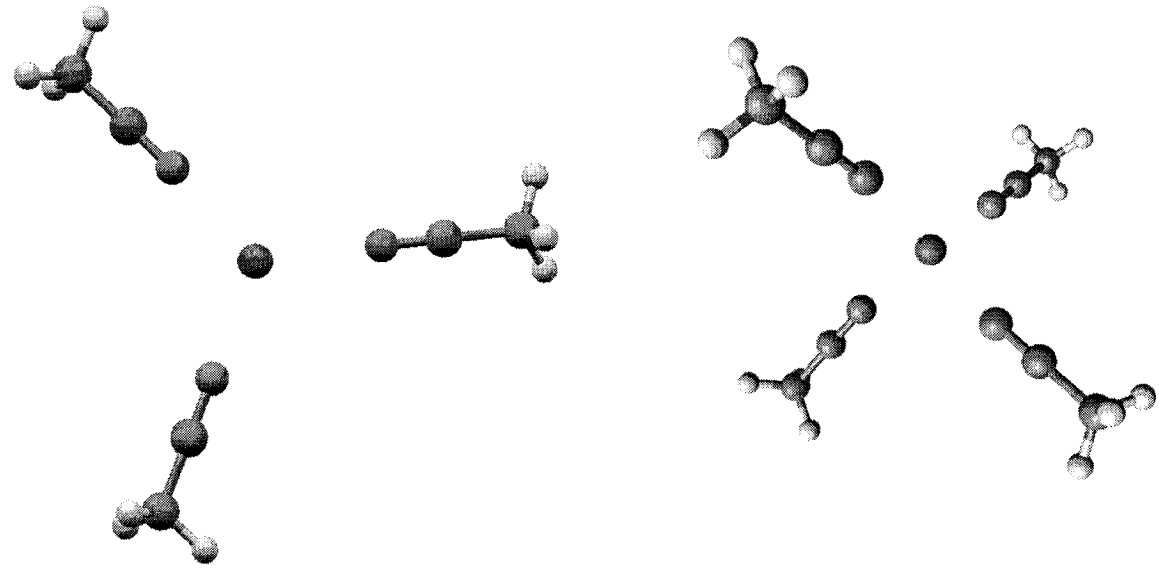

NaI(CH_3CN)

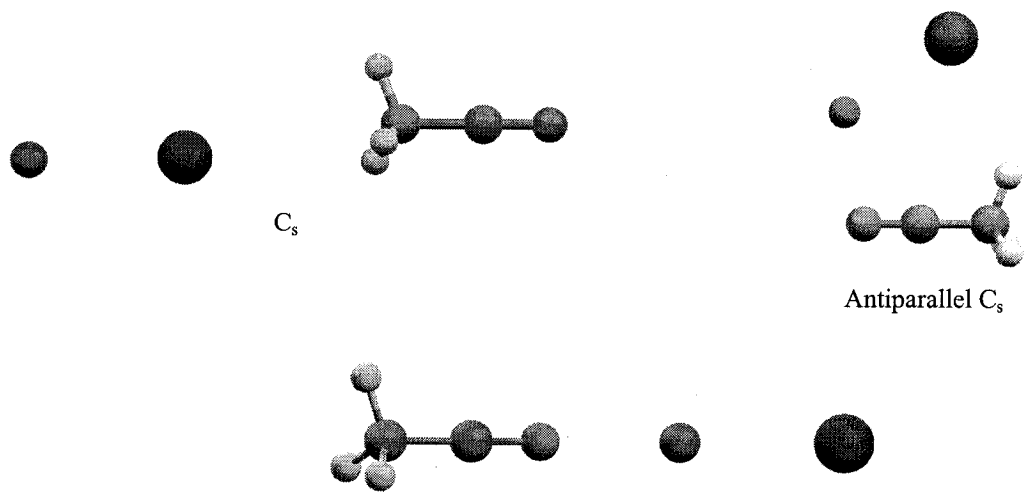

Fig. A4.1. Minimum energy structures for $(CH_3CN)_2$, $I^-(CH_3CN)_{1-2}$, $Na^+(CH_3CN)_{1-4}$, and $NaI(CH_3CN)$ stationary points predicted by quantum chemistry calculations.

Table A4.1. Small cluster properties.[a]

	Quant. chem.[b]	Expt.	Mod. pot.
		NaI	
r_{Na-I}	2.76[c]	2.71[d]	2.7
μ_{NaI}	9.7[c]	9.2[e]	9.7
$D_o^{n,n-1}$	115.8[c]	116.6[d]	120.7
		CH_3CN	
α		4.48[f]	4.50
μ_{CH_3CN}	3.92	3.9[g]	3.9
		$(CH_3CN)_2$ C_{3v}	
R_{C-C}	5.90		5.90
θ(C-N-CM)	180.0		180.0
μ_{CH_3CN}	4.3, 4.0		4.2, 4.0
$D_e^{n,n-1}$	3.0 (3.2)		
$D_0^{n,n-1}$	2.8 (2.9)		2.7
$D_{0/BSSE}^{n,n-1}$	2.2 (2.5)		
		$(CH_3CN)_2$ C_{2h}	
R_{C-C}	3.35		3.35
R_{N-H}	2.55		2.57
μ_{CH_3CN}	4.2		4.1
$D_e^{n,n-1}$	6.4 (6.0)		
$D_0^{n,n-1}$	5.7 (5.3)		5.0
$D_{0/BSSE}^{n,n-1}$	4.3 (4.7)		
		$Na^+(CH_3CN)$	
R_{Na-N}	2.31		2.31
θ(Na-N-C)	180.0		180.0
μ_{CH_3CN}	5.4		5.7
$D_e^{n,n-1}$	30.7 (31.1)		
$D_0^{n,n-1}$	30.0 (30.4)		30.2
$D_{0/BSSE}^{n,n-1}$	29.3 (29.5)		

a. Bond lengths are in angstroms (Å), binding energies in kcal/mol, dipole moments in Debye (D), angles in degrees and polarizabilities in $Å^3$. Quantum chemistry dipole moments calculated from ESP charge distributions.

	Quant. chem.[b]	Expt.	Mod. pot.
		$Na^+(CH_3CN)_2$	
$R_{Na\text{-}N}$	2.34		2.33
θ(Na-N-C)	180.0		180.0
μ_{CH_3CN}	4.9		5.5
$D_e^{n,n-1}$	26.7		
$D_0^{n,n-1}$	26.1		26.4
$D_{0/BSSE}^{n,n-1}$	25.1		
		$Na^+(CH_3CN)_3$	
$R_{Na\text{-}N}$	2.38		2.37
θ(Na-N-C)	180.0		180.0
μ_{CH_3CN}	4.8		5.2
$D_e^{n,n-1}$	20.3		
$D_0^{n,n-1}$	19.8		20.7
$D_{0/BSSE}^{n,n-1}$	19.1		
		$Na^+(CH_3CN)_4$	
$R_{Na\text{-}N}$	2.41		2.40
θ(Na-N-C)	180		180.0
μ_{CH_3CN}	4.7		5.0
$D_e^{n,n-1}$	16.2		
$D_0^{n,n-1}$	15.5		16.1
$D_{0/BSSE}^{n,n-1}$	14.2		
		$I^-(CH_3CN)$	
$R_{I\text{-}CM}$	3.70		3.66
θ(I-C_M-N)	172.4		180.0
μ_{CH_3CN}	5.4		5.0
$D_e^{n,n-1}$	11.5 (10.9)		
$D_0^{n,n-1}$	11.4 (10.9)		10.8
$D_{0/BSSE}^{n,n-1}$	9.9 (10.5)		

b. MP2/6-311+G(d) results. CCSD(T)/6-311+G(2df,pd)//MP2/6-311+G(d) results in parentheses. Ionic cluster properties taken from Ref. [145].
c. MP2/6-31+G** results taken from Ref. [42].
d. Taken from Ref. [154].
e. Taken from Ref. [155].

	Quant. chem.[b]	Expt.	Mod. pot.
	I-(CH3CN)$_2$ hydrogen-bonded		
R_{I-H}	2.65,4.02,4.12		2.89, 3.91, 4.18
R_{CM-CM}	3.57		3.52
$\theta(C_M\text{-}I\text{-}H)$	1.0		10.2
μ_{CH_3CN}	4.7		4.6
$D_e^{n,n-1}$	11.1		
$D_0^{n,n-1}$	10.1		8.9
$D_{0/BSSE}^{n,n-1}$	7.2		
	I-(CH3CN)$_2$ symmetric		
R_{I-C}	3.72		3.69
θ(I-CM-N)	175.4		180.0
μ_{CH_3CN}	4.8		4.9
$D_e^{n,n-1}$	10.0		
$D_0^{n,n-1}$	9.8		9.9
$D_{0/BSSE}^{n,n-1}$	9.0		
	I-(CH3CN)$_2$ asymmetric		
R_{I-CM}	3.65		3.64
R_{N-CM}	3.14		3.25
θ(N-I-N)	0.9		0.0
μ_{CH_3CN}	4.6		5.2
$D_e^{n,n-1}$	6.2		
$D_0^{n,n-1}$	6.2		5.7
$D_{0/BSSE}^{n,n-1}$	5.4		
	antiparallel C_s NaI(CH$_3$CN)		
R_{I-H}	3.29		3.13
R_{Na-N}	2.38		2.46
μ_{NaI}	10.2		10.7
μ_{CH_3CN}	4.1		4.9
$D_e^{n,n-1}$	18.6 (18.4)		
$D_0^{n,n-1}$	17.8 (18.3)		17.3
$D_{0/BSSE}^{n,n-1}$	17.2 (16.1)		

f. Isotropic polarizability in Å^3 from Ref. [114].
g. Taken from Ref. [98].

	Quant. chem.[b]	Expt.	Mod. pot.
		C_{3v} NaI(CH_3CN)	
$R_{I\text{-}CM}$	7.79		-
$R_{Na\text{-}N}$	2.39		-
μ_{NaI}	9.6		-
μ_{CH_3CN}	2.2		-
$D_e^{n,n-1}$	17.5 (17.6)		
$D_0^{n,n-1}$	16.9 (17.5)		-
$D_{0/BSSE}^{n,n-1}$	16.1 (16.1)		
		C_s NaI(CH_3CN)	
$R_{I\text{-}CM}$	3.86		-
$R_{Na\text{-}N}$	9.22		-
μ_{NaI}	11.9		-
μ_{CH_3CN}	3.5		-
$D_e^{n,n-1}$	3.9 (3.8)		
$D_0^{n,n-1}$	3.9 (3.8)		-
$D_{0/BSSE}^{n,n-1}$	3.6 (3.1)		

However, vibrational frequency analysis indicates that only the antiparallel C_s NaI(CH_3CN) configuration is a minimum energy structure, while the C_s NaI(CH_3CN) and C_{3v} NaI(CH_3CN) are second-order saddle points. Inspection of the binding energies reveals that the antiparallel C_s NaI(CH_3CN), and C_{3v} NaI(CH_3CN) binding energies lie within 1 kcal/mol. The orientation of the NaI ion pair in the antiparallel C_s NaI(CH_3CN) complex results in favorable dipole-dipole and I-H interactions, and suggests the existence of hydrogen-bonding interactions[153] similar to those observed in $I^-(CH_3CN)$ complexes.[111]

A4.II.C. Parameterization of Model Potentials

The parameters in our model potential include point charges (q_i), polarizabilities (α_i), repulsion-dispersion terms (A_{ij}, B_{ij}, C_{ij}) and hydrogen-bonding parameters (D_{ij}, E_{ij}). All parameters are derived on the basis of experimental data supplemented by quantum chemistry calculations, and are listed in Table A4.2.

Table A4.2. Model potential parameters[a]

Structural parameters						
	r_{CM-H}	r_{CM-C}	r_{C-N}		a_{H-C-H}	
	1.089	1.46	1.17		109.80	
Point charges and polarizabilities						
	CH_3CN					
	N	C	C_M	H	Na	I
q_i	-0.49	0.48	-0.56	0.19	1.00	-1.00
α_i	0.91	1.56	1.99		0.20	5.30
Solvent-solvent Lennard-Jones parameters						
	N-N	N-C	N-H	C-C	C-H	H-H
A	6410	1271400	72850	2100	37800	1
B	0	0	0	0	0	0
C	-35	-930	-160	-20	-115	-1
Ion-solvent Lennard-Jones parameters						
	Na-N	Na-C	Na-H	I-N	I-C	I-H
A	73180	812500	39100	44536700	14432900	1085300
B	7700	-4800	660	76200	-56700	1450
C	-1050	-1425	-940	-10	-5	-460
D	-	-	-	-	-	0.60
E	-	-	-	-	-	2.01

a. Distances are in Å, angles in degrees, point charges (q_i) in fractions of e, polarizabilities (α_i) in $Å^3$, A in kcal.$Å^{12}$, B in kcal.$Å^8$, C in kcal.$Å^6$, D and E are unitless.

Fractional atomic charges for acetonitrile are assigned on the basis of the MP2/6-311+G(d) ESP charge distribution,[156] while the ions simply carry a positive or negative unit charge. Polarizabilities are notoriously difficult to determine accurately with quantum chemistry, and thus the ionic and molecular polarizabilities are taken from gas-

phase experimental data.[113,114] The acetonitrile polarizabilities are distributed over the N, C, and methyl carbon (C_M) atoms, with the resulting total molecular polarizability[157]

$$\alpha_{CH_3CN} = \alpha_N + \alpha_C + \alpha_{C_M} \quad \text{(A4.9)}$$

The other parameters, namely the repulsion-dispersion and hydrogen-bonded terms are adjusted to fit the $(CH_3CN)_2$, $Na^+(CH_3CN)$, $I^-(CH_3CN)_{1-2}$ and $NaI(CH_3CN)$ geometries, binding energies and dipole moments from quantum chemistry calculations. The fitting procedure was performed with a non-linear-least-squares method based on the Marquardt-Levenberg algorithm.[77]

Structural properties of $(CH_3CN)_2$, $Na^+(CH_3CN)_{1-4}$, $I^-(CH_3CN)_{1-2}$ and $Na^+I^-(CH_3CN)$ determined with our model potentials are collected in Table A4.1, where they are compared with their quantum chemistry counterparts. Bond lengths are generally reproduced by the model potential within less than 0.05 Å. A slightly larger deviation of ~0.1 Å is observed in intermolecular distances for the hydrogen-bonded $I^-(CH_3CN)_2$ and $NaI(CH_3CN)$ complexes, as the delicate nature of the bonding involved in these clusters may be more difficult to reproduce with simple model potentials. Stepwise binding energies predicted by model potentials lie in between the D_o and $D_{o/BSSE}$ quantum chemistry values. Since the Counterpoise method is known to overestimate BSSE,[101] the model potential and quantum chemistry values can be considered to be in excellent agreement. For small $Na^+(CH_3CN)_n$ and $I^-(CH_3CN)_n$ clusters, the deviation from quantum chemistry data slightly increases with cluster size, but the model binding energies are still within the accepted error range of quantum chemistry calculations (1-2 kcal/mol), inspiring some confidence in our model potential. Finally, the model successfully reproduces the CH_3CN dipole moment increase from its gas-phase value when placed in

the vicinity of other molecules or ions. For instance, quantum chemistry calculations suggest that the acetonitrile dipole moment increases by ~0.3 D in the presence of another solvent molecule and by 0.7 D to 1.5 D in the presence of an ion. Our model potential reproduces these polarization effects on average within 7 %.

Our model potential employs fitted distributed polarizabilities, which were constrained to reproduce the acetonitrile experimental isotropic polarizability value of 4.45 $Å^3$. The predicted atomic polarizabilities are α_N= 0.91 $Å^3$, α_C= 1.56 $Å^3$ and α_{C_M} = 1.99 $Å^3$ for the N, C, and C_M sites, respectively. Considering that the polarizability of the C_M site represents that of the methyl group, this distribution compares well to those in previous models involving additive methods for polarizability calculations by Thole (α_N= 0.93 $Å^3$, α_C= 1.24 $Å^3$, α_H=0.43 $Å^3$, and as such α_{CH_3} = α_C+3.α_H=2.53 $Å^3$)[158] and by Miller, (α_N= 0.96 $Å^3$, α_C= 1.28 $Å^3$, α_{C_M} = 1.06 $Å^3$, α_H= 0.39 $Å^3$, and thus α_{CH_3} = α_C+3.α_H= 2.22 $Å^3$).[159] Vogel also proposed a model where the acetonitrile polarizability is distributed over the methyl group α_{CH_3} = 2.24 $Å^3$) and the nitrile group (α_{CN}= 2.16 $Å^3$),[160] which again is consistent with our model α_{CH_3} =α_{C_M} =1.99 $Å^3$, α_{CN}=α_C+α_N= 2.51 $Å^3$). Finally, we note that our model, which only employs 3 polarizable sites per solvent molecule, is simpler (and thus applicable to much larger clusters) than the 11-site model reported previously,[62] and yet appears to be superior to the previous model, which is not capable of reproducing the hydrogen bonded $I^-(CH_3CN)_2$ and antiparallel C_s $NaI(CH_3CN)$ structures predicted by quantum chemistry calculations. For instance, the previous model potential predicts a $NaI(CH_3CN)$ global minimum of C_{3v} symmetry, instead of the antiparallel C_s configuration.

A4.II.D. Monte Carlo Simulations

Canonical ensembles of $Na^+(CH_3CN)_n$, $I^-(CH_3CN)_n$, and $Na^+I^-(CH_3CN)_n$ cluster structures were generated via random-walk[64] Metropolis Monte Carlo simulations at 300 K.[76] We followed the procedure developed in previous work,[25] and we only outline its main features here for completeness. Independent simulations are carried out for clusters of various size, placing a given number n of CH_3CN molecules around an ion or the ion pair geometrical center. New trial solvent configurations are generated by randomly translating one acetonitrile molecule in each Cartesian direction and rotating it about its standard Euler angles θ, ψ, and φ.[78] Since each random walk involves the six degrees of freedom of only one acetonitrile molecule at a time, the length of the Markov chain is increased with cluster size, but only sampled configurations for which all the acetonitrile molecules have changed position are stored for structural analysis. Each run entails about 10^6 to 10^7 steps of equilibration, followed by an equivalent number of steps for data collection. The ranges of displacement for translational and rotational motion were chosen so as to obtain acceptance ratios of about 40-50 % for new configurations, typically corresponding to a displacement range of 0.25 Å for translation, and 25°, 0.25 and 25° for φ, cos θ and ψ, respectively. Finally, the clusters are periodically heated and cooled with a smooth temperature schedule in order to sample all possible local minima[79] and to reduce uncertainties in potential of mean force calculations.[42] In contrast to liquid simulations,[78] no potential truncation is necessary and no periodic boundary conditions are imposed in cluster simulations. However, complications arise from the fact that acetonitrile molecules may undergo evaporation at room temperature,[80] which results in a reduction in the size of the cluster being simulated.[81] Since our goal is to obtain a well-

defined equilibrium ensemble of clusters of a given size, each part of the Markov chain containing clusters that have undergone solvent evaporation is excluded from the final conformational sampling, which is formally equivalent to adding a stepfunction to the configurational integral, so as not to take into account clusters which are inappropriately sized.[82,83] In practice, an acetonitrile molecule is considered as evaporated when it moves further than 15 Å for $n \leq 12$ and 25 Å for $n > 12$ from the closest ion.

A4.II.E. Thermodynamics

Cluster enthalpies are computed from the average energies <V> of the canonical ensembles of configurations as:

$$\Delta H_n = \Delta U + \Delta(PV) = < V > + nRT \tag{A4.10}$$

where n is the number of solvent molecules in the cluster.[84] Stepwise binding enthalpies are obtained from the cluster enthalpies as:

$$\Delta H_{n,n-1} = \Delta H_{n-1} - \Delta H_n \tag{A4.11}$$

The stability of the NaI ion pair in clusters can be characterized by the PMF $W(r)$, which represents the free energy change along the interionic distance r.[144] In this work, the potential of mean force is calculated by statistical perturbation theory evaluation of free energy differences[161] in the course of Monte Carlo simulations by stretching the ion pair by a distance dr and collecting the potential energy differences $\Delta U(r) = U(r + dr) - U(r)$. PMF differences are evaluated from the canonical ensemble average as:

$$\Delta W(r) = W(r + dr) - W(r) = -kT \ln \left\langle e^{-\Delta U(r)/kT} \right\rangle_r \tag{A4.12}$$

In our simulations, we employ a double-wide sampling of the potential energy differences and calculate the equilibrium ensemble average with the acceptance ratio method of Bennett.[162] At each internuclear separation r, we make use of both a forward or backward perturbation, which provides an estimate of the statistical error associated with the free energy differences.[163] In this work, simulations are performed from r = 1.4 Å up to r = 20.0 Å, with a perturbation step size of 0.2 Å. Finally, the PMF $W(r)$ is obtained by summing the $\Delta W(r)$ free energy differences (and their statistical errors), and anchoring the potential of mean force to a long range $-e^2/r$ Coulombic potential term in the 15-20 Å range of NaI internuclear separations.

As mentioned earlier, ion pairs may exist as CIP or SSIP species in clusters. The CIP dissociation constant can be calculated from the PMF as[164]

$$K_{diss} = \frac{[Na^+][I^-]}{[Na^+I^-]} = \frac{1}{4\pi N_A \int_{CIP} r^2 e^{-W(r)/kT} dr} \tag{A4.13}$$

where N_A is Avogadro's number. The integration limits of the integral in Eq. (A4.13) are varied, until the dissociation constant is numerically and locally converged. In the case where a stable SSIP exists, the position of the CIP to SSIP free energy barrier determines the upper limit of the integral. The equilibrium constant between the CIP and the SSIP is then expressed as[165]

$$K_{SSIP/CIP} = \frac{[SSIP]}{[CIP]} = \frac{\int_{SSIP} r^2 e^{-W(r)/kT} dr}{\int_{CIP} r^2 e^{-W(r)/kT} dr} \tag{A4.14}$$

The lower limit of the numerator integral is the location of the free energy barrier between the CIP and the SSIP (i.e. the upper limit of the denominator integral). The upper limit for the numerator is varied until the equilibrium constant is locally

converged,[166] but it is assigned an upper bound corresponding to the average CIP cluster diameter,[167] which represents an extreme situation where both ions have moved apart to opposite sides of the solvent cluster.

A4.II.F. Structural Properties

Structural properties of the clusters are analyzed in terms of the normalized radial probability distribution function (PDF) $P(r)$, which is simply evaluated from configurations as the probability of finding a solvent molecule (in practice, we chose either the methyl carbon atom or the nitrogen atom of acetonitrile) at a distance r from the ion. The latter is normalized so that the distance-dependent coordination number $N_{coord}(r)$, obtained by integration of the PDF converges to the total number of solvent molecules in the cluster.

$$N_{coord}(r) = \int_0^r P(r')dr' \tag{A4.15}$$

Cluster structures are also analyzed in terms of the relative position of the ion(s) with respect to the cluster interior, in order to discriminate between interior and surface structures,[41,168] by inspecting the distributions of convenient coordinates r'_{cm} and θ. r'_{cm} is the distance between the ion and solvent cluster center of mass distance normalized by the cluster radius.[167] Values of $r'_{cm} \ll 1$ characterize interior solvation structures, while values of $r'_{cm} \sim 1$ suggest surface solvation structures. θ is the angle between the ion, the solvent cluster center of mass and a solvent molecule central carbon atom. Similarly, we define the angle Θ between the ion pair geometric center, the solvent cluster center-of-mass, and a given solvent molecule (central carbon atom) to describe the distribution of solvents molecule around the ion pair. An isotropic ($\sin\theta$ or $\sin\Theta$) distribution is to be

expected for a spherically symmetric interior solvation structure, and any deviation from this distribution reflects accumulation of solvent molecules on one side of the ion.

A4.III. ION-ACETONITRILE CLUSTERS

A4.III.A. Ionic Cluster Thermodynamics

Table A4.3 reports stepwise binding enthalpies obtained from the Monte Carlo simulations, along with their experimental counterparts,[105,117] the predictions of quantum chemistry calculations and other data obtained in earlier theoretical work.[145] The stepwise binding enthalpies agree well with experimental data, with a maximum deviation of 1.6 kcal/mol and 1.3 kcal/mol for $Na^+(CH_3CN)_n$ and $I^-(CH_3CN)_n$, respectively, which is within the range of the accepted accuracy of the quantum chemistry calculations (1-2 kcal/mol). Our new model potential yields an average deviation of 0.6 kcal/mol for the stepwise binding enthalpies, which suggests a performance similar to that of our previous model[145] (average deviations of 0.7 kcal/mol).

Table A4.3. Stepwise binding enthalpies of ion-solvent clusters.[a]

	$Na^+(CH_3CN)_n$				$I^-(CH_3CN)_n$			
n	This work[b]	Prev. work[c]	Quant. Chem.[d]	Expt.[e]	This work[b]	Prev. work[c]	Quant. chem.[d]	Expt.[f]
1	29.8	28.8	27.9	-	10.4	9.8	9.1	11.0
2	25.5	25.2	24.4	24.4	9.1	8.9	8.2	10.4
3	20.3	20.1	18.6	20.6	8.4	7.7	-	9.2
4	15.0	14.9	14.3	14.9	7.0	6.5	-	7.8
5	11.1	12.7	-	12.7	5.9	6.2	-	7.1

a. Stepwise binding enthalpies in kcal/mol. T=300 K.
b. From Monte Carlo simulations with model potentials.
c. From Monte Carlo simulations with the model potentials of Ref. [145].
d. MP2/6-311+G(d) calculations within the rigid rotor-harmonic oscillator approximation.
e. Taken from Ref. [105].
f. Taken from Ref. [117].

Our simulations confirm a value of 30 kcal/mol for the $Na^+(CH_3CN)$ binding enthalpy, which to the best of our knowledge has not yet been determined experimentally. Quantum chemistry estimates of the binding enthalpies exhibit a larger deviation with respect to experimental values (1.3 kcal/mol average deviation), maybe because of the rigid rotor-harmonic oscillator approximations employed in such calculations.

Total cluster enthalpies ΔH_n, along with reduced cluster enthalpies $\Delta H_n/n$, are plotted in Fig. A4.2 for both $Na^+(CH_3CN)_n$ and $I^-(CH_3CN)_n$. ΔH_n obviously increases much faster with cluster size for $Na^+(CH_3CN)_n$ than for $I^-(CH_3CN)_n$ because of stronger ion-solvent interactions. At larger cluster sizes, one can observe a slower increase of ΔH_n, with a transition occuring between 5 to 8 solvent molecules. This feature can be connected to a change in cluster structural properties, such as the completion of a solvation shell, as we will see shortly. Inspection of $\Delta H_n/n$ shows convergence towards the liquid acetonitrile heat of vaporization of 7.9 kcal/mol,[118] but to underestimated values (7.3 kcal/mol and 5.0 kcal/mol for $Na^+(CH_3CN)_{36}$ and $I^-(CH_3CN)_{36}$ clusters). Such an effect is typically attributed to cluster edge effects, where the deficiency of the molecules on the surface relative to the liquid situation leads to an underestimated enthalpies.[145] These findings, as well as the very slow convergence of cluster enthalpies to their bulk counterpart with cluster size, are consistent with earlier predictions of the liquid drop model.[120]

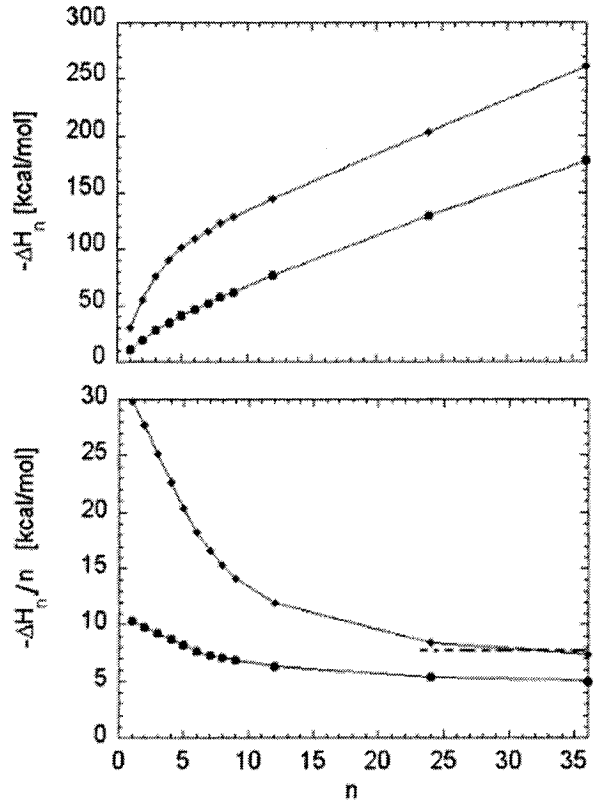

Fig. A4.2. Cluster enthalpies ΔH_n from room-temperature Monte Carlo simulations for $Na^+(CH_3CN)_n$ [diamonds], and $I^-(CH_3CN)_n$ [circles] as a function of cluster size. The bottom panel displays reduced cluster enthalpies $\Delta H_n / n$. The dashed line in the bottom panel is the acetonitrile experimental heat of vaporization.

A4.III.B. Ionic Cluster Solvation Structure

Representative structures from room-temperature simulations are shown in Fig. A4.3. Typically, cationic and anionic clusters have similar sizes, with a radius of ~10 Å at size 36.[167] Representative structures of ionic clusters suggest an interior solvation structure, which can be confirmed by inspection of the probability distributions of the scaled ion-solvent center-of-mass distance (r'_{cm}) shown in Fig. A4.4a. Indeed, the distributions hardly spread beyond a value of 0.35, and peak around 0.15, which clearly indicates an interior solvation structure. These results imply that ion-solvent interactions compensate for the free energy destabilization associated with the solvent network

disruption. Further insight into the solvent distribution can be obtained from the angular PDFs reported in Fig. A4.4b. An approximate sin θ dependence was obtained for all ionic clusters, revealing an isotropic solvent distribution around the central ion.

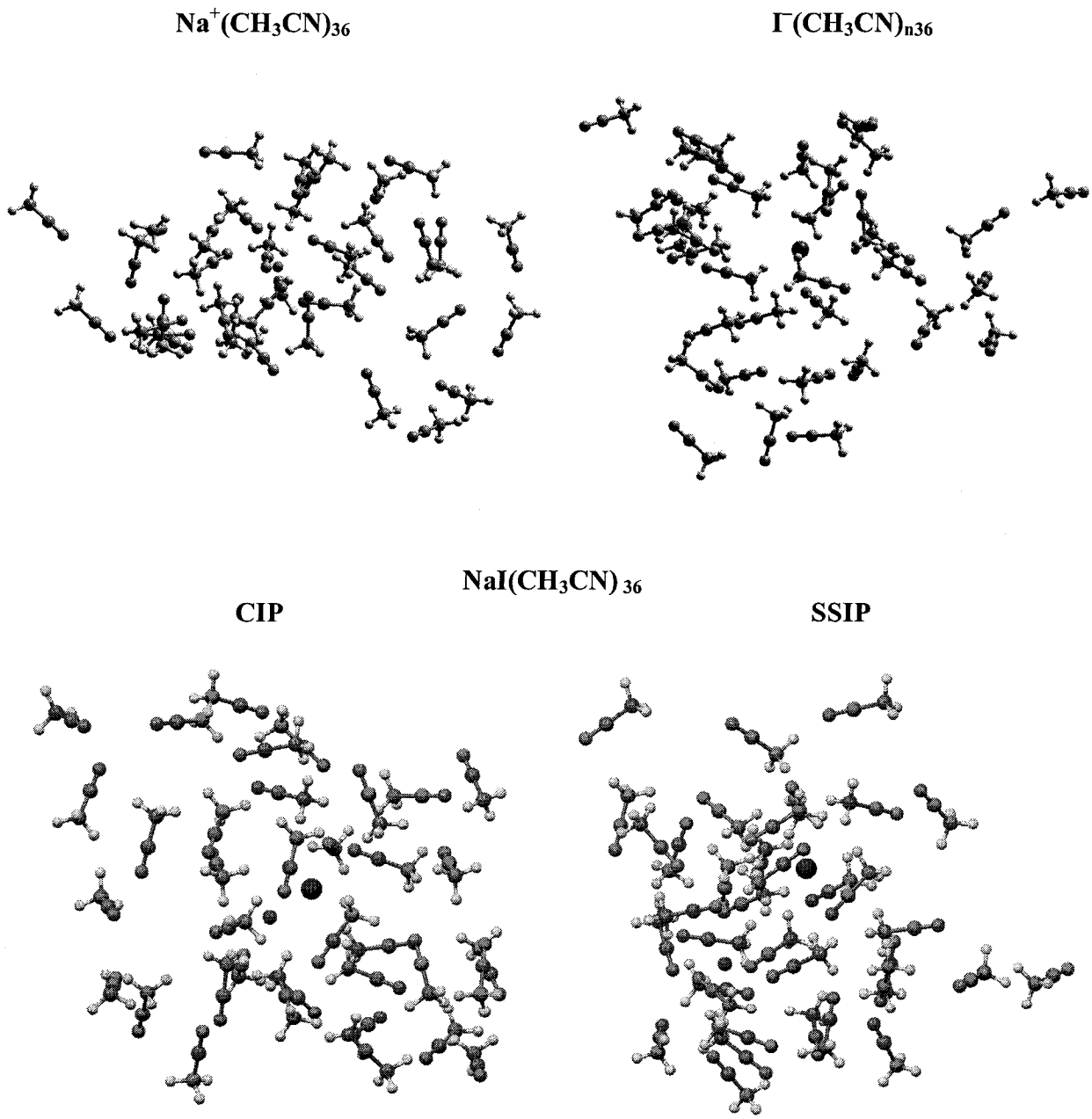

Fig. A4.3. Representative structures of room-temperature $Na^+(CH_3CN)_n$, $I^-(CH_3CN)_n$ and $NaI(CH_3CN)_n$ clusters (n=36) obtained from Monte Carlo simulations at 300 K.

Ion-solvent radial probability distributions and coordination numbers are reported in Fig. A4.4c for $Na^+(CH_3CN)_n$ and $I^-(CH_3CN)_n$ clusters, respectively. Even though I^- tends to interact with the hydrogen atoms of CH_3CN, we found it more appropriate to demonstrate the solvation shell structure by showing the I-C_M PDF, rather than the I-H PDF, because of peak broadening due to the interaction of the ion with the three hydrogen atoms. The sharp, distinct peaks in the PDFs, associated with plateaus in the coordination number function $N_{coord}(r)$ is clear evidence for well-defined solvation shells. The first solvation shells contain 5.4 and 8.0 solvent molecules for $Na^+(CH_3CN)_{32}$ and $I^-(CH_3CN)_{32}$ clusters, respectively. As $I^-(CH_3CN)_n$ clusters are characterized by weaker ion-solvent interactions than $Na^+(CH_3CN)_n$ clusters, broader peaks along with larger coordination numbers are naturally observed, as seen previously.[145] We note in passing that the value for the sodium ion first solvation shell coordination number of 5.4 is close to that computed for the liquid phase with another model potential.[86] The solvation shell structure can be connected to the evolution of the total cluster enthalpy with cluster size shown in Fig. A4.2. As the first solvation shell is completed, addition of molecules beyond the first solvation shell leads to smaller enthalpy changes as the acetonitrile molecules are located further away from the ion, and the stepwise binding enthalpies are greatly reduced.

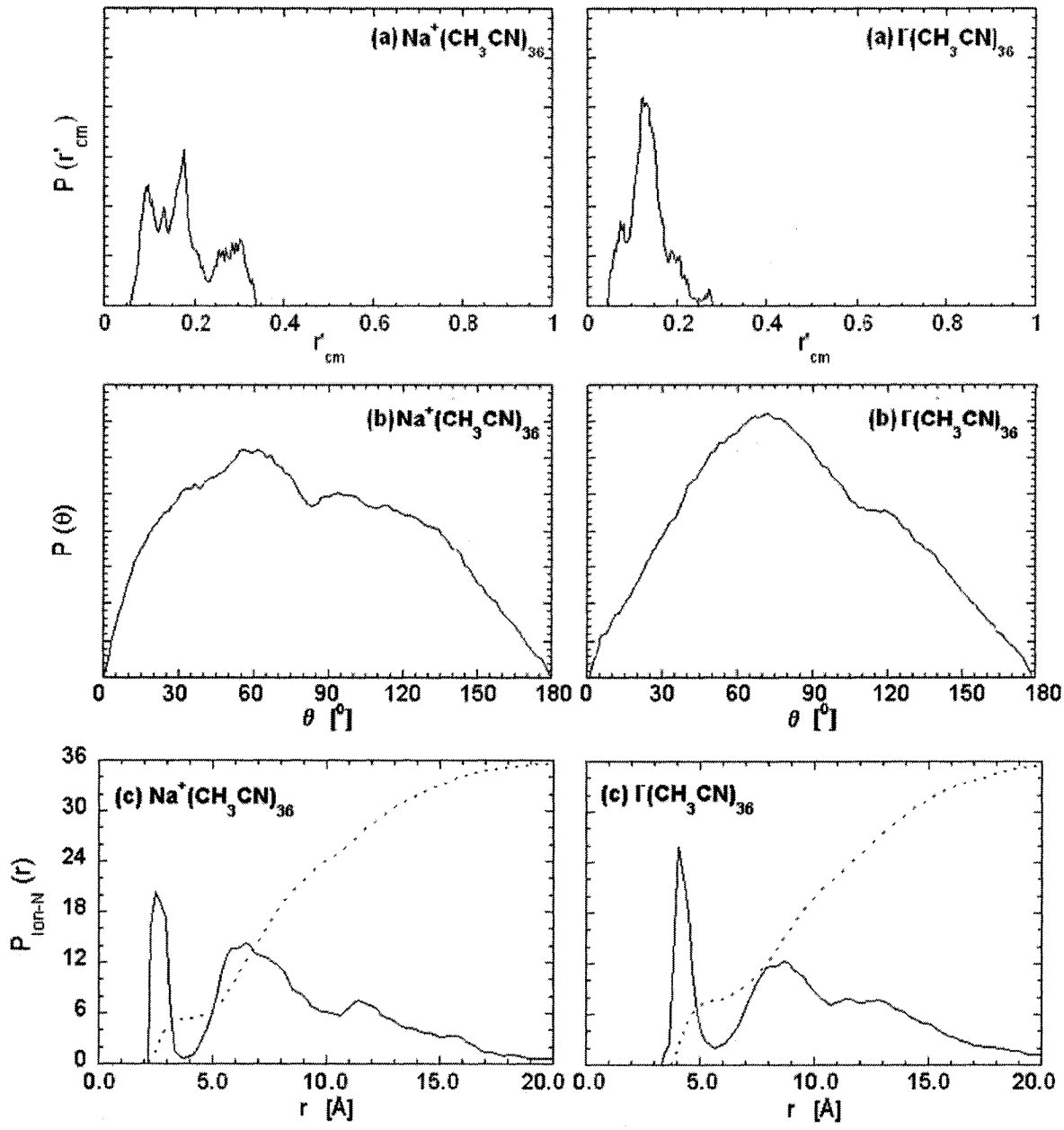

Fig. A4.4. Structural properties of $Na^+(CH_3CN)_n$ and $I^-(CH_3CN)_n$ clusters [n=12 and 36] obtained from Monte Carlo simulations at 300 K. (a) Probability distributions of the scaled ion to solvent center-of-mass distance r'_{cm}. (b) Angular probability distributions P(θ). (c) Ion-solvent distributions. Solid curves are radial probability distribution functions P(r), while dashed curves are the distance-dependent coordination number $N_{coord}(r)$. For $Na^+(CH_3CN)_n$ clusters, the coordinating atom is the nitrogen, whereas for $I^-(CH_3CN)_n$, the coordinating atom is the methyl carbon.

A4.IV. ION PAIR-ACETONITRILE CLUSTERS

A4.IV.A. Thermodynamics of Ion-Pair Clusters

We have investigated $NaI(CH_3CN)_n$ clusters up to size 36, and the resulting PMFs are displayed in Fig. A4.5. In the course of our simulations, the statistical uncertainty is no greater than 0.5 kcal/mol for stepwise free energy differences, and average errors range from 0.03 to 0.06 kcal/mol. As shown in Fig. A4.5, the sum of the latter uncertainties along the PMF, add up to relatively large numbers for the absolute PMF well depths, but the relative error in the stepwise free energy differences is lower than 1 %, suggesting reasonable accuracy. All clusters exhibit a deep minimum in the PMFs at small internuclear separations, which corresponds to CIP structures, with the ion pair close to its equilibrium structure (r_{NaI}=2.6-2.8 Å). The very small dissociation constants associated with these structures, reported in Table A4.4, demonstrate their thermodynamic stability with respect to dissociation into free ionic clusters. The PMF well depth progressively decreases and becomes shallower with cluster size increase. At cluster size 6 a second minimum in the PMF appears, signaling the presence of stable SSIP species, for which the NaI internuclear separation ranges from 5.2 to 6.6 Å. The SSIPs are also stable with respect to ionic dissociation, as can be seen from their very small dissociation constants, given by $K_{diss}/K_{SSIP/CIP}$. Such findings are in good agreement with earlier theoretical predictions,[42] based on a dielectric continuum model for cluster ion and cluster ion pair solvation energies, which showed that the stability of cluster ion pairs arises from a very slow convergence of cluster ion solvation free energies with increasing cluster size. Therefore, the separated cluster ions are thermodynamically

unfavorable, and ions rather tend to exist as CIP or SSIP species. Typical structures of those $NaI(CH_3CN)_n$ CIP and SSIP clusters at 300 K are shown in Fig. A4.3.

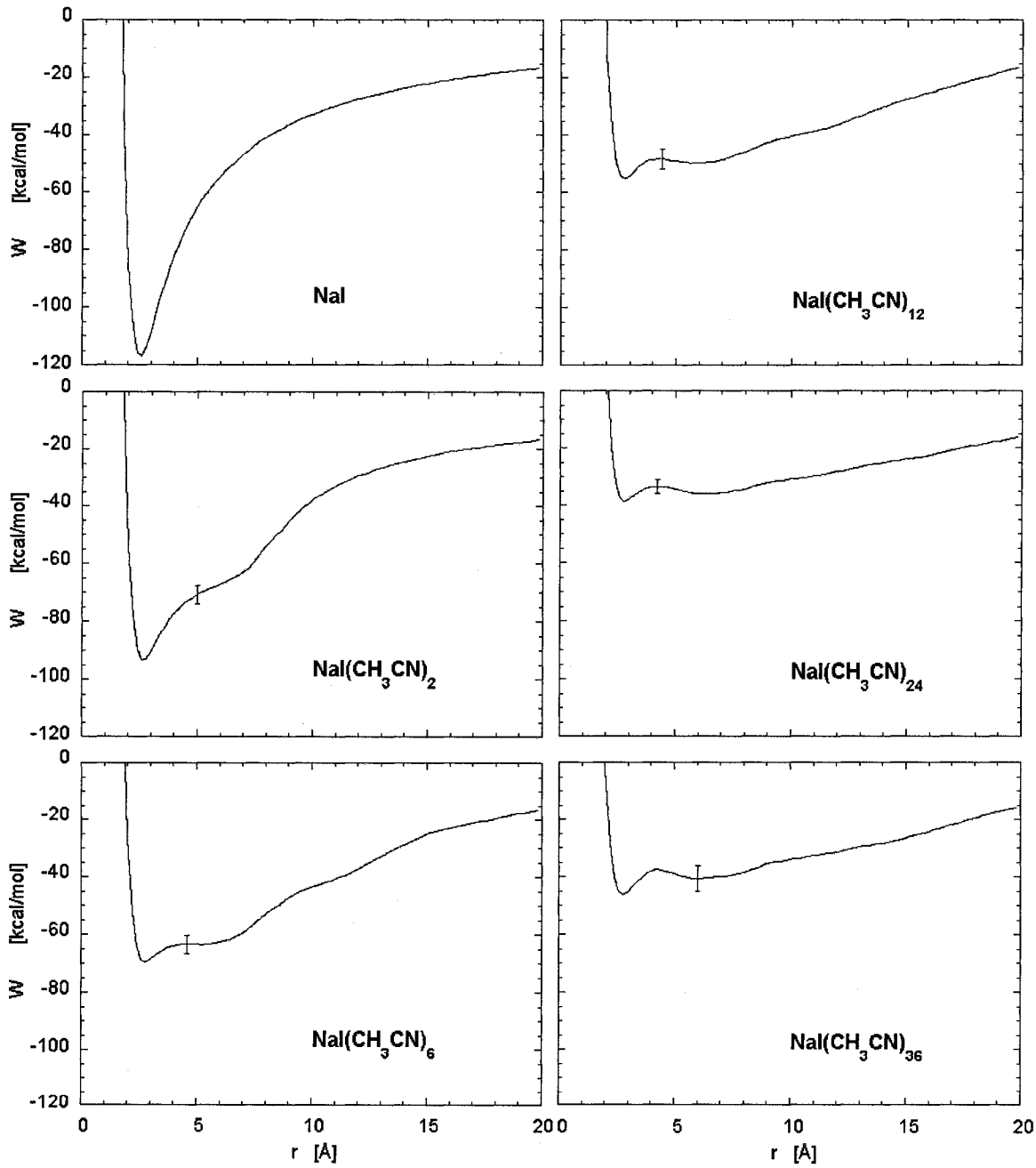

Fig. A4.5 Potentials of mean force for $NaI(CH_3CN)_n$ clusters at 300 K.

Table A4.4. Properties of the $NaI(CH_3CN)_n$ potentials of mean force.[a]

n	r_{min}^{CIP} [b]	$r_c^{\mp}$ [c]	r_{min}^{SSIP} [d]	$\Delta G_{CIP}^{\mp}$ [e]	$\Delta G_{SSIP/CIP}$ [f]	$K_{SSIP/CIP}$ [g]	Log K_{diss} [h]
1	2.59	-	-	-	-	-	108 ±1
2	2.66	-	-	-	-	-	85 ±1
4	2.71	-	-	-	-	-	85 ±1
6	2.76	4.60	5.26	6.2 ± 0.1	6.0 ± 0.1	10^{-5}	73 ±1
8	2.77	4.46	5.50	5.6 ± 0.1	4.8 ± 0.1	10^{-4}	64 ±1
12	2.77	4.33	6.01	7.2 ± 0.2	5.6 ± 0.1	$2\ 10^{-5}$	58 ±1
16	2.79	4.20	5.96	5.0 ± 0.0	2.9 ± 0.0	$1.5\ 10^{-2}$	47 ±1
20	2.78	4.22	6.43	5.1 ± 0.1	2.2 ± 0.1	$7\ 10^{-2}$	42 ±1
24	2.78	4.13	6.30	5.2 ± 0.0	2.6 ± 0.0	$4\ 10^{-2}$	40 ±1
30	2.81	4.15	6.57	4.7 ± 0.0	2.1 ± 0.1	10^{-1}	37 ±1
36	2.81	4.15	6.38	4.6 ± 0.0	1.2 ± 0.1	1.7	30 ±1

a. Free energies in kcal/mol and distances in Å.
b. NaI internuclear separation at the minimum of the CIP well.
c. NaI internuclear separation at the CIP to SSIP barrier.
d. NaI internuclear separation at the minimum in the SSIP well.
e. Free energy barrier height measured from the minimum in the CIP.
f. Free energy of the SSIP relative to that of the CIP.
g. CIP $\rightleftarrows$ SSIP equilibrium constant, from Eq. (A4.13).
h. Dissociation constant for the CIP, Eq. (A4.14), in $(mol/l)^{-1}$.

For all cluster sizes investigated, the PMFs predict CIP species lower in free energy than the SSIP species, as can be seen from Fig. A4.5 and the positive values of $\Delta G_{SSIP/CIP}$ in Table A4.4. Converged equilibrium constants are obtained with upper bounds for the SSIP population integral varying from 6 to 9 Å with increasing cluster size. As such, clusters with r_{NaI} exceeding the SSIP upper bound contribute minimally to the SSIP population, and extreme situations where the ions would be separated by the whole solvent cluster cannot be considered as SSIP structures.[41] The equilibrium constants $K_{SSIP/CIP}$ listed in Table A4.4 clearly indicate that the CIP is thermodynamically favored over the SSIP for small clusters up to size 36. As $K_{SSIP/CIP}$ tends to increase with cluster size, the SSIP population becomes thermodynamically more probable around cluster size 36.

A4.IV.B. Ion-Pair Solvation Structure

For the range of cluster sizes investigated, $NaI(CH_3CN)_n$ clusters were found to be thermodynamically stable as CIP species, with the NaI ion pair close to its equilibrium structure (r_{NaI}=2.6-2.8 Å). From cluster size 6 and up, the SSIP species are also thermodynamically stable, with NaI internuclear separations ranging from 5.3 Å to 6.4 Å. Typical structures of $NaI(CH_3CN)_n$ CIP and SSIP species are shown in Fig. A4.3. The ion pair is surrounded by solvent molecules, as both ions solvate well in ionic acetonitrile clusters. This interior solvation structure can be confirmed by inspection of the scaled ion-solvent cluster center-of-mass (r'_{cm}) and solvent angular probability distributions, shown in Figs. A4.6a and A4.6b, respectively. If the r'_{cm} distributions confirm that both ions reside in the cluster interior ($r'_{cm} < 1$), they also indicate that the ions are equidistant from the solvent center-of-mass. Naturally, the SSIP structures are characterized by larger r'_{cm} values, due to the larger interionic distance for the SSIP. Inspection of the solvent angular distribution shows that values of 90° are most probable, implying an isotropic distribution of solvent molecules, as there are enough molecules to solvate both ions and simultaneously establish a solvent network. Further similarities between the local solvent environment around the ion pair and that of single ion-acetonitrile can be observed. Indeed, the $NaI(CH_3CN)_n$ CIP and SSIP clusters are also characterized by a solvation shell structure, as can be seen from the sharp peaks of the ion-N PDFs in Fig. A4.6d. However, overlapping peaks can be observed in the ion pair–acetonitrile clusters PDFs, which reflect the perturbation brought about by the counter-ion.

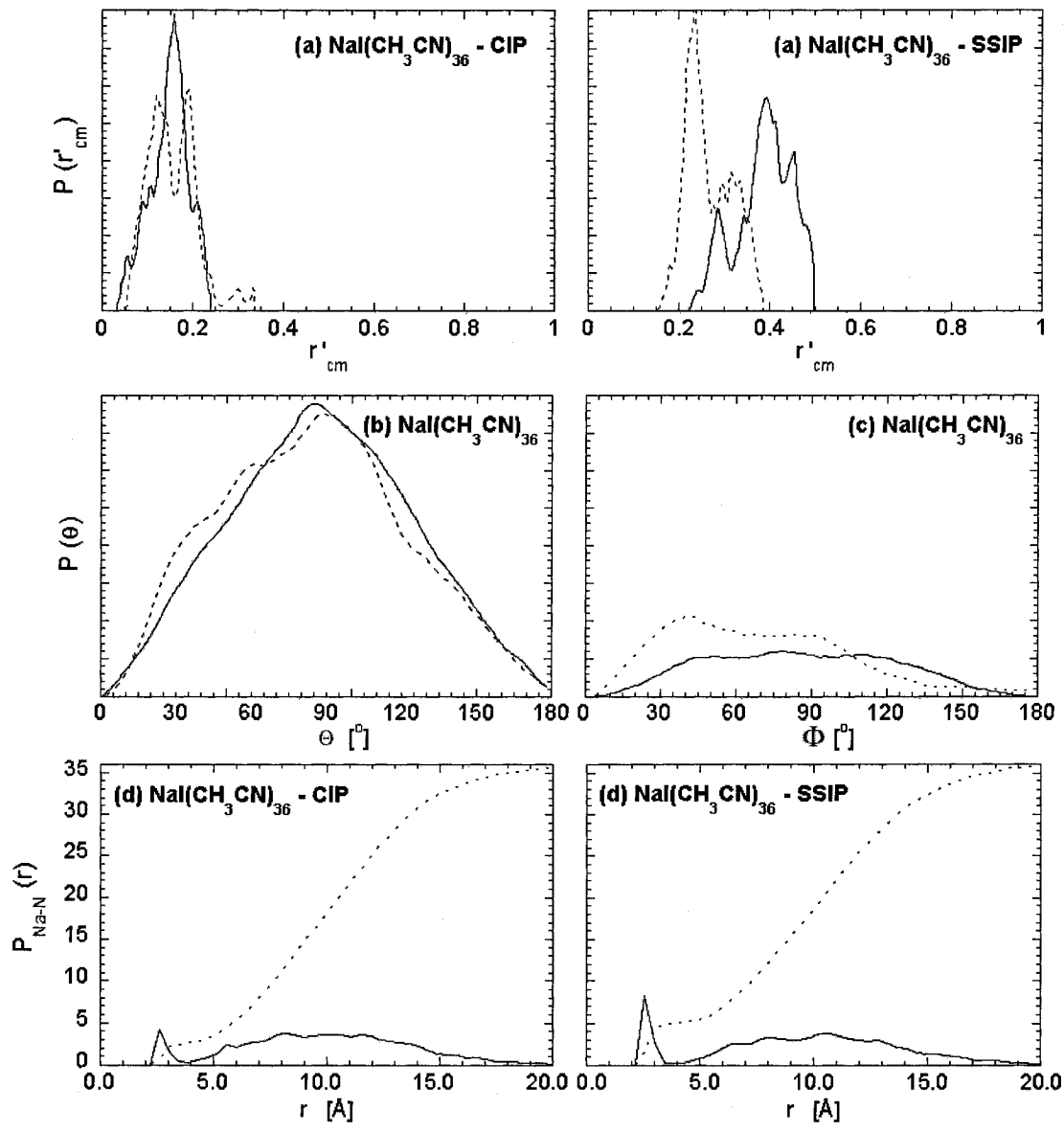

Fig. A4.6. Structural properties of $NaI(CH_3CN)_n$ clusters, obtained from Monte Carlo simulations at 300K. (a) Probability distributions of ion to solvent cluster center-of-mass distance r'_{cm} (see text). The solid line represents the Na^+ distributions, whereas the dashed line the I^- distributions. (b) Angular probability distributions $P(\Theta)$. The solid line represents the CIPs, while the dashed line represents the SSIPs. (c) Angular probability distributions for the ion first solvation shell of $NaI(CH_3CN)_n$ clusters.[169] The angle Φ is that between an individual solvent molecule dipole and the NaI ion pair. The solid line represents CIP distributions, while the dashed line represents those of SSIPs.

F

The proximity of the counter-ion perturbs the solvent network and prevents solvent molecules from entering the first solvation shell. As such, one generally observes a larger coordination number for the SSIP than for the CIP, but both coordination numbers are smaller than those of ionic clusters, as observed previously for water clusters.[41] For instance, at cluster size 36, the sodium coordination numbers are 3.0, 4.8 and 5.4 for the CIP, SSIP and ionic clusters, respectively, and those of iodide are 5.3, 7.8 and 8.0.

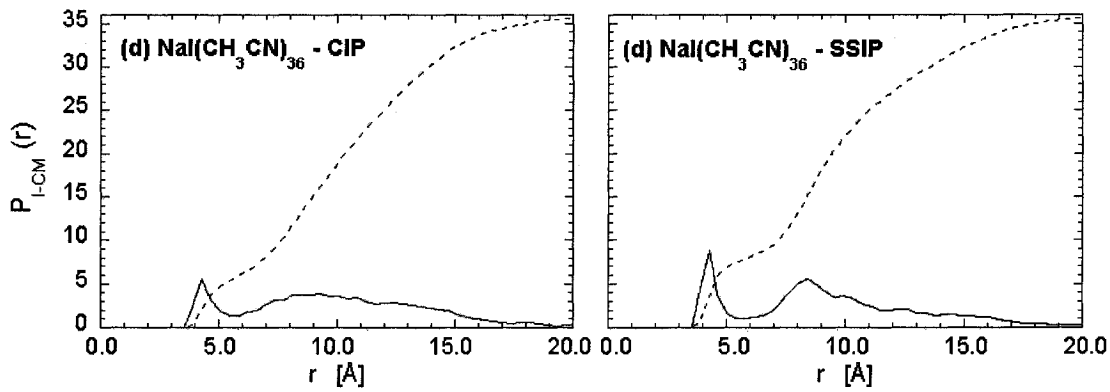

Fig. A4.6. (d) Ion-to-solvent distributions. Solid curves are radial probability distribution functions P(r), while dashed curves are the distance-dependent coordination number $N_{coord}(r)$.

Further insight into the local solvent distribution around the ion pair can be garnered by plotting the PDF of the angle Φ between NaI and the acetonitrile molecular dipoles in the first solvation shell.[169] As can be seen in Fig. A4.6c, a broad distribution characterizes the CIPs, suggesting little preferential orientation of the solvent molecules. However, in the SSIPs, a maximum is observed in the distribution around ~35-45°, which corresponds to acetonitrile molecules oriented similarly to that in the NaI(CH_3CN) SSIP model shown in Fig. A4.7. The increased dipole moment associated with the stretched

r_{NaI} distance induces local solvent ordering for SSIPs, whereas no preferential solvent orientation could be observed for CIPs. The shoulder observed at ~90° for SSIPs corresponds to solvent molecules located on each end of the NaI ion pair, and oriented in order to minimize dipole-dipole interactions and maximize Coulombic forces.

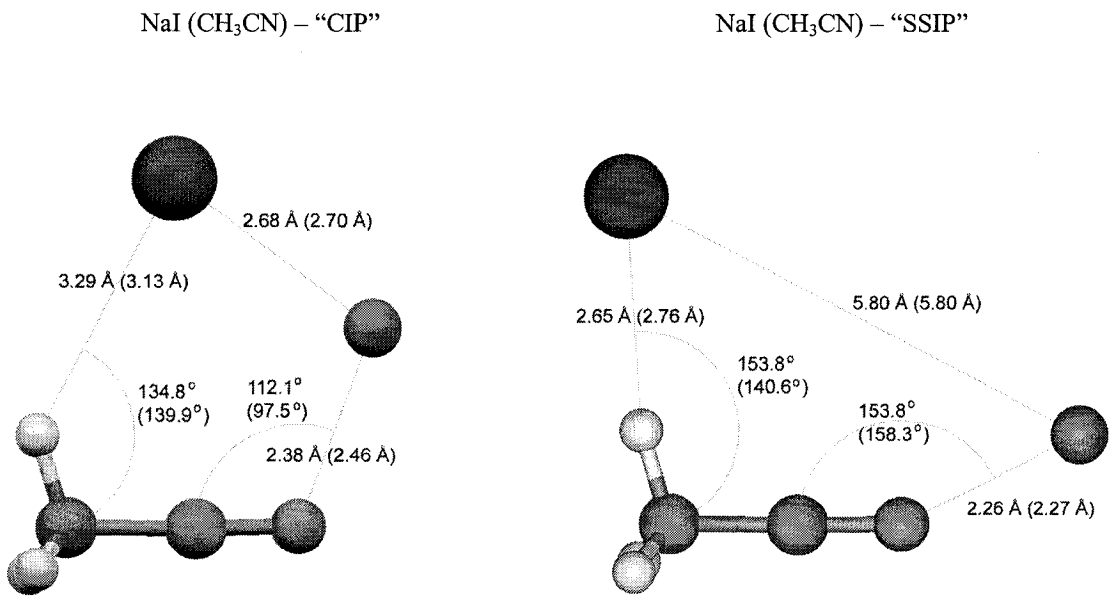

Fig. A4.7. NaI(CH_3CN) CIP and SSIP models. Bond lengths (in Å) and angles (in degrees) are obtained from quantum chemistry calculations (model potential values in parenthesis). The SSIP model was optimized with NaI constrained at a distance of 5.8 Å.

The structural and energetic properties of the model NaI(CH_3CN) SSIP shown in Fig. A4.7 (along with those of the CIP) agree very well with quantum chemistry results, with bond lengths within 0.1 Å, angles within 10°, and an energy difference relative to the CIP global minimum of 37.9 kcal/mol, which inspires further confidence in our model potentials. For larger NaI$(CH_3CN)_n$ clusters, inspection of the potential energy surfaces predicted by our model potentials and shown in Fig. A4.8 reveals that the CIP is the global minimum at least up to cluster size 6, at which cluster size stable SSIPs start

appearing. The latter species become increasingly more stable with respect to CIPs and become global minima (by only 1 kcal/mol) at cluster size 9. Our model potentials yield minimum energy structures in very good agreement with those predicted by the model potential of Gregoire *et al.*[62] However, while the SSIP is the global minimum energy structure for cluster size 9 and above, PMF calculations demonstrate that these species are not the most thermodynamically favorable, as CIP species are found more thermodynamically stable up to cluster size 36.

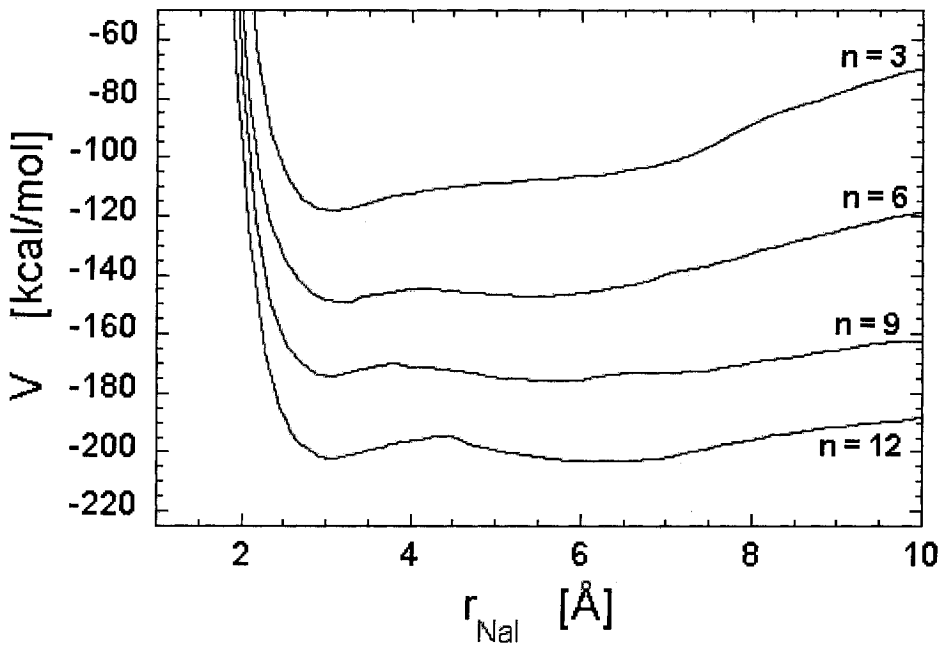

Fig. A4.8. $NaI(CH_3CN)_9$ potential energy surfaces along the r_{NaI} coordinate, predicted by model potentials.

A4.IV.C. Comparison with Aqueous Clusters and Implications for Multi-Photon Ionization Experiments

$NaI(CH_3CN)_n$ clusters exhibit some similarities with $NaI(H_2O)_n$ clusters, which have been studied previously.[41,42] In both cases, we observe deep PMF wells, with decreasing amplitude with cluster size increase, and the presence of thermodynamically stable CIP and SSIP cluster species with extremely small dissociation constants ($<10^{-35}$ and $<10^{-42}$ for $NaI(CH_3CN)_{32}$ and $NaI(H_2O)_{32}$ clusters, respectively). In small clusters of both acetonitrile and water, the ion pair only exists as a CIP, but SSIPs become more probable with cluster size increase. One noticeable difference is the existence of $NaI(H_2O)_n$ "surface" structures, due to the hydrophobicity of iodide which drags the ion pair towards the surface of the solvent network,[41] whereas the ion pair is found to solvate well in acetonitrile clusters.

The structural properties of ion pairs in clusters were shown to have some implications for cluster photodissociation dynamics. For instance, the presence of thermodynamically stable NaI ion pairs in clusters suggests favorable conditions for photodissociation experiments, in contrast to the bulk phase. This was confirmed by quantum chemistry characterization of the ground and first excited $^1\Sigma^+$ states of model $NaI(H_2O)_n$ clusters,[42] which showed that CIPs have optically accessible excited states akin to that of gas-phase NaI, with similar oscillator strengths, thus making photodissociation experiments feasible. On the other hand, SSIPs, which become thermodynamically more probable in large clusters, possess greatly reduced electronic transition oscillator strengths. As such, a photodissociation reaction mechanism akin to

that for gas-phase NaI is not possible for larger clusters, in agreement with recent experimental findings.[26,68,143]

We investigated the ground and first excited $^1\Sigma^+$ states of model $NaI(CH_3CN)_n$ clusters, employing geometries predicted by our model potentials, the configuration interaction with single excitations CI(S) method together with the aug-cc-pVDZ basis set[170] (and aug-cc-pVDZ-PP pseudopotentials for iodine).[171] Our calculations clearly reproduce the energy gap well between the ground and first excited states $^1\Sigma^+$, when compared to multireference configuration interaction with single and double excitations [MRCI(SD)] calculations,[172] or to experimental estimates (cf. Table A4.5). In previous work, the CI(S) method was also found to reproduce the dipole moments of the ground and first excited $^1\Sigma^+$ states,[42] and appeared more reliable than more sophisticated methods for the purpose of calculating Franck-Condon energy gaps and dipole moments.[173] Our results show that the transition oscillator strengths for $NaI(CH_3CN)_n$ are analogous to those of $NaI(H_2O)_n$. The oscillator strength of CIPs remains about constant upon addition of solvent molecules, implying that the presence of solvent molecules perturbs the NaI CIP electronic structure only marginally. For SSIP species however, the oscillator strength decreases drastically with increasing cluster size. Our Monte Carlo simulations suggest that $NaI(CH_3CN)_n$ CIPs are thermodynamically more probable up to cluster size 32, and model quantum chemistry calculations suggest that such CIPs would be photoexcitable. Yet, multi-photon ionization experiments predict no $Na^+(CH_3CN)_n$ cluster products larger than cluster size 6.[26] Thus, another explanation must be sought for $NaI(CH_3CN)_n$ multi-photon ionization experimental results.

Table A4.5. Properties of the first electronically excited $^1\Sigma^+$ $NaI(CH_3CN)_n$ states.

	ΔE^a	$\mu_{tr}{}^b$	$f_{osc}{}^c$
NaI (r=2.8 Å)[d]	4.5	-	-
Experimental laser[e]	~ 4.2	-	-
CI(S)/aug-cc-pVDZ, aug-cc-pVDZ-PP			
NaI (r=2.8 Å)	4.76	2.7	0.14
Antiparallel C_s $NaI(CH_3CN)$	5.43	2.4	0.12
Linear C_s $NaI(CH_3CN)$	4.98	3.0	0.17
$NaI(CH_3CN)_2$	6.09	2.2	0.12
$NaI(CH_3CN)_3$	6.23	2.3	0.12
NaI (r=5.8 Å)	1.10	5.6	0.13
$NaI(CH_3CN)$ (r=5.8 Å)	3.37	0.7	0.01

a. Energy gap between the ground state and the first $^1\Sigma^+$ excited-state in eV.
b. Transition dipole moment in D along the bonding NaI axis.
c. Oscillator strength of the electronic transition from the ground state.
d. MRCI(SD) calculations taken from Ref. [172].
e. Taken from Ref. [68].

The NaI ground ionic state is stabilized by polar solvent molecules to a much greater extent than the excited state in the Franck-Condon region, which is covalent. As the ion pair is increasingly solvated by acetonitrile molecules, the NaI Franck-Condon energy gap may increase to an extent that would render the laser wavelength inadequate for photoexcitation. This inhibition of the photoexcitation mechanism may be less pronounced in water clusters, not only because of weaker ion-solvent interactions, but also because of their characteristic surface solvation structures. Addition of solvent molecules on the cluster side, far from the ion pair, results in moderate stabilization of the ion pair and, in fact, very little change in the differential solvation energy of the ionic (ground) and covalent (excited) states (since water molecules tend to interact with each other rather than with NaI). Thus, in water clusters, it is plausible that the excited state remains accessible for larger cluster sizes, consistent with the large product clusters observed in $NaI(H_2O)_n$ multi-photon ionization experiments. Theoretical studies of the

Franck-Condon energy gaps and electronic transition oscillator strengths for $NaI(solvent)_n$ clusters are currently under way to test such hypothesis.[174] Alternate mechanisms may also be possible, involving for instance charge transfer to solvent (CTTS), which has been observed in ionic clusters and could be followed or not by electron photodetachment,[43-45,138] or even direct ionization, resulting in different dynamics. As the molecular dipole moment of acetonitrile in the gas phase is about twice that of water,[42] CTTS states can be expected to occur at smaller sizes in acetonitrile than in water clusters,[109] which would be consistent with experimental observations. Finally, solvent evaporation dynamics on the ionized state may be different for acetonitrile and water clusters. For instance, the NaI CIP is stretched to a smaller extent in acetonitrile clusters than in water clusters,[42] possibly resulting in larger Franck-Condon excess energies (due to excitation to the probe state repulsive wall), and in increased evaporation further reducing the size of acetonitrile product clusters. Furthermore, probe-state dissociation of $NaI(CH_3CN)_n^+$ clusters with interior solvation structures is more prone to reorganization than that of surface-structure $NaI(H_2O)_n^+$ clusters, where iodine is essentially free to leave the cluster without too much solvent network disruption, possibly allowing large $Na^+(H_2O)_n$ products to survive.

A4.V. CONCLUDING REMARKS

We have investigated the structural and thermodynamic properties of sodium and iodide ions and ion pairs in acetonitrile clusters by means of room-temperature Monte Carlo simulations. A model potential was developed to reproduce the properties of small ion-solvent and ion-pair-solvent clusters, such as binding energies, structure, and

molecular dipoles, obtained from quantum chemistry calculations. Comparison of the stepwise binding enthalpies obtained from Monte Carlo simulations with available experimental data suggests that our model potentials are adequate for describing many-body interactions in these clusters. Cluster enthalpies are closely related to the solvation structure of ionic clusters, and changes in their evolution with cluster size can be connected to the completion of ionic solvation shells, a finding that is less pronounced for $I^-(CH_3CN)_n$ clusters than in $Na^+(CH_3CN)_n$ clusters. Inspection of the PDFs confirmed that $Na^+(CH_3CN)_n$ and $I^-(CH_3CN)_n$ clusters have an interior solvation shell structure, with a first solvation shell constituted by ~6 and ~8 acetonitrile molecules respectively. Beyond the first solvation shell, solvent molecules tend to accumulate on one side of the cluster instead of forming a spherical droplet until at least cluster size 36.

The stability of the NaI ion pair in acetonitrile clusters was investigated via calculations of the potentials of mean force and resulting equilibrium constants. Our findings suggest that the ion pairs are thermodynamically stable with respect to dissociation into free ions, existing as either contact ion pairs (CIP) or solvent-separated ion pairs (SSIP). However, the former species are thermodynamically more favorable until at least cluster size 36. Both the CIPs and SSIPs adopt an interior solvation shell structure, which closely resembles that of the ions in ionic clusters, especially for SSIPs. $NaI(CH_3CN)_n$ clusters share similarities with $NaI(H_2O)_n$ clusters, such as the existence of CIP and SSIP structures, with CIPs being thermodynamically favored in small clusters, and SSIPs becoming increasingly more probable with cluster size increase. However, SSIPs become thermodynamically favored around cluster size 16 in water,[42] while the transition only occurs around cluster size 36 for acetonitrile. Hence, charge separation

occurs at much smaller cluster sizes for the very polar water solvent, in contrast to what was suggested earlier.[62,63]

Model quantum chemistry calculations showed that stable $NaI(CH_3CN)_n$ CIP species have optically accessible excited-states akin to that of gas-phase NaI, suggesting that multi-photon ionization experiments would in principle be possible up to at least cluster size 36. Yet, no cluster products containing more than 6 acetonitrile molecules have been observed experimentally.[26,68] Possible explanations for these findings include inhibition of photoexcitation by extensive solvation of the ground ionic state, a phenomenon that is likely to occur in smaller acetonitrile clusters than water clusters since the differential solvation energy may increase less rapidly in $NaI(H_2O)_n$ clusters due to surface solvation structures. Alternatively, $NaI(CH_3CN)_n$ clusters may be promoted to the ionized state by multi-photon excitation with a larger amount of excess energy, which, together with major solvent reorganization effects upon iodine detachment, may induce extensive solvent evaporation, hence preventing formation of large product fragments. Simulations of the NaI photoexcitation in clusters are necessary to understand the origin of the solvent selective behavior in the experiment.

CHAPTER A5
Microsolvation of Alkali - Halide Ions and Ions Pairs in Ammonia Clusters

A5.I. INTRODUCTION

We now turn our attention to clusters of ammonia. Despite all being polar solvents, ammonia, acetonitrile and water differ in terms of molecular size, dipole moment, and propensity to form hydrogen bonds, and a comparative investigation may allow better understanding of the origin of the different experimental findings associated with the various solvents.[26] In an earlier study, a solvent-selective behavior of NaI multi-photon ionization in clusters of water and ammonia was connected to differences in structural properties of the ion pair in clusters.[142] Consequently, we seek to investigate the structural and thermodynamic properties of $NaI(NH_3)_n$ clusters by means of Monte Carlo simulations, and the stability of the ion pair is inferred from computations of the potential of mean force (PMF) and related equilibrium constants.[144] Of paramount importance for these simulations are the development and validation of model potentials capable of adequately describing the intermolecular interactions between NaI and the solvent molecules in clusters. Accordingly, we have developed model potentials parameterized on the basis of quantum chemistry calculations for small clusters, and the model validation is achieved by comparing the results obtained from simulations with these potentials to available experimental thermochemical data for ionic clusters such as $Na^+(NH_3)_n$ and $I^-(NH_3)_n$.

The outline of this chapter is as follows. While an overview of the simulation procedure is presented in Sec. A5.II, the thermodynamic and structural properties of

$Na^+(NH_3)_n$ and $I^-(NH_3)_n$ clusters obtained from Monte Carlo simulations are presented and discussed in Sec. A5.III, where they are compared to available experimental data for validation of the model potentials. This will be followed by a presentation and discussion of $NaI(NH_3)_n$ cluster properties in Sec. A5.IV, with particular emphasis on the cluster thermodynamics and structures. Temperature effects will be discussed in Sec. A5.V, along with a comparison with other solvents and possible implications for cluster multi-photon ionization experiments. Concluding remarks follow in Sec. A5.VI.

A5.II. COMPUTATIONAL PROCEDURE

A5.II.A. Model Potentials

While a number of solvent model potentials have been reported for ammonia cluster simulations, most neglect polarization interactions.[148,175,176] Thus, we have decided to develop new model potentials which explicitly take polarization into account and consist of additive classical solvent-solvent and solute-solvent intermolecular potentials, along with NaI solute potentials obtained from semiempirical quantum chemistry. The analytical form proposed by Deng *et al.*[177] has been adopted for the solvent-solvent interactions, while the functional form we have developed in earlier work[178] is adopted for ion-solvent interactions. The solvent model employs rigid molecules fixed at the experimental gas-phase ammonia geometry.

The interaction energy between solvent molecules, and between solvent molecules and ions, consists of Coulombic, many-body polarization and repulsion-dispersion contributions

$$V = V_{Coul} + V_{pol} + V_{rep-disp}. \tag{A5.1}$$

The Coulombic part,

$$V_{Coul} = \sum_i \sum_{j<i} \frac{q_i . q_j}{|\mathbf{r}_i - \mathbf{r}_j|} \tag{A5.2}$$

represents the interactions between the fractional charges q_i on each charge site (at position $\mathbf{r}_i$) of the monomers. For the rigid ammonia molecule, the hydrogen atoms each bear a positive charge and the compensating negative charge is placed at a site M situated down the C_3 molecular axis at a distance $r_{M\text{-}N}$ from the nitrogen atom. The ions simply carry a positive or negative unit charge. As for polarization, one polarizable site is placed on each ion, and on the nitrogen atom of each ammonia molecule (which corresponds approximately to the position of the ammonia molecule center-of-mass), with polarizability α_i and induced dipole moments $\boldsymbol{\mu}_i$. The polarization contribution is expressed as[87]

$$V_{pol} = -\frac{1}{2} \sum_i \mathbf{E}_i^{\circ} . \boldsymbol{\mu}_i \tag{A5.3}$$

where the electric field $\mathbf{E}_i^{\circ}$ due to the permanent charges of other monomers is given by

$$\mathbf{E}_i^{\circ} = \frac{\sum_j q_j . \mathbf{r}_j}{|\mathbf{r}_i - \mathbf{r}_j|^3} \tag{A5.4}$$

and the induced dipole moments are calculated from

$$\boldsymbol{\mu}_i = \alpha_i . \mathbf{E}_i = \alpha_i \left[\mathbf{E}_i^{\circ} + \sum_{j \neq i} T_{ij} . \boldsymbol{\mu}_j \right] \tag{A5.5}$$

where T_{ij} is the dipole tensor.[87] Because of mutual polarization, the set of induced dipoles $\boldsymbol{\mu}_i$ is obtained in a self-consistent fashion by solving the set of linear equations in Eq.

(A5.5) by LU decomposition and backsubstitution.[77,88] Finally, short-range repulsion-dispersion interactions are modeled via generalized Lennard-Jones potentials[147]

$$V_{rep-disp} = \left(\sum_{i,j} A_{ij} r_{ij}^{-12} + B_{ij} r_{ij}^{-8} + C_{ij} r_{ij}^{-6} \right) \tag{A5.6}$$

Whereas a single nitrogen-nitrogen term was found to be necessary for solvent-solvent interactions, repulsion-dispersion terms between all atoms were required to properly describe ion-solvent interactions.

The NaI ion pair model potential has been reported in earlier publications,[41,42] to which the reader is referred to for details. Briefly, the potential energy expression contains Coulombic, polarization and core-core repulsion terms

$$V_{solute} = V_{Coulomb} + V_{pol} + V_{core-core} \tag{A5.7}$$

The Coulombic and polarization interactions are described by Eqs. (A5.2) and (A5.3) discussed earlier. The core-core potential is represented by an exponentially repulsive Born-Mayer potential[42]

$$V_{core-core} = Ae^{-Br} \tag{A5.8}$$

parameterized to reproduce the ground-state NaI potential curve determined from either experiment[149] or high level quantum chemistry[150] calculations (A=70810 kcal/mol, and B=0.326 A^{-1}).[179] Since the ion effective polarizability is affected by the presence of another ion, the Na^+ and I^- polarizabilities are attenuated with decreasing internuclear separations via a smooth switching function, in order to reproduce the bare ground-state NaI dipole moments from high-level quantum chemistry calculations.[179] We note that this model potential allows ions and solvent molecules to polarize each other. Since first-principles quantum chemistry calculations provide the basis for the parameterization of

these model potentials, we now turn our attention to quantum chemistry calculations for small clusters.

A5.II.B. Quantum Chemistry Calculations

Ground-state properties of $(NH_3)_{1-2}$, $Na^+(NH_3)$, $I^-(NH_3)$ and $NaI(NH_3)$ clusters were obtained from ab initio calculations with the Gaussian98 quantum chemistry package.[90] Geometry optimizations and frequency calculations were performed at the second-order Møller-Plesset (MP2)[91] level of theory, together with triple-zeta split correlation-consistent polarizable bases from Dunning, with augmented diffuse functions whenever available, i.e. the aug-cc-pVTZ basis was used for N, H, and I,[180,181] while the cc-pVTZ basis was used for Na.[180] Further, the ECP28MDF relativistic effective core potential was employed for iodine.[182] In cationic complexes, inclusion of the core electrons in the correlation space has previously been deemed important,[183] so core-core and core-valence correlation basis functions were added on the sodium[184] and nitrogen centers.[185] This overall model chemistry is further simply referred to as MP2/VTZ. Clusters were first optimized with ammonia molecules fixed at their experimental, gas-phase geometry, as our model potential employs rigid solvent molecules. This procedure allowed us to confirm that monomer geometry relaxation in clusters is insignificant, hence justifying the use of rigid solvent molecules for our model potential. Then, in order to locate true minimum energy structures, cluster geometries were further optimized with all coordinates relaxed. This was followed by a frequency calculation in order to characterize the stationary points and obtain harmonic zero-point energies.

The ammonia geometry obtained with MP2/VTZ is essentially the same as the experimental gas-phase geometry, with $R_{N-H} = 1.01$ Å and $R_{H-H} = 1.63$ Å. In addition, the

experimental ammonia dipole moment is reproduced within 0.05 D and the quadrupole moment within 0.1 D.Å, as seen from Table A5.1. We note that even though polarizabilities are notoriously difficult to determine accurately with quantum chemistry, our model chemistry reproduces the NH_3 isotropic polarizability within 0.1 $Å^3$.

Binding energies (D_e) are calculated via the supermolecule approach. In addition, a correction for zero-point energy (ZPE), calculated on the basis of harmonic frequencies, is included to yield D_o. Finally, the binding energy $D_{o/CBS}$ was corrected for Basis Set Superposition Error (BSSE) by extrapolation to the Complete Basis Set (CBS) limit, making use of energies obtained from a set of calculations with a series of systematically convergent correlation-consistent basis sets.[191] Accordingly, single-point energy calculations were performed with the double-zeta (DZ), triple-zeta (TZ), and quadruple-zeta (QZ) basis sets, with augmented diffuse functions, relativistic core potentials for iodine, and core-core and core valence basis functions, as discussed earlier, for the MP2/VTZ optimized geometries. An analytical solution[192] of a three-point extrapolation based on the exponential/Gaussian function of Woon and Dunning,[191]

$$E_{CBS} = \frac{E_{DZ}(e^{-7} - e^{-11}) + E_{TZ}(e^{-10} - e^{-4}) + E_{QZ}(e^{-3} - e^{-5})}{(e^{-7} - e^{-11}) + (e^{-10} + e^{-4}) + (e^{-3} - e^{-5})} \qquad \text{(A5.9)}$$

was then employed, where E_{DZ}, E_{TZ} and E_{QZ} correspond to energies calculated with the DZ, TZ, and QZ basis sets, respectively.

Table A5.1. Small cluster properties.[a]

	Experiment	Quant. chem.[b]	Mod. pot.
		NaI	
R_{Na-I}	2.71[c]	2.77	2.71
μ_{NaI}	9.2[d]	9.7	9.7
D_e		117.8, 120.8, 122.0	
D_o	116.6[c]	116.8, 120.4, 121.7	120.7
$D_{o/CBS}$		122.4	
		NH_3	
α	2.22[e]	2.1	2.22
μ_{NH_3}	1.47[e]	1.52	1.47
Θ_{zz}	2.9[f]	2.9	2.9
		Linear C_s $(NH_3)_2$	
r_{N-N}		3.31	3.31
r_{N-H}		2.26	2.30
r_{H-H}		2.75	2.55
μ_{NH_3}		1.72 / 1.82	1.48 / 1.73
D_e		3.6, 3.5, 3.5	
D_o		2.1, 2.1, 2.1	2.4
$D_{o/CBS}$		2.1	
		Asymmetric C_s $(NH_3)_2$	
r_{N-N}		3.23	3.31
r_{N-H}		2.3	2.30
r_{H-H}		2.36	2.55
μ_{NH_3}		1.52 / 1.73	1.48 / 1.73
D_e		3.7, 3.7, 3.8	
D_o		2.3, 2.3, 2.4	2.4
$D_{o/CBS}$		2.4	
$\Delta H_{1,0}$		1.7	
		$Na^+(NH_3)$	
r_{Na-N}		2.41	2.43
θ_{Na-N-M}		180.0	180.0
μ_{NH_3}		3.63	3.31
D_e		27.0, 27.4, 27.7	
D_o		25.2, 25.6, 25.8	25.8
$D_{o/CBS}$		26	
$\Delta H_{1,0}$	25.6±0.2[g] 24.4±1.3[h]	25.7	25.3[i]

	Experiment	Quant. chem.[b]	Mod. pot.
		$I^-(NH_3)$	
r_{I-N}		3.73	3.78
r_{I-H}		2.73	2.78
μ_{NH_3}		2.43	1.98
D_e		7.2, 8.0, 8.4	
D_o		6.5, 7.4, 7.7	8.0
$D_{o/CBS}$		7.9	
$\Delta H_{1,0}$	7.4±0.3[j]	7.8	7.1[i]
		C_s NaI(NH_3)	
r_{I-H}		2.87	2.74
r_{Na-N}		2.45	2.50
θ_{Na-N-I}		50.4	48.6
μ_{NH_3}		1.70	3.40
D_e		18.2, 18.5, 18.8	
D_o		16.6, 16.9, 17.2	18.9
$D_{o/CBS}$		17.4	
$\Delta H_{1,0}$		17.2	17.1[i]
		C_{3v} NaI(NH_3)	
r_{I-H}		5.62	5.80
r_{Na-N}		2.4	2.55
θ_{Na-N-I}		0.0	0.0
μ_{NH_3}		4.45	3.59
D_e		17.6, 17.3, 17.5	
D_o		15.7, 15.4, 15.6	14.9
$D_{o/CBS}$		15.8	
$\Delta H_{1,0}$		15.5	17.1[i]

a. Distances are in Å, angles (θ) in degrees, dipole moments (μ) in Debye, polarizabilities (α) in $Å^3$, quadrupole moments (Θ_{zz}) in Debye.Angtrom (D.Å), binding energies (D_e, D_o, $D_{o/CBS}$) and stepwise binding enthalpies ($\Delta H_{1,0}$) in kcal/mol.
b. The listed D_e and D_o are binding energies calculated with the DZ, TZ, and QZ split basis sets, respectively, for MP2/VTZ optimized geometries. $D_{o/CBS}$ is the binding energy corrected for ZPE and extrapolated to the CBS limit.
c. Taken from Ref. [154].
d. Taken from Ref. [155].
e. Taken from Ref. [114].
f. Taken from Ref. [186].
g. Stepwise binding enthalpy at 298 K taken from Ref. [187].
h. Stepwise binding enthalpy at 298 K taken from Ref. [188].
i. From Monte Carlo simulations at 300 K.
j. Stepwise binding enthalpy at 298 K taken from Refs. [189] and [190].

The NaI geometry was found to be reproduced well by MP2/VTZ (within 0.06 Å), and the binding energy within 5% (cf. Table A5.1). Surprisingly, we note that calculations with the DZ-quality basis set yield binding energies in better agreement with experimental data (within 1%) than calculations with larger basis sets or complete basis set extrapolation. The NaI dipole moment is also well reproduced, with a deviation of only 0.5 D (5 %).

The minimum energy structures of pure solvent clusters, ion-solvent clusters, and ion pair-solvent clusters obtained from quantum chemistry calculations are shown in Fig. A5.1, while selected geometrical parameters and binding energies are collected in Table A5.1. Non-corrected and corrected intermolecular interaction energies are reported, showing that the ZPE and BSSE corrections are typically of the order of 1-2 kcal/mol. The nature of the $(NH_3)_2$ minimum energy structure has been under heated debate since the early 1980's,[193,194] and despite many theoretical investigations, some discrepancies remain.[194-196] Early quantum chemistry calculations did not include electron correlation, or employed basis sets without polarization functions.[176,194] Other calculations either ignored or only approximately included typical corrections to the binding energy, such as BSSE[176,196,197] or ZPE corrections,[195,198,199] which are of similar magnitude as the binding energy itself. Our calculations predicted three $(NH_3)_2$ stationary points, which correspond to the isomers reported in previous work.[176,194-198] However, vibrational analysis suggests that only two structures are minimum-energy structures, and the third isomer is a transition state connecting the global minimum-energy structures by a rocking motion.[200] Inspection of Fig. A5.1 and Table A5.1 reveals that the two minima have very similar geometries. For instance, both r_{N-H} and r_{N-N} intermolecular distances are within 0.1 Å,

which is consistent with the very similar interaction energies for both isomers (within 0.5 kcal/mol). The main difference between both structures lies in the N-H-N angle (θ_{NHN}). While the θ_{NHN} angle for the so-called *linear* C_s complex is exactly 180.0°, suggesting that hydrogen bonding interactions prevail for that structure, the θ_{NHN} angle for the global minimum, which we refer to as the *asymmetric* C_s structure, is 152.6°, suggesting a subtle interplay between hydrogen bonding and dipole-dipole interactions that bring additional stabilization to the dimer.

We now turn our attention to the ion-ammonia complexes. As shown in Fig. A5.1, our calculations predict minimum energy structures of C_{3v} and C_s symmetry for $Na^+(NH_3)$ and $I^-(NH_3)$, respectively. Cationic cluster structures are obviously controlled by ion-dipole interactions, while anionic cluster structures reflect the importance of hydrogen bonding interactions. Several theoretical studies have been reported concerning the $Na^+(NH_3)$ complex.[188,201,202] Earlier calculations[201] with DZ quality basis sets yielded energies 5 kcal/mol larger than their experimental counterpart, which is not too surprising since it was demonstrated that TZ or QZ basis sets are generally necessary to obtain accurate energetics for small ionic clusters.[111] On the other hand, our $Na^+(NH_3)$ binding energy is within 1 kcal/mol of that predicted by more recent calculations that include electron correlation together with a minimum TZ split basis set.[111,187,188,203] To our knowledge, $I^-(NH_3)$ has only been studied at the Hartree-Fock level,[148] and neglect of electron correlation together with the use of a small basis set obviously resulted in a binding energy (D_e=4.4 kcal/mol) much smaller than the one predicted in the present work. Finally, stepwise binding enthalpies $\Delta H_{n,n-1}$ obtained from $D_{o/CBS}$, with thermal effects estimated under the rigid rotor-harmonic oscillator approximation with MP2/VTZ

were found in excellent agreement with experimental data, as can be seen from Table A5.1.

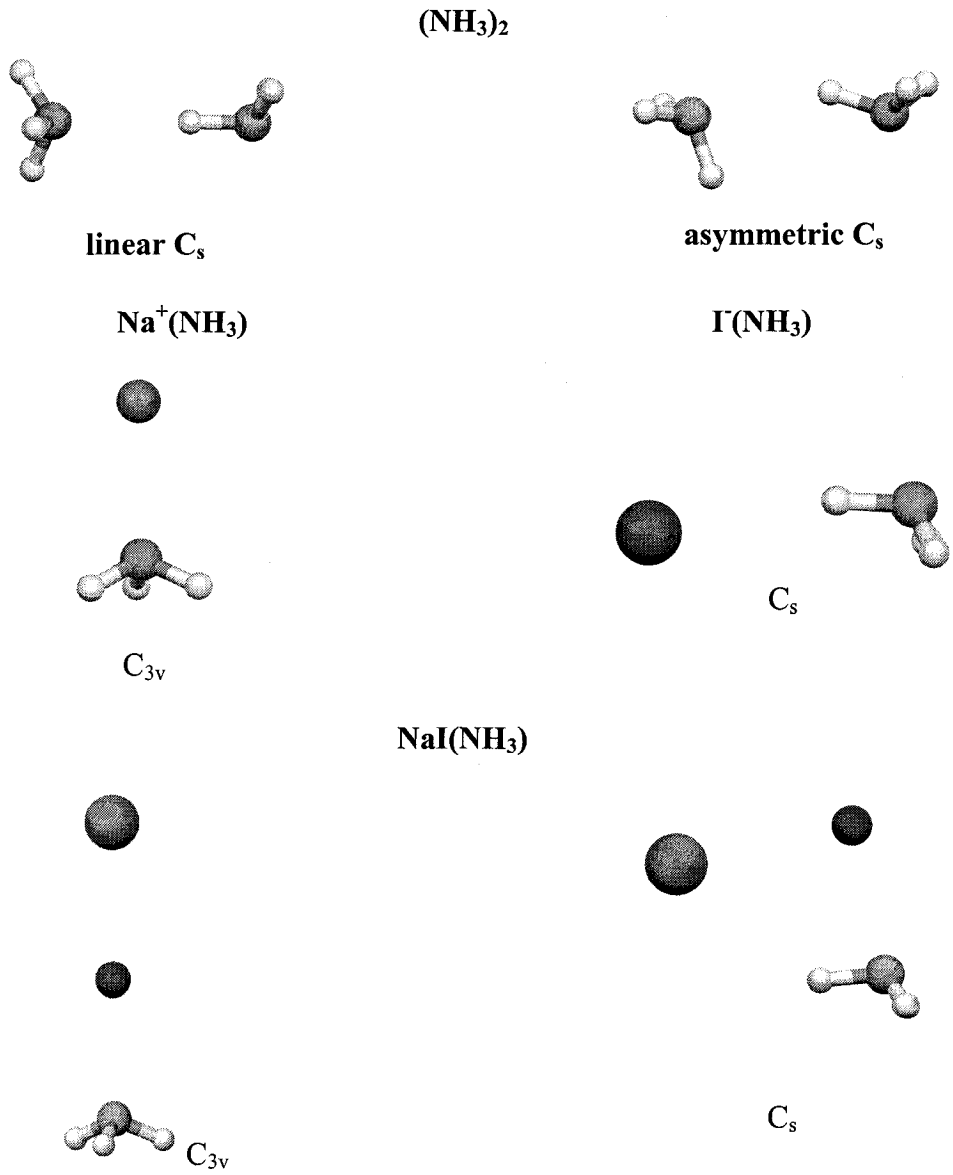

Fig. A5.1. Minimum energy structures for $(NH_3)_2$, $Na^+(NH_3)$, $I^-(NH_3)$ and $NaI(NH_3)$ clusters predicted by quantum chemistry calculations.

No first-principles study of the $NaI(NH_3)$ complex has been reported in the literature to date. Our calculations predict two minimum energy structures, which are shown in Fig. A5.1. The global minimum energy structure exhibits C_s symmetry, with the

ammonia and NaI dipole moments approximately aligned in a head-to-tail fashion. About 0.5 kcal/mol higher in energy lies the C_{3v} minimum, with aligned NaI and ammonia dipole moments. Both structures were included in the model potential parameterization.

Molecular dipole moments of individual monomers, evaluated from the ESP charge distribution[99] of the supermolecule are also reported in Table A5.1. Quantum chemistry calculations indicate that when placed in the vicinity of another solvent molecule or an ion, the ammonia dipole moment (μ_{NH_3}) increases significantly from its gas-phase value, reflecting the importance of polarization effects. The ion ESP charges (not listed) are *ca.* ±0.95e in ionic clusters, which indicates very little electron transfer between the ion and the solvent molecules and provides support for a model potential primarily based on electrostatics employing ion unit point charges. Molecular dipole moments are found to be larger in cationic clusters than in anionic clusters, due to stronger electrostatic interactions of ammonia with cations. In the $(NH_3)_2$ isomers, both NH_3 molecules undergo moderate mutual polarization. In contrast, the molecular dipole moments of NH_3 in the stable $NaI(NH_3)$ isomers vary widely: while the C_s structure is characterized by a NH_3 dipole moment that hardly differs from gas-phase NH_3 (within 0.2 D), the NH_3 dipole moment in the C_{3V} structure is almost three times larger than that of gas-phase NH_3, due to the alignment of the NaI and NH_3 dipoles. Again, this stresses the importance of polarization forces in such systems.

A5.II.C. Parameterization of Model Potentials

The model potential parameters include point charges (q_i), polarizabilities (α_i), and repulsion-dispersion terms (A_{ij}, B_{ij}, C_{ij}). All parameters, listed in Table A5.2, are derived on the basis of experimental data supplemented by quantum chemistry

calculations. The ammonia charge distribution was adjusted to reproduce the experimental gas-phase dipole and quadruple moment of the ammonia molecule (cf. Table A5.1), which represents a slight improvement from the original model of Deng *et al.*[177] which yielded μ_{NH3} = 1.53 D and Θ_{zz} = 2.1 D.Å values. The ionic and molecular polarizabilities are taken from gas-phase experimental data.[113,114] The repulsion-dispersion parameters are fit to reproduce the $(NH_3)_2$, $Na^+(NH_3)$, $I^-(NH_3)$, and $NaI(NH_3)$ calculated geometries and binding energies. Attention is also paid to the dipole moments of ammonia in clusters, which were compared to their quantum chemistry counterparts. The fitting was performed with a standard non-linear-least-squares method based on the Marquardt-Levenberg algorithm.[77] The cluster properties predicted by model potentials are listed in Table A5.1, where they can be compared to their quantum chemistry counterparts.

Table A5.2. Model potential parameters[a]

NH_3 geometrical parameters				
R_{N-H}	R_{H-H}	R_{N-M}	θ_{HNH}	
1.012	1.625	0.180	112.07	
Point charges and polarizabilities				
	H	M	N	Na^+	I^-
q_i	0.56	-1.68		1.0	-1.0
α_i			2.22	0.2	7.0
Lennard-Jones parameters				
	N-N	Na-N	Na-H	I-N	I-H
A	2676713	11200	40800	29126500	149750
B	0	23000	-4100	63400	-1000
C	-127	-1650	-50	-11800	-500

a. Distances are in Å, angles in degrees, point charges (q_i) in fractions of e, polarizabilities (α_i) in $Å^3$, A in kcal.$Å^{12}$, B in kcal.$Å^8$, C in kcal.$Å^6$.

Inspection of Table A5.1 shows that the structural properties for $(NH_3)_2$, $Na^+(NH_3)$, $I^-(NH_3)$ and $NaI(NH_3)$ determined with our model potentials agree well with their quantum chemistry counterparts. Our model potential predicts a single minimum energy structure for the $(NH_3)_2$ complex, with properties comparable to those of both quantum chemistry minima. For all complexes, bond lengths are generally reproduced within less than 0.05 Å, and binding energies within 1 kcal/mol. In addition, good agreement is generally observed between quantum chemistry and model potential estimates of the stepwise binding enthalpies, even though the quantum chemistry values are calculated under the rigid rotor-harmonic oscillator approximation. Slightly larger deviations in bond lengths and binding energies (ca. 0.1 Å and 1.5 kcal/mol, respectively) are observed for $NaI(NH_3)$ as the subtle balance between electrostatic and hydrogen bonding interactions is usually difficult to obtain with simple model potentials.[110,111] Nonetheless, such deviations remain within the range of accepted accuracy of quantum chemistry calculations (1-2 kcal/mol). We note that in pure solvent and ion-solvent complexes, our model potentials reproduce well the polarization of ammonia molecules (within 0.1-0.5 D). However, even though the trend in NH_3 dipole moments is qualitatively reproduced, a larger deviation is observed for μ_{NH_3} in $NaI(NH_3)$. This shortcoming may reflect the limitations of model potentials.[204]

A5.II.D. Monte Carlo Simulations

Canonical ensembles of $Na^+(NH_3)_n$, $I^-(NH_3)_n$, and $NaI(NH_3)_n$ cluster structures were generated via random-walk[64] Metropolis Monte Carlo simulations.[76] We followed the procedure developed in previous work,[41,42] and we only outline its main features here for completeness. Independent simulations are carried out for clusters of various size,

placing a given number n of NH_3 molecules around an ion or the ion pair geometrical center. New trial solvent configurations are generated by random translation of one solvent molecule in all three Cartesian directions and rotating it around its standard Euler angles θ, ψ, and φ.[78] Each run entails about 10^6 to 10^7 steps of equilibration, followed by an equivalent number of steps for data collection. The ranges of displacement for translational and rotational motion were chosen so as to obtain acceptance ratios of about 40-60 % for new configurations. Finally, the clusters are periodically heated and cooled with a smooth temperature schedule in order to sample all possible local minima[79] and to reduce uncertainties in PMF calculations.[42] Because our goal is to obtain a well-defined equilibrium ensemble of clusters of a given size, each fraction of the Markov chain containing clusters that have undergone solvent evaporation is excluded from the final conformational sampling (ammonia is considered as evaporated when it moves further than 20 Å from the closest ion). The temperature chosen for the simulations is 115 K, which roughly corresponds to the temperature of metastable ammonia clusters, according to the simple renormalized Trouton's rule of the Klots evaporative ensemble model.[205] We note that a more refined treatment indicated that clusters of different sizes have different internal temperatures, and the temperature of some small clusters has been reported to be larger by as much as a factor of 4 than that of the larger clusters,[53,54] and therefore, there is a wide uncertainty in the estimated cluster temperature of metastable $NaI(NH_3)_n$ clusters. Thus, simulations were also carried out at room temperature (300 K) for the purpose of assessing temperature effects.

A5.II.E. Thermodynamics

Cluster enthalpies are computed from the average energies <V> of the canonical ensembles of configurations as:

$$\Delta H_n = \Delta U + \Delta(PV) = < V > + nRT \tag{A5.10}$$

where n is the number of solvent molecules in the cluster.[84] Stepwise binding enthalpies are obtained from the cluster enthalpies as

$$\Delta H_{n,n-1} = \Delta H_{n-1} - \Delta H_n \tag{A5.11}$$

The stability of the NaI ion pair in clusters can be characterized by the PMF $W(r)$, which represents the free energy change along the interionic distance r.[144] In this work, the PMF is calculated by statistical perturbation theory evaluation of free energy differences,[161] in the course of Monte Carlo simulations, by stretching the ion pair by a distance dr and collecting potential energy differences $\Delta U(r) = U(r + dr) - U(r)$. PMF differences are evaluated from the canonical ensemble average as:

$$\Delta W(r) = W(r + dr) - W(r) = -kT \ln \left\langle e^{-\Delta U(r)/kT} \right\rangle \tag{A5.12}$$

In our simulations, we employ a double-wide sampling of the potential energy differences and calculate the equilibrium ensemble average with the acceptance ratio method of Bennett.[162] At each internuclear separation r, we make use of both a forward or backward perturbation, which provides an estimate of the statistical error associated with the free energy differences.[163] Simulations are performed from r = 1.6 Å up to r = 20.0 Å, with a perturbation step size of 0.2 Å. Finally, the PMF $W(r)$ is obtained by summing the $\Delta W(r)$ free energy differences (and their statistical errors), and anchoring

the PMF to a long range $-e^2/r$ Coulombic potential term in the 15-20 Å range of NaI internuclear separations.

As mentioned earlier, ion pairs may exist as CIP or SSIP species in clusters. The CIP dissociation constant can be calculated from the PMF as[164]

$$K_{diss} = \frac{[Na^+][I^-]}{[Na^+I^-]} = \frac{1}{4\pi N_A \int_{CIP} r^2 e^{-W(r)/kT} dr} \tag{A5.13}$$

where N_A is Avogadro's number. The integration limits of the integral in Eq. (A5.13) are varied, to ensure that the dissociation constant is numerically and locally converged. In the case where a stable SSIP exists, the position of the CIP to SSIP free energy barrier determines the upper limit of the integral, and the equilibrium constant between the CIP and SSIP is then expressed as[165]

$$K_{SSIP/CIP} = \frac{[SSIP]}{[CIP]} = \frac{\int_{SSIP} r^2 e^{-W(r)/kT} dr}{\int_{CIP} r^2 e^{-W(r)/kT} dr} \tag{A5.14}$$

The lower limit of the numerator integral is the location of the free energy barrier between the CIP and SSIP (i.e. the upper limit of the denominator integral). The upper limit for the numerator is varied until the equilibrium constant is locally converged, but it is assigned an upper bound corresponding to the average CIP cluster diameter,[167] which represents an extreme situation where both ions have moved apart to opposite sides of the solvent cluster.

A5.II.F. Structural Properties

Structural properties of the clusters are analyzed in terms of the normalized radial probability distribution function (PDF) $P(r)$, which is simply evaluated from configurations as the probability of finding a solvent molecule (in practice the ammonia

nitrogen atom) at a distance r from the ion. The latter is normalized so that the distance-dependent coordination number $N_{coord}(r)$, obtained by integration of the PDF converges to the total number of solvent molecules in the cluster.

$$N_{coord}(r) = \int_0^r P(r')dr' \qquad \text{(A5.15)}$$

Cluster structures are also analyzed in terms of the relative position of the ion(s) with respect to the cluster interior, in order to discriminate between interior and surface structures,[41,168] by inspecting the distributions of convenient coordinates r'_{cm} and θ. r'_{cm} is the distance between the ion and solvent cluster center of mass normalized by the cluster radius.[167] Values of $r'_{cm} \ll 1$ characterize interior solvation structures, while values of $r'_{cm} \sim 1$ suggest surface solvation structures. θ is the angle between the ion, the solvent cluster center of mass and a given solvent molecule nitrogen atom. Similarly, we define the angle Θ between the ion pair geometric center, the solvent cluster center of mass, and a given solvent molecule. An isotropic ($\sin\theta$ or $\sin\Theta$) distribution is to be expected for a spherically symmetric interior solvation structure, and any deviation from this distribution reflects accumulation of solvent molecules on one side of the ion(s).

A5.III. ION-AMMONIA CLUSTERS

A5.III.A. Ionic Cluster Thermodynamics

In Table A5.3 are reported the stepwise binding enthalpies ($\Delta H_{n,n-1}$) of small ionic clusters obtained from Monte Carlo simulations, along with available experimental data.[189,190,206] Comparison between the room-temperature data demonstrates very good agreement between theoretical and experimental values, with deviations as small as 0.1 kcal/mol for $Na^+(NH_3)$ and 0.3 kcal/mol for $I^-(NH_3)$. Inspection of $\Delta H_{n,n-1}$ for increasing

cluster sizes reveals a progressive decrease of the stepwise binding enthalpy, which can simply be related to the distribution of the strong ion-solvent interaction to an increased number of solvent molecules. As will be discussed in more detail later, ionic clusters containing more than 7 and 9 solvent molecules for $Na^+(NH_3)_n$ and $I^-(NH_3)_n$ clusters, respectively, were found to be unstable, with respect to solvent evaporation.

Table A5.3. Stepwise binding enthalpies of ion-solvent clusters[a]

	$Na^+(NH_3)_n$			$I^-(NH_3)_n$		
N	Calc. 115 K	Calc. 300 K	Expt.	Calc. 115 K	Calc. 300 K	Expt.
1	26.0	25.3	25.6±0.2[b] 24.4±1.3[c]	8.1	7.1	7.4±0.1[d]
2	21.8	21.0	-	7.9	6.8	-
3	16.4	15.5	-	7.7	6.3	-
4	12.1	10.9	-	7.4	6.1	-
5	8.9	6.6	-	6.9	4.8	-
6	8.5	6.0	-	6.7	4.8	-

a. Enthalpies in kcal/mol. Calculated values are obtained from Monte Carlo simulations.
b. Stepwise binding enthalpy at 298 K taken from Ref. [187].
c. Stepwise binding enthalpy at 298 K taken from Ref. [188].
d. Taken from Refs. [189] and [190].

Total cluster enthalpies (ΔH_n) and the reduced binding enthalpies $\Delta H_n/n$ are shown in Fig. A5.2 as a function of cluster size for simulations at 115 K. Inspection of ΔH_n reveals that the total cluster enthalpy increases faster for $Na^+(NH_3)_n$ clusters than for $I^-(NH_3)_n$ clusters, due to the stronger ion-solvent interactions. From cluster size 4-5 for $Na^+(NH_3)_n$ and 7-9 for $I^-(NH_3)_n$, the total cluster enthalpy increases very slowly. However, this feature is less apparent in $I^-(NH_3)_n$ clusters, where the increase with cluster size is almost linear, and is attributed to the weaker interaction of the anion with solvent molecules. This change of slope corresponds to a change in cluster structural properties, such as the completion of a solvation shell.[145,178] As the first solvation shell is completed,

additional solvent molecules will be located further away from the ion, and will cause a smaller enthalpy change. In principle, the reduced binding enthalpies should converge towards the enthalpy of vaporization of liquid ammonia.[145] The reduced binding enthalpy limit, which was extrapolated from the data using a single exponential fit, was found to be 4.91 kcal/mol and 4.81 kcal/mol for $Na^+(NH_3)_n$ and $I^-(NH_3)_n$ clusters, respectively, in excellent agreement with the experimental heat of vaporization of 4.75 kcal/mol at room temperature.[114]

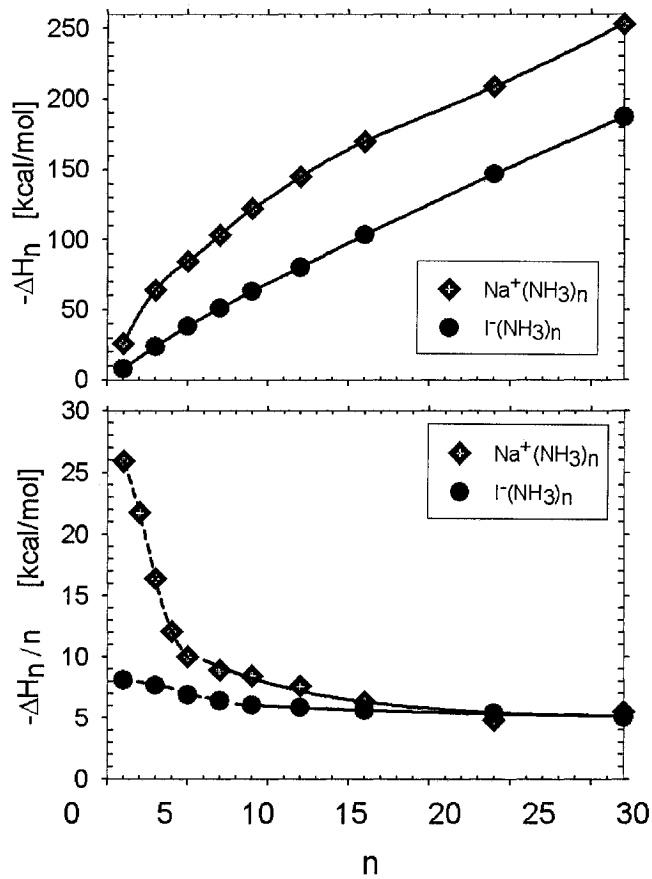

Fig. A5.2. Cluster enthalpies from 115 K Monte Carlo simulations for $Na^+(NH_3)_n$ [diamonds], and $I^-(NH_3)_n$ [circles] as a function of cluster size. Total cluster enthalpies ΔH_n (top panel). Reduced cluster enthalpies $\Delta H_n/n$ (bottom panel). The solid line represents the data fitted to an exponential decay.

A5.III.B. Ionic Cluster Solvation Structure

Representative structures from 115 K simulations are shown in Fig. A5.3 for ionic clusters of various sizes. $Na^+(NH_3)_n$ and $I^-(NH_3)_n$ clusters are of similar size, with a radius of ~7 Å at cluster size 32.[167] The representative structures of the ionic clusters suggest an interior solvation structure, which can be confirmed by inspection of the probability distributions of the scaled ion-solvent center-of-mass distance (r'_{cm}) shown in Fig. A5.4. The distributions hardly spread beyond a value of 0.5, and peak at low values, typically around 0.2, that are indicative of the fact that the ion is typically located within the interior of the solvent cluster. Smaller clusters are characterized by broader r'_{cm} distributions, as the small cluster radius naturally increases the spread of *relative* r'_{cm} values. Interior solvation structures are the result of strong ion-solvent interactions, which compensate for the free energy destabilization associated with the solvent network disruption. Probability distributions of the angle θ are also shown in Fig. A5.4. An approximate sin θ distribution is obtained for all ionic clusters, revealing an isotropic solvent distribution around the central ion and confirming interior solvation.

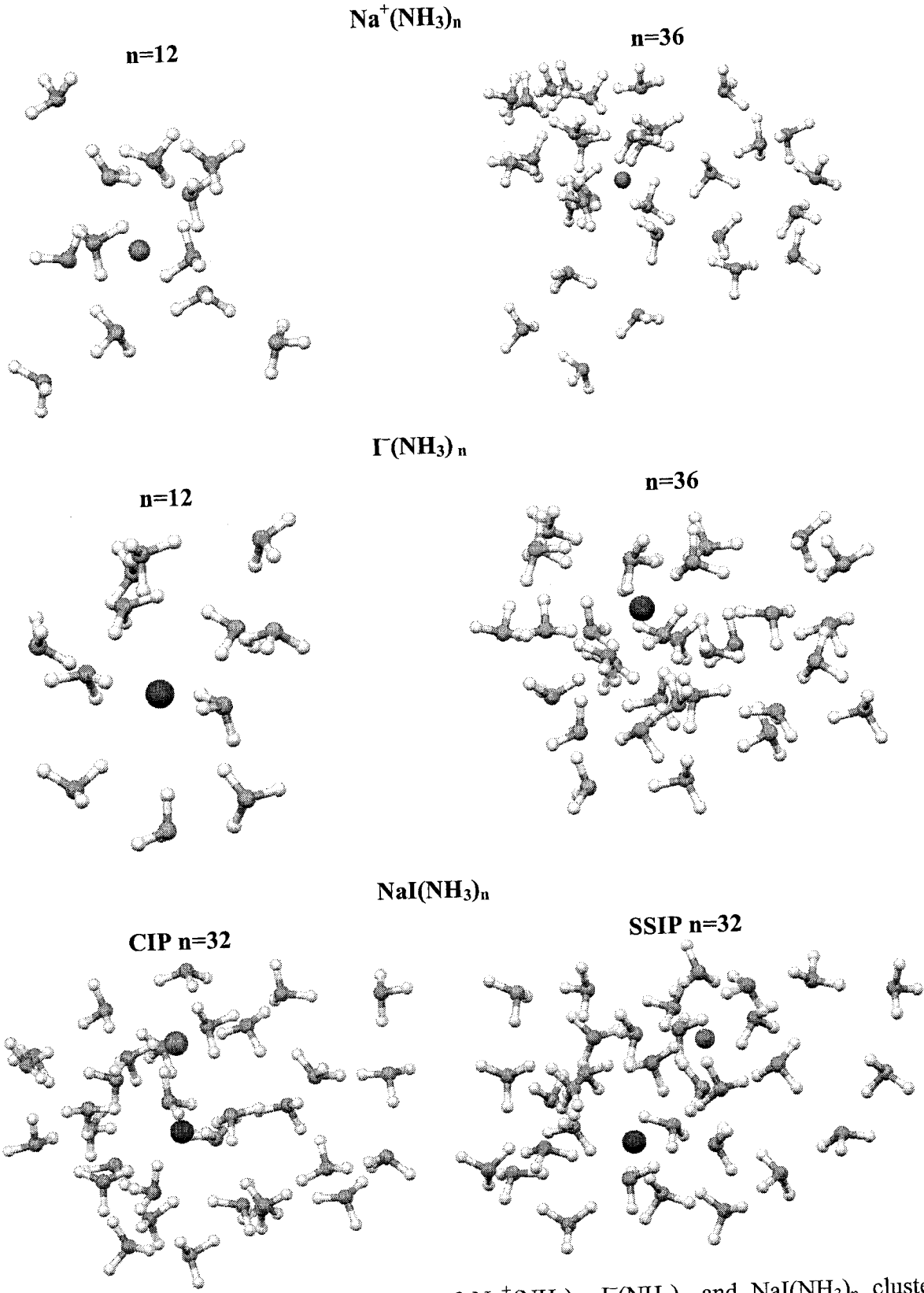

Fig. A5.3. Representative structures of $Na^+(NH_3)_n$, $I^-(NH_3)_n$ and $NaI(NH_3)_n$ clusters obtained from Monte Carlo simulations at 115K.

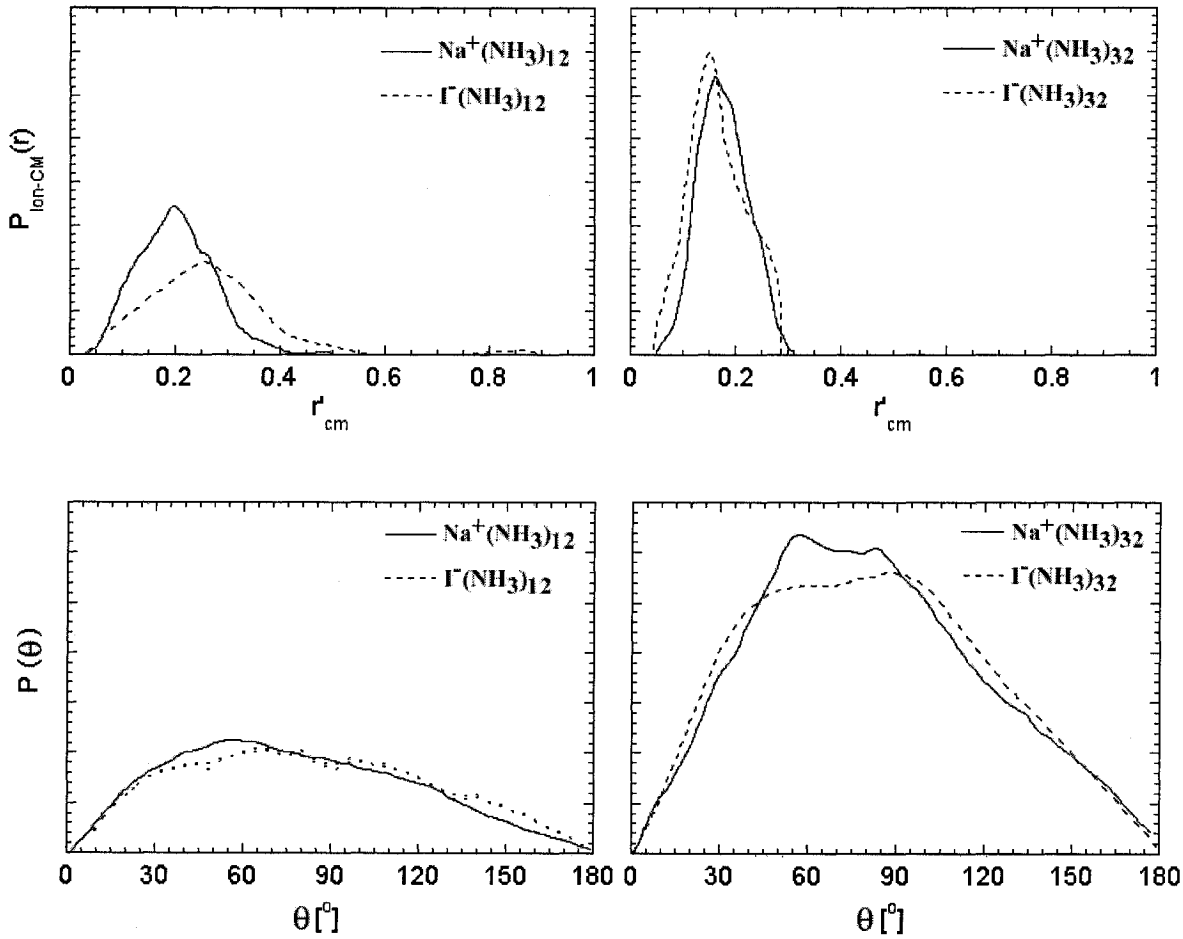

Fig. A5.4. Structural properties of $Na^+(NH_3)_n$ and $I^-(NH_3)_n$ clusters obtained from Monte Carlo simulations at 115K. Probability distributions of the scaled ion-to-solvent-center-of-mass distance r'_{cm} (top panel) and angular probability distributions P(θ) (bottom panel). The solid line represents the Na^+ distributions, whereas the dashed line the I^- distributions.

Ion-solvent radial probability functions and coordination numbers are shown in Fig. A5.5 for $Na^+(NH_3)_n$ and $I^-(NH_3)_n$ clusters. The sharp, distinct peaks in the PDFs, associated with plateaus in the coordination number $N_{coord}(r)$ is evidence for well-defined solvation shells. The first solvation shells contain 5.3 and 9.8 solvent molecules for $Na^+(NH_3)_{32}$ and $I^-(NH_3)_{32}$ clusters, respectively.

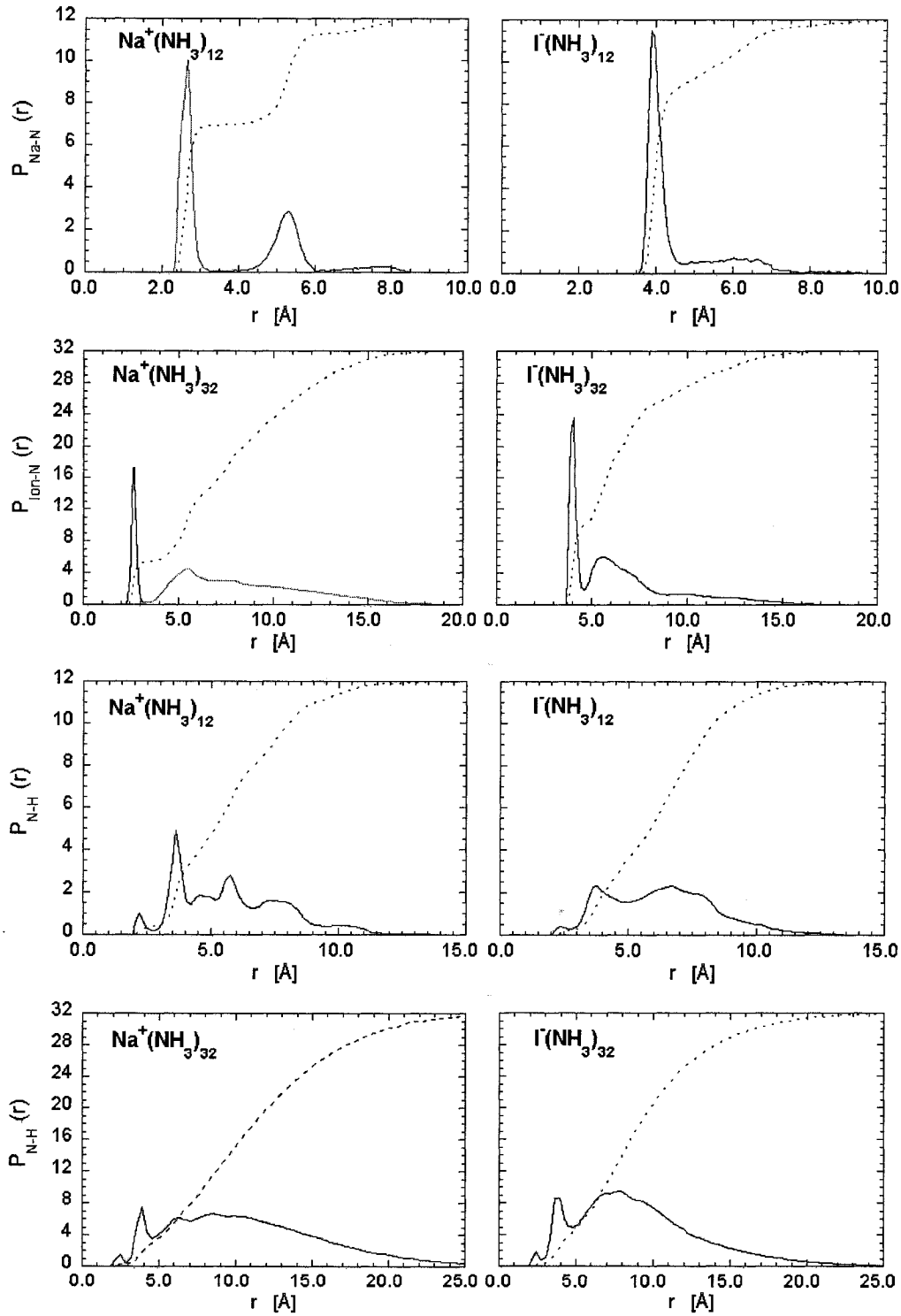

Fig. A5.5. Structural properties of $Na^+(NH_3)_n$ and $I^-(NH_3)_n$ clusters obtained from Monte Carlo simulations at 115K. Solid curves are radial probability distribution functions P(r), while dashed curves are the distance-dependent coordination number $N_{coord}(r)$. Ion-to-nitrogen (2 top panels) and hydrogen-to-nitrogen intermolecular distributions (2 bottom panels).

Even though I^- interacts with NH_3 through hydrogen bonding, we found more appropriate to demonstrate the solvation shell structure by showing the I-N PDF, rather than the I-H PDF, because of peak broadening due to the interaction of the ion with the three hydrogen atoms. As $I^-(NH_3)_n$ clusters are characterized by weaker ion-solvent interactions than $Na^+(NH_3)_n$ clusters, broader peaks, along with larger coordination numbers, are naturally observed in $I^-(NH_3)_n$. Iodide-solvent clusters are indeed expected to have larger coordination numbers than their sodium ion-solvent counterparts, due to a larger ion to solvent equilibrium distance, which results in an increased solvation shell size.[41,145] We note than in earlier Molecular Dynamics simulations of iodide in liquid ammonia at 240 K, a coordination number of 12-15 was reported.[148] The fact that we obtain a lower cluster coordination number of 9.8 for $I^-(NH_3)_{32}$ is consistent with this liquid data, since liquid simulations impose density constraints, solvent molecules are forced into a specific volume and larger coordination numbers than those for clusters are typically observed.[78] For larger clusters, beyond the first solvation shell, we observe a broad tail with some features suggesting some solvent ordering. The intermolecular N-H PDF, also shown in Fig. A5.5, reflect a moderate degree of solvent ordering, which is arising from a weakly hydrogen-bonded solvent network, found qualitatively similar to that of liquid ammonia reported elsewhere.[207]

A5.IV. ION PAIR-AMMONIA CLUSTERS

A5.IV.A. Thermodynamics of Ion-Pair Clusters

Potentials of mean force (PMF) are shown in Fig. A5.6 for $NaI(NH_3)_n$ clusters up to size 64 at 115 K. In our simulations, the statistical uncertainty on stepwise free energy differences was no greater than 0.5-0.8 kcal/mol, with an average uncertainty in the range 0.09-0.25 kcal/mol. The latter uncertainties, when summed up together along the PMF, add up to seemingly large numbers for absolute PMF data, as shown in Fig. A5.6, but actually correspond to a relative error in stepwise free energy differences inferior to 1.5 %, suggesting reasonable accuracy. All PMFs are characterized by a deep minimum at small internuclear separations, corresponding to CIP structures, with the NaI ion pair close to its gas-phase equilibrium structure (r_{NaI}=2.6-3.0 Å). As cluster size increases, the PMF well depth progressively decreases and becomes shallower. A precursor of SSIPs manifests itself as a shoulder in the PMFs of $NaI(NH_3)_{12-24}$ around a NaI internuclear separation of 4.8 Å. A second minimum in the PMF signals the emergence of stable SSIP species for cluster size 32 and above, with NaI internuclear separations between 4.1 Å and 4.9 Å. Typical structures of $NaI(NH_3)_n$ CIP and SSIP clusters at 115 K are shown in Fig. A5.3. Key properties of the PMFs are collected in Table A5.4. Both CIP and SSIP species are characterized by very small dissociation constants (for SSIPs, the dissociation constant is given by $K_{diss}/K_{SSIP/CIP}$), implying that both the CIP and SSIP species are very stable with respect to ionic dissociation.

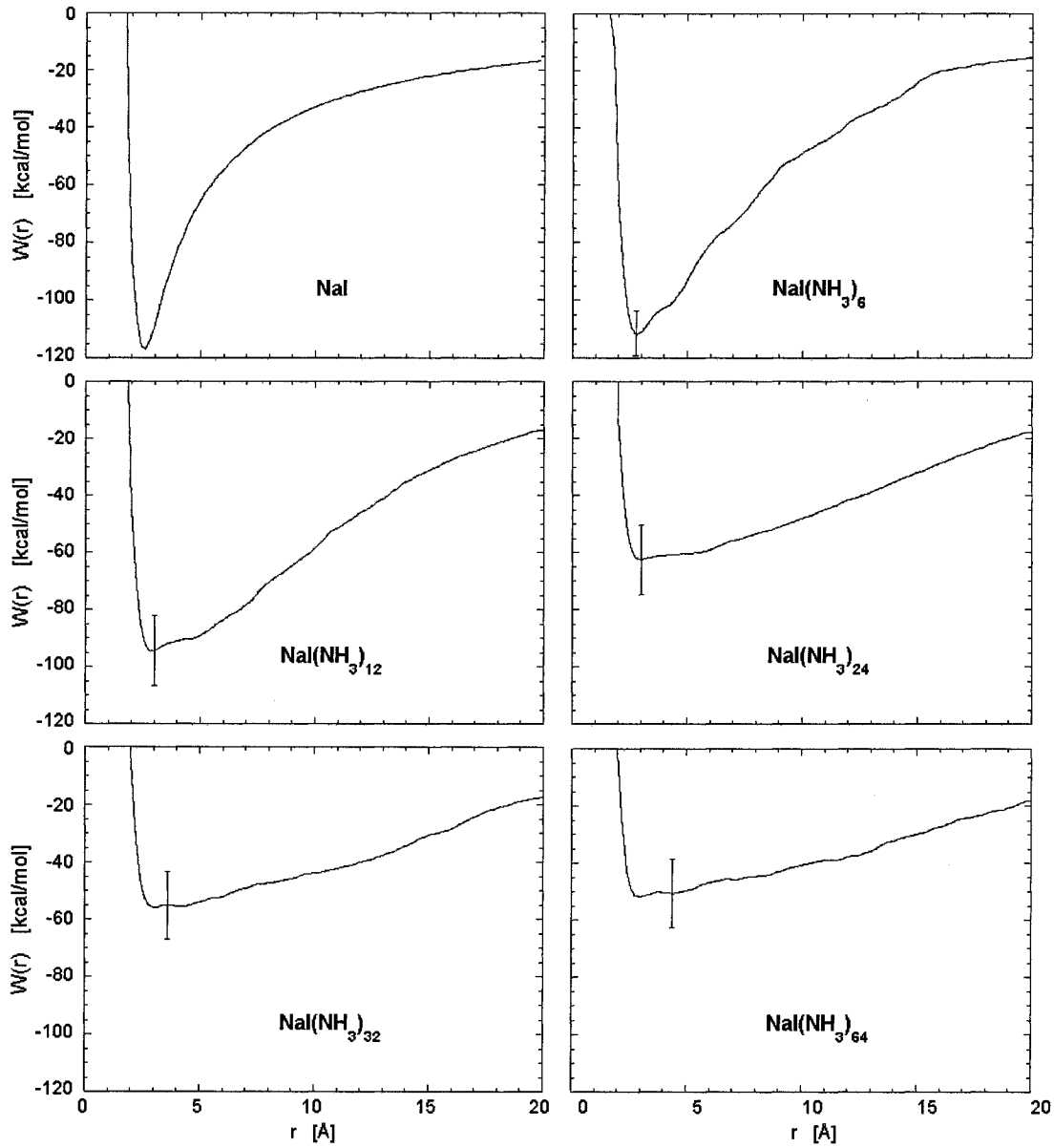

Fig. A5.6. Potentials of mean force for $NaI(NH_3)_n$ clusters at 115 K.

Table A5.4. Properties of the potentials of mean force[a]

n	r_{min}^{CIP} [b]	$r_c^{\mp}$ [c]	r_{min}^{SSIP} [d]	$\Delta G_{CIP}^{\mp}$ [e]	$\Delta G_{SSIP/CIP}$ [f]	$K_{SSIP/CIP}$ [g]	Log K_{diss} [h]
				T = 115 K			
1	2.59	-	-	-	-	-	-117 ±1
2	2.66	-	-	-	-	-	-116 ±1
4	2.77	-	-	-	-	-	-114 ±1
6	2.82	-	-	-	-	-	-110 ±2
8	2.84	-	-	-	-	-	-110 ±1
9	2.87	-	-	-	-	-	-108 ±2
10	2.89	-	-	-	-	-	-105 ±1
12	2.91	-	-	-	-	-	-100 ±1
16	2.92	-	-	-	-	-	-89 ±1
24	3.03	-	-	-	-	-	-66 ±1
32	3.03	3.59	4.09	0.7 ± 0.1	0.4 ± 0.1	0.1	-59 ±1
36	2.94	4.26	4.94	1.1 ± 0.1	0.7 ± 0.1	0.3	-58 ±1
48	2.95	4.06	4.64	1.5 ± 0.1	1.0 ± 0.1	0.7	-53 ±1
64	2.93	3.82	4.35	1.8 ± 0.1	1.3 ± 0.1	0.9	-51 ±1
				T = 300 K			
1	2.60	-	-	-	-	-	-120 ±1
2	2.66	-	-	-	-	-	-111 ±1
4	2.75	-	-	-	-	-	-106 ±1
6	2.79	-	-	-	-	-	-102 ±1
8	2.79	-	-	-	-	-	-98 ±1
9	2.80	-	-	-	-	-	-94 ±1

a. Free energies in kcal/mol and distances in Å. Converged equilibrium constants are obtained with upper bounds for the SSIP population integral varying from 6 to 9 Å with increasing cluster size.
b. NaI internuclear separation at the minimum of the CIP well
c. NaI internuclear separation at the CIP to SSIP barrier
d. NaI internuclear separation at the minimum in the SSIP well.
e. Free energy barrier height measured from the CIP.
f. Free energy of the SSIP relative to that of the CIP.
g. CIP $\rightleftarrows$ SSIP equilibrium constant, Eq. (A5.14).
h. CIP dissociation constant, Eq. (A5.13), in $(mol/l)^{-1}$.

Such findings are in good agreement with earlier theoretical work, which showed that the stability of ion pair arises from a very slow convergence of the separate cluster ion solvation energies with cluster size, such that separated cluster ions are thermodynamically unfavorable.[42] For clusters up to at least size 64, our calculations

predict CIP species lower in free energy than SSIP species, as can be seen from positive values of $\Delta G_{SSIP/CIP}$ in Table A5.4. The resulting equilibrium constants $K_{SSIP/CIP}$ listed in Table A5.4 clearly indicate that the CIP is thermodynamically favorable up to cluster size 64, where CIP and SSIP species become almost equally probable.

A5.IV.B. Ion-Pair Solvation Structure

For the range of cluster sizes investigated (n=1-64), $NaI(NH_3)_n$ clusters were found to be thermodynamically stable as CIP species, whereas SSIP species only become thermodynamically stable around cluster size 32. For both CIP and SSIP species, inspection of representative structures (cf. Fig. A5.3) reveals that both ions are surrounded by solvent molecules, which is not surprising, as we previously showed that $Na^+(NH_3)_n$ and $I^-(NH_3)_n$ clusters tend to adopt interior solvation structures. This interior solvation structure can be confirmed by inspection of the scaled ion-solvent cluster center-of-mass (r'_{cm}) and solvent angular probability distributions, shown in Fig. A5.7. If the r'_{cm} distributions confirms that both ions reside in the cluster interior ($r'_{cm} < 1$), they also indicate that, for CIPs, the sodium ion tends to reside closer to the solvent cluster center of mass (peak in the distribution at $r'_{cm} \sim 0.15$), while the iodide tends to reside more towards the cluster surface (peak in the distribution at $r'_{cm} \sim 0.5$), whereas for SSIPs, the ions are equidistant from the solvent center of mass. This is consistent with a picture where the sodium ion is solvated first in CIPs because of the stronger Na^+-NH_3 interaction, and is further reflected in the slight deficiency of solvent molecules on the iodide side (large θ angles) of $NaI(NH_3)_{32}$ CIPs shown in Fig. A5.7. As a matter of fact, the solvent angular distributions for small clusters such as $NaI(NH_3)_{12}$ (not shown)

clearly indicate that solvent molecules accumulate preferentially on the sodium side of the ion pair, most likely due to the stronger Na^+-NH_3 interaction (cf. Table A5.1). Larger clusters exhibit a fully isotropic distribution of solvent molecules, as there are enough molecules to solvate both ions, and even establish a solvent network. The sharp peaks of the ion-N PDFs shown in Fig. A5.7 for $NaI(NH_3)_n$ CIP and SSIP species evidence a well-defined solvation shell structure. The local solvent environment around the ions is very similar to that for the single ion-acetonitrile clusters (cf. Fig. A5.5), but beyond the ion first solvation shell, the solvation structure appears more disorganized, with overlapping peaks in the PDFs, as a result of the perturbation in the solvent network brought about by the counter-ion. The proximity of a counter-ion prevents some solvent molecules from entering the ion first solvation shell, and one generally observes smaller ion coordination numbers in CIPs than in SSIPs, and both are smaller than that in ionic clusters, as observed previously for $NaI(CH_3CN)_n$[178] and $NaI(H_2O)_n$.[41] For iodide in $NaI(NH_3)_{32}$, the ion first solvation shell coordination number is indeed smaller for the CIP (8.4) than for the SSIP (9.9), but the latter is very similar to that in ionic clusters (9.8). As for the sodium ion in $NaI(NH3)_{32}$, the ion first solvation shell coordination number is also smaller for the CIP (6.0) than the SSIP (7.0), but both are significantly larger than that in $Na_+(NH_3)_{32}$, in contrast to what is usually observed.[41,178] This can be attributed to the larger ion first solvation shell in $NaI(NH_3)_n$ clusters, which is obviously distorted by the presence of the counter-ion, as can be seen from the shallower peaks in the Na-N PDFs (cf. Figs. A5.5 and A5.7), and which naturally leads to larger coordination numbers.

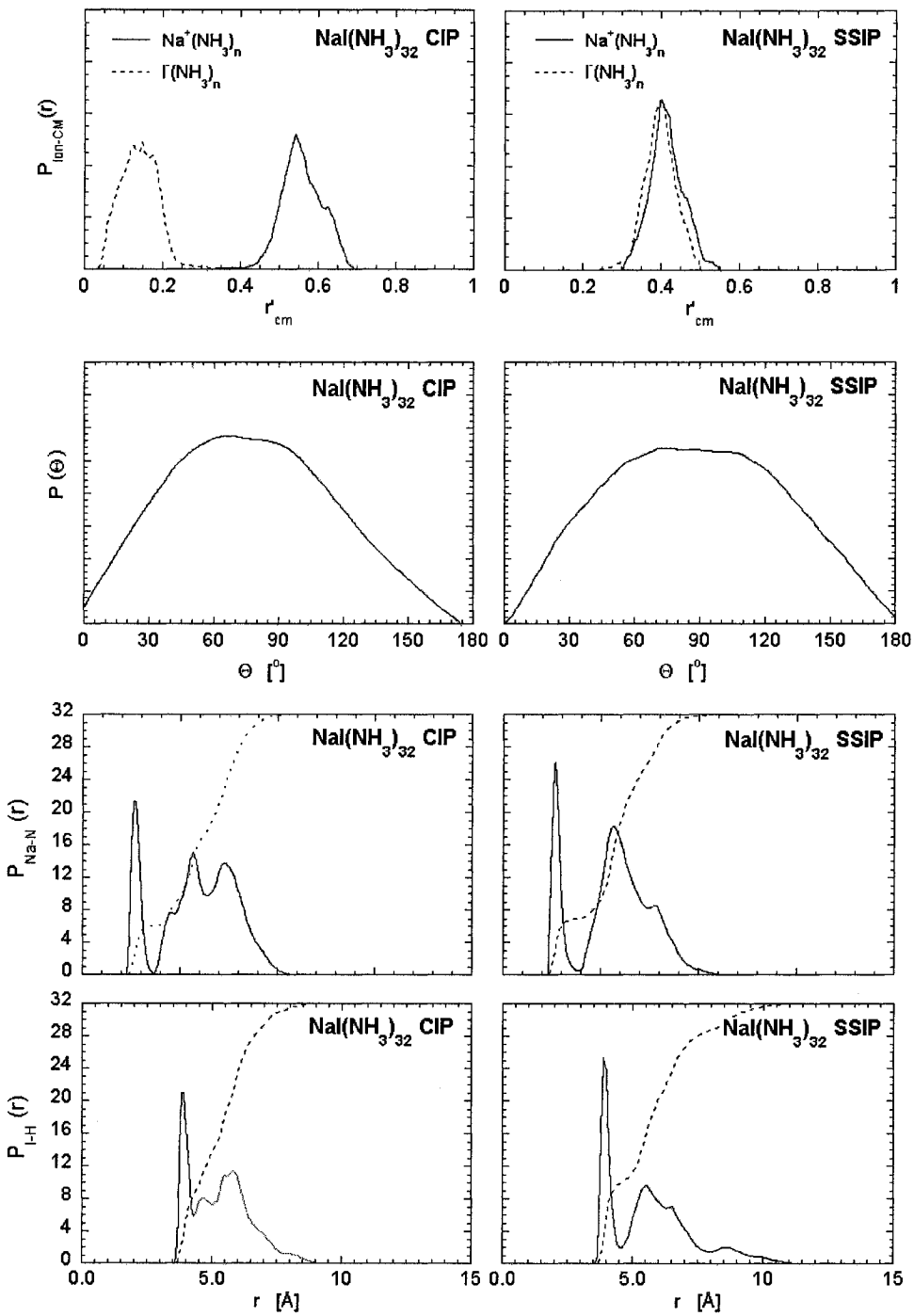

Fig. A5.7. Structural properties of $NaI(NH_3)_n$ clusters, obtained from Monte Carlo simulations at 115K. Probability distributions of the scaled ion to solvent center-of-mass distance r'_{cm} and angular probability distributions $P(\Theta)$, (2 top panels). The solid line represents Na^+ distributions, whereas the dashed line I^- distributions. Ion-to-nitrogen distributions (2 bottom panels). Solid curves are radial probability distribution functions P(r), while dashed curves are the distance-dependent coordination number $N_{coord}(r)$.

A5.V. DISCUSSION

A5.V.A. Temperature Effects on Cluster Stability

As mentioned earlier, there is a wide uncertainty in the cluster temperature, and accordingly, Monte Carlo simulations of $Na^+(NH_3)_n$, $I^-(NH_3)_n$ and $NaI(NH_3)_n$ clusters were also performed at 300 K. The most striking feature of the room-temperature results lies in the impossibility of generating stable clusters containing many more molecules than that corresponding to a single solvation shell, i.e. 8, 6 and 9 solvent molecules for $Na^+(NH_3)_n$, $I^-(NH_3)_n$ and $NaI(NH_3)_n$, respectively, due to systematic solvent evaporation. This can be explained by the fact that, upon completion of the first solvation shell, additional solvent molecules will interact only weakly with the ion, and the low solvent-solvent interaction energy (consistent with the fact that ammonia is a gas at room temperature) may not be sufficient to prevent evaporation, such that the clusters can only retain a few molecules (or none at all) beyond the ion first solvation shell. Larger clusters can obviously be produced more easily with Na^+ than with I^-, because of stronger ion-solvent interactions, and in the case of ion-pair clusters, even larger clusters are observed due to the attraction of solvent molecules to both ions.

Potentials of mean force for $NaI(NH_3)_n$ clusters at 300 K and 115 K are compared in Fig. A5.8, while the resulting equilibrium constants are listed in Table A5.4. Inspection of the results in Fig. A5.8 and Table A5.4 show that CIPs are less stable with respect to dissociation with temperature increase, yet they remain very stable with respect to ionic dissociation at room temperature. However, no stable SSIP can be found for the small clusters generated under these conditions. Clusters also tend to adopt less clearly defined

structures, indicating a lower degree of compactness and ordering at high temperatures, as previously observed for water clusters.[41]

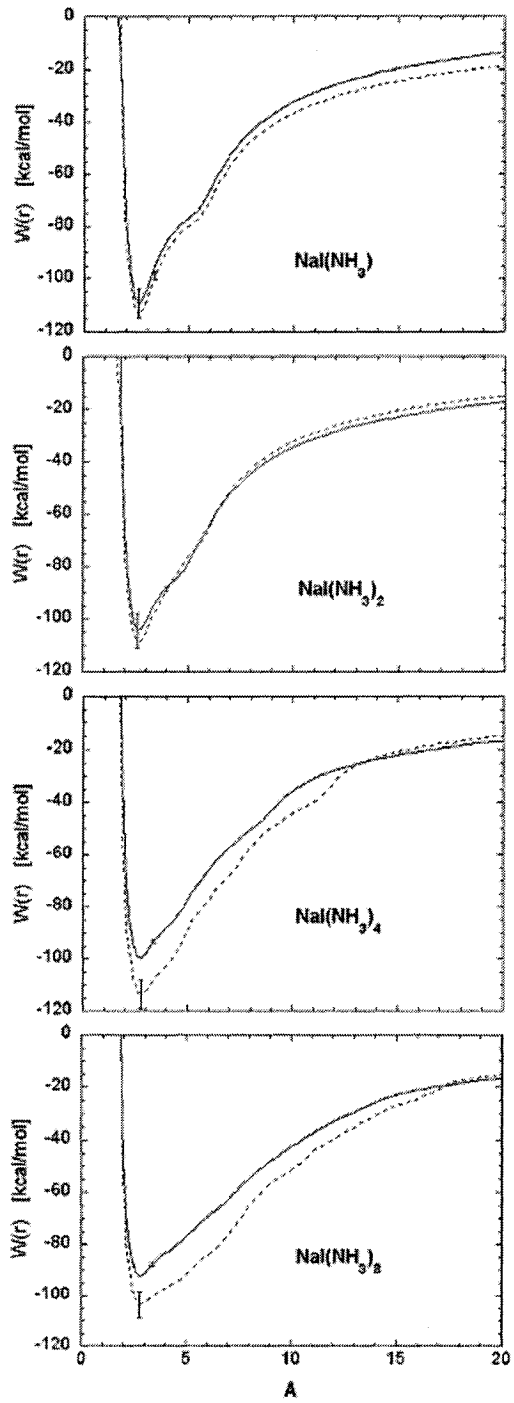

Fig. A5.8. Potentials of mean force for $NaI(NH_3)_n$ clusters at 300 K (solid lines) and 115 K (dashed lines).

A5.V.B. Comparison with Other Ion-Solvent Clusters

We now compare the present findings for ionic ammonia clusters with analogous ionic water[41] and acetonitrile[145,178] clusters. All sodium ion-solvent clusters exhibit an interior solvation shell structure. Sodium ion-solvent complexes exhibit a similar C_v equilibrium structure, that is governed by dominant ion-dipole electrostatic forces. As a result, the strong electrostatic interactions between solvent molecules and the small, charge-concentrated cation will favor a situation where the ion is surrounded by solvent molecules. On the other hand, iodide-solvent clusters exhibit solvent-selective structural properties. $I^-(NH_3)_n$ and $I^-(CH_3CN)_n$ clusters exhibit interior solvation shell structures, whereas $I^-(H_2O)_n$ clusters are known to adopt a surface solvation structure, arising from the strong hydrogen bonds which stabilize the solvent network.[41] Such hydrogen bonds are very directional in nature and induce ordering of the water network while preventing solvation of the large iodide ion. In ammonia clusters, the hydrogen-bond strength lies between that of water and acetonitrile, and not surprisingly, the properties of ionic ammonia clusters share features of both ionic acetonitrile and ionic water clusters. For instance, the $I^-(NH_3)$ and $(NH_3)_2$ minimum energy structures involve hydrogen-bonding either of the solvent to iodide or of the solvent to itself, similarly to their water cluster counterparts,[41] whereas acetonitrile tends to interact with iodide and with itself via ion-dipole interactions.[145] However, hydrogen bonds between ammonia molecules are not strong enough to overcome ionic solvation, i.e. solvent-solvent interactions are not strong enough, relative to solute-solvent interactions, to dictate cluster structures where the large, polarizable ion would sit at the surface of a stable solvent network, and $I^-(NH_3)_n$ clusters exhibit an interior solvation structure similar to that of $I^-(CH_3CN)_n$ clusters.[145,178]

We note however, that in the absence of enough ammonia molecules to solvate a NaI ion pair, while the sodium ion will tend to be solvated first, the iodide ion will tend to locate towards the surface of the cluster, as mentioned earlier.

A5.V.C. Comparison with Other Ion Pair-Solvent Clusters and Implications for multi-photon ionization Experiments

We now compare and contrast our findings for $NaI(NH_3)_n$ with those previously reported for analogous water[41,42] and acetonitrile [145,178] clusters. The most striking difference between ammonia clusters and its water and acetonitrile counterparts lies in the instability of $NaI(NH_3)_n$ with respect to solvent evaporation at room temperature. This should not be too surprising, since ammonia is gaseous at room temperature (T_{evap}= 239 K), whereas acetonitrile and water are liquids (T_{evap} = 355 K and 373 K, respectively). Under temperatures where they are stable however, $NaI(NH_3)_n$ clusters exhibit similarities with $NaI(H_2O)_n$ and $NaI(CH_3CN)_n$ clusters, in that they are very stable with respect to ground state ionic dissociation. The deep wells in the PMFs observed for all species infer CIP clusters that are thermodynamically stable with respect to dissociation into free ions, as illustrated by extremely small dissociation constants (e.g. 10^{-59}, 10^{-36} and 10^{-42} in ammonia, acetonitrile[178] and water clusters,[41] respectively, around cluster size 32). The decreasing well depth of the PMFs with cluster size increase indicates that ion pairs become less stable with respect to dissociation as cluster size increases, but they still remain very stable for very large cluster sizes.[42] However, $NaI(NH_3)_n$ clusters contrast with $NaI(H_2O)_n$ and $NaI(CH_3CN)_n$ clusters, in that SSIPs become thermodynamically stable at much larger cluster sizes for ammonia (n=32), than for water

(n=16) and acetonitrile (n=6). Interestingly, the $NaI(NH_3)_n$ and $NaI(CH_3CN)_n$[178] CIPs are lower in free energy up to cluster sizes n=64 and n=32, respectively, whereas the $NaI(H_2O)_n$ SSIPs are lower in free energy from cluster size n=32 and above.[41] Finally, the free energy difference between the SSIP and CIP increases with cluster size in $NaI(NH_3)_n$ clusters, whereas a decrease in $\Delta G_{SSIP/CIP}$ was observed in $NaI(CH_3CN)_n$ and $NaI(H_2O)_n$ clusters. Around cluster size n=32, CIPs are significantly more probable than SSIPs for both ammonia and acetonitrile clusters ($K_{SSIP/CIP}$ ~0.1),[178] while SSIPs are much more probable than CIPs (by one order of magnitude or more) for water clusters ($K_{SSIP/CIP}$ >50),[41] and hence charge separation occurs at much smaller cluster sizes for the very polar water solvent. In terms of solvation structure, the NaI ion pair tends to preferably locate inside the cluster for $NaI(NH_3)_n$ and $NaI(CH_3CN)_n$ clusters, since both ions adopt interior solvation structures with both solvents. However, $NaI(H_2O)_n$ exhibit surface solvation structures, as the iodide ion drags the ion pair towards the surface of the solvent network.[41]

The presence of thermodynamically stable NaI ion pairs in ammonia clusters suggests favorable conditions for multi-photon ionization experiments. Recall that previous model quantum chemistry calculations suggested that the NaI CIP surrounded by solvent molecules possesses optically accessible excited-states relatively similar to those of the isolated NaI molecule, suggesting a possible photodissociation route akin to the gas-phase one, in contrast to the SSIP counterparts.[42,143,178] For $NaI(H_2O)_n$, SSIPs are the dominant species in large clusters, which is consistent with the fact that no $Na^+(H_2O)_n$ clusters of size larger than 50 molecules were experimentally observed following photoexcitation.[42] Yet, as mentioned above, charge separation occurs much earlier for

water than for ammonia and acetonitrile clusters, and only small ionized product clusters are observed for the latter two solvents. In $NaI(CH_3CN)_n$ clusters, ground-state charge separation does not seem to occur before cluster size n=32, yet no ionized cluster products beyond size n=6 could be observed experimentally, and other reasons such as increased solvent evaporation and reorganization on the ionized state or possible CTTS were invoked to explain experimental observations.[178] The present simulations of $NaI(NH_3)_n$ clusters at 115 K demonstrate that stable SSIPs do not appear before cluster size n=32, and despite the lack of significant ground-state charge separation, up to large cluster sizes, $Na^+(NH_3)_n$ cluster products only up to cluster size n=9 are observed in multi-photon ionization experiments. Furthermore, the small dipole moment of ammonia precludes the possibility of CTTS and an alternative explanation must be sought.

During the experimental preparation of $NaI(NH_3)_n$ clusters, the NaI ion pair is first vaporized, which requires temperatures exceeding 500 K, then passed above an ammonia bath, where solvent molecules are picked up and clusters formed through a growing process. As discussed in section A5.II.D, not only small clusters may be stable at temperatures much larger than the metastable temperature of ammonia clusters, but evaporation may also prevent formation of larger clusters at high temperatures. The cluster beam is generated via a supersonic expansion, where solvent molecules may further evaporate from the cluster in order to cool down to the temperature of thermodynamic stability. Our present room-temperature simulations suggest that the $NaI(NH_3)_n$ maximum cluster size that can be produced at high temperatures corresponds to 9 solvent molecules, which incidentally is the size at which the product signal vanishes in multi-photon ionization experiments.

Furthermore, it has been shown theoretically[179,208] that $NaI(H_2O)_n$ clusters promoted to their electronic excited-states undergo massive solvent evaporation, as cooling of the excited clusters is achieved by solvent evaporation.[208] Our present room-temperature simulations suggest that large ionic ammonia clusters containing more ammonia molecules than a single ion solvation shell readily undergo solvent evaporation at high temperatures. As a result it is conceivable that hot $Na^+(NH_3)_n$ products of photoexcitation undergo further evaporation on the ionized state and very few cluster products containing more solvent molecules than a single ion solvation shell for metastable clusters (coordination number of 5 for sodium) will be observed in multi-photon ionization experiments.

A5.VI. CONCLUDING REMARKS

We have investigated the structural and thermodynamic properties of sodium and iodide ions and ion pairs in ammonia clusters by means of Monte Carlo simulations at 115 K. A model potential has been developed to properly describe intermolecular interactions and reproduce the structural and energetic properties of small ammonia clusters predicted by quantum chemistry calculations. Validation of our model potential was achieved via successful comparison of ion-ammonia cluster binding enthalpies with experimental ones. The evolution of binding enthalpies with cluster size revealed the completion of ion solvation shells, and inspection of the probability distribution functions confirmed that $Na^+(NH_3)_n$ and $I^-(NH_3)_n$ clusters adopt an interior solvation shell structure, with the first solvation shell containing 5.3 and 9.8 ammonia molecules at cluster size 32, respectively. Comparison with analogous clusters of acetonitrile[145] and water[41] showed

that, even though ammonia is a hydrogen-bonding solvent with hydrogen-bond strength intermediate between that of water and acetonitrile, $I^-(NH_3)_n$ clusters exhibit features similar to $I^-(CH_3CN)_n$, contrasting with those of $I^-(H_2O)_n$. Only $I^-(H_2O)_n$ clusters exhibit surface solvation, as iodide tends to sit at the surface of a stable solvent network held together by strong hydrogen bonds. Interestingly, our simulations suggest that stable $Na^+(NH_3)_n$ and $I^-(NH_3)_n$ clusters containing solvent molecules beyond the first ion solvation shell cannot be produced at room-temperature, due to the low solvent-solvent interaction strength and the resulting solvent evaporation.

The stability of the NaI ion pair in ammonia clusters was investigated via potentials of mean force calculations. Our findings suggest that the ion pair is thermodynamically stable with respect to dissociation into free ions. Both ions in $NaI(NH_3)_n$ clusters adopt an interior solvation structure, in a fashion similar to $NaI(CH_3CN)_n$ clusters,[178] and in contrast to $NaI(H_2O)_n$ clusters which exhibit "surface" solvation due again to the hydrophobicity of iodide. $NaI(NH_3)_n$ clusters were found to exist primarily as CIP species up to cluster size n=64, where CIPs and SSIPs become almost equally probable. Ground-state charge separation appears to occur at much larger cluster sizes for ammonia (and acetonitrile)[178] than for water.[41] The thermodynamic stability of the $NaI(NH_3)_n$ CIP confirms the feasibility of multi-photon ionization experiments for a range of cluster sizes, as the NaI CIP was shown to possess an optically excited-state akin to that of gas-phase NaI.[42] We suggest that the lack of $Na^+(NH_3)_n$ product signal beyond size 9 observed in multi-photon ionization experiments is connected to the low evaporation temperature of ammonia.

Upon cluster generation and promotion to the excited-state, solvent evaporation may prevent formation of large $NaI(NH_3)_n$ species. The clusters are generated by a growing process at a relatively high temperature, which favors the formation of small clusters and discriminates against larger clusters with a lower temperature for thermodynamic stability.[53,54] Furthermore, photoexcited clusters were found to undergo solvent evaporation very easily, due to the excess kinetic energy acquired by the system upon both pump and probe excitation, such that massive solvent evaporation occurs in the course of the multi-photon ionization reaction.[209] Room-temperature simulations of $Na^+(NH_3)_n$ clusters showed that only species with a single ion solvation shell are metastable at high temperatures, as molecules beyond the first ion solvation shell are prone to solvent evaporation. This is in good agreement with the sharp decrease of the $Na^+(NH_3)_n$ product signal beyond cluster size n=5, which incidentally is the coordination number of $Na^+(NH_3)_n$ in room-temperature cluster simulations, and th e vanishing of the signal at cluster size n=9, which incidentally is the maximum cluster size of stable $NaI(NH_3)_n$ clusters at room temperature.

PART B

CLUSTERS IN CATALYSIS STUDIES

CHAPTER B1
Introduction on the "Chemistry with a Hammer": Clusters as a New Class of Reactants

The field of cluster-surface reactive collisions is a rapidly growing research area. Not only such are processes of great fundamental interest, but they can also lead to an important number of technological applications.[22] Much effort has been invested to identify and explore new methods for characterizing weakly bound clusters on the one hand, and the nature of the surface on the other.[22,210] Depending mostly on the colliding cluster properties, such as incident velocity and temperature, interaction of the cluster with a surface leads to either cluster deposition, cluster fragmentation, even cluster ionization or electron sputtering.[211] So far, experimental studies concerning cluster-surface interactions have mainly focused on surface-induced dissociation reactions (see Ref. [212] and references herein).

The impact of clusters consisting of many aggregated particles onto rigid surfaces results in much more complex and interesting phenomena than collisions of a single atom or molecule with a surface. It has been demonstrated that surface impact of a cluster results in an accumulation process leading to high-energy collision cascades.[213] Clusters were found to reach transient configurations characterized by extreme conditions, propagating in the cluster on a very short time scale, similarly to a shockwave. The very high conditions of pressure and temperature that are generated upon cluster impact, as well as the local confinement of reacting species, provide an exceptionally favorable environment for inducing physical and chemical processes,[213-215] such that clusters can be used as ''microreactors'' to induce chemical reactions that would not be possible otherwise. This aspect motivated experiments of cluster-surface scattering, allowing the

reactants to experience an extremely high heating rate under very high-pressure conditions, such that impact-induced chemistry was found to occur within the cluster itself[216-218] or with the surface.[215,219,220]

Whereas this "chemistry with a hammer"[221] concept seems quite promising for the field of chemical catalysis, it remains to be thoroughly investigated.[222] For instance, a previous theoretical study by Levine *et al.* suggested possible intracluster reaction in a mixed N_2/O_2 cluster heated by supersonic impact on an inert surface, leading to production of NO and the so-called "burning of air".[217] However, no experimental evidence has been reported to date, and a detailed study of energy redistribution upon cluster impact may help understand this phenomenon and why it has not been observed experimentally.

A major concern in the analysis of such processes is the dynamics of decomposition of van der Waals clusters which collide with solid surfaces. Unlike monomer-surface collisions, in which major pathways of energy transfer are now well understood,[223] the mechanisms of cluster scattering are complicated by a larger number of degrees of freedom. While early studies provided a qualitative description of cluster-surface scattering events,[224,225] recent studies on the dynamics of collisions between $(N_2)_n$ van der Waals clusters and metallic surfaces have shed light onto energy transfer processes.[226,227] Molecular translational and rotational excitation occurring in such low energy cluster-surface collisions has been investigated in detail, both experimentally[225,226,228-230] and theoretically.[227,231-233] However, Levine suggested that the burning of air reaction[217] would occur at 1800 $m.s^{-1}$, while no strong vibrational excitation has been observed experimentally in the surface scattering of $(N_2)_n$ clusters

onto graphite surfaces with typical incident cluster velocities of 750 $m.s^{-1}$, as one might have expected.[230]

Another unclear process involving catalysis by cluster-surface scattering can be found in the recent experiment of Daineka *et al*,[234] in which a neutral $(O_2)_n$ cluster beam was impacted onto a hot, clean silicon surface at supersonic velocities, and evidence was found for a completely new oxidation process.[215] The resulting cluster impact spot is composed of two distinct zones, with formation of a protective oxide layer in the central part of the impact spot, and a circular groove with a steep inner and slightly sloping outer wall on the outskirts, formed as a result of surface etching. Despite the abundant literature on silicon surface oxidation by either atomic of molecular components, such distinctive pattern was never observed previously,[235-238] and the oxidation mechanism underlying the Daineka experiment remains unresolved to this day.

Because a similar surface oxidation does not occur when employing single oxygen molecules, this reaction is a prototype for cluster-catalyzed reactions,[215] and the aim of this work was to characterize the mechanism of silicon oxidation by $(O_2)_n$ clusters, and to gain insight into the "chemistry with a hammer". Two possible reaction mechanisms may come to mind to explain the Daineka experiment. (a) The chemical reaction may occur in a two step process, with dissociation of oxygen molecules upon cluster impact, followed by surface oxidation with atomic components. Atomic oxygen readily reacts with silicon through a barrierless reaction, as shown both theoretically[236] and experimentally,[238,239] leading to adsorption and insertion into the silicon backbone.[240,241] (b) Another possible pathway involves direct chemical reaction with ground state O_2, a one-step process characterized by a reaction activation barrier of ~60

kcal/mol, which does not occur in typical single-molecule experiments.[241]

In the first part of this work (Chapter B2), we investigated the energy partitioning in collisions of van der Waals $(O_2)_2$ and $(N_2)_2$ clusters with a rigid surface, simulating the cluster collision process by means of classical Molecular Dynamics simulations. We investigated the influence of cluster properties (cluster size, incident velocity) on the evaporated product energy distributions and energy transfer mechanisms, in order to devise appropriate experimental conditions to observe the "burning of air" reaction. In addition, an inspection of the vibrational energy distribution at various incident velocities may allow connection with the experimental results reported in the studies by de Martino[230] and Levine.[217] Finally, we also turned our attention to the dissociation probability of oxygen molecules after cluster impact, in order to evaluate the feasability of the atomic pathway in the Daineka silicon cluster oxidation experiment.

In the second part of this work (Chapter B3), focus was placed on the molecular oxidation pathway as a possible mechanism in the Daineka experiment. This was achieved by investigation of the internal energy distribution in the course of the cluster collisional event. We then concluded that, whereas the reaction can in principle occur upon cluster collision, the reaction yield is far too small to explain experimental results. We then briefly investigated the possibility of non-adiabatic chemistry made possible by cluster distortion and compression upon scattering. To test such hypothesis, we have performed preliminary ab initio calculations of the electronic states of a $(O_2)_2$ cluster model, which suggests that an electronically non-adiabatic pathway may account for the Daineka experiment. In addition, our findings have some implication for the presence of an unexplained reaction channel observed experimentally for the enhanced vibrational

relaxation of highly excited oxygen molecules during ozone photolysis in the stratosphere.[242]

In the third part of this work (Chapter B4), we present an in-depth study of the possibility of molecular electronic excitation catalyzed by mechanical collisions during cluster impact, based on systematic high-level ab initio calculations of a $(O_2)_n$ cluster model. We investigated the potential energy surfaces of the $(O_2)_2$ cluster, paying particular attention to various conformations of the dimer. We placed particular emphasis on the implications of the results for the Daineka silicon cluster-oxidation experiment. Thus, structural analysis of $(O_2)_n$ clusters in the course of the scattering event is necessary in order to determine whether the non-equilibrium cluster regions where electronic excitation is allowed, can be accessed upon surface impact under the experimental conditions employed.

CHAPTER B2
Molecular Dissociation and Vibrational Excitation in the Surface Scattering of $(N_2)_n$ and $(O_2)_n$ Clusters

B2.I. INTRODUCTION

Cluster impact chemistry has been an area of intense research for about two decades.[213,227,232,243-245] Of particular interest are the dynamics of cluster and surface interactions,[246,247] or the possible use of cluster systems as "microreactors" to catalyze chemical reactions that would not be possible in normal environments.[217,248-250] Such cluster-catalyzed reactions have been predicted to promote physical and chemical processes due to the extreme temperature and pressure produced within the cluster surface impact. This concept, known as "chemistry with a hammer",[221] may be a promising approach for making multi-center reactions with large activation barriers feasible. Among many such studies,[217,248,249,251-253] we refer to the "burning of air",[217] $N_2 + O_2 \rightarrow 2NO$, which was predicted theoretically to take place under such extreme conditions. However, no experimental evidence has been reported for this reaction to date. A better understanding of the energy transfer mechanisms during cluster scattering may be needed in order to devise optimal experimental conditions for such reactions.

In the past, experimental[226,228,230,254] and theoretical[231,232,245,255,256] studies of cluster-surface scattering have centered mainly on energy transfer to the translational degrees of freedom of scattered molecules. Only recently has attention been paid to both the translational and rotational distributions of monomer products of $(N_2)_n$ cluster-surface scattering by experimental[230] and theoretical[227] means. In both studies, the translational energy distributions of the products of $(N_2)_n$ scattering were found to follow a single

Maxwell-Boltzmann distribution, whereas the rotational state distributions were better represented by a sum of two distinct Boltzmann distributions. A detailed analysis of the dynamics of cluster-surface scattering indicated that translational excitation of the scattered products depends on the instantaneous cluster temperature at which monomers evaporate, which results in a thermal distribution of product translational energies. For the rotational distributions, the hot component was attributed to evaporation from the outskirts of the cluster during surface impact, and the cold component of evaporation of molecules that were caged within the interior of the cluster during surface impact. Only a few studies have been reported so far on energy transfer mechanisms to the vibrational degrees of freedom of evaporated products of Van der Waals cluster-surface scattering.[226,256] Such studies are essential in understanding possible multi-center cluster-catalyzed reactions, as mentioned previously.

In this work, we extend our previous theoretical study of $(N_2)_n$ cluster-surface scattering and pay particular attention to molecular dissociation and vibrational excitation mechanisms. The N_2 molecule is characterized by a rather stiff bond with a vibrational frequency of 2359 cm^{-1}. We also investigate surface collisions of clusters composed of O_2 molecules, as the latter may be more prone to vibrational excitation due to a lower vibrational frequency of 1580 cm^{-1}. A comparative study of $(N_2)_n$ and $(O_2)_n$ cluster surface scattering may help elucidate the dependence of vibrational excitation on the stiffness of the monomers constituting the clusters. Evidence of oxidation of silicon surfaces by $(O_2)_n$ cluster-surface scattering experiments has also been reported.[215] However, a straightforward oxidation mechanism could not be inferred from

experimental results, and further theoretical investigations may shed light on a possible molecular dissociation mechanism.

In the present chapter, we investigate molecular N_2 and O_2 vibrational excitation and molecular dissociation induced by cluster-surface impact by means of molecular dynamics simulations. Cluster-surface scattering is simulated under typical experimental conditions, and vibrational excitation and molecular dissociation are monitored for various cluster sizes and incident velocities. Particular attention is paid to the influence of surface-to-cluster heat transfer on the molecular product energy distributions. The outline of the chapter is the following. The simulation procedure is summarized in Sec. B2.II. The simulation results are presented and discussed in Sec. B2.III., which in turn is divided into three subsections, addressing cluster size effects, the role of incident velocity, and surface-to-cluster heat transfer, respectively. Concluding remarks follow in Sec. B2.IV.

B2.II. COMPUTATIONAL PROCEDURE

We employ classical trajectory simulations in order to investigate the product energy distributions of $(N_2)_n$ and $(O_2)_n$ clusters scattered from a rigid surface. We use a Morse potential to describe the intramolecular N-N and O-O interactions:

$$V(r) = D_e[1 - e^{-\beta(r-r_e)}]^2 \qquad \text{(B2.1)}$$

where D_e is the dissociation energy and r_e the equilibrium bond length. The potential parameters for N_2 are D_e=229 kcal/mol, r_e=1.11 Å and β=2.657 A^{-1}, which were obtained by fitting the results of high-level ab initio calculations.[257] For O_2, we use the spectroscopically derived parameters D_e=120 kcal/mol, r_e=1.20 Å and β=2.958 A^{-1}.[258] It

is known that $(N_2)_n$ and $(O_2)_n$ clusters have a rather floppy structure characteristic of weakly-bound van der Waals complexes,[259,260] thus intermolecular interactions were modeled with a four-center Lennard-Jones potential:

$$V_{LJ}(r) = 4\varepsilon\left[\left(\frac{\sigma}{r}\right)^{12} - \left(\frac{\sigma}{r}\right)^{6}\right] \tag{B2.2}$$

with σ=3.293 Å and ε=0.07296 kcal/mol for N_2.[261] These parameters were experimentally derived from liquid studies of N_2.[261,262] In our previous theoretical work,[227] we found that these parameters also describe the N_2-N_2 interactions adequately, as experimentally derived, and ab initio CCSD(T)//MP2/6-311+G(3df,pd) potential energy curves compared well. Such model potentials were also successfully employed to elucidate energy transfer mechanisms in cluster-surface scattering from simulations, while producing results in good agreement with experiment.[227,263] For O_2, we employed Lennard-Jones parameters derived from experiment, σ=2.988 Å and ε=0.08766 kcal/mol.[258] These parameters were employed successfully in simulations of desorption of low-temperature solid O_2 induced by either electronic or vibrational excitation. [258,264] Further, the energy distribution of surface-scattered clusters, evaluated with these potentials were found in excellent agreement with experimental results.[258,264]

Two different surface models are employed here in order to investigate in detail the influence of the surface properties on the resulting product energy distributions. The simplest model is an elastic reflection model where atomic velocities in the direction normal to the surface are reversed upon impact with the surface.[265] The second model takes into account surface-to-cluster energy transfer effects in order to assess whether possible energy transfer from the surface may affect molecular vibrational excitation

under experimental conditions. For this purpose, we designed a model that mimics extreme surface-to-cluster energy transfer upon impact, where the component of the momentum along the surface normal is not only reversed, as in the simplest surface model, but also an amount of energy corresponding to the surface temperature T_{surf} is added to the normal component of the momentum, as

$$p_n' = -sign(p_n)\left(|p_n| + \sqrt{2mRT_{surf}}\right) \tag{B2.3}$$

where p_n and p_n' represent the old and new normal components of the momentum at surface impact respectively, m is the atomic mass, and R the rare gas constant. The surface temperature is taken to be 1100 K, which roughly corresponds to the maximum temperature employed in typical experiments.

Molecular clusters of approximately spherical shape containing up to 1024 molecular monomers were generated and annealed for 20 ps with a stepsize of 0.01 fs in order to obtain relatively stable structures. In this work, all trajectories are propagated by solving Hamilton equations of motion[78] with a fifth-order Gear algorithm.[266] The cluster structures are then thermalized for 200 ps at a temperature of 32 K, which is the typical temperature of clusters in molecular beams measured by electron diffraction spectroscopy.[267] Surface-scattering trajectories are initiated using the thermalized clusters placed at a distance between 10 Å to 35 Å (depending on cluster size) from the surface, with a random initial orientation. Kinetic energies corresponding to center-of-mass velocities v between 500 $m.s^{-1}$ and 15000 $m.s^{-1}$ were selected, which covers a wide range of possible experimental conditions. Trajectories are then propagated for 120 ps with a stepsize of 0.05 fs, which results in a maximum total energy deviation of 0.5 % along a given trajectory. Molecules are considered evaporated from the cluster as soon as the

monomer's center of mass reaches a distance larger than a preset value of 1.9σ from all other monomers,[78,227,232] where σ is the intermolecular Lennard-Jones parameter. Once evaporation has occurred, an analysis of the product energies is performed and the monomer product vibrational energy is evaluated as:

$$E_{vib} = E_{int} - E_{rot} = E_{int} - \frac{j^2}{2I} \tag{B2.4}$$

where E_{int} is the monomer internal energy, E_{rot} its rotational energy, j its rotational angular momentum and I its moment of inertia. The monomer internal energy E_{int} is just the sum of the kinetic energy corresponding to the relative motion of the atoms in the monomer center-of-mass frame and the potential energy of the diatom with respect to its equilibrium position. Because of possible vibrational-rotational coupling, the rotational energy E_{rot} is averaged over a few periods of vibration of the diatomic molecule.

As we will see shortly, the vibrational energy distributions are bimodal. Accordingly, the vibrational energy distribution of evaporated monomers is fitted to a sum of two Boltzmann distributions:

$$P(E_{vib}) = w\left(\frac{1}{RT_{vib}^{cold}}\right)e^{-E_{vib}/RT_{vib}^{cold}} + (1-w)\left(\frac{1}{RT_{vib}^{hot}}\right)e^{-E_{vib}/RT_{vib}^{hot}} \tag{B2.5}$$

where w determines the relative weight of the cold component in the distributions, and T_{vib}^{cold} and T_{vib}^{hot} are the temperatures of the cold and hot components, respectively, of the vibrational energy distributions. In addition, the standard deviation between the actual monomer energy distribution and the fit to the Boltzmann curve were evaluated as an estimate of the quality of the fits. Monomers that dissociate on the timescale of the

simulations are obviously not included in the calculation of vibrational energy distributions.

B2.III. RESULTS AND DISCUSSION

B2.III.A. Vibrational Energy Product Distribution

Our previous theoretical work on $(N_2)_n$ clusters[227,263] showed that the monomer product translational energy distributions follow one-temperature Maxwell-Boltzmann distributions, while the rotational energy distributions are better represented by a sum of two Boltzmann distributions. In Fig. B2.1, we display some typical product vibrational energy distributions $P(E_{vib})$, both in normal and logarithmic scale, for both $(N_2)_n$ and $(O_2)_n$ clusters. The very existence of two product vibrational temperatures is obvious from the logarithmic plot of $P(E_{vib})$ *vs* E_{vib}. The log plot would be linear if the energy distribution could be fitted by one Boltzmann distribution, but our results produce biexponential plots, as shown in Figs. B2.1a and B2.1c, which can be fitted by a sum of two Boltzmann distributions. Figs B2.1b and B2.1d show that the product vibrational energy distributions are indeed very well represented by a sum of two Boltzmann distributions. This conclusion is further supported by the small standard deviations of the fits that typically range between 0.01 and 0.06. Two vibrational temperatures are obtained for all initial cluster-surface scattering conditions employed here. The range covered by the cold and hot vibrational temperatures are very wide, and appear to be quite sensitive to the choice of initial conditions. However, for a given set of initial conditions, i.e. cluster size and incident velocity, the hot and cold temperature are clearly distinct, with a hot component temperature typically 3 to 50 times larger than that of the

cold component. The vibrational temperatures are reported in Figs. B2.5c and B2.5d as a function of cluster size, and in Figs. B2.6d and B2.6e as a function of incident cluster velocity, and will be further discussed later.

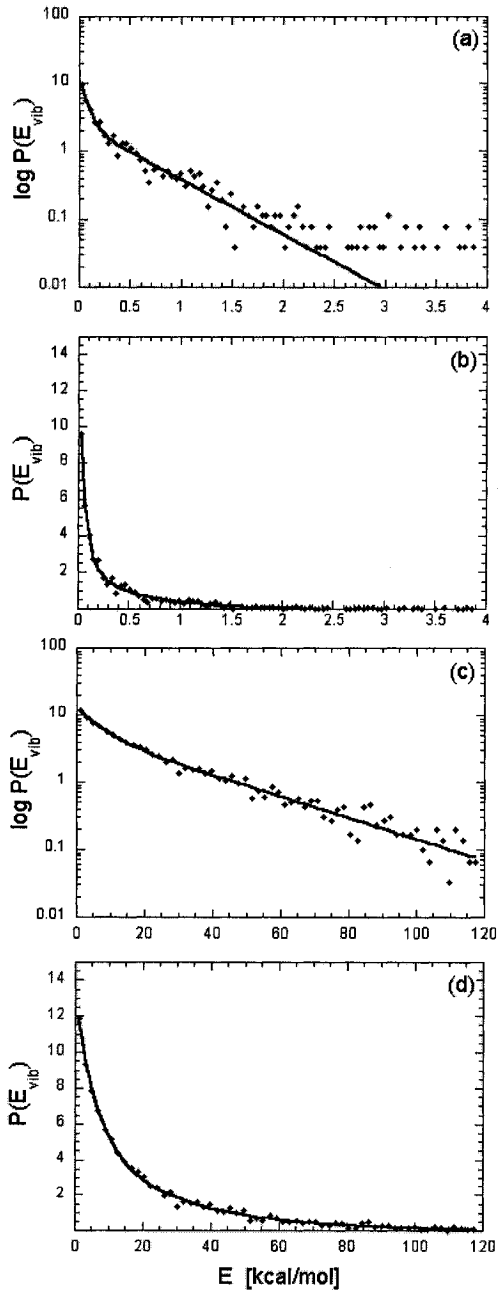

Fig. B2.1. Monomer products vibrational state distributions. Panels (a) and (c) are logarithmic plots of the product vibrational energy distribution, for $(N_2)_{766}$ (v = 1200 m.s^{-1}) and $(O_2)_{64}$ (v = 6000 m.s^{-1}) respectively. Panels (b) and (d) represent the product vibrational energy distribution for $(N_2)_{766}$ (v = 1200 m.s^{-1}) and $(O_2)_{64}$ (v = 6000 m.s^{-1}). Dots represent the calculated values and the lines are fits of the data (see text for details).

(a) beginning of impact

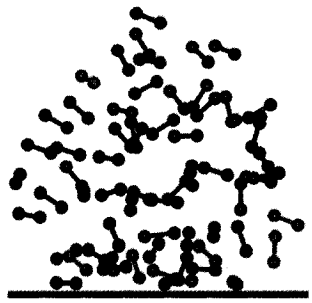

300 fs

(b) cluster compression

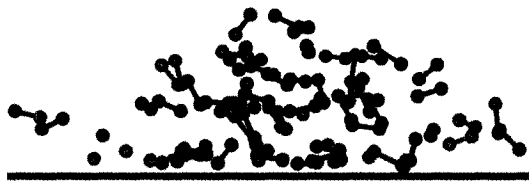

400 fs

(c) cluster expansion

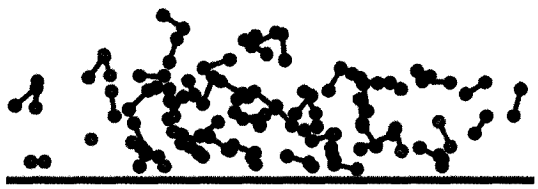

450 fs

(d) cluster fragmentation

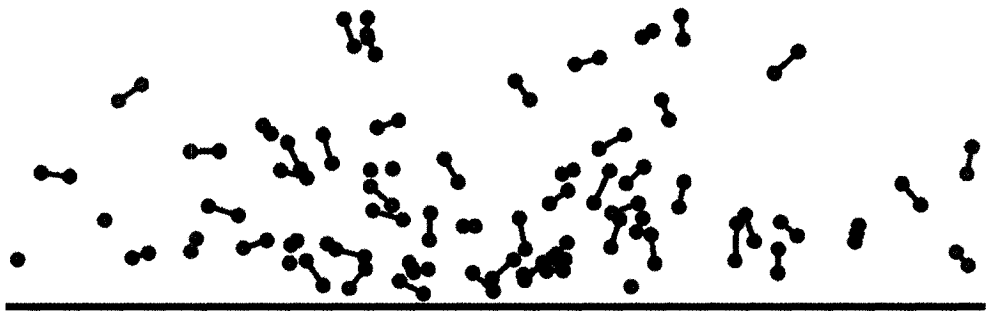

600 fs

Fig. B2.2. Illustration of the initial spatial origin of molecules that end up vibrationally very hot, very cold, or dissociated after the scattering of $(O_2)_{64}$, v = 8000 $m.s^{-1}$. Monomers with vibrational energies higher than 60 kcal/mol are considered vibrationally very hot and are shown in blue, while those with energies lower than 0.5 kcal/mol are vibrationally very cold and shown in violet. The dissociating monomers are shown in green.

Monitoring the position of monomers during the scattering event allows us to elucidate the origin of the two vibrational components. Fig. B2.2 displays the typical positions of molecules that are very hot, very cold, or dissociated after the scattering of $(O_2)_{64}$ clusters at an incident velocity of 8000 $m.s^{-1}$. The relative position of vibrationally very cold, very hot or dissociated monomers demonstrates that the vibrationally excited monomers originate from the first layers at the outskirts of the cluster. As the cluster becomes compressed during impact, the molecules in the cluster interior are subject to inelastic intermolecular collisions that produce a rapid heating of the cluster and subsequent evaporation of molecules lying at the outskirts of the cluster. The evaporation obviously mainly takes place from the outer layers of the cluster, where molecules interact with fewer neighbours.[224,268] During surface impact, those molecules are in a region of lower density than the molecules that are trapped within the interior of the compressed cluster. As molecules evaporate from the outskirts, the cluster undergoes a rearrangement in which molecules that were originally trapped within the cluster during the heating period reach the cluster surface and eventually evaporate as well. This process continues until all of the excess vibrational energy gained due to surface impact has been released through evaporation. Therefore, the cold component originates from the cluster interior, where they are subject to significant cage effects during surface impact.

Such findings are consistent with the Dynamic Zone Structure (DZS) model proposed by Vach *et al.*,[232] which has already been applied successfully to explain the rotational and translational energy distributions in $(N_2)_n$ cluster surface scattering.[227] In the present study, it also provides a solid basis for understanding the mechanism of energy transfer to the vibrational degrees of freedom of evaporated products. The DZS

model draws a parallel between the Leidenfrost phenomenon of droplet evaporation from a hot plate to that of cluster-surface collisions to describe the dynamics of cluster scattering. Contrary to a droplet where energy for evaporation is supplied by an external hot plate, in the DZS model, energy is supplied almost entirely by the cluster's center-of-mass incident normal momentum, as originally proposed for the interaction of molecules with surfaces by Logan and Stickney.[269] Accordingly, the amount of energy transferred to the internal degrees of freedom of monomers that evaporate after being elastically scattered off a rigid non-interacting surface is proportional to the cluster's center-of-mass momentum, in accord with the hard-cube model.[269] However, the increased intermolecular collisions within large clusters during surface impact greatly complicate both energy transfer and evaporation processes. To understand the cluster scattering dynamics and the resulting product energy distributions better, the DZS model postulates that the cluster is separated into various zones that dynamically change in size throughout the scattering event. Fig. B2.3 is an illustration of the DZS model scheme of the scattering dynamics, which clearly shows how the cluster can be decomposed into three zones. The first zone (z_1) is composed of molecules trapped between the surface and the remaining incoming cluster during surface impact, forming a region comparable to a "vapor cushion".[232] The second zone (z_2) is constituted by the monomers lying at the outskirts of the cluster. Finally, the third zone (z_3) is the internal part of the cluster, i.e. it consists of molecules trapped in the interior between the vapor cushion (z_1) and molecules at the outskirts (z_2).

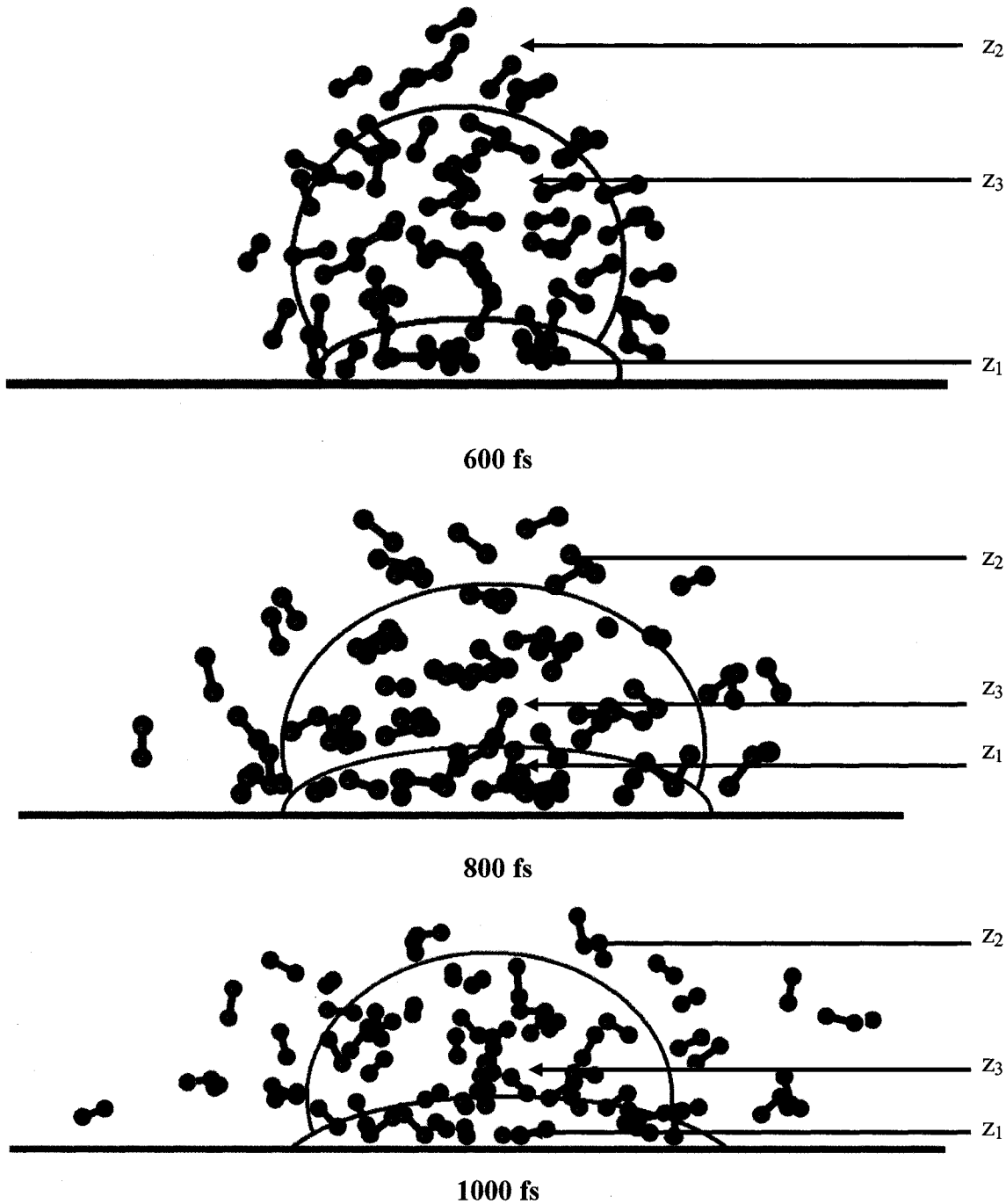

Fig. B2.3. Illustration of the DZS model in the surface scattering of a molecular cluster of size n=64.

Since there are more ongoing collisions in the cluster interior zone (z_3), vibrational relaxation is naturally more efficient and the energy is more effectively distributed throughout the cluster interior, resulting in colder monomers. At high velocities (above 5000 $m.s^{-1}$ for O_2 and above 6000 $m.s^{-1}$ for N_2), it appears that the majority of the dissociating species originate from molecules in the layers closest to the graphite surface, i.e. the vapor cushion (z_1), which is not surprising since the species in this region are exposed to the largest number of collisions between the surface and incoming monomers. Fig. B2.4 displays the vibrational energies of evaporated monomers as a function of evaporation time t_{evap}. The highest vibrational energies are obviously reached very early in the cluster scattering process, as was shown in our previous study for rotational excitation.[227] The largest fraction of vibrationally hot monomers is produced at the beginning of the impact event, thus further supporting the fact that vibrationally hot monomers evaporate from the cluster outskirts immediately after surface impact, whereas the vibrationally cold monomers originate from the dense interior of the cluster and evaporate only after cluster rearrangement and further vibrational relaxation. Vibrational energy relaxation is enhanced by intermolecular collisions due to resonant vibrational energy transfer.[270] In fact, gas-phase vibrational relaxation notoriously involves a large number of collisions between molecules. In the case of diatomic Van der Waals clusters, for instance, about 2700 collisions are necessary before a NO molecule in the first vibrational state relaxes to its vibrational ground state.[271] Therefore, vibrational energy relaxation is more efficient at higher pressures and densities, such as in zones z_1 and z_3 during cluster-surface impact,[227,272] which explains why the cold component

originates from the high-density interior of the cluster, while the hot component monomers come from the cluster outskirts (z_2).

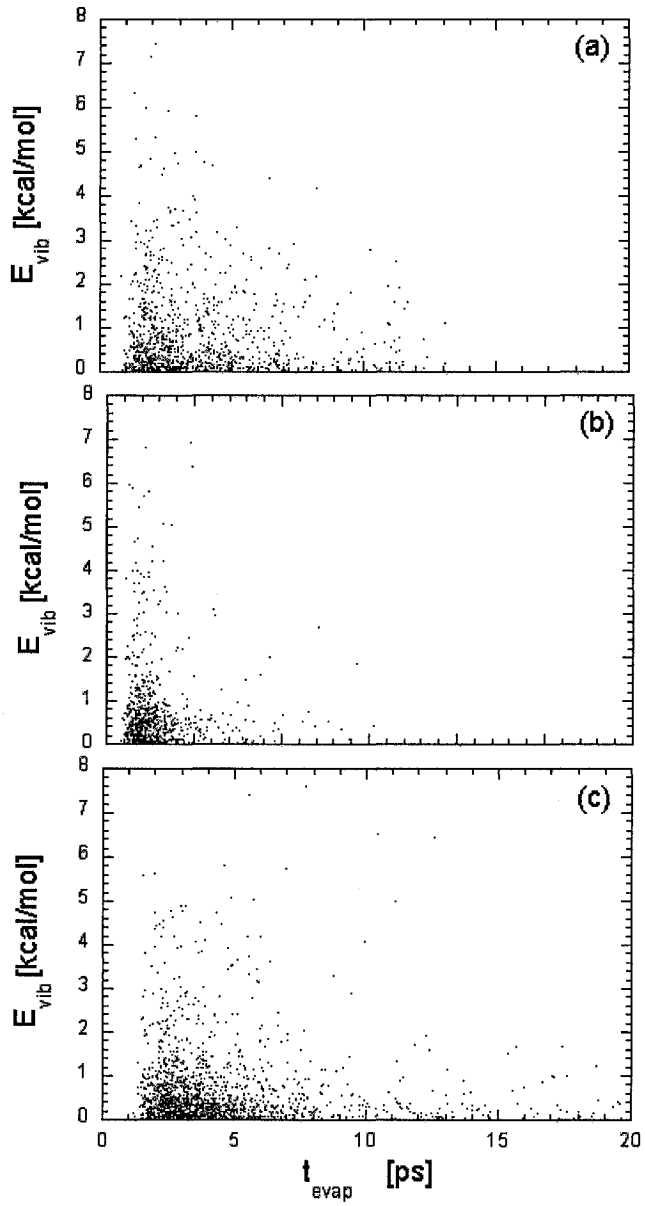

Fig. B2.4. Vibrational energies E_{vib} of evaporated monomers as a function of evaporation time t_{evap}. The conditions employed are (a) $(N_2)_{64}$ with v = 1200 m.s^{-1}, (b) $(O_2)_{64}$ with v = 2500 m.s^{-1} and (c) $(O_2)_{128}$ with v = 1200 m.s^{-1}.

B2.III.B. Role of Cluster Size

We carried out a comparative study of various properties of the scattered products as a function of initial incident cluster size. Fig. B2.5 shows the evolution of the product vibrational energies, the hot and cold component temperatures, and the probability of monomer dissociation as a function of cluster size.

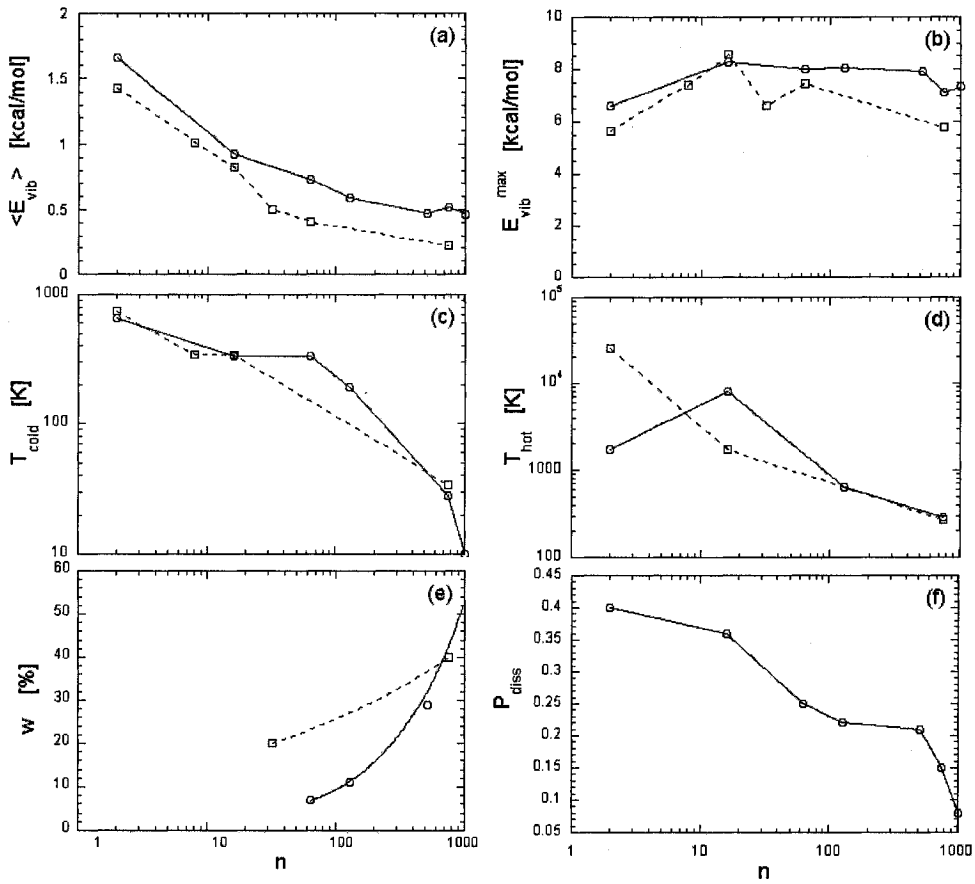

Fig. B2.5. Cluster scattering product properties as a function of cluster size for $(N_2)_n$ [- - □ - -] and $(O_2)_n$ [—○—] clusters. If not stated otherwise, the impact velocity is 1200 $m.s^{-1}$ as in typical experiments. The top panel (a) represents the average monomer vibrational energy $<E_{vib}>$, panel (b) the maximum vibrational energy attained by a monomer E_{vib}^{max}, panels (c) and (d) the evolution of the temperature of the cold and hot components, and panel (e) the weight of the cold component of the distribution. Panel (f) displays the probability of molecular dissociation P_{diss} of the O_2 product molecules at a cluster incident velocity of 8000 $m.s^{-1}$.

Ensemble-averaged product vibrational energies $<E_{vib}>$ and maximum product vibrational energies E_{vib}^{max} appear to be higher for $(O_2)_n$ than for their $(N_2)_n$ counterpart (cf. Figs. B2.5a and B2.5b, respectively). This is not a surprising result since the N_2 molecule has a much stiffer bond than the O_2 molecule. Therefore, the O_2 molecule will be more prone to vibrational excitation than N_2 during the scattering event. This also suggests that O_2 dissociation will occur at lower impact energies than for N_2, reflecting the weaker O_2 bond dissociation energy.

When simulating cluster impact under experimental conditions (v_i = 750 to 1500 $m.s^{-1}$), the product monomers are found to be only slightly vibrationally excited for all cluster sizes investigated. Further, inspection of Fig. B2.5b. suggests that the maximum product vibrational energy E_{vib}^{max} does not exhibit any clear dependence on cluster size. Even for large clusters, vibrational excitation and intramolecular dissociation are not significant under current experimental scattering conditions.[230] Since experiments involve large clusters containing typically a few hundred to a few thousand molecules, this suggests that little or no vibrational excitation occurs in typical experiments at moderate incident velocities. Contrary to what one might expect in cluster-catalyzed reactions, the average vibrational energy $<E_{vib}>$ is found to decrease with cluster size increase, as evident from Fig. B2.5a. Similarly, we observe from Fig. B2.5c and B2.5d that both vibrational temperatures tend to decrease with increasing cluster size. As cluster size increases, the size of the surviving cluster after surface impact increases, along with the number of potential intermolecular collisions within the surviving cluster, hence promoting vibrational relaxation and resulting in lower (hot and cold) vibrational temperature. Finally, inspection of Fig. B2.5e shows that the weight of the cold

component of the vibrational energy distribution increases with cluster size, and the population of cold molecules becomes prevalent over that of the hot monomers with increasing cluster size. This is in agreement with our previous findings that the cold monomer population originates from the cluster interior, while hot monomers originate from the cluster outskirts since, as cluster size increases, the number of monomers in the interior of the cluster grows faster than the number of monomers at the surface of the cluster.

To investigate the dynamics of energy transfer in greater detail, the total product energy partitioning between translational, rotational and vibrational degrees of freedom of the evaporated molecules, as well as the kinetic energy of the final surviving cluster were evaluated and are listed in Table B2.1.

Table B2.1. Energy partitioning of scattered clusters.

$(N_2)_n$ clusters - v_i = 1200 m.s^{-1}				
n	E_{trans} (%)[a]	E_{rot} (%)	E_{vib} (%)	E_{cl} (%)[b]
8	57.5	14.6	20.1	7.8
16	60.7	13.2	16.8	9.4
32	68.3	15.7	10.4	5.6
64	73.4	13.8	8.8	4.0
766	62.0	5.6	3.3	29.1
$(O_2)_n$ clusters - v_i = 1200 m.s^{-1}				
n	E_{trans} (%)[a]	E_{rot} (%)	E_{vib} (%)	E_{cl} (%)[b]
16	62.6	18.0	16.0	3.5
64	72.7	13.0	12.3	1.9
128	76.4	11.6	10.8	1.2
512	82.0	9.3	8.3	0.5
766	84.6	7.3	7.8	0.4
1024	81.1	6.6	12.1	0.1

a. E_{trans} is the translational energy defined in the laboratory frame, not the cluster frame.
b. E_{cl} is the kinetic energy of the surviving cluster.

Evidently, the average monomer rotational energy proportion decreases progressively with increasing cluster size (from 14.6 % to 5.6 % for N_2 clusters and 18.0 % to 6.6 % for O_2 clusters). This is consistent with our previous work, in which a decrease of the rotational temperature with increasing cluster size was observed.[227] More importantly, the average monomer vibrational energy also tends to decrease with increasing cluster size, whereas translational excitation becomes increasingly important as cluster size increases. Therefore, the decrease of both vibrational and rotational energies is compensated by translational excitation of the product molecules.

The molecular dissociation probability P_{diss}, shown in Fig. B2.5f for a relatively large incident cluster velocity (v_i = 8000 m.s^{-1}), tends to decrease with increasing cluster size. This suggests that increasing cluster size will not necessarily catalyze, but may rather hinder monomer dissociation. More specifically, in reactions involving monomer dissociation, such as in Zeldovich type atom-diatom reaction,[273] one may expect the reaction yield to decrease with increasing cluster size. However, clusters need to be large enough to hold the reactants together, and yet they need to be small enough to minimize vibrational relaxation. Therefore, the present results suggest that there is an optimal cluster size giving the highest reaction yield, which seems to be in the range 64 to 512 in the present study.

B2.III.C. Role of Incident Velocity

Fig. B2.6 displays the average product vibrational energy $<E_{vib}>$, maximum product vibrational energy E_{vib}^{max} and monomer dissociation probability P_{diss} as a function of incident velocity. Inspection of Figs. B2.6a and B2.6b immediately reveals that $<E_{vib}>$ and E_{vib}^{max} rapidly increase with incident cluster velocity.

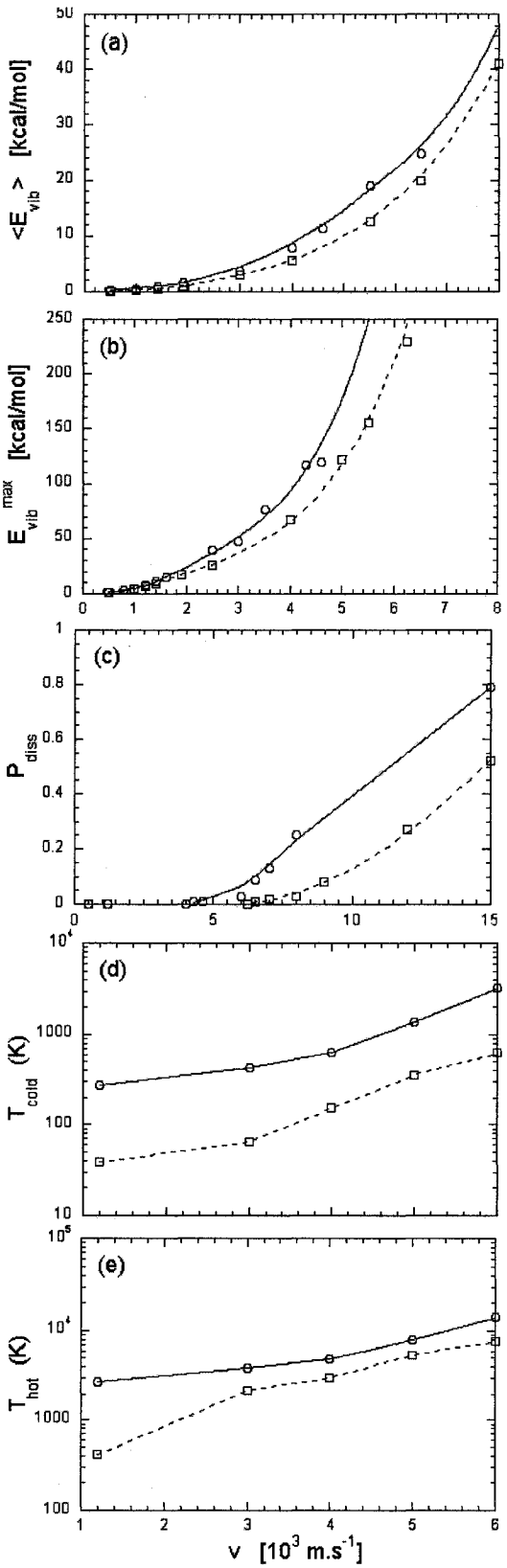

Fig. B2.6. Cluster scattering product properties as a function of cluster incident velocity for $(N_2)_{64}$ [- - □ - -] and $(O_2)_{64}$ [—○—]. Panels (a) and (b) display the average monomer product vibrational energy $<E_{vib}>$ and the maximum monomer product vibrational energy E_{vib}^{max}, respectively. Panel (c) shows the probability of molecular dissociation P_{diss} of O_2 product molecules. Panels (d) and (e) show the evolution of the cold and hot vibrational temperatures, respectively.

The evolution of the dissociation probability as a function of incident velocity, shown in Fig. B2.6c, suggests that dissociation of the monomers starts occurring at incident velocities of about 6500 $m.s^{-1}$ and 4300 $m.s^{-1}$ for $(N_2)_n$ and $(O_2)_n$, respectively.

The dissociation probability curves indicate that $(O_2)_m$ clusters dissociate readily, which is again due to the weaker O-O bond (120 kcal/mol)[258] compared to that of the N-N bond (230 kcal/mol).[257] The increase of the dissociation probability with incident velocity is relatively moderate, such that a significant dissociation rate (above 20 %) only occurs at substantially larger incident velocities, roughly 12 000 $m.s^{-1}$ for $(N_2)_n$ and 8 000 $m.s^{-1}$ for $(O_2)_n$. We define the molecular dissociation time t_d as the time of the last turning point in the relative diatomic motion. The resulting distribution of molecular dissociation times is displayed in Fig. B2.7.

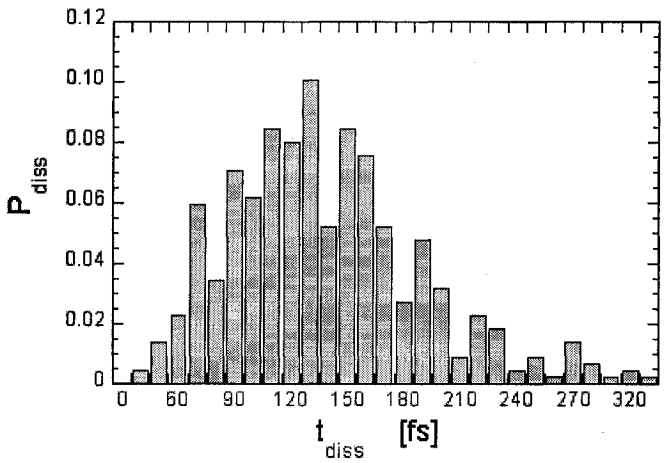

Fig. B2.7. Distribution of molecular dissociation times for $(O_2)_{64}$ with an incident velocity of 8000 $m.s^{-1}$.

Our results indicate that molecular dissociation occurs very early, in the initial phase of the scattering event. For instance, molecular dissociation occurs around 100 and 200 fs after surface impact for a $(O_2)_{64}$ cluster with an incident velocity of 8000 $m.s^{-1}$. As

illustrated in Fig. B2.2, the dissociating molecules are generally located close to the graphite surface at surface impact, *i.e.* in the vapor cushion z_1, where the scattering conditions are the most extreme. When increasing the incident velocity, an increasing proportion of the dissociating molecules are found to originate from that cluster zone, where the number of intermolecular collisions is maximized.

The vibrational temperatures T_{vib}^{cold} and T_{vib}^{hot} are also found to rapidly increase with incident cluster velocity, as shown in Figs. B2.6d and B2.6e, due to a more significant transfer of cluster incident kinetic energy to the vibrational modes of the scattered species. The product vibrational energy distributions as well as the average product vibrational energies $<E_{vib}>$ are relatively similar for $(O_2)_m$ and $(N_2)_m$ clusters, which may be surprising since the vibrational frequencies of O_2 and N_2 are relatively different. As illustrated in Fig. B2.1, the distribution of the product vibrational energies is more widely spread at large incident velocities than at lower ones. Such a broadening of the distribution might be interpreted as interferences from mechanisms that might not necessarily be thermal in nature. A number of previous studies[213,274,275] actually attributed non-thermal effects to the creation of shock waves inside the cluster. Intense collisions of the cluster with a surface certainly lead to short periods of non-equilibrium conditions, where thermal energy redistribution is not possible.

B2.III.D. Surface-to-cluster Heat Transfer Effects

As discussed above, cluster size does not seem to promote molecular dissociation under the "mild" conditions employed in typical experiments, i.e. typical experimental incident velocities for neutral Van der Waals clusters were found to be insufficient to produce significant molecular vibrational excitation and molecular dissociation. Another

possible source of energy for promoting molecular dissociation may lie in surface-to-cluster heat transfer. In order to investigate this effect, we used a surface model that allows for highly efficient (extreme) energy transfer from the surface to the cluster monomers as discussed in Sec. B2.II. We present the evolution of various properties obtained from simulations with this model as a function of cluster size in Fig. B2.8 and as a function of the cluster incident velocity in Fig. B2.9.

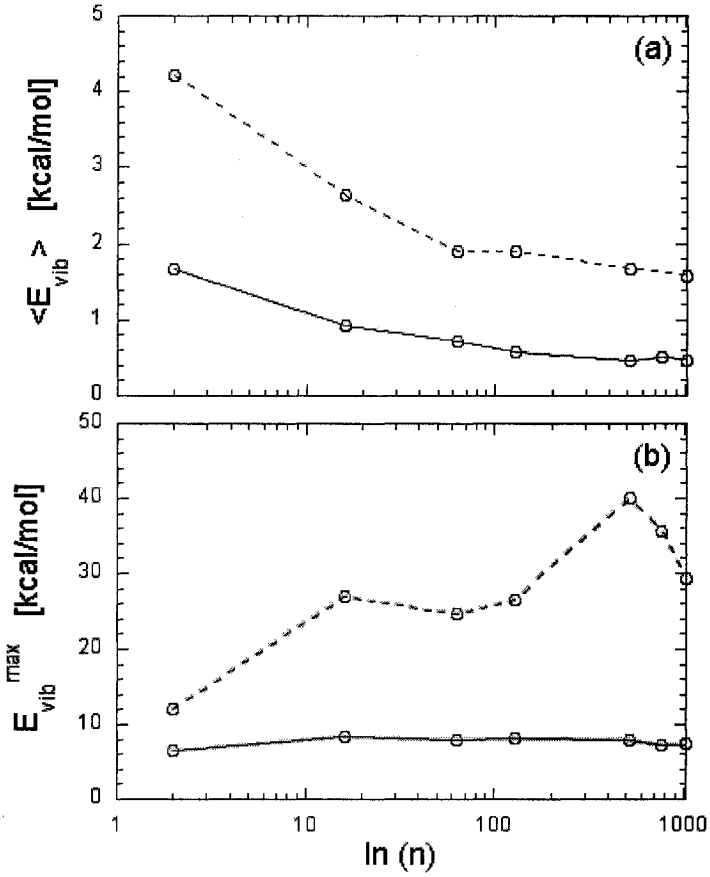

Fig. B2.8. Product vibrational energies as a function of cluster size for $(O_2)_n$ clusters, with an incident velocity of 1200 $m.s^{-1}$, with surface-to-cluster heat transfer effect [ ], and without surface-to-cluster heat transfer [ ]. Panel (a) represents the average monomer vibrational energy $<E_{vib}>$ and panel (b) displays the maximum vibrational energy E_{vib}^{max}.

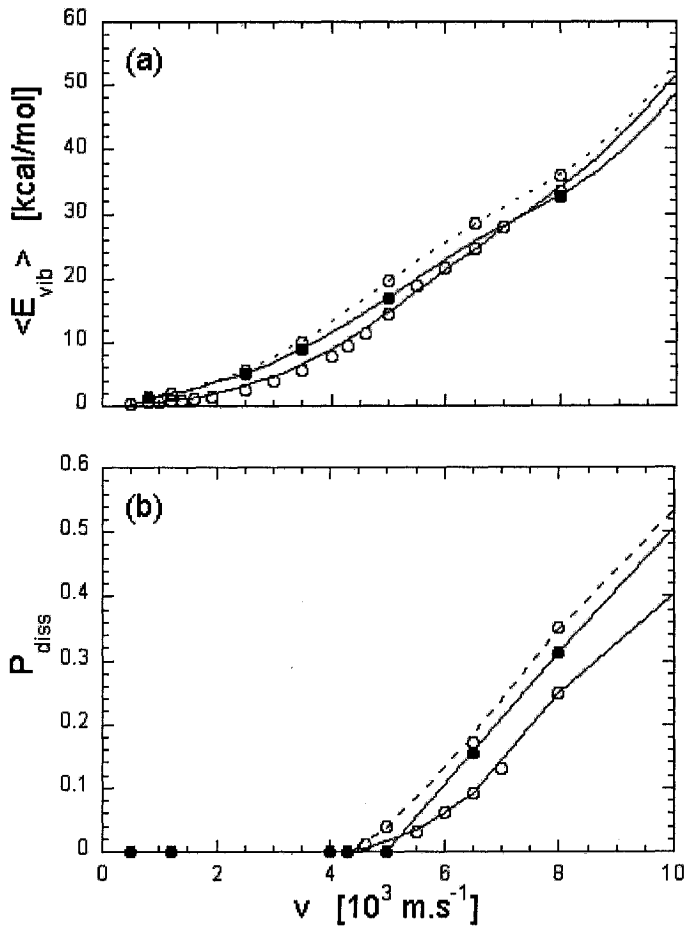

Fig. B2.9. Product vibrational energies for $(O_2)_n$ clusters as a function of cluster incident velocity, for $(O_2)_{64}$ with [ ] and without [ ] surface-to-cluster heat transfer, and $(O_2)_{128}$ cluster with surface-to-cluster heat transfer [ ]. Panels (a) and (b) represent the average monomer vibrational energy $<E_{vib}>$ and the probability of molecular dissociation P_{diss}, respectively.

The most striking feature of the simulation results is that surface-to-cluster energy transfer does not alter the trends in neither the product vibrational energies nor the monomer dissociation probabilities. Surface-to-monomer heat transfer naturally increases both the average product vibrational energy, as shown in Figs. B2.8a and B2.9a, and the maximum monomer vibrational energy, as shown in Fig B2.8b, but the increase is not significant enough to promote molecular dissociation under typical experimental

conditions. Indeed, Fig. B2.8b shows that the O_2 maximum vibrational energy increases from roughly 12 kcal/mol for cluster size 2 to 40 kcal/mol for cluster size 512, and decreases thereafter. In contrast, a constant value of ~7 kcal/mol was obtained in simulations where surface-to-monomer heat transfer was not taken into account. While energy transfer from the surface surely tends to promote molecular vibrational excitation as well as molecular dissociation, even extreme energy transfer does not allow for substantial molecular dissociation at typical experimental velocities and, as can be seen from Fig. B2.9b, significant dissociation is only attained for impact velocities exceeding 5500 $m.s^{-1}$, which is 3 to 6 times the present experimental velocity.

B2.IV. SUMMARY AND CONCLUDING REMARKS

The present study of $(N_2)_n$ and $(O_2)_n$ cluster surface scattering was motivated by the interest in the possible vibrational excitation and molecular dissociation induced by cluster collisions with surfaces. Following the "chemistry with a hammer" concept,[221] one would expect some vibrational excitation and molecular dissociation of monomers in the scattering of molecular clusters on a graphite surface,[230] as expected for typical cluster catalyzed reactions.[217,252,275] In the molecular dynamics simulations presented here, we carried out a comparative study of $(N_2)_n$ and $(O_2)_n$ clusters fragmenting after collision with a hard surface. For all conditions employed, monomer vibrational energy distributions are best represented by a two-temperature Boltzmann distribution. For the highest velocities, a slight increase of the standard deviation was observed (roughly from 1% to 4%), which may tentatively be attributed to more pronounced non-thermal effects. For instance, shock wave effects were shown to develop at high velocities.[275]

Furthermore, a detailed analysis of the molecular dynamics simulation results in terms of the DZS model seems to provide an explanation for the two vibrational product state distributions. The cold component of the distribution was shown to involve monomers originating from the cluster interior while the hot component of the distribution is made up of monomers essentially lying at the outskirts of the cluster at surface impact.

We showed that under current experimental conditions for neutral Van der Waals cluster beams, increasing cluster size does not enhance, but rather hinders vibrational excitation due to more efficient vibrational energy relaxation with increasing cluster size. In fact, an increasing fraction of the energy goes into the translational modes of evaporated molecules, and the transfer of incident cluster translational energy into monomer vibrational energy becomes less and less efficient in larger clusters. Clearly, current experimental conditions do not appear to lead to subsequent monomer vibrational excitation or allow for N_2 or O_2 molecular dissociation. For cluster sizes typical of experimental conditions, a very large incident velocity, about 3 to 6 times larger than the ones currently used experimentally, are necessary to obtain a significant probability of product molecular dissociation. This observation suggests that larger cluster incident velocities or smaller clusters should be used in order to experimentally observe significant molecular dissociation. Also, surface-to-cluster energy transfer results in a substantial enhancement of vibrational excitation and molecular dissociation. However, it still does not allow significant impact-induced molecular dissociation under present experimental conditions. Finally, we propose the existence of an optimal cluster size between 64 and 512 molecules for cluster-catalyzed reactions, where the cluster is large

enough to confine the reactants and yet small enough to minimize vibrational energy relaxation.

These results are especially interesting in light of previous studies by Levine and coworkers[217,248,249,251-253] of chemical reaction catalysis under extreme conditions generated by cluster-surface impact. In the "burning of air" study,[217] the reaction is predicted to occur with incident velocities of 1800 $m.s^{-1}$, and it was shown that cluster collisions catalyze chemical reactions in a similar fashion in other "chemistry with a hammer" studies.[217,221,248,249,251-253] Further, no evidence was reported of a possible stepwise Zeldovich-type mechanism, because of fast cluster dissociation that prevents holding the reactants together long enough to allow the reaction to proceed. Instead, the reaction was shown to proceed via a four-center concerted mechanism with an activation energy of 305 kcal/mol,[253] which is much higher than the O_2 and N_2 dissociation energies. Therefore, one would have expected to observe monomer vibrational excitation and possibly product molecular dissociation in the surface scattering of $(N_2)_n$ and $(O_2)_n$ clusters at the experimental conditions employed by Martino *et al.*,[230] i.e. incident cluster velocities ranging from 750 $m.s^{-1}$ to 1500 $m.s^{-1}$ and clusters composed of a few hundred molecules, especially since a kinematic model suggests that the reaction efficiency is considerably enhanced by the initial vibrational excitation of the N_2 and O_2 reactants, which may help drive the products apart.[249] To our knowledge, no successful experimental demonstration of the "burning of air"[217] has been reported to date, but experiments typically involve clusters containing several hundreds or even thousands of molecules. Therefore, we suggest the use of smaller clusters to make the "chemistry with a hammer" experimentally feasible.

CHAPTER B3
Non-adiabatic Ladder Climbing during Molecular Collisions

In the eternal quest for a better understanding of physical phenomena on the atomic scale, major progress has been achieved since Born and Oppenheimer proposed that the electronic motion and the nuclear motion in molecules could be separated.[276] Since nuclei are so much heavier than electrons, the former can be considered as being fixed. This approximation leads thus to electronic wave functions that depend on the nuclear positions, but not on their velocities. Recently, convincing experimental evidence has been presented that the Born-Oppenheimer approximation breaks down for chemical reactions at metal surfaces,[277,278] while it remains in general valid and well accepted for gas-phase reactions.[279] Here we demonstrate how even relatively mild molecular collisions can lead to a significant coupling between atomic and electronic motion. To this end, we show how a non-adiabatic "ladder climbing" mechanism allows us to understand two recent and ground-breaking experiments that remained largely unexplained until now.

The first experiment we would like to address concerns the striking observation by Daineka *et al.* that silicon oxidation by molecular oxygen clusters is significantly enhanced over that observed with oxygen molecules.[215] The low oxidation probability of silicon surfaces by oxygen molecules is a result of the relatively high energy barrier of 2.7 eV[241] that is unlikely to be overcome by impacting molecules that only possess an average internal energy of about 0.21 eV in the Daineka experiment. The idea of the "chemistry with a hammer"[252,280] might, therefore, play the key role in the observed cluster-catalyzed reaction. Notably for the impact of a cluster on a surface, it has been suggested that the incident kinetic energy of the entire cluster can be "channeled" into only a few cluster

particles that are close to the surface and that cannot escape because of steric confinement by other cluster particles.[217] In this manner, energy barriers can be overcome that are normally too high for simple gas-phase reactions, leading to cluster-catalyzed reactions. While this idea has been proposed more than a decade ago, no direct experimental evidence for such a reaction mechanism has been reported for neutral clusters until now.

Using classical molecular dynamics (MD) simulations with model potentials,[281] we investigated three possible reaction pathways. Since silicon oxidation by oxygen atoms is known to proceed without an activation barrier,[236,238,239] we first evaluated the molecular oxygen dissociation probability during cluster impact. To this end, we simulated the impact of $(O_2)_n$ clusters (with $2 < n < 1024$) on a surface at a temperature of 1100 K.[265] While the formation of oxygen atoms could have explained the observed highly efficient etching in a straight-forward way, our simulations show without ambiguity that this reaction path must be ruled out since molecular dissociation is completely negligible at the experimental impact velocities.[281]

The maximum internal energy that can be gained by a given molecule during the scattering event is displayed in Fig. B3.1a. This energy increases with cluster size n to become rapidly large enough to render oxidation possible. While cluster impact does lead to an energy increase of an order of magnitude for some molecules, it can not by itself explain the observed etching since it only applies to a very small number of molecules. In Fig. B3.1b, we show that less than 0.25 % of the cluster molecules aquire a sufficient energy to overcome the necessary activation barrier for direct oxidation while the experimental value is nearly one hundred times larger.[215] Therefore, we explored another reaction scheme. It is well known that oxygen molecules in their first excited electronic

state $O_2(^1\Delta_g)$ are so chemically reactive that they could readily cause the observed oxidation without an activation barrier.[282] The energy splitting between the ground $O_2(^3\Sigma_g^-)$ and the singlet $O_2(^1\Delta_g)$ states is 0.97 eV.[283,284] In excellent agreement with the experimental observation, our MD simulations reveal that about 25 % of the incident molecules obtain a sufficient amount of energy for the triplet/singlet transition during cluster impact (see Fig. B3.1c).

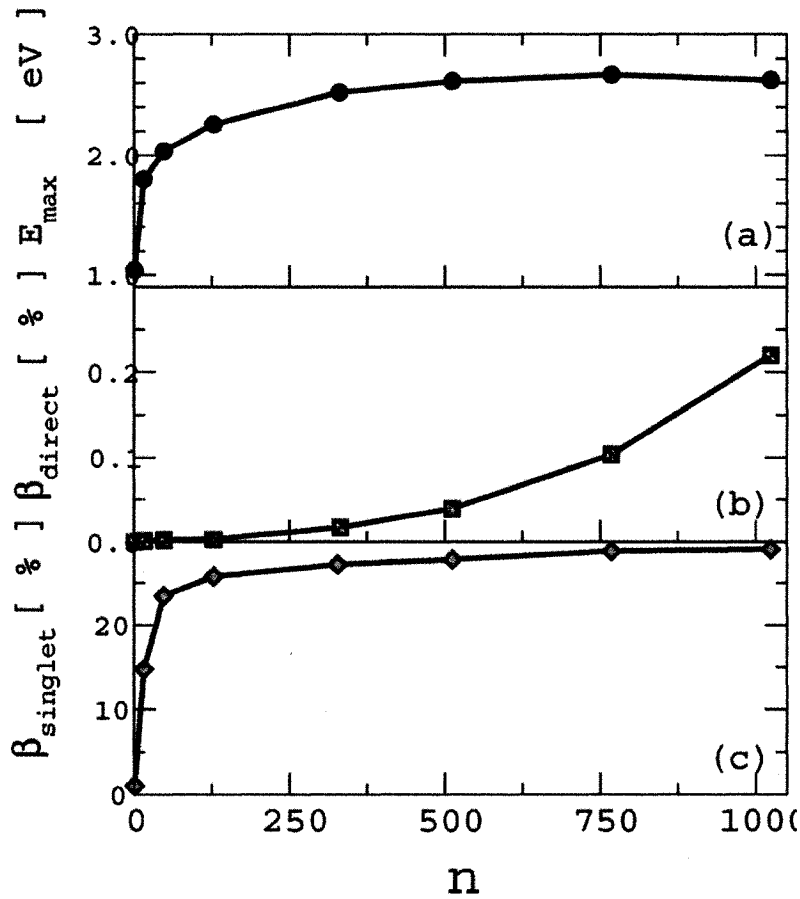

Fig. B3.1. Summary of the MD simulations, (a) maximum internal energy that a given cluster molecule can gain during the surface scattering event; (b) fraction of incident molecules that acquire more than 2.7 eV of internal energy necessary for direct oxidation; (c) fraction of incident molecules that acquire more than 0.97 eV of internal energy necessary for a possible triplet/singlet transition as a function of the molecule number *n* in the cluster.

For an individual molecule, however, the necessary transition is very unlikely since it simultaneously violates several selection rules of quantum mechanics.[284] In the present case, however, the impact-induced, mechanical cluster compression leads to a deformation of the electronic structure of the cluster molecules that may render such electronic transitions possible. To test this hypothesis, we performed multi-configurational complete active space self-consistent field (CASSCF) calculations with a large basis set (aug-cc-pVTZ) and a (16,12) active space[285,286] using the MOLPRO package.[287,288] While known for providing reliable information on both ground and excited states, those computations are numerically very intensive. Therefore, we focus here on the electronic structure dynamics of model oxygen dimers $(O_2)_2$ under conditions typically encountered inside large oxygen clusters during their surface impact according to our aforementioned MD calculations. In these CASSCF calculations, the oxygen 1s and 2s orbitals are kept doubly occupied and the remaining 16 valence electrons are distributed in 12 orbitals.[289]

Fig. B3.2 illustrates how the change of symmetry increases the complexity of the monomer electronic structure when two oxygen molecules are brought together to form a dimer. While other dimer configurations are possible, we focus here on the *H* geometry since it is the minimum energy structure of the dimer.[290] The dimer potential energy surfaces for O_2 molecules at their equilibrium internuclear distance are shown in Fig. B3.3 as a function of the intermolecular distance $R_{O_2\text{-}O_2}$ in the range observed in our MD simulations. As is evident from Fig. B3.3a, several potential energy surfaces cross each other making collision-induced transitions possible. In Fig. B3.3b, we illustrate how the proposed *non-adiabatic ladder climbing scheme* exploits subsequent dimer compression and relaxation

to permit the ground state dimer ($^3\Sigma_g^- + {}^3\Sigma_g^-$) to first afford the spin-forbidden transition for one molecule ($^3\Sigma_g^- + {}^1\Delta_g$) and then also for the second one ($^1\Delta_g + {}^1\Delta_g$).

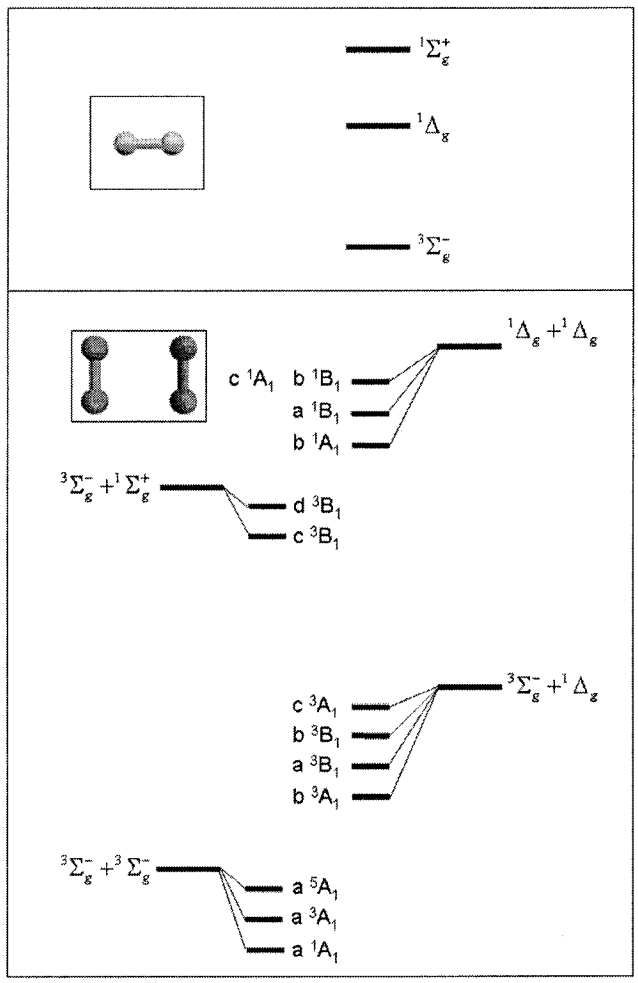

Fig. B3.2. Illustration of the energy splittings that have to be considered when two infinitely separated oxygen molecules are brought together to form an equilibrium dimer in the *H* configuration using the C_{2v} point group.

While curve crossing is a necessary condition for the collision-induced non-adiabatic transition, there also must be a strong coupling between the electronic spin and the orbital momentum to make the necessary spin-forbidden transition possible.[291] To this end, we calculated all spin-orbit couplings involved (SOC) for the dimer

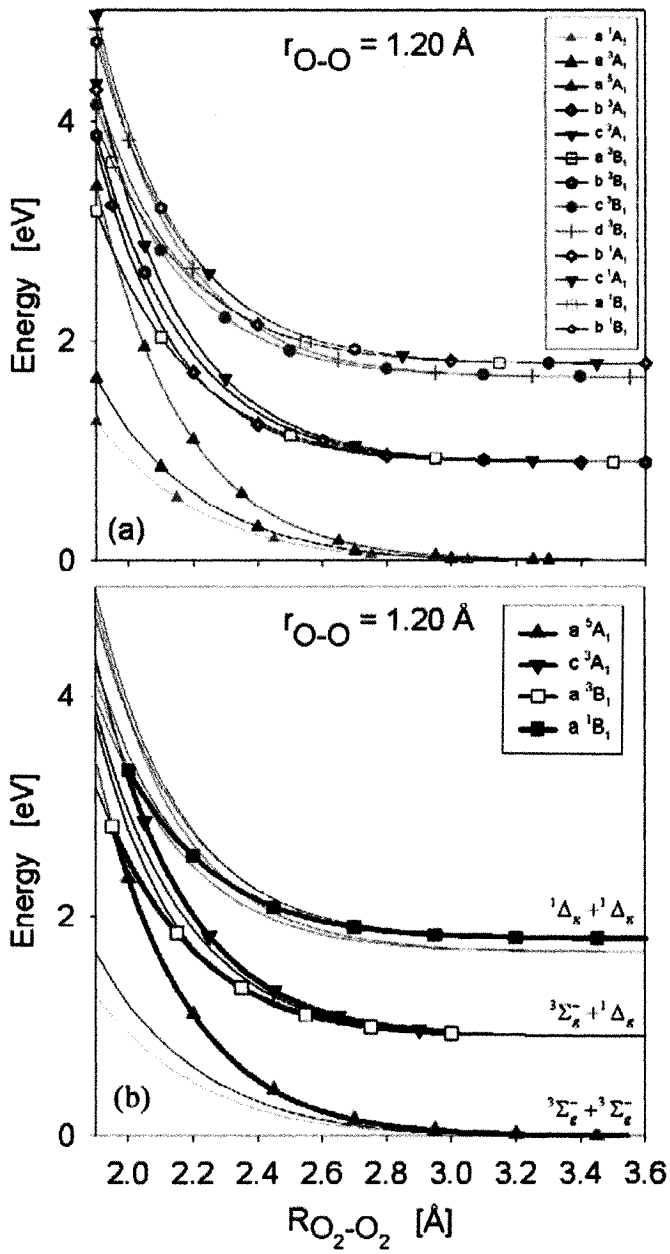

Fig. B3.3. $(O_2)_2$ potential energy surfaces as a function of the experimentally available intermolecular distance $R_{O_2-O_2}$ with both oxygen molecules kept at their equilibrium internuclear distance of 1.20A in a H configuration.

In Fig. B3.4, we show that the mechanical dimer compression actually leads to an increase of the spin-orbit coupling by almost three orders of magnitude within the experimentally available compression range. Consequently, the collision-induced formation of singlet oxygen molecules becomes possible via non-adiabatic transitions at the curve crossings shown in our ladder climbing scheme in Fig. B3.3, explaining the observed and highly efficient surface etching.[215]

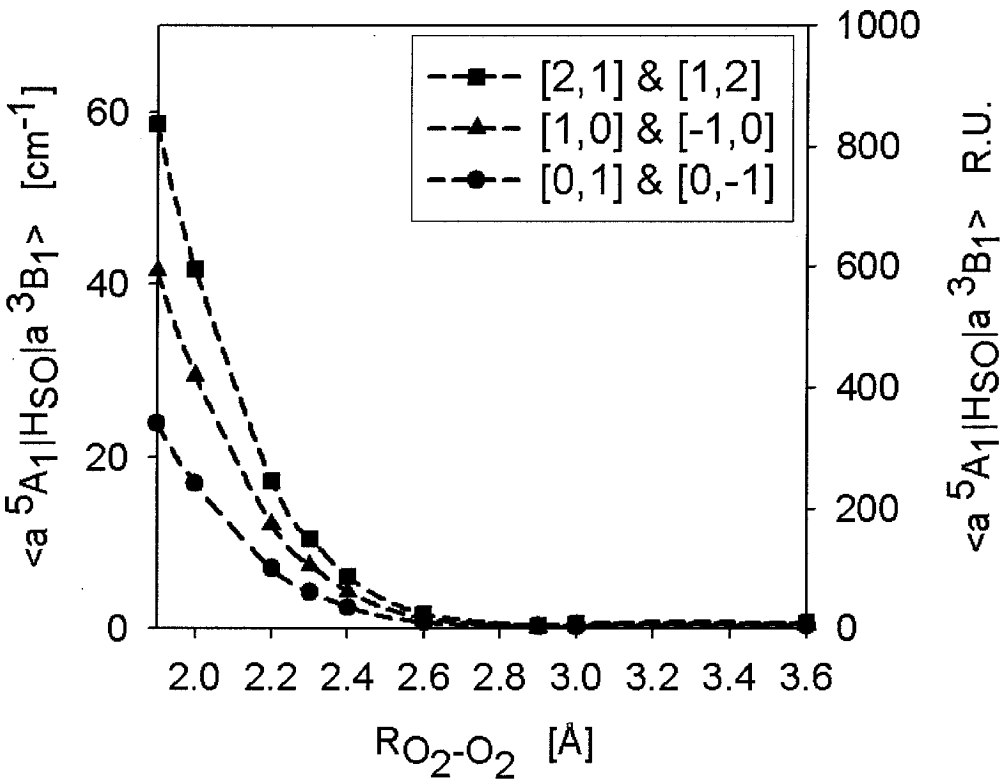

Fig. B3.4. Absolute and relative spin-orbit couplings for all contributing m_s state combinations as function of the intermolecular distance $R_{O_2\text{-}O_2}$ for the first spin-forbidden transition; for the c $^3A_1$ / a $^1B_1$ curve crossing (see Fig. B3.3), we also calculated a spin-orbit coupling of 29 cm^{-1} for both contributing m_s combinations.

The second phenomena that might be understood in the light of our non-adiabatic ladder climbing scheme concerns the existence of a mysterious "dark channel" that has been postulated for the enhanced vibrational relaxation of highly excited oxygen molecules during ozone photolysis in the stratosphere.[242] The underlying mechanism has caused considerable dispute between experimentalists and theoreticians.[292,293] While the potential importance of vibrational to electronic energy transfer has previously been suggested,[292,294] no precise mechanism has yet been proposed to explain how such an energy transfer becomes physically possible.

As above, we calculated the potential energy surfaces of the $(O_2)_2$ dimer in the H configuration. Now, however, we kept the intermolecular distance constant and only stretched one of the two oxygen molecules up to a distance that roughly corresponds to the outer turning point for an oxygen molecule in the *v=26* vibrational state. In Fig. B3.5, we demonstrate how large-amplitude molecular vibrations are exploited in the ladder climbing scheme to reach the potential energy surfaces resulting from the combination of a ground-state $O_2(^3\Sigma_g^-)$ molecule and an excited-state O_2 $(^1\Sigma_g^+)$ molecule. In contrast to the etching experiment, however, the spin-orbit couplings necessary to reach yet higher levels corresponding to both oxygen molecules being in a $^1\Delta_g$ state are negligible. Consequently, the O_2 molecules can not access any level higher than the d^3B_1 level which is in excellent agreement with the suggestion of the Wodtke group that the $b^1\Sigma_g^+$ state becomes efficiently populated as a result of vibrational relaxation. Inclusion of this triplet/singlet relaxation scheme in the non-equilibrium ozone formation mechanism of atmospheric models[292] might thus help reconcile observations and model predictions.

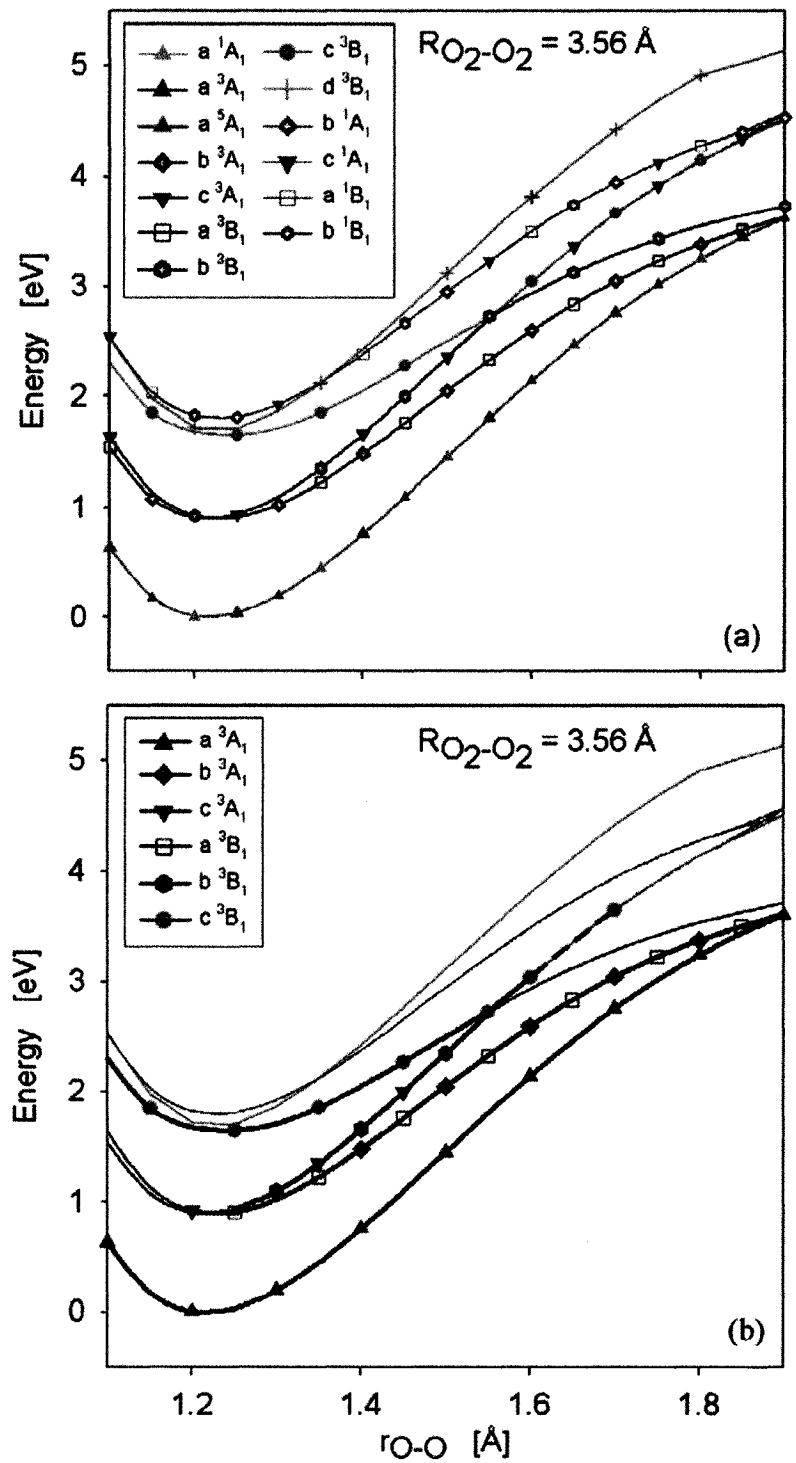

Fig. B3.5. $(O_2)_2$ potential energy surfaces for the *H* configuration dimer at its equilibrium intermolecular distance of 3.56 Å as a function of the internuclear distance $r_{o\text{-}o}$, only one oxygen molecule is stretched while the other one is kept at its equilibrium internuclear distance of 1.20 Å.

While all necessary transitions are both spin and symmetry allowed in the present case, the curve crossings necessary for vibrational relaxation can only be reached due to the large molecular amplitude of the vibrationally excited molecule confirming the experimental observation of enhanced vibrational relaxation above v = 25. As in a very recent experiment involving the interaction of highly vibrationally excited *NO* molecules with a metal surface,[277] it is again the large-amplitude molecular vibration that is responsible for the breakdown of the Born-Oppenheimer approximation and, thus, for the efficient vibrational relaxation in the ozone photolysis.

In conclusion, we showed that even relatively mild molecular collisions can lead to a breakdown of the Born-Oppenheimer approximation. As a result, the experimentally observed etching of silicon surfaces by molecular oxygen clusters becomes possible due to a non-adiabatic extension of the "chemistry with a hammer" dynamics which allows violation of quantum mechanical selection rules. Consequently, lower energy barrier reaction path-ways can be followed that would be forbidden without compression of the cluster molecules, explaining the efficient etching. Moreover, our proposed "non-adiabatic ladder climbing" mechanism may help elucidate a long-lasting controversy concerning a relaxation effect occurring during ozone photolysis in the stratosphere.

CHAPTER B4
Mechanically-Induced Generation of Highly Reactive Excited-State Oxygen Molecules in Clusters

B4.I. INTRODUCTION

The area of cluster collisions with solid surfaces has been the subject of intense research for over two decades,[213,227,243,245,248] motivated by the quest to better understand, for instance, the dynamics of cluster-surface interactions,[246] adsorption processes,[247] and cluster and surface-catalyzed reactions.[250,252] Cluster scattering provides a unique environment for promoting physical and chemical processes, as cluster impact on a rigid surface involves significant energy transfer in a very short time and within a localized surface area, and the resulting extreme conditions of pressure and temperature combined with extreme confinement, may catalyze chemical reactions that are not possible under normal conditions.[218,220,251,295] This concept, known as the "chemistry with a hammer",[221,280,296] may be a promising approach for making feasible multi-center reactions with large activation barriers.[248,251,252] For example, the mechanically-induced "burning of air" reaction[217] $N_2 + O_2 \longrightarrow 2NO$ was predicted theoretically more than a decade ago. However, no direct experimental evidence has been reported for this reaction to date, and a better understanding of the energy transfer mechanisms during cluster scattering may be required to predict optimal experimental conditions for such a reaction.

Another example of cluster-induced chemical reaction has been reported recently by Daineka *et al.*[215] who studied the impact of a supersonic $(O_2)_n$ ($n \approx 60 - 4000$) cluster beam on a clean silicon (100) surface. The resulting beam impact spot is composed of two distinct zones corresponding to active and passive oxidation.[215] Due to the relatively

high impact flux, the central part of the spot is subject to passive oxidation, leading to a protective oxide layer via a $Si + O_2 \rightarrow SiO_2$ crystallization reaction. The outskirts of the spot can be characterized by a circular groove with a steep inner and slightly sloping outer wall, which is formed as a result of surface etching via the $2Si + O_2 \rightarrow 2SiO$ reaction, because of the corresponding relatively weak $(O_2)_n$ flux. The abrupt increase of the etching rate at the inner wall of the groove marks the transition between the two oxidation mechanisms. Both processes could lead to direct applications in the nano-electronics industry, such as milling of nano-structures by controlled evaporation of SiO molecules, nano-writing on silicon surfaces by combining cluster-induced oxidation with laser-induced local heating, or more efficient procedures for designing ultrathin silicon oxide films, which are attractive targets for commercial metal-oxide semiconductor devices.[297] However, efficient design of industrial applications requires a detailed understanding of the reaction mechanism, which so far remains unclear.

In a previous theoretical study,[281] we investigated the possibility of molecular O_2 dissociation upon $(O_2)_2$ cluster collision, as a precursor step to surface oxidation. Since silicon oxidation by atomic oxygen is a barrierless reaction,[236,238,239] the generation of oxygen atoms upon cluster impact would have explained the observed highly efficient etching of the surface in a straightforward manner. However, our simulations of $(O_2)_n$ cluster surface scattering demonstrate that, under experimental conditions, O_2 molecules do not acquire enough energy to dissociate in the course of the scattering event, ruling out a cluster-catalyzed molecular dissociation mechanism.[281] Direct oxidation by ground-state O_2 is possible in principle, but the probability is too small to account for the observed experimental yields.[298] Therefore, we recently suggested an alternate pathway

to account for the experimental results, involving the generation of electronically-excited, singlet O_2 molecules upon cluster impact, based on preliminary quantum chemistry calculations of a $(O_2)_2$ cluster model.[298] Further evidence of electronic excitation in high energy $(O_2)_2$ complexes was also reported in another theoretical study, where a simple four-electron model was employed to understand the relative stability of the electronic states in $(O_2)_2$.[299]

Molecular O_2 has a ground-state $^3\Sigma_g^-$ configuration, which is rather unusual for a stable molecule, and two low-lying excited states, $^1\Delta_g$ and $^1\Sigma_g^+$, as illustrated in Fig. B4.1.[283] Both electronic transitions from the triplet ground state to the singlet excited states are strongly forbidden by selection rules,[284] and the $^1\Delta_g \leftrightarrow {}^3\Sigma_g^-$ transition has been described as "the most forbidden transition in nature".[300] Nonetheless, non-spin-conservative transitions may occur when two states are coupled by spin-orbit coupling (SOC), which is particularly strong in molecular oxygen between the $^3\Sigma_g^-$ and $^1\Sigma_g^+$ states.[301] Furthermore, it has been observed that, if the molecule is stretched such that the $^1\Sigma_g^+$ surface becomes sufficiently close in energy to the curve-crossing point between the $^3\Sigma_g^-$ and $^1\Delta_g$ surfaces, SOC arises between those latter states as a result of mixing with the $^1\Sigma_g^+$ state in the configuration interaction.[302]

Generation of electronically excited O_2 molecules upon surface impact in cluster collisions would account for silicon cluster oxidation. Indeed, as singlet O_2 is a well-known strong oxidant,[282,303] oxidation of the silicon surface would readily occur. In fact, early theoretical studies of $O_2 + Si_n$ reaction showed that the oxidation proceeds via an activation barrier one order of magnitude lower on the excited-state surface, compared to

that for the ground-state reaction.[237,304] While we defer the characterization of the detailed mechanism of the reaction of singlet O_2 with the silicon surface to a separate study, we focus in this chapter on the mechanistic aspects of mechanically-induced singlet oxygen generation. More specifically, we investigate the possibility of electronic transitions in $(O_2)_n$ clusters upon surface scattering by combining first-principle quantum chemistry calculations with molecular dynamics simulations.

Combination of several O_2 molecules removes the degeneracy of the partially filled $(1\pi_g)^2$ orbitals and leads to several electronic states with various multiplicities. The proper description of the $(O_2)_n$ cluster structure has long been a challenge for theoretical chemists,[305] and the $(O_2)_2$ dimer has been used as a prototype model to investigate O_2-O_2 intermolecular interactions.[290,302,306,307] The potential energy surfaces corresponding to the lowest electronic states of $(O_2)_2$ have been reported extensively,[306,307] but most attention has been paid to the lowest energy configurations. In cluster scattering experiments, electronic transitions may only occur at intersections between electronic states, which are only found in regions corresponding to significant geometrical distortion of the $(O_2)_2$ complex, and cluster geometries where electronic states intersect remain to be explored. Potential energy surface (PES) scans of the $(O_2)_2$ dimer are performed along selected internuclear and intermolecular coordinates to locate the position of possible curve-crossing points and calculate, if necessary, the associated SOC for all non spin-conservative transitions. In order to relate these quantum chemistry results to experiment,[215] i.e. to assess which regions of the PES are accessed by clustered molecules in the course of the scattering event, classical molecular dynamics simulations of $(O_2)_n$ cluster scattering on a rigid surface are performed under the experimental conditions.

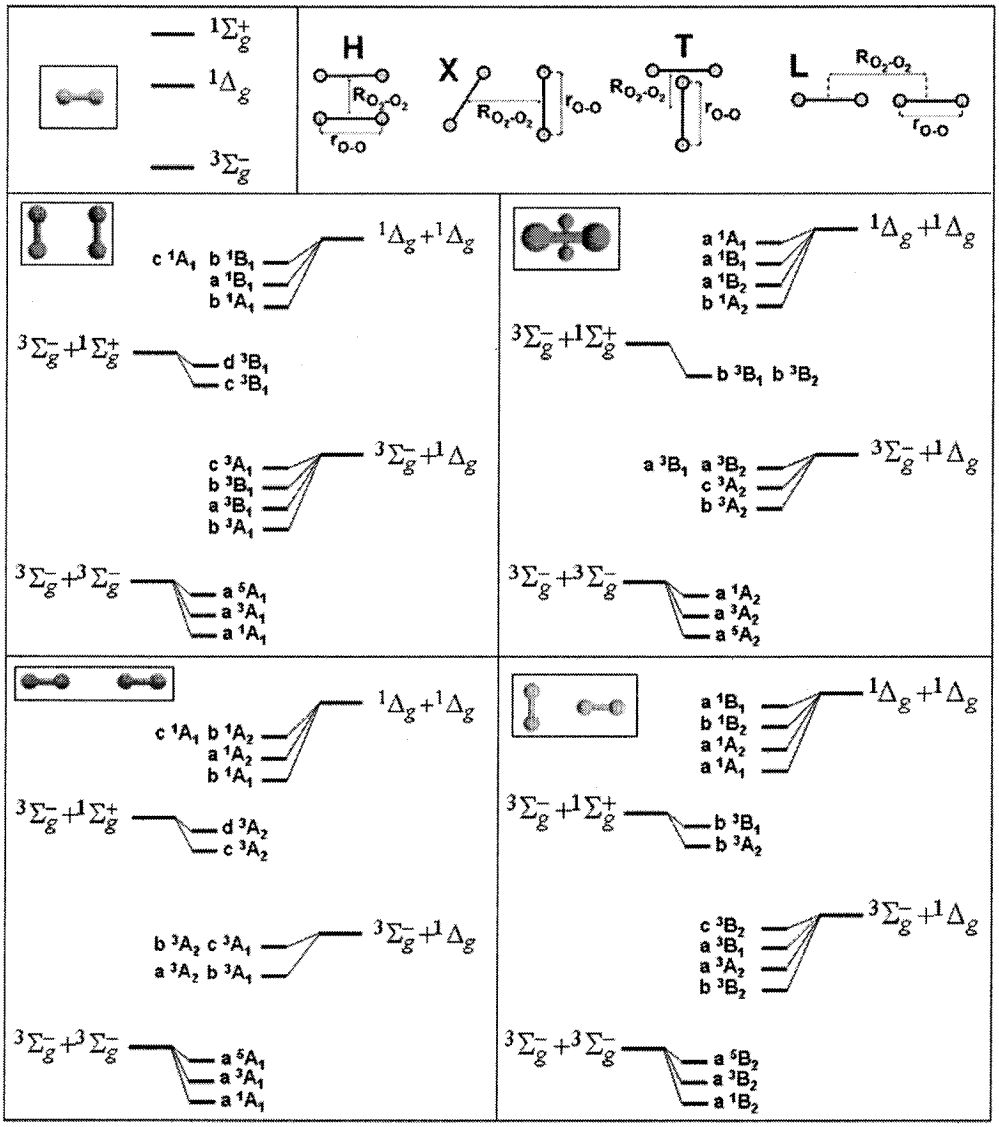

Fig. B4.1. Energy diagrams of O_2 and $(O_2)_2$ for the H, X, L, and T isomers. The electronic state ordering represents that of the most stable configuration.

The outline of this chapter is as follows. After a brief account of the computational procedure in Sec. B4.II, the results of our quantum chemistry calculations for model $(O_2)_2$ clusters are presented and discussed in Sec. B4.III. The possible implications of these results for the experimental problem are then discussed, in connection with the results from molecular dynamics simulations of $(O_2)_n$ cluster/surface collisions. Concluding remarks follow in Sec. B4.IV.

B4.II. METHODOLOGY

B4.II.A. Model Chemistry and Electronic States of O_2

Due to the complex electronic structure of the oxygen molecule, multiconfigurational methods are necessary for a proper description of its ground and excited states. The complete active space self-consistent field (CASSCF) method[285,308] has been used in this work, with an active space for the O_2 molecule that includes 8 electrons distributed in the full valence space of 6 orbitals [$3\sigma_g$, $1\pi_u$, $1\pi_g$, $3\sigma_u$]. For $(O_2)_2$, the active space chosen naturally consists of 16 electrons in the full valence space of 12 orbitals. The correlation-consistent augmented triple-zeta polarizable basis set (aug-cc-pVTZ) of Dunning is used to characterize the $(O_2)_2$ PES.[309] For a O_2 molecule at its equilibrium distance of 1.20 Å,[258] these calculations yield triplet-singlet energy gaps of 0.90 eV and 1.67 eV, respectively, which compare well with their experimental counterparts of 0.97 eV and 1.63 eV.[283] Furthermore, electronic structure calculations of $(O_2)_2$ with the CASPT2 method revealed curve-crossing points within 0.02 Å of the CASSCF counterparts, along with energies 10% lower, demonstrating the validity of the CASSCF method in the range of for the geometries investigated.

The transition probability between electronic states with different spin states depends on the spin-orbit coupling strength, defined as

$$SOC(\psi^1[M_s^1],\psi^2[M_s^2]) = \left\langle \psi^1(M_s^1) \mid H_{so} \mid \psi^2(M_s^2) \right\rangle \qquad \text{(B4.1)}$$

where $M_s \in Z^* \cap [-(2S+1), (2S+1)]$, S is the total spin of a given electronic state and H_{so} is the spin-orbit operator. In this work, the full Breit-Pauli spin-orbit operator[310] was used. Instead of the aug-cc-pVTZ basis set (46 basis functions for one oxygen atom) used in the PES scans, a 6-311G basis set[311] (26 basis functions) was employed for SOC

B4.II. METHODOLOGY

B4.II.A. Model Chemistry and Electronic States of O_2

Due to the complex electronic structure of the oxygen molecule, multiconfigurational methods are necessary for a proper description of its ground and excited states. The complete active space self-consistent field (CASSCF) method[285,308] has been used in this work, with an active space for the O_2 molecule that includes 8 electrons distributed in the full valence space of 6 orbitals [$3\sigma_g$, $1\pi_u$, $1\pi_g$, $3\sigma_u$]. For $(O_2)_2$, the active space chosen naturally consists of 16 electrons in the full valence space of 12 orbitals. The correlation-consistent augmented triple-zeta polarizable basis set (aug-cc-pVTZ) of Dunning is used to characterize the $(O_2)_2$ PES.[309] For a O_2 molecule at its equilibrium distance of 1.20 Å,[258] these calculations yield triplet-singlet energy gaps of 0.90 eV and 1.67 eV, respectively, which compare well with their experimental counterparts of 0.97 eV and 1.63 eV.[283] Furthermore, electronic structure calculations of $(O_2)_2$ with the CASPT2 method revealed curve-crossing points within 0.02 Å of the CASSCF counterparts, along with energies 10% lower, demonstrating the validity of the CASSCF method in the range of for the geometries investigated.

The transition probability between electronic states with different spin states depends on the spin-orbit coupling strength, defined as

$$SOC(\psi^1[M_s^1],\psi^2[M_s^2]) = \left\langle \psi^1(M_s^1) \mid H_{so} \mid \psi^2(M_s^2) \right\rangle \qquad \text{(B4.1)}$$

where $M_S \in Z^* \cap [-(2S+1), (2S+1)]$, S is the total spin of a given electronic state and H_{so} is the spin-orbit operator. In this work, the full Breit-Pauli spin-orbit operator[310] was used. Instead of the aug-cc-pVTZ basis set (46 basis functions for one oxygen atom) used in the PES scans, a 6-311G basis set[311] (26 basis functions) was employed for SOC

calculations in order to keep the computational cost of the calculations manageable. The use of a smaller basis set does not alter the quality of our results, as calculations of the O_2 SOC($^3\Sigma_g^-[0], ^1\Sigma_g^+[0]$) with the 6-311G, the 5s4p3d2f atomic natural orbital[312] and the aug-cc-pVTZ[309] basis sets yield very similar values of 169 cm^{-1}, 173 cm^{-1} and 168 cm^{-1}, respectively, which compare all equally well to the experimental estimate of 200 ±20 cm^{-1}.[292] All quantum chemistry calculations were performed with the MOLPRO suite of programs.[287]

B4.II.B. Molecular Dynamics Simulations

Since curve-crossing regions correspond to significantly distorted structures, as we shall see shortly, classical molecular dynamics simulations were performed to investigate the conditions required to access a given curve-crossing point for $(O_2)_n$ clusters impacting onto a rigid surface. As details of the simulation procedure have been presented elsewhere,[281] only the main features are outlined here. Morse and Lennard-Jones potentials are employed to describe intramolecular and intermolecular interactions in $(O_2)_n$ clusters, respectively. Clusters up to size n = 1024 were first thermalized at a temperature of 32 K, and then directed toward the surface with an incident center-of-mass velocity of 1200 $m.s^{-1}$, which correspond to the initial cluster temperature and incident velocity employed in experiment. A rigid surface model, including surface-to-cluster energy transfer was employed,[281] along with surface temperatures up to 1500 K representative of that in the experiment.[265] Cluster structural properties and monomer internal energy distributions are investigated in the course of cluster collision for various cluster sizes and surface temperatures,[313] A detailed analysis of these properties may assess whether the curve-crossing regions characterized by model $(O_2)_2$ quantum

chemistry calculations are accessible under experimental conditions and whether the electronic transitions are energetically possible.

B4.III. RESULTS AND DISCUSSION

B4.III.A. Ab initio Investigation of $(O_2)_2$

Dimer formation implies changes of orbital and spin symmetries, depending on the symmetry of the complex formed. The dimer structures chosen correspond to the four known stable isomers of $(O_2)_2$,[307] shown in Fig. B4.1, and typically referred to as H, X, L and T structures. The electronic structure of the 4 isomers is reported in Fig. B4.1 along with the asymptotic limit they correlate to.[307] We have focused on the 13 first electronic states of $(O_2)_2$, which dissociate into $({}^3\Sigma_g^- + {}^3\Sigma_g^-)$, $({}^3\Sigma_g^- + {}^1\Delta_g)$, $({}^3\Sigma_g^- + {}^1\Sigma_g^+)$ and $({}^1\Delta_g + {}^1\Delta_g)$ pairs of O_2 molecules. Three distinct potential energy surfaces arise from the $({}^3\Sigma_g^- + {}^3\Sigma_g^-)$ pair, corresponding to singlet, triplet and quintet states.[314] Similarly, the $({}^3\Sigma_g^- + {}^1\Delta_g)$ and $({}^3\Sigma_g^- + {}^1\Sigma_g^+)$ pairs are the asymptotic limits of four and two triplet states, respectively, while the association of two O_2 ${}^1\Delta_g$ molecules results in four singlet states.

B4.III.A.1. Angular PES scans

Interconversion between the different planar isomers (i.e. T, H, and L configurations) can be performed by rotations along the angles θ_1 and θ_2, defined in Fig. B4.2. An angular PES scans were performed with C_s point group symmetry constraint, with one molecule kept at its equilibrium distance of 1.20 Å and the other monomer at $r_{O\text{-}O} = 1.40$ Å.

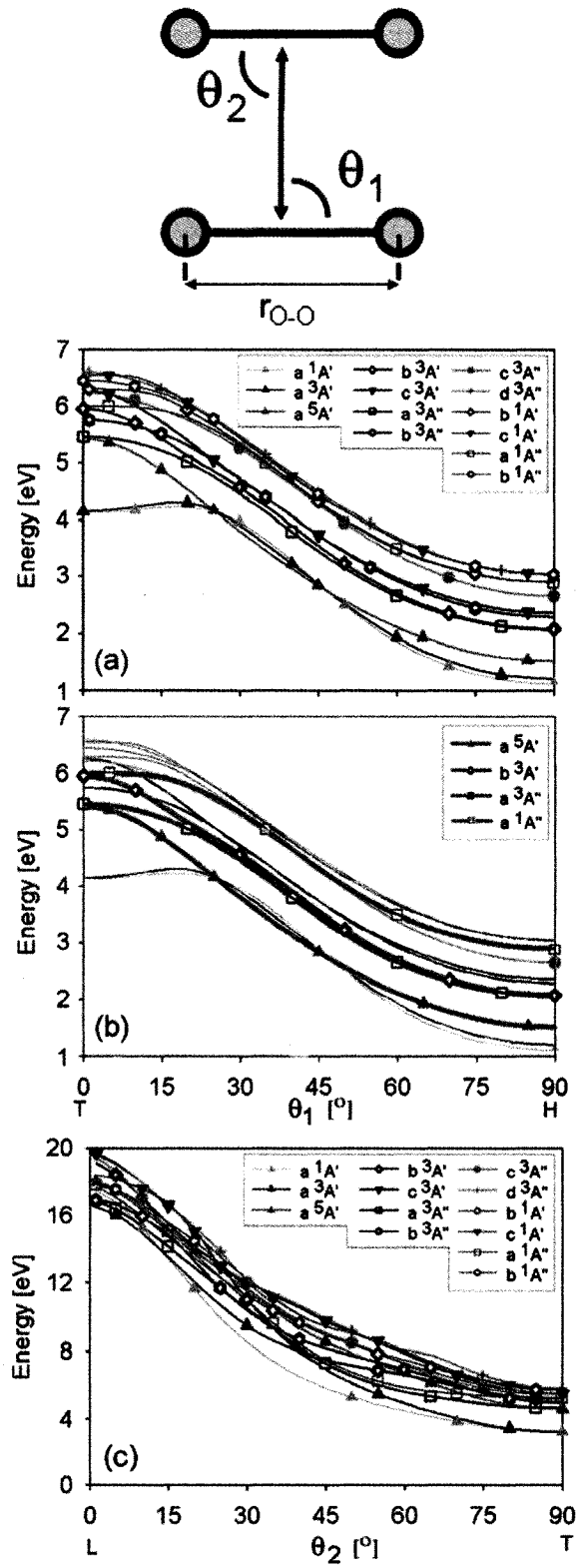

Fig. B4.2. Potential energy surfaces along the θ_1 and θ_2 angles of $(O_2)_2$. $r_{O\text{-}O}$ = 1.4 Å, $R_{O_2\text{-}O_2}$ = 2.30 Å. (a) and (b) $\theta_2 = 90^\circ$, (c) $\theta_1 = 0^\circ$.

As we shall see later, the latter distance corresponds to the maximum interatomic distance reached in molecular dynamics simulations of $(O_2)_n$ cluster surface scattering, and employing a stretched molecule may allow an assessment of the effect of vibrational excitation. An intermolecular distance $R_{O_2-O_2}$ = 2.30 Å is chosen, also following the results of molecular dynamics simulations of $(O_2)_n$ cluster scattering on a rigid surface, since 25 % of the O_2 molecules were found to access such an intermolecular separation at T_s = 1500 K, as shown on Fig. B4.3.

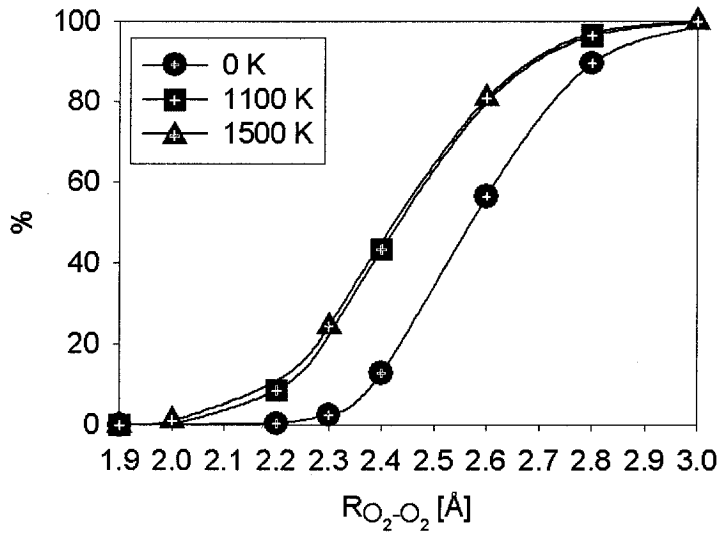

Fig. B4.3. Fraction of $(O_2)_2$ dimers with intermolecular distances lower than R_{O2-O2} obtained from molecular dynamics simulations of $(O_2)_n$ cluster surface scattering.

In Fig. B4.2 are shown PES scans characterizing the transition between the H and T isomers (cf. Fig. B4.2a), obtained with $\theta_2 = 90^\circ$ and $\theta_1 \in [0^\circ, 90^\circ]$, followed by interconversion between the T and L structures, with $\theta_1 = 0^\circ$ and $\theta_2 \in [0^\circ, 90^\circ]$ (cf. Fig. B4.2b). Comparison of the ground-state energies of the four compressed isomers reveals that the H configuration corresponds to the lowest energies, which is not too surprising, since the H configuration is the global minimum of the $(O_2)_2$ complex (r_{O-O} = 1.2 Å,

$R_{O_2-O_2}$ = 3.56 Å).[307] Upon rotation of a molecule around the θ_1 angle by 90°, the ground-state energy is increased by about 3 eV, as the dimer reaches the T configuration. The C_s point group was used for all angular PES scans. A striking feature in Fig. B4.2 is the presence of multiple curve-crossing intersections between electronic states, implying that transition may occur upon rotational motion, i.e. isomer interconversion may be accompanied by electronic transitions in such compressed conditions. Furthermore, the dimer may undergo several consecutive electronic transitions upon relative rotation, climbing from one state to another as different curve-crossing points are accessed. For instance, starting in the H configuration in the a^5A' state, the a^5A' and a^3A'' states cross in the T configuration. In Table B4.1 are reported major SOC coupling for the four isomers, which shows that the SOC between the a^5A' and a^3A'' (a^5B_2 and a^3B_1 in the C_{2v} point group notation) states is relatively strong, and e.g. SOC($a^5A'[1]$, $a^3A''[1]$) = SOC($a^5A'[-1]$, $a^3A''[-1]$) = 49.2 cm^{-1}, and SOC($a^5A'[0]$, $a^3A''[0]$) = 56.8 cm^{-1} suggest that transitions between these states are quite possible. The O_2 molecule can further rotate by an extra 90° down the a^3A'' state, which intersects the b^3A' state back in the H configuration; the transition associated with this curve-crossing is allowed by both spin and orbital selection rules. Upon further rotation of the O_2 molecule, the b^3A' state crosses the a^1A'' state (b^3B_2 and a^1B_1 states in C_{2v}) in T configuration, at a point characterized by SOC($a^1B_1[0]$, $b^3B_2[0]$) = 56.6 cm^{-1}. Upon another 90° rotation of the angle θ_1, the a^1A'' state crosses the b^1A' state in the H configuration and again the transition is allowed by all selection rules. Therefore, a $(O_2)_2$ dimer in the ground-state can access the highest electronic state included in our calculations via 3 molecular rotations.

Table B4.1. Major Spin-Orbit Couplings for $(O_2)_2$ X, H, T and L geometries.[a]

X		comp.[b]		eq.[c]		sep.[d]
		SOC	EF[e]	SOC	EF[e]	SOC
		$(^3\Sigma^-_g+^3\Sigma^-_g) \rightarrow (^3\Sigma^-_g+^1\Sigma^+_g)$ or $(^3\Sigma^-_g+^1\Delta_g)$				
a $^5A_2$ [2,-2]	b $^3B_1$ [1,-1]	120.7	1.0	120.9	1.0	121.1
a $^5A_2$ [2,-2]	b $^3B_2$ [1,-1]	115.9	1.0	120.9	1.0	121.1
a $^5A_2$ [1,-1]	b $^3B_1$ [0,0]	85.4	1.0	85.5	1.0	85.6
a $^5A_2$ [1,-1]	b $^3B_2$ [0,0]	81.9	1.0	85.5	1.0	85.6
a $^5A_2$ [0,0]	b $^3B_1$ [-1,1]	49.3	1.0	49.4	1.0	49.42
a $^5A_2$ [0,0]	b $^3B_2$ [-1,1]	47.3	1.0	49.4	1.0	49.42
		$(^3\Sigma^-_g+^1\Delta_g) \rightarrow (^1\Delta_g+^1\Delta_g)$				
b $^1A_2$ [0,0]	b $^3B_1$ [-1,1]	69.7	0.8	69.8	0.8	85.5
b $^1A_2$ [0,0]	b $^3B_2$ [-1,1]	66.9	0.8	69.8	0.8	85.7
		$(^3\Sigma^-_g+^1\Sigma^+_g) \rightarrow (^1\Delta_g+^1\Delta_g)$				
a $^1A_1$ [0,0]	a $^3B_1$ [-1,1]	115.6	1.7	85.3	1.2	69.9
a $^1A_1$ [0,0]	a $^3B_2$ [-1,1]	6.6	0.1	85.7	1.2	69.9

H		comp.[b]		eq.[c]		sep.[d]
		SOC	EF[e]	SOC	EF[e]	SOC
		$(^3\Sigma^-_g+^3\Sigma^-_g) \rightarrow (^3\Sigma^-_g+^1\Sigma^+_g)$ or $(^3\Sigma^-_g+^1\Delta_g)$				
a $^5A_1$ [2],-2	a $^3B_1$ [1,-1]	16.9	$4.\ 10^2$	0.7	17.5	0.0
a $^5A_1$ [2,-2]	c $^3B_1$ [1,-1]	131.7	2.0	171.2	2.6	66.3
a $^5A_1$ [2,-2]	d $^3B_1$ [1,-1]	99.9	0.8	0.8	0.0	121.0
a $^5A_1$ [1,-1]	a $^3B_1$ [0,0]	11.9	$4.\ 10^2$	0.5	16.7	0.0
a $^5A_1$ [1,-1]	c $^3B_1$ [0,0]	93.1	2.0	121.1	2.6	46.9
a $^5A_1$ [1,-1]	d $^3B_1$ [2,-2]	70.6	0.8	0.6	0.0	85.6
a $^5A_1$ [0,0]	c $^3B_1$ [-1,1]	53.8	2.0	69.9	2.6	27.1
a $^5A_1$ [0,0]	d $^3B_1$ [-1,1]	44.8	0.9	0.3	0.0	49.4
		$(^3\Sigma^-_g+^1\Delta_g) \rightarrow (^1\Delta_g+^1\Delta_g)$				
b $^1A_1$ [0,0]	b $^3B_1$ [-1,1]	11.3	$2.\ 10^2$	0.2	3.0	0.06
b $^1B_1$ [0,0]	b $^3B_1$ [-1,1]	14.1	$3.\ 10^2$	0.2	3.0	0.05
		$(^3\Sigma^-_g+^1\Sigma^+_g) \rightarrow (^1\Delta_g+^1\Delta_g)$				
b $^1A_1$ [0,0]	c $^3B_1$ [-1,1]	11.9	10^2	0.5	4.8	0.1

a. Spin orbit coupling matrix elements in cm^{-1}. In our notation, $A[M_s^1,M_s^2]$ coupling with $B[M_s^3,M_s^4]$ denotes SOC($A[M_s^1]$, $B[M_s^3]$) and SOC ($A[M_s^2, M_s^4]$). SOC terms < 10 cm^{-1} are not reported.

b. Compressed structures are defined by $R_{O_2-O_2}$ = 2.30 Å, and r_{O-O} = 1.4 Å.

c. Equilibrium structures are defined by r_{O-O} = 1.2 Å, and $R_{O_2-O_2}$ = 3.60 Å, 3.56 Å, 4.26 Å, and 3.74 Å for X, H, L and T geometries, respectively.[307]

d. Separated monomers, with r_{O-O} = 1.2 Å,, and $R_{O_2-O_2}$ = 5.7 Å (see text).

T		comp.[b]		eq.[c]		sep.[d]
		SOC	EF[e]	SOC	EF[e]	SOC
$(^3\Sigma^-_g+^3\Sigma^-_g) \rightarrow (^3\Sigma^-_g+^1\Sigma^+_g)$ or $(^3\Sigma^-_g+^1\Delta_g)$						
a^5B_2 [1,-1]	a^3B_1 [1,-1]	49.2	10^3	0.6	15.0	0.0
a^5B_2 [0]	a^3B_1 [0]	56.8	10^3	0.7	14.0	0.1
$(^3\Sigma^-_g+^1\Delta_g) \rightarrow (^1\Delta_g+^1\Delta_g)$						
a^1A_2 [0,0]	b^3B_2 [-1;1]	24.1	$3.\ 10^2$	0.7	7.8	0.1
a^1A_2 [0,0]	c^3B_2 [-1;1]	25.4	$2.\ 10^2$	0.8	6.2	0.1
a^1A_1 [0]	a^3A_2 [0]	41.0	$7.\ 10^2$	0.8	13.3	0.1
a^1A_1 [0,0]	a^3B_1 [-1;1]	13.8	10^2	1.0	7.1	0.1
a^1B_1 [0]	b^3B_2[0]	56.6	10^5	0.6	10^3	0.0
$(^3\Sigma^-_g+^1\Sigma^+_g) \rightarrow (^1\Delta_g+^1\Delta_g)$						
b^1B_2 [0,0]	b^3A_2 [-1;1]	17.9	$4.\ 10^4$	0.1	$2.\ 10^2$	0.0
b^1B_2 [0]	b^3B_1 [0]	19.4	10^5	0.1	$6.\ 10^2$	0.0
a^1A_1 [0]	b^3A_2 [0]	41.6	$2.\ 10^4$	0.6	30.0	0.0
a^1A_1 [0,0]	b^3B_1 [-1;1]	51.9	$5.\ 10^4$	0.4	40.0	0.0

L		comp.[b]		eq.[c]		sep.[d]
		SOC	EF[e]	SOC	EF[e]	SOC
$(^3\Sigma^-_g+^3\Sigma^-_g) \rightarrow (^3\Sigma^-_g+^1\Sigma^+_g)$ or $(^3\Sigma^-_g+^1\Delta_g)$						
a^5A_1 [1,-1]	c^3A_2 [1,-1]	19.7	0.1	0.1	0.0	170.7
a^5A_1 [1,-1]	d^3A_2 [1,-1]	0.0	0.0	171.2	1.4	122.4
a^5A_1 [0]	c^3A_2 [0]	22.7	0.1	0.1	0.0	197.1
a^5A_1 [0]	d^3A_2 [0]	0.0	0.0	197.7	1.4	141.3
a^3A_1 [0]	b^1A_2 [0]	17.0	$2.\ 10^8$	0.0	10^5	0.0
a^1A_1 [0]	a^3A_2 [0]	67.9	$2.\ 10^4$	0.0	1.0	0.0
a^1A_1 [0]	c^3A_2 [0]	11.1	0.1	139.7	1.0	139.5
$(^3\Sigma^-_g+^1\Delta_g) \rightarrow (^1\Delta_g+^1\Delta_g)$						
b^1A_1[0]	b^3A_2 [0]	23.8	$6.\ 10^3$	0.0	2.3	0.0
c^1A_1 [0]	a^3A_2 [0]	183.1	$6.\ 10^5$	0.0	31.0	0.0
a^1A_2[0]	b^3A_1 [0]	23.8	$6.\ 10^3$	0.0	1.8	0.0
$(^3\Sigma^-_g+^1\Sigma^+_g) \rightarrow (^1\Delta_g+^1\Delta_g)$						
c^1A_1 [0]	d^3A_2 [0]	32.6	$7.\ 10^3$	0.0	2.2	0.0

e. Enhancement Factor (EF), defined as the relative amplitude of the SOC at a given geometry with that calculated for separated monomers, which allows evaluation of the catalytic effect associated to cluster *compression*.

The large number of curve-crossing points suggests the existence of multiple excitation pathways. For instance, excitation may also occur from b^1A'' to c^3A' (a^1A_2 with c^3B_2 in

C_{2v}), since the SOC($b^1A''[0]$, $c^3A'[-1]$) and SOC($b^1A''[0]$, $c^3A'[1]$) strengths are 25.4 cm^{-1} at the curve-crossing.

Starting from the T configuration ($\theta_1=0^o$, $\theta_2=90^o$), the $(O_2)_2$ dimer converts into the L isomer upon rotation around the angle θ_2. For rotation around the angle θ_2, electronic states intersect even more, allowing rapid access to upper states. However, as can be seen in Fig. B4.2c, an energy of ~12 eV is necessary to convert into the compressed L configuration, which is thus highly unstable. Moreover, the energies associated with the compressed L configuration are found to be 16-20 eV above the energy of separated monomers, considerably exceeding the O_2 molecular binding energy of 5.2 eV,[258] and molecular dissociation may occur before the system can reach the compressed L geometry. Therefore, only the rotational interconversion between the H and T configurations may effectively lead to formation of electronically excited O_2 molecules (see Figs. B4.2a and B4.2b).

B4.III.A.2. Intermolecular Distance PES scans

Further insight into the distortion of the electronic structure of $(O_2)_n$ upon cluster scattering may be accessed by cluster compression. Accordingly, intermolecular distance PES scans have been performed in the C_{2v} point group representation, with intermolecular distances varying from 1.9 Å to 3.6 Å, which corresponds to the range observed in collision events, as shown in Fig. B4.3. Results from the PES scans of the X, H, T and L configurations are reported in Figs. B4.4, B4.5, B4.6 and B4.7, respectively. PES scans were performed with both molecules kept rigid at their equilibrium geometry, i.e. $r_{O\text{-}O}$ = 1.2 Å and at a distance of $r_{O\text{-}O}$ = 1.4 Å to explore the influence of vibrational excitation.

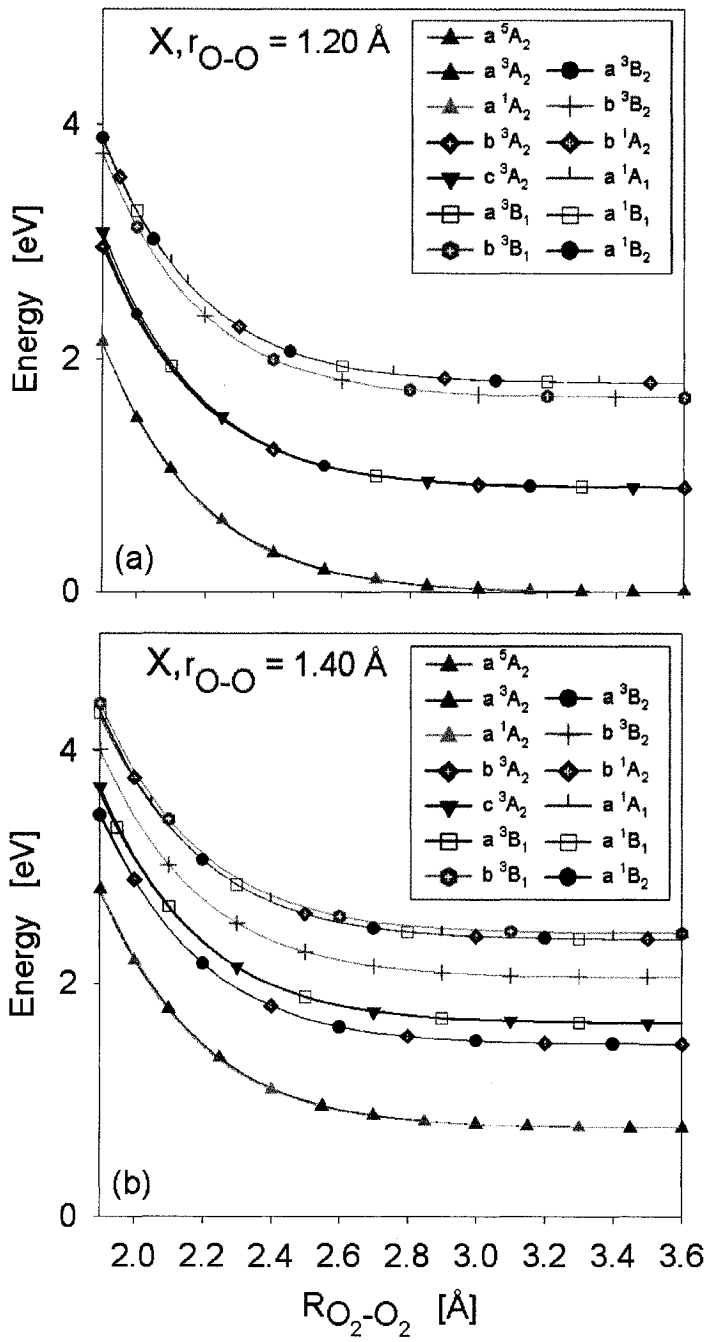

Fig. B4.4. Intermolecular potential energy surface scans for $(O_2)_2$ in the X geometry with CASSCF(16,12)/aug-cc-pVTZ. The energy reference corresponds to two ground state monomers separated by an infinite distance.

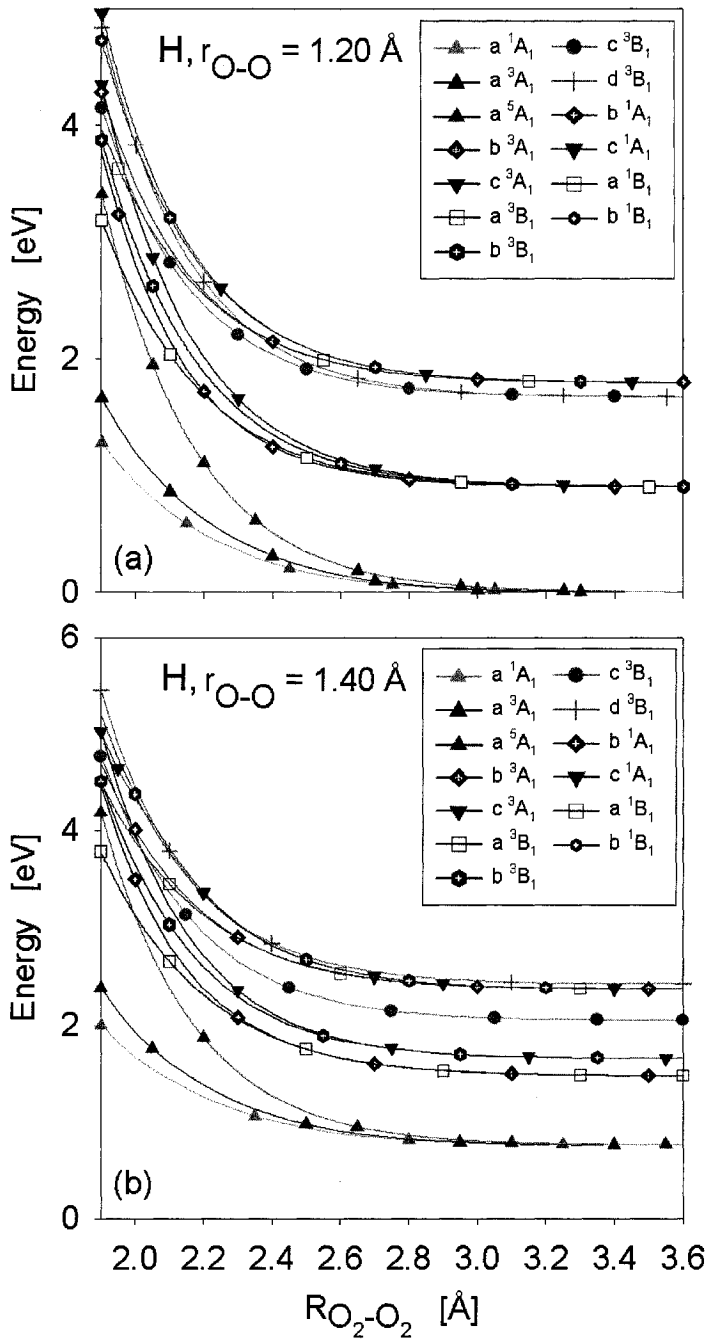

Fig. B4.5. Intermolecular potential energy surface scans for $(O_2)_2$ in the H geometry with CASSCF(16,12)/aug-cc-pVTZ. The energy reference corresponds to two ground state monomers separated by an infinite distance.

A comparison of all PES reveals rather different behaviors upon compression of the four isomers. In Fig. B4.4, the PES of the X isomer does not exhibit any curve crossing upon

compression in the range of intermolecular distances investigated. Further compression, however, will likely result in curve crossing between the a^5A_2, a^3A_2 and a^3A_2 states correlating with the $(^3\Sigma_g^- + ^3\Sigma_g^-)$ asymptotic pair and higher electronic states since their energy gaps clearly decrease at the smallest intermolecular separations investigated. Furthermore, vibrational excitation of one molecule results in only marginal differences in the relative positions of the electronic states upon compression, as can be seen from a comparison of Figs. B4.4a and B4.4b.

PES scans along the $R_{O_2-O_2}$ intermolecular distance for the H configuration are displayed in Fig. B4.5. Whereas the PES of the H structure with both molecules at their equilibrium geometry (Fig. B4.5a) has already been reported,[298] it is shown here for comparison with those of the other three configurations. The energy gaps between the electronic states exhibit a clear dependence on cluster compression, and the a^5A_1 state intersects the a^3B_1 state at $R_{O_2-O_2}$ = 1.95 Å. When one O_2 molecule is stretched to r_{O-O} = 1.40 Å (see Fig. B4.5b), the same curve-crossing point occurs at a larger $R_{O_2-O_2}$ distance of 2.0 Å, suggesting that vibrational excitation of O_2 enhances the non-adabiatic transition probability as it provides a fraction of the energy required to reach the curve-crossing point. A a^5A_1 to a^3B_1 transition may then occur due to spin-orbit coupling, since SOC(a^5A_1[2], a^3B_1[1]) = SOC(a^5A_1[-2], a^3B_1[-1]) = 50.0 cm^{-1}, SOC(a^5A_1[1], a^3B_1[0]) = SOC(a^5A_1[-1], a^3B_1[0]) = 29.0 cm^{-1}, and SOC(a^5A_1[0], a^3B_1[1]) = SOC(a^5A_1[0], a^3B_1[-1]) = 20.4 cm^{-1} (with r_{O-O} = 1.2Å) are significant. Subsequent transition to the b^3B_1 state may then occur, as the a^3B_1 to b^3B_1 transition is allowed by selection rules. Finally, transition to the b^1A_1 state is possible at the b^3B_1 to b^1A_1 crossing, given the magnitude of spin-orbit coupling, as SOC(b^3B_1[0], b^1A_1[-1]) = SOC(b^3B_1[0], b^1A_1[1]) = 11.3 cm^{-1}, (cf. Table

B4.1). Since the b^1A_1 state correlates asymptotically with the $(^1\Delta_g + ^1\Delta_g)$ pair of O_2 molecules, these results suggest possible $^1\Delta_g$ O_2 generation through various possible pathways arising from the many curve-crossing points. Clearly, the perturbation of the electronic structure upon compression is more pronounced in the H configuration than in the X one, a finding that is tentatively attributed to the closer proximity of the monomer atoms in the compressed H isomer than in the X isomer for the same intermolecular distance.

We now turn our attention to the compressed T configuration (cf. Fig. B4.6). The perturbation of the electronic states upon cluster compression is even more drastic than in the H configuration, which is not too surprising since the relative orientation of the molecules is such that compression of the T cluster brings a monomer atom very close to the center of mass of the other monomer, resulting in strong perturbation of the dimer electronic structure. For the H configuration, inspection of Fig. B4.6b reveals that vibrational excitation makes the curve-crossing region more easily accessible, shifting it to larger intermolecular distances, as the a^5B_2 and a^3B_1 states intersect at $R_{O_2-O_2} = 2.20$ Å when $r_{O-O} = 1.20$ Å, but at $R_{O_2-O_2} = 2.30$ Å when $r_{O-O} = 1.40$ Å. These states are strongly spin-orbit coupled, with values of SOC($a^5B_2[-1]$, $a^3B_1[-1]$) = SOC($a^5B_2[1]$, $a^3B_1[1]$) = 49.2 cm^{-1}, and SOC($a^5B_2[0]$, $a^3B_1[0]$) = 49.2 cm^{-1} when $r_{O-O} = 1.40$ Å (cf. Table B4.1). Again, a cascade of successive excitations is possible up to the singlet a^1A_1 state, which correlates to the $(^1\Delta_g + ^1\Delta_g)$ pair of O_2 molecules, starting with a a^3B_1 to a^3A_2 state transition, followed by transition to the a^1A_1 state at the curve crossing point at 2.10 Å, with SOC($a^1A_1[0]$, $a^3A_2[0]$) = 41.0 cm^{-1}.

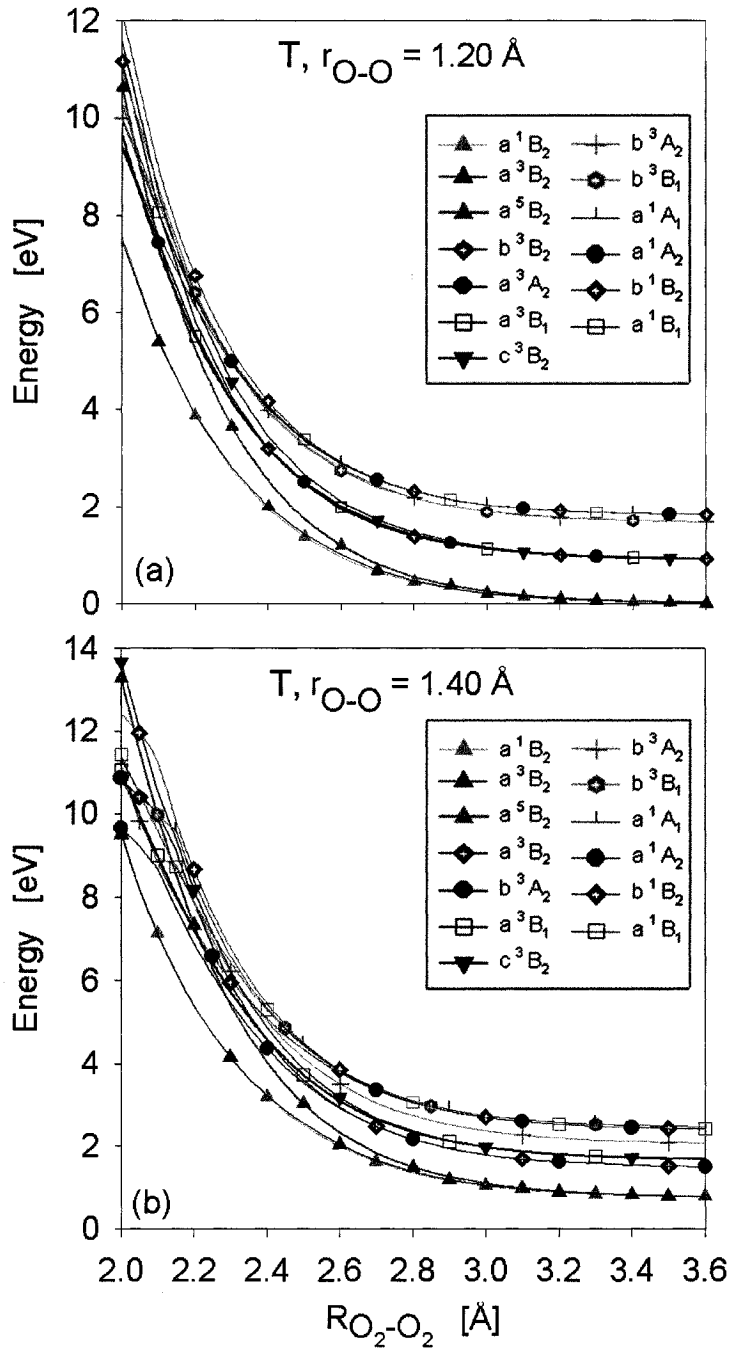

Fig. B4.6. Intermolecular potential energy surface scans for $(O_2)_2$ in the T geometry with CASSCF(16,12)/aug-cc-pVTZ. The energy reference corresponds to two ground state monomers separated by an infinite distance.

However, much more energy is required for the T isomer to reach the curve-crossing points than for the H isomer, since compression to an intermolecular distance of 2.1 Å results in energies of ~9 eV for the T isomers, compared to 5 eV for the H configuration.

The L configuration is the isomer exhibiting the strongest dependence of the electronic structure on compression (cf. Fig. B4.7). The energies of the highest states included in our calculations reach up to 30 eV when molecules are brought within 2.20 Å of each other. Such a strong dependence may not be surprising, since at intermolecular distances smaller than 2.4 Å, two atoms from different "monomers" reach distances smaller than the equilibrium molecular distance in molecular oxygen and the electronic structure of the compressed dimer is strongly perturbed. As a result, the curve-crossing region is accessible upon only a small compression. For instance, the a^5A_1 to c^3A_2 curve crossing (with SOC(a^5A_1[1], c^3A_2[1]) = SOC(a^5A_1[-1], c^3A_2[-1]) = 7.3 cm^{-1}, and SOC(a^5A_1[0], c^3A_2[0]) = 8.4 cm^{-1}) occurs at $R_{O_2-O_2}$ = 2.75 Å and 2.80 Å for r_{O-O} = 1.2 Å and r_{O-O} = 1.4 Å, respectively (cf. Fig. B4.7). In the curve-crossing region, many electronic states intersect each other, and many excitation pathways may lead to a state correlating with the $(^1\Delta_g + ^1\Delta_g)$ pair of O_2 molecules, as all possible transitions are favored by strong spin-orbit couplings (cf. Table B4.1). Interestingly, inflexion points are observed for several singlet and triplet excited states, in the neighborhood of $R_{O_2-O_2}$ = 2.50 Å, an observation which may again be connected to the fact that at such a distance, atoms from two distinct "monomers" are found at a $R_{O_2-O_2}$ distance smaller than the intramonomer interatomic distance, thus rendering the definition of monomers ambiguous. Another interesting feature is the presence of curve-crossings between the a^3A_1 state, which correlates to the asymptotic $(^3\Sigma_g^- + ^3\Sigma_g^-)$ pair, and the triplet states correlating to the $(^3\Sigma_g^- + ^1\Delta_g)$ pair at about 2.4 Å, and transitions are expected to occur easily at this point since they are allowed by all selection rules.

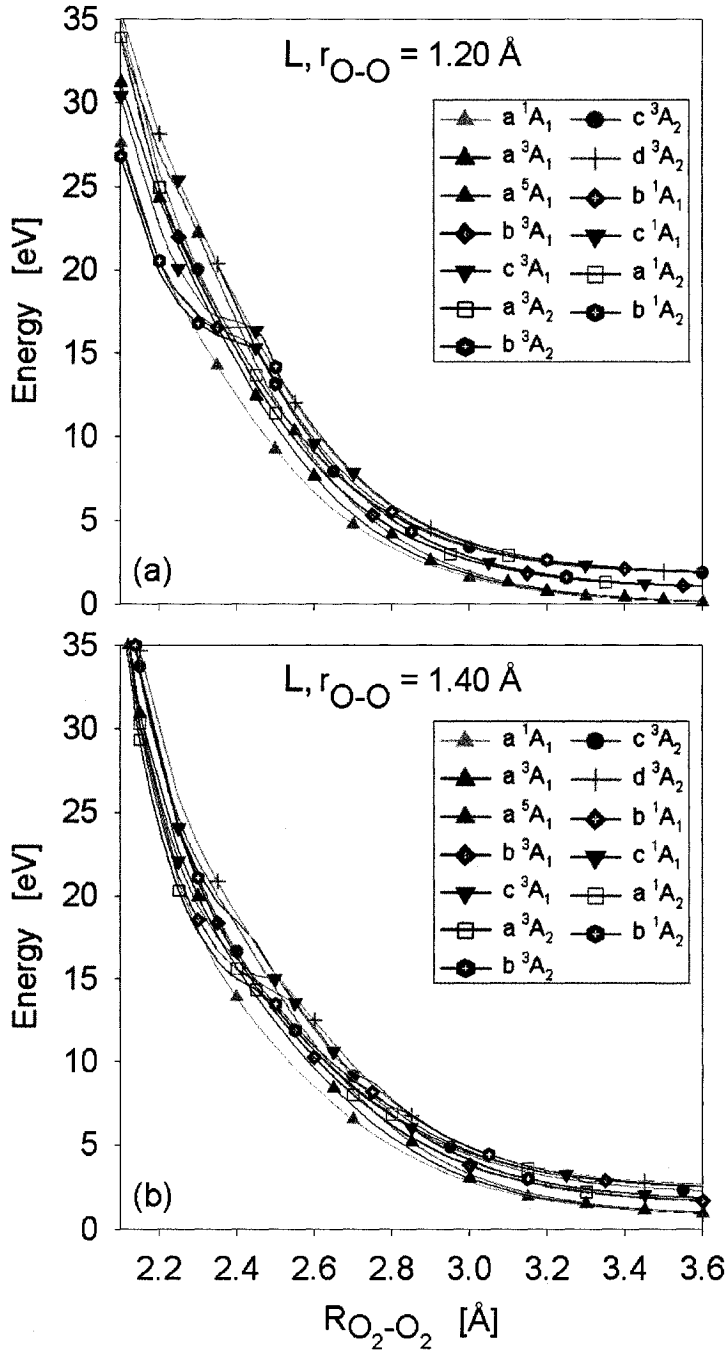

Fig. B4.7. Intermolecular potential energy surface scans for $(O_2)_2$ in the L geometry with CASSCF(16,12)/aug-cc-pVTZ. The energy reference corresponds to two ground state monomers separated by an infinite distance.

B4.III.A.3. Other Possible Pathways for Non-adiabatic Transitions

Compression and vibrational excitation of O_2 molecules lower the symmetry, perturb the electronic state ordering, and induce significant changes of total orbital and spin angular momenta, leading to the weakening of selection rules which normally prevent the $^3\Sigma_g^- \longrightarrow {}^1\Delta_g$ transition.[300] Indeed the major SOCs presented in Table B4.1 for the four isomers reveal increased SOCs compared to that in separated monomers. Transitions between electronic states are associated with each non-zero SOC matrix element. It was suggested that transitions should occur through a reaction path with optimum SOC,[315] and in clusters, such a pathway may imply geometric rearrangement over several internal coordinates between each electronic transition. However, in cluster collisions, the chaotic nature of the collisions rather suggests that a distribution of pathways will be obtained. For instance, the a^5A_1 and c^3B_1 states of the H configuration display 6 non-zero SOC terms, as seen from Table B4.1, and each of these non-zero SOC matrix element contributes to the total transition probability between the a^5A_1 and c^3B_1 states.

The SOC enhancement upon cluster compression is best described by an enhancement factor (EF), as defined in Table B4.1. The molecules were considered effectively separated when the centers of mass of the monomers are separated by a distance larger than 5.7 Å where the attractive energy becomes negligible.[232] As can be seen from Table B4.1, the highest EF can reach up to 2.10^8 (eg. SOC(a^3A_1 [0], b^1A_2 [0])), suggesting very high efficiency of electronic excitation of O_2 molecules upon compression. An example of the evolution of the SOC with cluster distortion is shown in

Fig. B4.8 for the SOC(a^5A_1, a^3B_1) of the H configuration as a function of intermolecular distance.

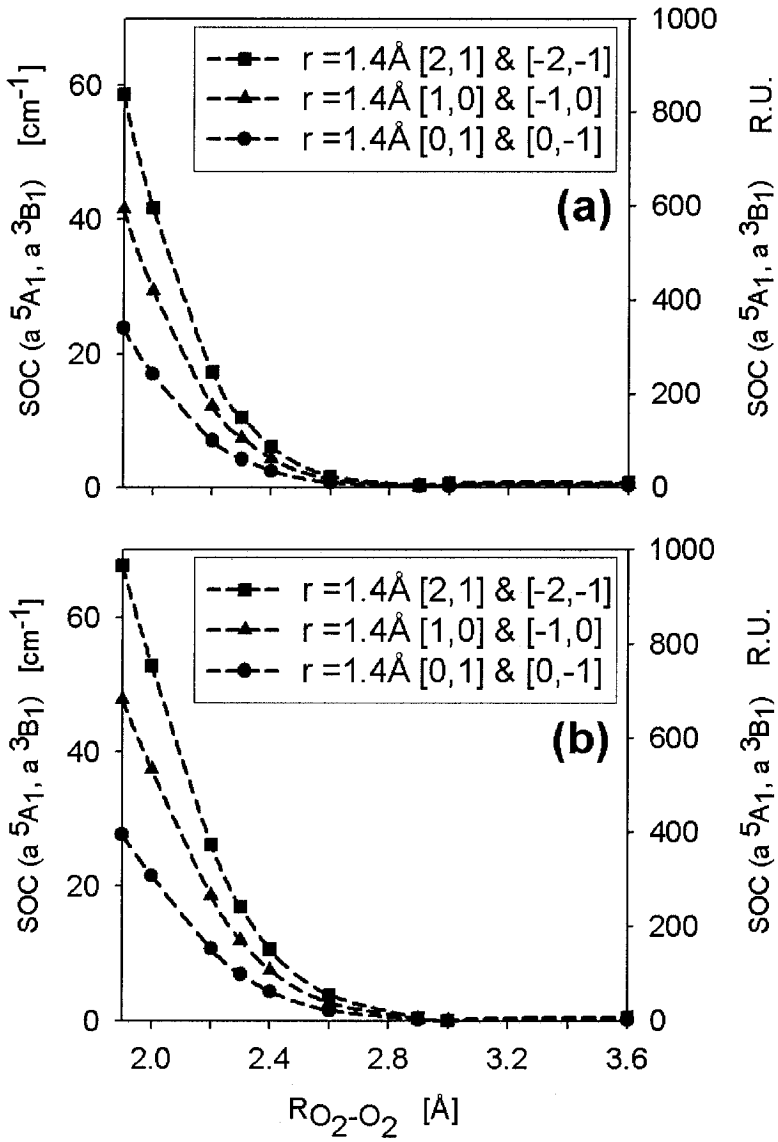

Fig. B4.8. Spin-Orbit Coupling between the a^5A_1 and a^3B_1 states for $(O_2)_2$ in the H configuration, as a function of the intermolecular distance $R_{O_2-O_2}$. (a) r_{O-O} = 1.2 Å, (b) r_{O-O} = 1.4 Å.

The SOC exhibits exponential increase with cluster compression for both r_{O-O} = 1.20 Å and r_{O-O} = 1.40 Å. Vibrationally excited molecules (r_{O-O} = 1.4 Å) exhibit additional

enhancement of the SOC strength with respect to that of separate monomers at their equilibrium geometries (r_{O-O} = 1.2 Å). Thus, the cluster can act as a "reactor", where non-adiabatic transitions which would not be possible under normal conditions are enhanced, an effect closely related to the "chemistry with a hammer" concept.[221,280,296] As compression and vibrational excitation can both lead to electronic transitions in $(O_2)_n$ clusters, the atomic and electronic motions cannot be separated, and the Born-Oppenheimer approximation[276] breaks down in "chemistry with a hammer" processes.

B4.III.B. Extrapolation of the $(O_2)_2$ Results to Large Molecular Clusters

Extrapolation of our findings for the dimer $(O_2)_2$ model suggests a major enhancement of the mechanically-induced electronic transitions at larger cluster sizes. Because the number of electronic states generated grows rapidly with cluster size, the number of pathways can be expected to increase concurrently. For instance, the 3 lowest electronic states of the O_2 molecule combine to 18 states in the $(O_2)_2$ dimer. For the large cluster sizes typical in experiments, a continuum of states will replace the discrete curve-crossing points of $(O_2)_2$, and the number of possible excitation pathways may ultimately be infinite in a continuum of states.

Another factor for the increase of the efficiency of the non-adiabatic process arises from the fact that transition probabilities may also be expected to increase. Larger clusters are characterized by lower symmetry as cluster size increases, implying that the different electronic states generated upon monomer addition become increasingly similar, until all states completely lose symmetry. This effect greatly weakens the selection rules related to orbital and spin symmetry, increasing non-adiabatic transition probabilities in possible curve-crossing regions. Additionally, combination of several O_2 $^3\Sigma_g^-$ molecules

leads to high-spin multiplicities and consequently to an increase in the number of possible reaction pathways. In a single O_2 molecule, for example, spin-orbit selection rules only give rise to one non-zero spin-orbit coupling, SOC($^3\Sigma_g^-[0]$, $^1\Delta_g[0]$), but in the dimer, there are up to 6 non-zero SOC terms between states correlating with ($^3\Sigma_g^- + ^3\Sigma_g^-$) and ($^3\Sigma_g^- + ^1\Delta_g$). Because $M_S \in [-(2S+1), (2S+1)]$, and the spin selection rules for non-zero SOC are $\Delta M_S = 0 \pm 1$, the number of SOC matrix elements should increase drastically with cluster size, which can be interpreted as an increased number of possible excitation channels, and thus an increase of the total transition probability. Furthermore, combination of several $^3\Sigma_g^-$ O_2 molecules may result in intersections between states with similar multiplicities, which correlate with different electronic states of the monomers. For instance, both the ($^3\Sigma_g^- + ^3\Sigma_g^-$) and ($^3\Sigma_g^- + ^1\Delta_g$) pairs lead to triplet states in the $(O_2)_2$ complex. Thus, transitions may readily occur in clusters that are sufficiently distorted to allow interstate crossings.

The curve crossing region can be expected to be more easily accessible at larger cluster sizes. As such clusters will tend to possess even higher multiplicities, electronic states of higher multiplicities can be expected to exhibit larger electronic perturbations under mechanical compression due to the Pauli principle. For instance, it is clear that the a^5A_1 state is destabilized much faster in energy upon compression than the a^3A_1 and a^1A_1 states in the H isomer (cf. Fig. B4.5).

Finally, we suggest that an increased fraction of molecules acquire sufficient energy to reach the curve-crossing points and undergo non-adiabatic transitions. As we will show shortly, larger clusters are characterized by an increased fraction of O_2

molecules acquiring sufficient energy to reach the $^1\Delta_g$ state. This is attributed to the increased number of intermolecular collisions in larger clusters, allowing for more efficient energy.

B4.III. C. Implications for the Experimental Problem

In previous work, it was demonstrated that a very small fraction of cluster molecules would acquire sufficient energy to undergo direct silicon oxidation from ground-state oxygen, when considering a surface temperature of T_s = 1100 K.[298] More precisely, less than 0.2 % of the molecules would have enough energy to overcome the corresponding activation barrier of 2.70 eV.[236,241] In experiments, however, the surface was heated up to 1500 K, prompting an investigation of the influence of T_s on the monomer's energetic properties for different cluster sizes. In Fig. B4.9a is reported E_{max}, the maximum internal energy acquired by a given monomer in the course of the collision process. For all cluster sizes (up to n = 1024) investigated, E_{max} quickly increases with T_s to become large enough to render surface oxidation possible. A plateau seems to be reached at high temperatures, with a threshold value of about 3.8 eV for the largest cluster sizes. As the average incident kinetic energy per molecule is about 0.22 eV, these results illustrate that the kinetic energy of the entire cluster can be "focused" into only a few cluster particles that are retained close to the surface due to steric confinement by other cluster particles, as previously suggested for the "chemistry with a hammer."[217]

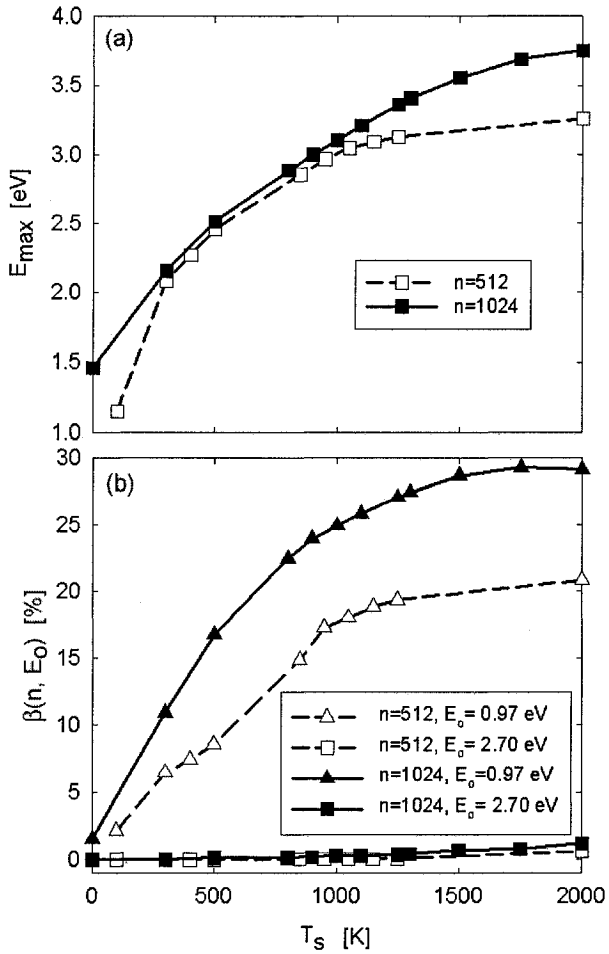

Fig. B4.9. Evolution of the energetic properties of O_2 monomers with the surface temperature T_s, obtained from molecular dynamics simulations of $(O_2)_n$ scattering (a) E_{max}, the maximum internal energy gained by a given monomer in the course of the collision. (b) β is the proportion of molecules acquiring an internal energy above E_0 inside a cluster of n molecules.

Therefore, a finite population of monomers will gain sufficient energy to react with the silicon surface via the ground-state pathway with activation barrier of 2.70 eV. The importance of this population can be characterized by the fraction β of cluster molecules with E_{max} beyond a threshold value of E_o, as reported in Fig. B4.9b. For E_o = 2.70 eV, β increases only slightly with cluster size and surface temperature, and only about 2% of all cluster molecules would gain enough energy to cause ground state oxidation, even at the

highest temperatures. The experimental yield, however, is measured to be about 25%,[215] suggesting that the ground state reaction alone cannot account for the experimental results.

The present quantum chemistry calculations for the $(O_2)_2$ model show that scattering of clustered triplet $^3\Sigma_g^-$ O_2 molecules can result in the production of singlet $^1\Delta_g$ O_2 molecules. Analysis of the molecular dynamics results show that the fraction β of all cluster molecules that acquire enough energy to accomplish the triplet/singlet ($^3\Sigma_g^- \longrightarrow {}^1\Delta_g$) transition (in Fig. B4.9b) in the course of the cluster/surface scattering, and thus a large fraction of molecules acquire sufficient energy to reach the $^1\Delta_g$ state upon cluster impact, suggesting that O_2 electronic excitation is energetically possible. β rapidly increases with T_s up to a plateau (at about 1000 K), and this strong temperature dependence suggests that the efficiency of the nonadiabatic mechanism could readily be controlled by local heating of the surface. Further, β increases with cluster size, i.e. clusters with 512 and 1024 molecules reach β values of 20% and 30%, respectively. This effect may be attributed to the larger number of intermolecular collisions in larger clusters, causing increased energy transfer and resulting in a larger fraction of molecules with enough energy to reach the $^1\Delta_g$ state.

Our quantum chemistry calculations also illustrate that, for a given intermolecular distance, the curve-crossing region strongly depends on the dimer geometry, i.e. on the relative orientation of O_2 molecules in the cluster. The typical distribution of relative monomer orientations in clusters before and during scattering is displayed in Fig. B4.10. Fig. B4.10a shows dimers before collision primarily adopt an X configuration, but other

H, T and L configurations exist to a smaller extent. During the scattering event, X isomers also represent the largest population in clusters, as can be seen from Figs. B4.10b to B4.10d. These structural features are in good agreement with experimental investigations of the $(O_2)_n$ clusters, which were shown to have an ordered, crystalline structure.[260] Quantum chemistry calculations showed that curve crossing for the X configuration would occur below $R_{O_2-O_2}$ = 1.90 Å (cf. Fig. B4.4). However, our molecular dynamics simulations of $(O_2)_n$ cluster scattering show that oxygen molecules never get closer to each other than 2.0 Å under experimental conditions (cf. Fig. B4.3). Although a large fraction of dimers are in the X configuration, they cannot undergo electronic transition, and thus may be responsible for non-adiabatic dynamic processes in the experiment.

The curve-crossing regions of the L isomer are found below 2.8 Å (see Fig. B4.7). Whereas a small population of L species may exist in the cluster before collision (cf. Fig. B4.10a), inspection of Fig. B4.10b reveals, however, that there is no L dimer population with $R_{O_2-O_2} < 2.8$ Å upon cluster scattering. Similarly, Fig. B4.10c shows that there are no T dimers with intermolecular distance smaller than 2.3 Å, the distance which corresponds to the beginning of the curve-crossing region (cf. Fig. B4.6). Therefore, neither the L nor T isomers can undergo electronic transitions when large $(O_2)_n$ clusters impact on a rigid surface under experimental conditions. However, the structural analysis of the compressed clusters in Fig. B4.10d shows a finite population of H structures reaching $R_{O_2-O_2} < 2.0$ Å, where the curve-crossing point can be accessed (cf. Fig. B4.5). Thus, only the H isomer experiences enough geometrical distortion to allow for electronic transitions in experiments. Whereas only a minor fraction of the $(O_2)_2$ species

adopt the appropriate H configuration, the presence of a non-adiabatic ladder suggests mechanisms of successive $^1\Delta_g$ O_2 production throughout the colliding cluster. At cluster sizes typical of experiments, a large fraction of O_2 molecules may be promoted to the $^1\Delta_g$ state, resulting in silicon surface oxidation.

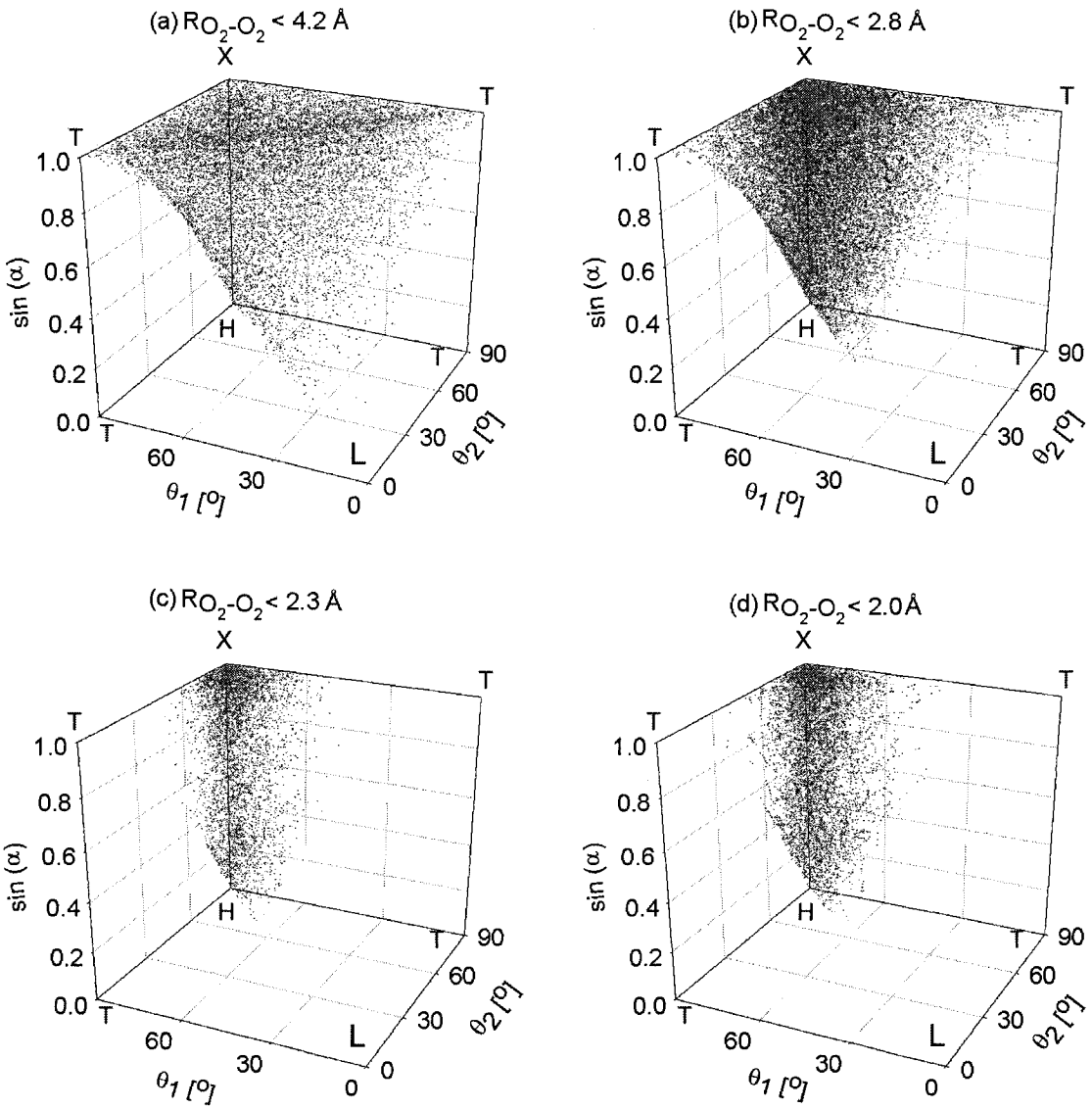

Fig. B4.10. Structural analysis of the $(O_2)_2$ population, obtained from molecular dynamics simulations of $(O_2)_{512}$ surface scattering. The θ_1 and θ_2 angles are as defined in Fig. B4.3, and α is the angle between the molecular axis. (a) shows $R_{O_2\text{-}O_2}$ < 3.7 Å for a cluster thermalized at a temperature of 32 K, before surface impact. (b), (c) and (d) show

$R_{O_2-O_2} < 2.8$ Å, $R_{O_2-O_2} < 2.3$ Å and $R_{O_2-O_2} < 2.0$ Å, respectively, for a cluster scattering onto a hot surface ($T_s = 1500$ K).

B4.IV. CONCLUSIONS

Complete active-space self-consistent-field (CASSCF) electronic structure calculations were performed for the 13 lowest electronic states of the X, H, T, and L isomers of the $(O_2)_2$ complex. The calculations show that cluster compression and vibrational excitation leads to a significant deformation of the electronic structure from that at equilibrium. Multiple crossings of electronic state potential energy surfaces are observed, suggesting that mechanically-induced non-adiabatic transitions may occur under "chemistry with a hammer" conditions. Although the transition between the $^3\Sigma_g^-$ and $^1\Delta_g$ states is strongly forbidden by selection rules for individual oxygen molecules, in a $(O_2)_2$ complex formed by two colliding oxygen molecules the electronic structure is perturbed strongly enough that violation of spin selection rules may occur, due to enhanced spin orbit coupling. We found a number of possible pathways with multiple electronic transitions, which suggests that non-adiabatic transitions are possible even in relatively mild molecular collisions. Extrapolation of the $(O_2)_2$ cluster model to large clusters size suggests a dramatic increase of the mechanically-induced electronic transitions. Larger clusters would be characterized by much wider curve-crossing regions which are more easily accessible upon geometrical distortion. Further, the number of both spin-conservative and non-spin-conservative transitions can be expected to increase with cluster size, leading to larger transition probabilities. Inspection of potential energy surface scans from combined quantum chemistry and molecular dynamics simulations of $(O_2)_n$ clusters colliding on a hot surface has provided insight into recent experimental

results concerning the cluster-catalyzed oxidation of silicon surfaces. In particular, a significant number of dimers in the H configuration are found to be distorted enough to access the curve-crossing regions, making the electronic transitions possible upon cluster/surface collision. This provides a plausible mechanism for the cluster-catalyzed silicon oxidation experiments, and may imply that "chemistry with a hammer" mechanisms involve significant non-adiabaticity.

CONCLUSIONS AND FUTURE PERSPECTIVES

I. CONCLUSIONS

In this work, we exploited the properties of clusters as a novel phase of matter. We first investigated solvent effects on the chemical properties of clusters (Part A), and the potential use of clusters as a new class of reactants (Part B).

We focused on room-temperature thermodynamic and structural properties of acetonitrile clusters containing alkali ions (Na^+, Cs^+) or halide ions (I^-) (Chapter A1), where we employed Monte Carlo simulations with model potentials parameterized on the basis of quantum chemistry calculations and supplemented by experimental data whenever available. While the structure of ionic acetonitrile clusters was generally thought to be governed by electrostatic and polarization interactions, quantum chemistry calculations revealed the existence of a $I^-(CH_3CN)_2$ hydrogen-bonded complex, along with two linear structures that are more intuitive on the basis of pure ion-dipole interactions (Chapter A2). Quantum chemistry calculations of binding energies and vertical excitation energies for the linear symmetric and nonlinear hydrogen-bonded $I^-(CH_3CN)_2$ isomers are in very good agreement with available experimental data, unlike those of the linear asymmetric structure, which led to a revision of experimental work on the concept of asymmetric solvation in $I^-(CH_3CN)_2$ clusters (Chapter A2).[44] Hydrogen bonding in halide–acetonitrile clusters manifested itself, not only in the fact that a stable nonlinear hydrogen-bonded isomer exists, but also in slight geometrical distortions of the linear cluster structures. In a further study, the properties of $Na^+(CH_3CN)_n$ and $I^-(CH_3CN)_n$ clusters were then revisited with another model potential (Chapter A3). Calculated cluster thermodynamic properties such as binding enthalpies converged very

slowly to their bulk limit, and their evolution with cluster size is closely related to the solvation structure of the ions, which were found to adopt an interior solvation shell structure. Comparison with previous results for ion-water clusters demonstrated the importance of the relative strengths of ion-solvent and solvent-solvent interactions in the determination of interior *vs.* surface ionic cluster structures. For example, $I^-(CH_3CN)_n$ clusters clearly exhibit an interior solvation structure, in net contrast with the surface structures observed for $I^-(H_2O)_n$ clusters, which arise from strong solvent-solvent hydrogen bonding interactions. A comparative investigation of $Na^+(NH_3)_n$ and $I^-(NH_3)_n$ clusters at 115 K (Chapter A4) revealed that ions adopt an interior solvation shell structure in ammonia clusters similar to that of acetonitrile clusters. However, our simulations suggest that no stable ion-ammonia clusters containing more than a single solvation shell could be produced at room temperature, due to low solvent self-interaction strength and solvent evaporation.

Our theoretical studies also allowed the investigation of solvation effects on chemical reactivity. In a recent experimental study of the NaI ion pair multi-photon ionization in polar solvent clusters of water, acetonitrile and ammonia, a strong solvent selective behavior was observed on the $Na^+(solvent)_n$ photoionized product size distributions.[26] Monte Carlo simulations were employed to investigate the structural and thermodynamic properties of $NaI(solvent)_n$ clusters, with acetonitrile at 300 K (Chapter A3) and ammonia at 115 K (Chapter A4) as solvents. Appropriate intermolecular model potentials have been developed to reproduce the structural and energetic properties of small clusters. Potentials of mean force calculations demonstrated that in both acetonitrile and ammonia clusters, the NaI ion pair is thermodynamically stable with respect to ionic

dissociation, suggesting the feasibility of the photoionization route akin to that of gas-phase NaI. $NaI(CH_3CN)_n$ and $NaI(NH_3)_n$ clusters shared similar features with $NaI(H_2O)_n$ clusters, with the presence of contact ion pairs (CIP) and solvent separated ion pairs (SSIP) structures, with the CIP species being thermodynamically favored in small clusters. Both ions in $NaI(CH_3CN)_n$ and $NaI(NH_3)_n$ clusters adopt an interior solvation shell structure, in contrast with $NaI(H_2O)_n$ clusters where "surface" solvated structures were observed. $NaI(CH_3CN)_n$ and $NaI(NH_3)_n$ clusters exist primarily as contact ion pair species up to cluster sizes 36 and 64, respectively, after which SSIPs become thermodynamically more stable.

In $NaI(CH_3CN)_n$ multi-photon ionization experiments,[26] the lack of large fragment products might arise from inhibition of photoexcitation by extensive solvation of the ground ionic state, a phenomenon that is likely to occur in smaller acetonitrile clusters than water clusters since the differential solvation energy in $NaI(H_2O)_n$ clusters may increase less rapidly due to surface solvation structures. Alternatively, $NaI(CH_3CN)_n$ clusters may be promoted to the ionized state by multi-photon ionization with a larger amount of excess energy which, together with major solvent reorganization upon iodine detachment, may induce extensive solvent evaporation, hence preventing survival of large $Na^+(CH_3CN)_n$ product fragments. The surface structure of $NaI(H_2O)_n$ clusters should damper such a mechanism, as ejection of iodine from the surface of a well organized solvent cluster may only implicate minor solvent reorganization. On the other hand, the lack of large product signal in $NaI(NH_3)_n$ multi-photon ionization experiments might be connected to the low evaporation temperature of ammonia, which may prevent production of large parent ground-state $NaI(NH_3)_n$ clusters, and result in massive solvent

evaporation on the excited states. Our findings are in good agreement with the sharp decrease of the $Na^+(NH_3)_n$ photoionization product signal beyond cluster size 5, which incidentally is the coordination number of $Na^+(NH_3)_n$ in room-temperature cluster simulations, and vanishing of the signal at cluster size 9, which incidentally is the maximum cluster size of stable $NaI(NH_3)_n$ clusters at room temperature.

In the second part of this thesis, we investigated clusters as a new class of reactants (Part B). In particular, we focused on the potential of cluster/surface collisions, and the intense conditions generated upon cluster impact, which may allow catalysis of multi-center reactions with large activation barriers. To obtain a better fundamental understanding of such process, we first focused on the dynamics of energy transfer to the vibrational degrees of freedom of the products of $(N_2)_n$ and $(O_2)_n$ cluster-surface scattering by means of classical molecular dynamics simulations (Chapter B1). The monomer product vibrational energy distributions are found to be best fitted by a sum of two Boltzmann distributions, suggesting that two distinct thermal-like processes of vibrational excitation occur during cluster scattering. The cold component of the distribution was shown to involve monomers originating from the cluster interior while the hot component of the distribution is made up of monomers essentially lying at the outskirts of the cluster at surface impact. This work allowed reconciliation of several conflicting results. Theoretical studies have predicted the possibility of the "burning of air" reaction via the "chemistry with a hammer",[217] a phenomenon that has yet to be observed experimentally. Recent experimental results revealed little vibrational excitation or molecular dissociation in the scattering of molecular Van der Waals clusters on a graphite surface.[230] Further, simulations of $(N_2)_n$ and $(O_2)_n$ cluster-surface scattering

under current experimental conditions revealed that cluster products are only slightly vibrationally excited. Only a small fraction of the incident cluster kinetic energy is transferred to the monomer product vibrational modes, such that molecular dissociation is not possible under typical experimental conditions, and a much larger incident kinetic energy is required to obtain a significant probability of surface-induced monomer dissociation. Furthermore, our results indicate that increasing cluster size does not catalyze, but rather hinders monomer vibrational excitation, and enhances vibrational relaxation. Our findings suggest the existence of an optimal cluster size for experimental studies of cluster-catalyzed reactions.

Recent experimental results showed the presence of a cluster-catalyzed oxidation mechanism of a silicon surface by a $(O_2)_n$ cluster beam.[215] While the reaction mechanism remains so far unresolved, the cluster/surface simulations of $(O_2)_n$ under experimental conditions clearly ruled out the possibility of molecular dissociation before surface reaction, as no atomic oxygen could be produced upon cluster impact (Chapter B1). An alternate mechanism was investigated, involving direct oxidation by ground state O_2 (Chapter B2). Analysis of the molecular energy available in the course of the $(O_2)_n$ surface scattering process revealed that too small a fraction of O_2 molecules would possess enough energy to overcome the reaction barrier. Consequently, a non-adiabatic pathway was proposed, implying the generation of singlet oxygen followed by surface oxidation by highly reactive singlet O_2 molecules, as a result of molecular dynamics simulations and high-level quantum chemistry calculations. While the former demonstrate that a significant fraction of O_2 molecules gain enough energy upon collision to undergo electronic excitation to the singlet state, the latter show that formation of highly reactive

singlet oxygen molecules via a novel "ladder climbing" mechanism is possible even in relatively mild cluster/surface collisions. Such mechanically-induced O_2 electronic excitation process was also found potentially relevant to the explanation of the presence of a "dark channel" in the enhanced vibrational relaxation of highly excited oxygen molecules during ozone photolysis in the stratosphere (Chapter B2).[292] Electronic excitation of various $(O_2)_2$ isomers subject to cluster compression and vibrational excitation was then investigated in further details. The calculations showed the emergence of possible pathways for singlet O_2 generation upon mechanical collisions, due to the presence of electronic state curve-crossing points and spin-orbit coupling effects. In addition, molecular dynamics simulations of $(O_2)_n$ cluster surface scattering demonstrate that a considerable fraction of $(O_2)_2$ compressed species could access the curve-crossing region, thus suggesting efficient O_2 ($^1\Sigma_g^+$) generation. Extrapolation of those results to the large cluster sizes employed experimentally suggests a dramatic increase of the singlet oxygen reaction efficiency. This work illustrated that the well accepted Born-Oppenheimer approximation[276] can be violated even under in relatively mild cluster collision conditions, and that non-adiabatic processes may play a key role in the "chemistry with a hammer" (Chapter B3).

II. FUTURE PERSPECTIVES

Regarding NaI multi-photon ionization in polar solvent clusters,[26] conclusive arguments were found regarding the solvent selectivity in the $Na^+(solvent)_n$ product signal in water clusters. However, only speculative arguments were proposed to explain the lack of large clusters products in acetonitrile and ammonia. In order to assess whether

the laser wavelength remains adequate for the photoionization of large clusters, quantum chemistry calculations of Frank-Condon energy gaps and electronic transition oscillator strengths in $NaI(solvent)_n$ clusters are currently being conducted.[174] Further, molecular dynamic simulations with quantum transitions may allow investigation of the excited-state dynamics of $NaI(CH_3CN)_n$ and $NaI(NH_3)_n$ clusters, assessement of the issue of solvent evaporation effects, and allow a comparison with the mechanism occurring in $NaI(H_2O)_n$ clusters. Finally, an inspection of quantum effects in $NaI(NH_3)_n$ clusters at low temperature should allow verification of the applicability of classical methods in low temperature simulations. Notably, a convenient method for inclusion of quantum effects in finite temperature cluster simulations implies Feynman's path integral formulation of quantum statistical mechanics.[316]

The investigation of solvation effects on clusters properties illustrate how microscopic aspects of condensed-phase phenomena can be elucidated and how the cluster phase displays unique properties not found in their corresponding bulk states. Theoretical studies are reaching a point where the bulk phase properties can be extrapolated from their evolution with cluster size, providing a benchmark of the accuracy of theoretical calculations. Thus, in the future, continued progress can be expected in the understanding of solvation and solid-state phenomena through the study of clusters. The application of new experimental and theoretical techniques to this field will ensure further insight into the structure, energetics, and dynamics of chemical phenomena at the microscopic level. Also, the area of cluster reactions is a subject of growing interest motivated by both scientific questions in the area of chemical dynamics and the availability of emerging new technologies to investigate the molecular details of

phenomena. Ultrafast pump-probe techniques[36] have opened up the prospects of investigating the course of reactions as influenced by both solvation and confinement to restricted geometries. This is a promising area where we can also expect to see bridging to other fields such as biochemistry, where solvation-mediated phenomena are critically important.

The theoretical studies on cluster/surface scattering suggested the existence of an optimal cluster size for the "chemistry with a hammer"[221] (Chapter B1), but further investigations may allow us to understand optimal conditions for reactivity. As for the case of the "burning of air reaction",[217] quantum chemistry investigations of $(O_2)_2$ clusters (Chapters B2 and B3) suggested the importance of non-adiabatic processes, an effect which has been neglected. A quantum chemistry investigation of the "burning of air" mechanism, including non-adiabatic processes, may also to asses the potential of such reaction. As we predicted non-adiabatic effects in relatively mild cluster collisions, one may reconsider the accepted range of validity of the Born-Oppenheimer approximation,[276] which might have fundamental implications in chemical reaction dynamics. While a possible direction lies in the identification of the classes of chemical reactions that are most susceptible to these effects, the ultimate goal consists in achieving an exact quantum prediction for electronically non-adiabatic dynamics.

Finally, further studies may be required to gain a better understanding of the mechanism leading to silicon surface oxidation by $(O_2)_n$ cluster impact.[215] Specific attention should be paid to the interaction of oxygen with the silicon surface, and in particular on the reactivity differences between the different states generated by the combination between molecular oxygen (in its different electronic states) with a silicon

surface, which also has low lying excited states. Comparison of the potential energy surfaces generated should allow identification of the lowest energy pathway connecting reactants, transition state and products. In addition, new experiments may be designed to find optimal conditions for such a process. For instance, one can try to excite a $(O_2)_2$ complex by surface collision, and investigate how the probability of transition corresponds to the measured reaction probability in the cluster oxidation experiment. By modeling explicitly the silicon surface one could investigate the mechanisms of the Si(100) + n O_2 and the Si(100) + $(O_2)_n$ reactions, the latter one being characterized by passive and active oxidation effects. The role of incident cluster flux and surface temperature on active and passive oxidation, or on the etching depth and rate should also be further investigated. Furthermore, we can explore if evaporating silica molecules can react with incoming oxygen clusters, or explore the possible roles of temporary local heating versus steric effects induced by cluster impact. Other possible future work may include experiments with mixed oxygen clusters with simultaneous etching and deposition processes on silicon surfaces, assess the role of hydrogen on the silicon surface and predict how the presence or absence of hydrogen influences the cluster induced etching process.

As illustrated from the research presented herein, the field of cluster dynamics is vital and diverse, reaching into many aspects of fundamental and application-driven science. For instance, charge transfer processes and hydrogen bonding are of central importance in biological systems, and knowledge of fundamental mechanisms of solvation effects and photochemistry contribute to a more detailed understanding of atmospheric chemistry. At the same time, information obtained from the studies implying

semiconductor materials have promising applications in nanotechnology, and interest in the prospect of cluster materials can also be expected to continue its rapid growth. In comparison with gas and condensed phase chemistry and physics, cluster science is really quite young. Nevertheless, the experimental and theoretical methods developed in the past two decades provided powerful tools for studying molecular interactions at a level of detail not previously possible. The future of this field will see an even stronger interplay between theory and experiment, and the systems discussed in this thesis and the myriad of other potentially interesting systems promise to keep the field of cluster science growing for years to come.

REFERENCES

(1) Bacic, Z.; Miller, R. E. *J. Phys. Chem.* **1996**, *100*, 12945.

(2) Haberland, H. *Clusters of Atoms and Molecules;* Berlin, Heidelberg, 1994.

(3) Thomas, J. M. *Michael Faraday and The Royal Institution;* Bistol, 1991; Coulier, M. *J. Pharm. Chim. Parts* **1875**, *22*, 165.

(4) Wilson, J. G. *The Principles of Cloud-Chamber Technique*; Cambridge Universtiy Press: Cambridge, 1951; Ramsey, N. F. *Phys. Rev.* **1948**, *74*, 286; Ochs, S. A.; Coté, R. E.; Kusch, P. J. *J. Chem. Phys.* **1953**, *21*, 459; Aitken, J. *Collected Scientific Papers of John Aitken*; Cambridge University Press: Cambridge, 1923.

(5) Bentley, P. G. *Nature* **1961**, *190*, 432; Henkes, W. Z. *Naturforsch* **1961**, *16A*, 842.

(6) Castleman, A. W., Jr.; Bowen, K. H. *J. Phys. Chem.* **1996**, *100*, 12911.

(7) Berry, R. S. *J. Phys. Chem.* **1994**, *98*, 6910.

(8) Wales, D. J.; Berry, R. S. *J. Chem. Phys.* **1990**, *92*, 4283.

(9) Scoles, G.; Bassi, D.; Buck, U.; Lainé, D. *Atomic and Molecular Beam Methods*; Oxford University Press: Oxford, 1988.

(10) Halberstadt, N.; Janda, K. C.; Eds *Dynamics of Polyatomic and der Waals Complexes*; Plenum: New York, 1990.

(11) Blades, A. T.; Jayaweera, P.; Ikonomou, M. G.; Kebarle, P. *J. Chem. Phys.* **1990**, *92*, 5900.

(12) Nishi, N.; Yamamoto, K. *J. Am. Chem. Soc.* **1987**, *109*, 7353.

(13) Muhlbach, J.; Pfau, P.; Sattler, K.; Recknagel, E. *Z. Phys. B.* **1982**, *47*, 233; Martin, T. P. *Chem. Phys.* **1984**, *81*, 4426; McHugh, K. M.; Sarkas, H. W.; Eaton, J. G.; Westgate, C. R.; Bowen, K. H. *Z. Phys. D.* **1989**, *12*, 3.

(14) Heer, W. A. d.; Knight, W. D. Elemental and Molecular Clusters; Springer-Verlad, Ed. Verlin, 1988; p 45.

(15) Zhong, Q.; Castleman, A. W., Jr. *Chem. Rev.* **2000**, *100*, 4039.

(16) Yamdagni, R.; Kebarle, P. *J. Am. Chem. Soc.* **1971**, *94*, 2940.

(17) Bernstein, E. R. *Chemical Reactions in Clusters*; Oxford University Press: New York, 1996.

(18) Jellinek, J.; Beck, T. L.; Berry, R. S. *J. Chem. Phys.* **1986**, *84*, 2783.

(19) Castleman, A. W., Jr. In *Advances in Gas-Phase Ion Chemistry*; Babcock, L. M., Adams, N. G., Eds.; JAI Press: Stamford, CT, 1998; Vol. 3; p 185.

(20) Castleman, A. W., Jr. Advances in Mass Spectrometry; Elsevier Science: New York, 1992; Vol. 12; p 167.

(21) Shin, S. K.; Wittig, C.; Goddard, W. A. *J. Chem. Phys.* **1991**, *95*, 8408; Jaques, C.; Valachoivc, L.; Ionov, S. *J. Chem. Soc., Fraraday Trans.* **1993**, *89*, 1419.

(22) Cooks, R. G.; Ast, T.; Mabud, M. A. *Int. J. Mass Spectrom. Ion Processes* **1990**, *100*, 209.

(23) Castleman, A. W., Jr.; Wei, W. S. *Annu. Rev. Phys. Chem.* **1994**, *45*, 685; Castleman, A. W., Jr. *Int. J. Mass Spectrom. Ion Processes* **1992**, *118/119*, 167.

(24) Castleman, A. W., Jr.; Keese, R. G. *Science* **1988**, *241*, 36; Miller, R. E. *Acc. Chem. Res.* **1990**, *23*, 10; Jortner, J.; Levine, R. D.; Pullman, B.; Eds.; Kluwer Academic: Dordrecht, Holland, 1994; Bernstein, E. R. *Annu. Rev. Phys. Chem.* **1995**, *197*, 46.

(25) Desfrancois, C.; Carles, S.; Schermann, J. P. *Chem. Rev.* **2000**, *100*, 3943.

(26) Grégoire, G.; Mons, M.; Dedonder-Lardeux, C.; Jouvet, C. *Eur. Phys. J. D* **1998**, *1*, 5.

(27) R. A. Marcus, *J. Chem. Phys.* **24**, 979 (1956); *ibid.*, **26**, 867 (1957); *ibid.*, **26**, 872 (1957); *Trans. N. Y. Acad. Sci.* **19**, 423 (1957); ONR Technical Report No. 12, Project NR 051-331 (1957), reproduced in Special Topics in Electrochemistry, P. A. Rock, ed., Elsevier, New York, 1977, p 181; *Can. J. Chem.* **37**, 155 (1959); *Disc. Far. Soc.* **29**, 21 (1960); *J. Phys. Chem.* **67**, 853, 2889 (1963); *J. Chem. Phys.* **38**, 1858 (1963); *ibid.*, **39**, 1734 (1963); *Ann. Rev. Phys. Chem.* **15**, 155 (1964); *J. Chem. Phys.* **43**, 679 (1965); *ibid.*, **43**, 1261 (1965); *ibid.*, **43**, 2654 (1965), (corr.) **52**, 2803 (1970); *J. Phys. Chem.* **72**, 891 (1968).

(28) Miller, J. R.; Calcaterra, L. T.; Gloss, G. L. *J. Am. Chem. Soc.* **1984**, *106*, 3047; Deisernhofer, J.; Epp, O.; Miki, K.; Huber, R.; Michel, H. *J. Mol. Bio.* **1984**, *180*, 385; Deisenhofer, J.; Michel, H. *Angew. Chem. Int. Ed. Engl.* **1989**, *28*, 829; Yeates, T. G.; Komiya, H.; Rees, D. C.; Allen, J. P.; Feher, G. *Proc. Nat. Acad. Sci.* **1987**, *84*, 6438.

(29) Marcus, R. A. *Nobel Lectures, Chemistry 1991-1995*; Worl Scientific Publishing Co.: Singapore, 1997.

(30) Sunsstrom, V. E. *Femtochemistry and Femtobiology*; Imperial College Press: London, 1996; Fox, M. A.; Barton, J. K. *Science* **1999**, *283*, 375.

(31) Miller, T. M.; Ling, J. H.; Saxon, R. P.; Moseley, J. T. *Phys. Rev. A* **1976**, *13*, 2171; Vestal, M. L.; Mauclaire, G. H. *Chem. Phys. Lett.* **1976**, *43*, 499; Moseley, J. T.; Saxon, R. P.; Huber, B. A.; Cosby, P. C.; Abouaf, R.; Tadjeddine, M. *J. Chem. Phys.* **1977**, *67*, 1659; Less, L. C.; Smith, G. P. *Phys. Rev. A* **1979**, *19*, 2329.

(32) Levinger, N. E.; Ray, M. L.; Alexander, M. L.; Lineberger, W. C. *J. Chem. Phys.* **1988**, *89*, 5654; Woodward, C. A.; Upharn, J. E.; Stace, A. J.; Murrel, J. N. *J. Chem. Phys.* **1989**, *91*, 7612; Nagata, T.; Hirokawa, J.; Kondow, T. *Chem. Phys. Lett.* **1991**, *176*, 526; Jones, A. B.; Buxey, A. L. M.; Jukes, P. R.; Smith, J. A.; Stace, A. J. *J. Chem. Phys.* **1995**, *103*, 474.

(33) Moseley, J. T.; Cosby, P. C.; Bennett, R. A.; Peterson, J. R. *J. Chem. Phys.* **1975**, *64*, 4826; Posey, L. A.; DeLuca, M. J.; Johnson, M. J. *Chem. Phys. Lett.* **1986**, *131*, 170; Jarrold, M. F.; Illies, A. J.; Bowers, M. T. *J. Chem. Phys.* **1984**, *81*, 222; Hiller, J. F.; Vestal, M. L. *J. Chem. Phys.* **1980**, *72*, 4713.

(34) Dantus, M.; Rosker, M. J.; Zewail, A. H. *J. Chem. Phys.* **1987**, *84*, 4708.

(35) Zewail, A. H. *Science* **1988**, *242*, 1645.

(36) Zewail, A. *Nobel Lectures, Chemistry 1996-2000*; World Scientific Publishing Co.: Singapore, 2003.

(37) Zhong, D.; Zewail, A. H. *Proc. Natl. Acad. Sci. U.S.A.* **1999**, *96*, 2602; DeBoer, G.; Burnett, J. W.; Fujimoto, A.; Young, M. A. *J. Phys. Chem.* **1996**, *100*, 14882.

(38) Cheng, P. Y.; Zhong, D.; Zewail, A. H. *Chem. Phys. Lett.* **1995**, *242*, 369.

(39) Benest, H. A.; Hildebrand, J. H. *J. Am. Chem. Soc.* **1949**, *71*, 2703; Mulliken, R. S. *J. Am. Chem. Soc.* **1950**, *72*, 610; Cheng, P. Y.; Zhong, D.; Zewail, A. H. *J. Chem. Phys.* **1996**, *105*, 6216.

(40) Rosker, M. J.; Rose, T. S.; Zewail, A. H. *Chem. Phys. Lett.* **1988**, *146*, 175. Rose, T. S.; Rosker, M. J.; Zewail, A. H. *J. Chem. Phys.* **1988**, *88*, 6672. Rose, T. S.; Rosker, M. J.; Zewail, A. H. *J. Chem. Phys.* **1989**, *91*, 7415. Cong, P.; Mohktari, A.; Zewail, A. H. *Chem. Phys. Lett.* **1990**, *172*, 109. Mohktari, A.; Cong, P.; Herek, J.L.; Zewail, A. H.

Nature **1990**, *348*, 225. Cong, P.; Roberts, G.; Herek, J. L.; Mohktari, A.; Zewail, A. H. *J. Chem. Phys.* **1996**, *100*, 7832.

(41) Peslherbe, G. H.; Ladanyi, B. M.; Hynes, J. T. *Chem. Phys.* **2000**, *258*, 201.

(42) Peslherbe, G. H.; Ladanyi, B. M.; Hynes, J. T. *J. Phys. Chem. A* **2000**, *104*, 4533.

(43) Dessent, C. E. H.; Bailey, C. G.; Johnson, M. A. *J. Chem. Phys.* **1995**, *102*, 6335.

(44) Dessent, C. E. H.; Bailey, C. G.; Johnson, M. A. *J. Chem. Phys.* **1995**, *103*, 2006.

(45) Serxner, D.; Dessent, C. E. H.; Johnson, M. A. *J. Chem. Phys.* **1996**, *105*, 7231.

(46) Dessent, C. E., H.; Kim, J.; Johnson, M. A. *Accounts of Chemical Research* **1998**, *31*, 527.

(47) Morgan, S.; Keesee, R. G.; Castleman, A. W. *J. Am. Chem. Soc.* **1989**, *111*, 3841; Markovich, G.; Pollack, S.; Giniger, R.; Cheshnovsky, O. *J. Chem. Phys.* **1994**, *101*, 9344; Abraham, M. H. *Prog. Phys. Org. Chem.* **1974**, *11.1*; Parker, A. J. *Chem. Rev.* **1969**, *1*, 69; Marchi, M.; Sprik, M.; Klein, M. L. *Faraday Discuss. Chem. Soc.* **1988**, *85*, 373.

(48) Tzeng, W. B.; Wei, S.; Castleman, A. W. *J. Am. Chem. Soc.* **1989**, *111*, 6035; Batista, V. S.; Coker, D. F. *J. Chem. Phys.* **1997**, *106*, 7102; Snyder, E. M.; Castleman, A. W. *J. Chem. Phys.* **1997**, *107*, 744; Syage, J. A.; Steadman, J. *J. Phys. Chem.* **1992**, *96*, 9606; Radlof, W.; Freudenberg, T.; Stert, V.; Ritze, H.-H.; Noack, F.; Hertel, I. V. *Chem. Phys. Lett.* **1997**, *264*, 210.

(49) Gough, T. In *Atomic and Molecular Beam Methods*; Scoles, G., Lainé, D., Valbusa, U., Eds.; Oxford University Press: Oxford, 1992; Vol. 2.

(50) Jorgensen, W. L.; Bigot, B.; Chandrasekhar, J. *J. Am. Chem. Soc.* **1981**, *104*, 4584.

(51) Markovich, G.; Perera, L.; Berkowitz, M. L.; Cheshnovsky, O. *J. Chem. Phys.* **1996**, *105*, 2675.

(52) Hirao, K.; Yamabe, S.; Sano, M. *J. Chem. Phys.* **1982**, *86*, 2626.

(53) Draves, J. A.; Luthey-Schulten, Z.; Liu, W.-L.; Lisy, J. M. *J. Chem. Phys.* **1990**, *93*, 4589.

(54) Selegue, T. J.; Moe, N.; Draves, J. A.; Lisy, J. M. *J. Chem. Phys.* **1992**, *96*, 7268.

(55) Serxner, D.; Dessent, C.E.H.; Johnson, M.A. *J. Chem. Phys.* **1996**, *105*, 7231. Ayotte, P.; Bailey, C.G.; Weddle, G.H.; Johnson, M.A. *J. Phys. Chem. A* **1998**, *102*, 3067

(56) Ayala, R.; Martinez, J. M.; Pappalardo, R. R.; Marcos, E. S. *J. Phys. Chem. A* **2000**, *104*, 2799.

(57) Okuno, Y. *J. Phys. Chem. A* **1999**, *103*, 190.

(58) Asada, T.; Nishimoto, K. *Chem. Phys. Lett.* **1995**, *232*, 518.

(59) Gertner, B. J.; Peslherbe, G. H.; Hynes, J. T. *Isr. J. Chem.* **2000**, *40*, 273; Kusada, I.; Wang, Z.-G.; Seinfeld, J. H. *J. Chem. Phys.* **1998**, *108*, 6829; Wang, W.; Low, P. J.; Carty, A. J.; Sappa, E.; Gervasio, G.; Mealli, C.; Ienco, A.; Perez-Carreno, E. *Inorg. Chem.* **2000**, *39*, 998.

(60) Kim, S. K.; Breen, J. J.; Willberg, D. M.; Peng, L. W.; Heikal, A.; Syage, J. A.; Zewail, A. *J. Phys. Chem.* **1995**, *99*, 7421; Jungwirth, P. *J. Phys. Chem. A* **2000**, *104*, 145; Re, S.; Osamura, Y.; Morokuma, K. *J. Phys. Chem. A* **1999**, *103(18)*, 3535.

(61) Grégoire, G.; Mons, M.; Dimicoli, I.; Dedonder-Lardeux, C.; Jouvet, C.; Martrenchard, S.; Soldagi, D. *J. Chem. Phys.* **1999**, *110*, 1521.

(62) Grégoire, G.; Brenner, V.; Millié, P. *J. Phys. Chem. A* **2000**, *104*, 5204.

(63) Dedonder-Lardeux, C.; Grégoire, G.; Jouvet, C.; Martrenchard, S.; Solgadi, D. *Chem. Rev.* **2000**, *100*, 4023.

(64) Jensen, F. *Introduction to Computational Chemistry*; Wiley: West Sussex, England, 1999.

(65) Engel, V.; Metiu, H. *J. Chem. Phys.* **1989**, *90*, 6116.

(66) Braun, M.; Meier, C.; Engel, V. *J. Chem. Phys.* **1996**, *105*, 530; Martinez, T. J.; Levine, R. D. *Chem. Phys. Lett.* **1996**, *259*, 252.

(67) Rosker, M. J.; Rose, T. S.; Zewail, A. H. *Chem. Phys. Lett.* **1988**, *146*, 175. Rose, T. S.; Rosker, M. J.; Zewail, A. H. *J. Chem. Phys.* **1988**, *88*, 6672. Rose, T. S.; Rosker, M. J.; Zewail, A. H. *J. Chem. Phys.* **1989**, *91*, 7415. Cong, P.; Mohktari, A.; Zewail, A. H. *Chem. Phys. Lett.* **1990**, *172*, 109. Mohktari, A.; Cong, P.; Herek, J. L.; Zewail, A. H. *Nature* **1990**, *348*, 225. Cong, P.; Roberts, G.; Herek, J. L.; Mohktari, A.; Zewail, A. H. *J. Chem. Phys.* **1996**, *100*, 7832

(68) Jouvet, C.; Martrenchard, S.; Solgadi, D.; Dedonder-Lardeux, C.; Mons, M.; Grégoire, G.; Dimicoli, I.; Piuzzi, F.; Visticot, J. P.; Mestdagh, J. M.; Doliveira, P.; Meynadier, P.; Perdrix, M. *J. Phys. Chem.* **1997**, *101*, 2555.

(69) Peslherbe, G. H.; Ladanyi, B. M.; Hynes, J. T. *J. Phys. Chem. A* **1998**, *102*, 4100.

(70) Perera, L.; Berkowitz, M.L. *J. Chem. Phys.* **1993**, *99*, 4236. *ibid.* **1993**, *99*, 4222. Dang, L.X.; Garrett, B.C. *J. Chem. Phys.* **1993**, *99*, 2972. Dang, L.X.; Smith, D.E. *J. Chem. Phys.* **1993**, *99*, 6950.

(71) Nguyen, T.-N.; Harpham, M. H.; Ladanyi, B. M.; Peslherbe, G. H., submitted to *J. Phys. Chem. A*.

(72) Edwards, H. J.; Madden, P. A.; McDonald, I. R. *Mol. Phys.* **1984**, *51*, 1141; Jorgensen, W. L.; Briggs, J. M. *Mol. Phys.* **1988**, *61*, 3845.

(73) Bohm, H. J.; McDonald, I. R.; Madden, P. A. *Mol. Phys.* **1983**, *49*, 347.

(74) Cabaleiro-Lago, E. M.; Rios, M. A. *J. Phys. Chem. A* **1997**, *101*, 8327.

(75) Hiraoka, K.; Mizuse, S.; Yamabe, S. *J. Phys. Chem.* **1988**, *92*, 3943.

(76) Metropolis, N.; Rosenbluth, A. W.; Rosenbluth, M. N.; Teller, A. H.; Teller, E. In *Simulations of Liquids and Solids*; Ciccotti, G., Frenkel, D., McDonald, I. R., Eds.; North-Holland: New York, 1987.

(77) Press, W. H.; Teulkolsky, S. A.; Vetterling, W. T.; Flannery, B. P. *Numerical Recipes, The Art of Scientific Computing*; Cambridge University Press: Cambridge, 1992.

(78) Allen, M. P.; Tildesley, D. J. *Computer Simulations of Liquids*; Oxford University Press: New York, 1989.

(79) Asher, R. L.; Micha, D. A.; Brucat, P. J. *J. Chem. Phys.* **1992**, *96*, 7683.

(80) The boiling point of liquid acetonitrile is 81.6°C.

(81) Cabarcos, O. M.; Lisy, J. M. *Chem. Phys. Lett.* **1996**, *257*, 265.

(82) Lu, D. S.; Singer, S. J. *J. Chem. Phys.* **1995**, *103*, 1913.

(83) Lu, D. S.; Singer, S. J. *J. Chem. Phys.* **1996**, *105*, 3700.

(84) Rappé, A. K.; Casewit, C. J. *Molecular Mechanics across Chemistry*; University Science Books: Sausalito, California, 1997; p.407.

(85) The distributed polarizability model fails to reproduce the solvent induced dipole moments predicted by ab initio calculations for small ion-acetonitrile clusters

(86) Cabaleiro-Lago, E. M.; Rios, M. A. *Chem. Phys.* **1998**, *236*, 235.

(87) Dang, L. X.; Chang, T. M. *J. Chem. Phys.* **1997**, *106*, 8149.

(88) Perera, L.; Amar, F. G. *J. Chem. Phys.* **1989**, *90*, 8274.

(89) Schmidt, M. W.; Balridge, K. K.; Boatz, J. A.; Elbert, S. T.; Gordon, M. S.; Jensen, J. H.; Matsunaga, N.; Nguyen, K. A.; Su, S. J.; Windus, T. L.; Dupuis, M.; Montgomery, J. A. *J. Comput. Chem.* **1993**, *14*, 1347.

(90) Frisch, M. J.; Trucks, G. W.; Schlegel, H. B.; Scuseria, G. E.; Robb, M. A.; Cheeseman, J. R.; Zakrzewski, V. G.; Jr., J. A. M.; Stratmann, R. E.; Burant, J. C.; Dapprich, S.; Millam, J. M.; Daniels, A. D.; Kudin, K. N.; Strain, M. C.; Farkas, O.; Tomasi, J.; Barone, V.; Cossi, M.; Cammi, R.; Mennucci, B.; Pomelli, C.; Adamo, C.; Clifford, S.; Ochterski, J.; Petersson, G. A.; Ayala, P. Y.; Cui, Q.; Morokuma, K.; Malick, D. K.; Rabuck, A. D.; Raghavachari, K.; Foresman, J. B.; Cioslowski, J.; Ortiz, J. V.; Stefanov, B. B.; Liu, G.; Liashenko, A.; Piskorz, P.; Komaromi, I.; Gomperts, R.; Martin, R. L.; Fox, D. J.; Keith, T.; Al-Laham, M. A.; Peng, C. Y.; Nanayakkara, A.; Gonzalez, C.; Challacombe, M.; Gill, P. M. W.; Johnson, B.; Chen, W.; Wong, M. W.; Andres, J. L.; Gonzalez, C.; Head-Gordon, M.; Replogle, E. S.; Pople, J. A. *Gaussian 98*, Rev. A11. Gaussian Inc., Pittsburg.

(91) Hehre, W. J.; Radom, L.; Schleyer, P. v. R.; Pople, J. A. *Ab Initio Molecular Orbital Theory*; John Wiley and Sons: New York et al., 1985.

(92) Levine, I. N. *Quantum chemistry*; Prentice Hall Inc., 1991.

(93) Becke, A. D. *J. Chem. Phys.* **1993**, *98*, 5648.

(94) Bergner, A.; Dolg, M.; Kuchle, W.; Stoll, H.; Preuss, H. *Mol. Phys.* **1993**, *80*, 1431.

(95) Glukhovtsev, M. N.; Pross, A.; McGrath, M. P.; Radom, L. *J. Chem. Phys.* **1995**, *103*, 1878.

(96) Bases of 6-311+G(2df) quality have not been reported for iodide and cesium. We augmented the iodide 6-311+G(df) and cesium/iodide SDD bases accordingly with diffuse and/or polarization functions with optimized exponents.

(97) Bertagnolli, H.; Chieux, P.; Zeidler, M. D. *Mol. Phys.* **1976**, *32*, 759.

(98) Steiner, P. A.; Gordy, W. *J. Mol. Spectrosc.* **1966**, *21*, 291.

(99) Singh, U. C.; Kollman, P. A. *J. Comput. Chem.* **1984**, *5*, 129.

(100) Boys, S. F.; Bernardi, F. *Mol. Phys.* **1970**, *19*, 553.

(101) Chalasinski, G.; Szczesniak, M. *Chem. Rev.* **1994**, *94*, 1723; VanDuijneveldt, F. B.; VanDuijneveldt-VanDeRijdt, J. G. C. M.; VanLenthle, J. H. *Chem. Rev.* **1994**, *94*, 1873.

(102) Reimers, J. R.; Hall, L. E. *J. Am. Chem. Soc.* **1999**, *121*, 3730.

(103) Popelier, P. L. A.; Stone, A. J.; Wales, D. J. *Faraday Discuss.* **1994**, *97*, 243.

(104) Dessent, C. E. H.; Kim, J.; Johnson, M. A. *J. Phys. Chem.* **1996**, *100*, 12.

(105) Quina, F. H.; Politi, M. J.; Cuccovia, J. M.; Baumgarten, E.; Martins-Franchetti, S. M.; Chaimovich, H. *J. Phys. Chem.* **1980**, *84*, 361.

(106) Radnai, T.; Itoh, S.; Ohtaki, H. *Bull. Chem. Soc.* **1988**, *61*, 3845.

(107) Davidson, W. R.; Kebarle, P. *J. Am. Chem. Soc.* **1976**, *98*, 6125.

(108) Glendening, E. D.; Feller, D. *J. Phys. Chem.* **1995**, *99*, 3060.

(109) Timerghazin, Q. K.; Peslherbe, G. H. *Chem. Phys. Lett.* **2002**, *354*, 31.

(110) Timerghazin, Q. K.; Nguyen, T.-N.; Peslherbe, G. H. *J. Chem. Phys.* **2002**, *116*, 6867.

(111) Timerghazin, Q. K.; Nguyen, T.-N.; Peslherbe, G. H., to be submitted to *J. Am. Chem. Soc.*

(112) Schleyer, P. V. R. *Encyclopedia of Computational Chemistry*; Wiley: New York, 1998.

(113) Tessman, J. R.; Kahn, A. H. *Phys. Rev.* **1953**, *92*, 890.

(114) Lide, D. R. *The CRC Handbook of Chemistry and Physics*, 75th ed.; CRC Press: Boca Raton, Florida, 1994.

(115) The σ_{ij} size parameters were expressed via the the usual Lorentz-Berthelot combination rule as a function of atomic σ_i and σ_j, which we tried to keep proportional to the atomic and/or ionic Van der Waals radii of the particules during the fitting procedure. However, we found necessary to derive each ε_{ij} parameter independently, without any actual physical constraint.

(116) We note that the MP2 level of theory seems to systematically underestimate the cluster binding energies, compared to the higher-level CCSD(T). Thus, for the larger clusters where no CCSD(T) data is available, we preferentially choose model parameters that tend to predict model binding energies that are higher than their MP2 counterparts.

(117) Hiraoka, K.; Takimoto, H.; Yamabe, S. *J. Phys. Chem.* **1986**, *90*, 5910.

(118) Putnam, W. E.; McEachern, D. M.; Kilpatrick, J. E. *J. Chem. Phys.* **1965**, *42*, 749.

(119) Liquid simulations with our model potentials are under way for a consistent comparison of cluster and liquid results. Nguyen, T.-N.; Peslherbe, G. H. work in progress

(120) Peslherbe, G. H.; Ladanyi, B. M.; Hynes, J. T. *J. Phys. Chem. A* **1999**, *103*, 2561.

(121) Marcus, Y. *Ion solvation*; Wiley: Chichester, 1985.

(122) Dessent, C. E. H.; Kim, J.; Johnson, M. A. *Acc. Chem. Res.* **1998**, *31*, 527.

(123) Blandamer, M. J.; Fox, M. F. *Chem. Rev.* **1970**, *70*, 59.

(124) Buck, U.; Gu, X. J.; Krohne, R.; Laurensten, C. *Chem. Phys. Lett.* **1990**, *174*, 247.

(125) Schwenke, D. W.; Truhlar, D. G. *J. Chem. Phys.* **1985**, *82*, 2418.

(126) Valiron, P.; Mayer, I. *Chem. Phys. Lett.* **1997**, *275*, 46.

(127) Kim, K.; Tarakeshwar, P.; Yong Lee, Y. *Chem. Rev.* **2000**, *100*, 4145.

(128) Meot-Ner (Mautner), M. M.; Lias, S. G. Binding Energies Between Ions and Molecules, and The Thermochemistry of Cluster Ions. In *NIST Chemistry WebBook, NIST Standard Reference Database Number 69*; Linstrom, P. J., Mallard, W. G., Eds.; National Institute of Standards and Technology, 2001.

(129) Simon, S.; Duran, M.; Dannenberg, J. J. *J. Phys. Chem. A* **1999**, *103*, 1640.

(130) Bader, R. F. W. *Atoms in Molecules: A Quantum Theory*; Oxford Univ. Press: Oxford, 1990.

(131) Timerghazin, Q. K.; Peslherbe, G. H. *work in progress.*

(132) Casida, M. E.; Jamorski, C.; Casida, K. C.; Salahub, D. R. *J. Chem. Phys.* **1998**, *108*, 4439.

(133) Majumdar, D.; Kim, J.; Kim, K. S. *J. Chem. Phys.* **2000**, *112*, 101.

(134) Gora, R. W.; Roszak, S.; Leszczynski, J. *Chem. Phys. Lett.* **2000**, *325*, 7.

(135) Nguyen, T.-N.; Peslherbe, G. H., unpublished.

(136) Johnson, M. A., personal communication.

(137) Coe, J. V. *J. Phys. Chem.* **1997**, *229*, 161; Weinheimer, C. J.; Lisy, J. M. *J. Phys. Chem.* **1996**, *100*, 15305; Tobias, D. J.; Jungwirth, P.; Parrinello, M. *J. Chem. Phys.* **2001**, *114*, 7036; Gai, H. D.; Schenter, G. K.; Dang, L. X.; Garrett, B. C. *J. Chem. Phys.* **1996**, *105*, 8835.

(138) Ayotte, P.; Bailey, C. G.; Weddle, G. H.; Johnson, M. A. *J. Chem. Phys.* **1998**, *102*, 3067.

(139) Laria, D.; Fernandez-Prini, R. *J. Chem. Phys.* **1995**, *102*, 7664.

(140) Balzani, V. *Electron transfer in chemistry*; Weinheim: New York, 2001.

(141) Peslherbe, G. H.; Bianco, R.; Ladanyi, B. M.; Hynes, J. T. *J. Chem. Soc., Far. Trans.* **1997**, *93*, 977.

(142) Grégoire, G.; Mons, M.; Dimicoli, I.; Dedonder-Lardeux, C.; Jouvet, C.; Martrenchard, S.; Soldagi, D. *J. Chem. Phys.* **2000**, *112*, 8794.

(143) Godinho, S. S. M. C.; Couto, P. C. d.; Cabral, N. J. C. *Chem. Phys. Lett.* **2004**, *399*, 200.

(144) Hill, T. L. *Statistical Mechanics, Principles and Selected Applications;*New York, 1956; p.193.

(145) Nguyen, T.-N.; Peslherbe, G. H. *J. Phys. Chem. A* **2003**, *107*, 1540.

(146) For instance, the $I^-(CH_3CN)_2$ cluster has two low-energy isomers within 1 kcal/mol of each other, one of them involving hydrogen bonding to iodide. Our previous model potential failed to properly reproduce this structure, and predicted instead a structure with two hydrogen atoms of the methyl group equidistant to iodide.

(147) Lennard-Jones, J. E. *Proc. R. Soc. London ser.* **1924**, *A106*, 463; Adamska, C. M.; Sloma, P.; Tomaszewski, J. *Phys. Stat. Sol.* **1997**, *200*, 451.

(148) Tongraar, A.; Hannongbua, S.; Rode, B. M. *Chem. Phys.* **1997**, *219*, 279.

(149) Zewail, A. H. *Femtochemistry - Ultrafast Dynamics of the Chemical Bond;* Singapore, 1994.

(150) Sakai, Y.; Miyoshi, E.; Anno, T. *Can. J. Chem.* **1992**, *70*, 309.

(151) The use of rigid solvent molecules typically introduces an error of 0.01 Å on geometries, and 0.05 kcal/mol on interaction energies.

(152) Wells, B. H.; Wilson, S. *Chem. Phys. Lett.* **1983**, *101*, 429.

(153) The nature of interatomic interactions was characterized via an analysis of the electronic density within the Atoms-In-Molecules (AIM) framework (see e.g. Bader, R. F. W. *Atoms in Molecules: A Quantum Theory*; Oxford, **1990**; Jonas, V.; Frenking, G.; Reetz, M. T. *J. Am. Chem. Soc.* **1994**, 116, 8741; Bone, R. G. A.; Bader, R. F. W. *J. Phys. Chem.* **1996**, 100, 10892; Popelier, P. L. A. *J. Phys. Chem. A* **1998**, 102, 1873) and properties of the I-H interaction for $NaI(CH_3CN)$ models were tested against a series of criteria for hydrogen bonding established by Popelier (Koch, U.; Popelier, P. L. A. *J. Phys. Chem. A* **1995**, 99, 9747) and Cremer (Cremer, D.; E, K. *Angew. Chem, Int. Ed. Engl.* **1984**, 23, 627). The topology of the electronic density ρ, the gradient field $\nabla\rho$, and the Laplacian $\nabla^2\rho$ for the antiparallel C_s $NaI(CH_3CN)$ global minimum are provided as supplemental information. Inspection of the properties of the I-H interaction reveals that the criteria for hydrogen bonding are only barely fulfilled for the antiparallel C_s $NaI(CH_3CN)$, indicating only a weak hydrogen bond in this complex. Indeed, the H-I internuclear distance of 3.29 Å is considerably larger than that of a prototypical, hydrogen bond (typically ~ 2.0-2.5 Å, see e.g. Speakman, J. C. *The hydrogen bond and other intermolecular forces*; Chemical Society: London, **1975**) and the iodine atom is off the C-H axis of the acetonitrile molecule, where the hydrogen bonding interaction would be maximized. A similar analysis of the $NaI(CH_3CN)$ SSIP model, also provided as supplemental information, reveals a more apparent hydrogen-bonded character than for the $NaI(CH_3CN)$ CIP global minimum. Therefore, the stability of SSIP structures may

arise from a combination of hydrogen-bonding interactions coupled with partial alignment of molecular dipoles.

(154) Varshni, Y. P.; Shukla, R. C. *J. Mol. Spectr.* **1965**, *16*, 63.

(155) Hebert, A. J.; Lovas, F. J.; Melenders, C. A.; Hollowell, C. D.; Story, T. L.; Street, K. J. *J. Chem. Phys.* **1968**, *48*, 2834.

(156) Besler, B. H.; Jr., K. M. M.; Kollman, P. A. *J. Comp. Chem.* **1990**, *11*, 431.

(157) Stone, A. J. *The Theory of Intermolecular Forces*; Oxford University Press: New York, 1997.

(158) Thole, B. T. *Chem. Phys.* **1981**, *59*, 341; Duijnen, P. T. v.; Swart, M. *J. Phys. Chem. A* **1998**, *102*, 2399.

(159) Miller, K. J. *J. Am. Chem. Soc.* **1990**, *112*, 8533.

(160) Vogel, A. *J. Chem. Soc.* **1948**, 1833.

(161) Buckner, J. K.; Jorgensen, W. L. *J. Am. Chem. Soc.* **1989**, *111*, 2507.

(162) Bennett, C. H. *J. Comput. Phys.* **1976**, *22*, 245.

(163) Jorgensen, W. L.; Blake, J. F.; Buckner, J. K. *Chem. Phys.* **1989**, *129*, 193.

(164) Prue, J. E. *J. Chem. Educ.* **1969**, *46*, 13.

(165) Ciccotti, G.; Ferrario, M.; Hynes, J. T.; Kapral, R. *Chem. Phys.* **1989**, *129*, 241.

(166) The convergence referred to is "local", in that contributions from more than a few kT units above the SSIP minimum are negligible, as long as one restricts the integration to the neighborhood of the SSIP well.

(167) The cluster radius is estimated from the geometric average of the cluster principal moment of inertia, averaged over a few thousands cluster configurations.

(168) Koch, D. M.; Peslherbe, G. H., to be submitted to *J. Phys. Chem. A*.

(169) The first solvation shell around the NaI ion pair only includes solvent molecules within the ion first solvation shells. In practice, this corresponds to solvent molecules within 3.8 Å of Na^+ and within 5.8 Å of I^-.

(170) Dunning, T. H., Jr. *J. Chem. Phys.* **1989**, *90*, 1007; Woon, D. E.; Dunning, T. H., Jr. *J. Chem. Phys.* **1993**, *98*, 1358.

(171) Peterson, K. E.; Figgen, D.; Goll, E.; Stoll, H.; Dolg, M. *J. Chem. Phys* **2003**.

(172) Alekseyev, A. B.; Liebermann, H.-P.; Buenker, R. J.; Balakrishnan, N.; Sadeghpour, H. R.; Cornett, S. T. *J. Chem. Phys.* **2000**, *113*, 1514.

(173) The CI(S) method was found to yield more reliable Franck-Condon energy gaps and dipole moments than time-dependent density functional theory calculations (TD-DFT), and the multiconfigurational self-consistent field method (CASSCF), given the basis set employed. Nonetheless, transition dipoles and associated oscillator strengths are qualitatively similar, regardless of the method employed.

(174) Koch, D. M.; Peslherbe, G. H., work in progress.

(175) Kroemer, R. T.; Michopoulos, Y.; Rode, B. M. *Phys. Sci.* **1990**, *45*, 1303; Heinzinger, K. *J. Mol. Liq.* **2000**, *88*, 77; Kincaid, R. H.; Scheraga, H. A. *J. Phys. Chem.* **1982**, *86*, 833.

(176) Honda, K. *Bull. Chem. Soc. Jpn.* **2000**, *73*, 289.

(177) Deng, Z.; Martyna, G. J.; Klein, M. L. *J. Chem. Phys.* **1994**, *100*, 7590.

(178) Nguyen, T.-N.; Hughes, S. R.; Peslherbe, G. H., submitted to *J. Phys. Chem. A.*

(179) Peslherbe, G. H.; Ladanyi, B. M.; Hynes, J. T. *J. Phys. Chem.* **1998**, *102*, 4100.

(180) Dunning, T. H., Jr. *J. Chem. Phys.* **1989**, *90*, 1007.

(181) Kendall, R. A.; Dunning, T. H., Jr., Harrison, R. J. *J. Chem. Phys.* **1992**, *96*, 6796.

(182) Peterson, K. A.; Figgen, D.; Goll, E.; Stoll, H.; Dolg, M. *J. Chem. Phys.* **2003**, in press.

(183) Ma, N.; Siu, F. M.; Tsang, C. W. *Chem. Phys.* **2000**, *322*, 65; Cai, Z.-L.; Francois, J. P. *Chem. Phys.* **1998**, *234*, 59; Hill, S. E.; Glendening, E. D.; Feller, D. *J. Phys. Chem. A* **1997**, *101*, 6125.

(184) Woon, D. E.; Peterson, K. A.; Dunning, T. H., Jr., to be published.

(185) Peterson, K. A.; Dunning, T. H., Jr., to be published.

(186) Ruud, K.; Astrand, P.-O.; Taylor, P. R. *J. Chem. Phys.* **2000**, *112*, 2668.

(187) Hoyau, S.; Norrman, K.; McMahon, T. B.; Ohanessian, G. *J. Am. Chem. Soc.* **1999**, *121*, 8864.

(188) Armentrout, P. B.; Rogers, M. T. *J. Phys. Chem. A* **2000**, *104*, 2238.

(189) Caldwell, G. W.; Masucci, J. A.; Ikonomou, M. G. *Org. Mass. Spectrom.* **1989**, *24*, 8.

(190) Evans, D. H.; Keesee, R. G.; Jr., Castleman, A. W., Jr. *J. Chem. Phys.* **1986**, *86*, 2927.

(191) Feller, D. *J. Chem. Phys.* **1993**, *98*, 7059.

(192) Timerghazin, Q. K.; Peslherbe, G. H., work in progress.

(193) Loeser, J.; Schmuttermaer, C.; Cohen, R.; Elrod, M.; Steyert, D.; Saykally, R.; Bumgarner, R.; Blake, G. *J. Chem. Phys.* **1992**, *97*, 2449; Brammer, L.; McCann, M. C.; Bullock, R. M.; McMullan, R. K.; Sherwood, P. *Organometallics* **1992**, *11*, 2339; Linnartz, H.; Kips, A.; Meerts, W.; Havenith, M. *J. Chem. Phys.* **1993**, *99*, 449; Lough, A. J.; Park, S.; Ramachandran, R.; Morris, R. H. *J. Am. Chem. Soc.* **1994**, *116*, 8356; Lee, J. C.; Rheingold, A. L.; Muller, B.; Pregosin, P. S.; Crabtree, R. H. *J. Chem. Soc., Chem.*

Comm. **1994**, 1021; Mielke, Z.; Tokhadze, K. G.; Hulkiewicz, M.; Schriver-Mazzuoli, M.; Schriver, A.; Roux, F. *J. Chem. Phys.* **1995**, *99*, 10498.

(194) Scheiner, S. In *Hydrogen Bonding, A theoretical Perspective*; Oxford, Ed.; Oxford University Press: New York, 1997; pp 85.

(195) Pecul, M.; Sadlej, J. *Chem. Phys. Lett.* **2002**, *360*, 272.

(196) Jursic, B. S. *J. Mol. Struc. (Theochem)* **1998**, *434*, 29; Stalring, J.; Schutz, M.; Lindh, R.; Karlstrom, G.; Widmark, P. O. *Mol. Phys.* **2002**, *100*, 3389; Govender, M. G.; Rootman, S. M.; Ford, T. A. *Crys. Eng.* **2003**, *6*, 263.

(197) Kulkarni, S. A.; Pathak, R. K. *Chem. Phys. Lett.* **2001**, *336*, 278.

(198) Bende, A.; Vibok, A.; Halasz, G. J.; Suhai, S. *Int. J. of Quant. Chem.* **2004**, *99*, 585.

(199) Lee, J. S.; Park, S. Y. *J. Chem. Phys.* **2000**, 230.

(200) All three isomers are found to be minima when basis sets without polarization functions are employed. See Ref. [194].

(201) Hashimoto, K.; Morokuma, K. *J. Am. Chem. Soc.* **1995**, *117*, 4151.

(202) Tuttle, T. R., Jr.; Malaxos, S.; Coe, J. V. *J. Phys. Chem. A* **2002**, *106*, 925.

(203) Aribi, H. E.; Rodrigez, C. F.; Shoeib, T.; Ling, Y.; Hopkinson, A. C.; Siu, K. W. *J. Phys. Chem. A* **2002**, *106*, 8798; Corral, I.; Mo, O.; Yanez, M.; Radom, L. *J. Phys. Chem. A* **2005**, in press.

(204) No real improvement of the induced dipole description was obtained with inclusion of anisotropic polarization in the model.

(205) Klots, C. E. *Nature* **1984**, *327*, 222.

(206) Castleman, A. W., Jr.; Holland, P. M.; Lindsay, D. M.; Peterson, K. I. *J. Am. Chem. Soc.* **1978**, *100*, 6039.

(207) Hannongbua, S. *J. Chem. Phys.* **2000**, *113*, 4707.

(208) Koch, D. M.; Timerghazin, Q. K.; Ladanyi, B. M.; Hynes, J. T.; Peslherbe, G. H.

(209) Koch, D. M.; Timerghazin, Q. K.; Peslherbe, G. H.; Ladanyi, B. M.; Hynes, J. T.

(210) Hanley, L.; Ed., V. S. *Int. J. Mass Spectrom* **1998**, *174*.

(211) Mair, C.; Fiegele, T.; Biasioli, F.; Worgotter, R.; Grill, V.; Lezius, M.; Mark, T. D. *Plasma Sources Sci. Technol.* **1999**, *8*, 191.

(212) Grill, V.; Worgotter, R.; Futrell, J. H.; Mark, T. D. *Z. Phys.* **1997**, *D40*, 111.

(213) Cleveland, C. L.; Landman, U. *Science* **1992**, *260*, 1304.

(214) John, P. M. S.; Beck, R. D.; Whetten, R. L. *Phys. Rev. Lett.* **1992**, *69*, 1467; Check, I.; Raz, T.; Levine, R. D.; Jortner, J. *J. Chem. Phys.* **1994**, *101*, 8596.

(215) Daineka, D. V.; Pradère, F.; Châtelet, M.; Fort, E. *J. Appl. Phys.* **2002**, *92*, 1.

(216) Raz, T.; Scheck, I.; Ben-Nun, M.; Even, U.; Jortner, J.; Levine, R. D. *J. Chem. Phys.* **1994**, *101*, 8606.

(217) Raz, T.; Levine, R. D. *Chem. Phys. Lett.* **1995**, *246*, 405.

(218) Gupta, M.; Walters, E. A.; Blais, N. C. *J. Chem. Phys.* **1996**, *104*, 100; Yasumatsu, H.; Terasaki, A.; Kindow, T. *J. Chem. Phys.* **1997**, *106*, 3806.

(219) Beauregard, J. N.; Mayne, H. R. *J. Chem. Phys.* **1993**, *99*, 6667.

(220) Klopcic, S. A.; Jarrold, M. F. *J. Chem. Phys.* **1997**, *106*, 8855.

(221) Beckerle, J. D.; Johnson, A. D.; Ceyer, S. T. *J. Chem. Phys.* **1990**, *93*, 4047.

(222) Worsnop, D. R.; Buelow, S. J.; Herschbach, D. R. *J. Phys. Chem.* **1986**, *90*, 5121.

(223) Barker, J. A.; Auerbach, D. J. *Surf. Sci. Rep.* **1985**, *4*, 1.

(224) Gspann, J.; Krieg, G. *J. Chem. Phys.* **1974**, *61*, 4037.

(225) Vostrikov, A. A.; Mironov, S. G.; Semyachkin, B. E. *Sov. Phys. Tech. Phys.* **1982**, *27*, 705.

(226) Holland, R. J.; Xu, G. Q.; Levkoff, J.; Robertson, J.; Bernasek, S. L. *J. Chem. Phys.* **1988**, *88*, 7952.

(227) Koch, D. M.; Peslherbe, G. H. *J. Chem. Phys.* **2001**, *115*, 7685.

(228) Châtelet, M.; Martino, A. D.; Pettersson, J.; Pradère, F.; Vach, H. *Chem. Phys. Lett.* **1992**, *196*, 563; Vach, H.; Martino, A. D.; Benslimane, M.; Châtelet, M.; Pradère, F. *J. Chem. Phys.* **1994**, *100*, 8526.

(229) Martino, A. D.; Benslimane, M.; Châtelet, M.; Pradère, F.; Vach, H. *J. Chem. Phys.* **1996**, *105*, 7828; Menzel, C.; Knoner, A.; Kutzner, J.; Zacharias, H. *Z. Phys. D.* **1996**, *38*, 179; Pradère, F.; Benslimane, M.; Châtelet, M.; Martino, A. D.; Vach, H. *Surf. Sci. Lett.* **1997**, *375*, L375.

(230) Martino, A. D.; Châtelet, M.; Pradère, F.; Fort, E.; Vach, H. *J. Chem. Phys.* **1999**, *111*, 7038.

(231) Pettersson, J. B. C.; Markovic, N. *Chem. Phys. Lett.* **1993**, *201*, 421; Markovic, N.; Pettersson, J. B. C. *J. Chem. Phys.* **1994**, *100*, 3911.

(232) Vach, H.; Benslimane, M.; Châtelet, M.; Martino, A. D.; Pradère, F. *J. Chem. Phys.* **1995**, *103*, 1972.

(233) Svanberg, M.; Markovic, N.; Pettersson, J. B. C. *Chem. Phys.* **1997**, *220*, 137.

(234) Daineka, D. V.; Pradère, F.; Châtelet, M. *Surf. Sci.* **2002**, *519*, 64.

(235) Engstom, J. R.; Bonser, D. J.; Nelson, M. M.; Engel, T. *Surf. Sci.* **1991**, *256*, 317; Engel, T. *Surf. Sci. Rep.* **1993**, *18*, 91; Memmert, U.; Yu, M. L. *Surf. Sci. Lett.* **1991**, *245*,

185; Watanabe, H.; Kato, K.; Uda, T.; Fujita, K.; Ichikawa, M.; Kawamura, T.; Terakura, K. *Physical Review Letter* **1998**, *80*, 345; D'Evelyn, M. P.; Nelson, M. M.; Engel, T. *Surface Science* **1987**, *186*, 75; Silvestre, C.; Shayegan, M. *Phys. Rev. B* **1988**, *37*, 10432; Shimura, F. *Oxygen in Silicon, Semiconductors and Semimetals, Vol. 42*; Academic Press: London, 1994; Lamontagne, B.; Roy, D.; Sporken, R.; Caudano, R. *Progress in Surface Science* **1995**, *50*, 315; Miyake, T.; Soeki, S.; Kato, H.; Nakamura, T.; Namiki, A. *Phys. Rev. B* **1990**, *42*, 11801; Silvestre, C.; Hadky, J.; Shayegan, M. *Journal of Vaccum Science Technology A* **1990**, *8*, 2743; Hoshino, T.; Nishioka, Y. *Phys. Rev. Lett.* **2000**, *84*, 4633.

(236) Hoshino, T. *Phys. Rev. B* **1999**, *59*, 2332.

(237) Kato, K.; Uda, T.; Terakura, K. *Phys. Rev. Lett.* **1998**, *80*, 2000.

(238) Hofer, U.; Morgen, P.; Wurth, W.; Umbach, E. *Phys. Rev. B* **1989**, *40*, 1130.

(239) Ibach, H.; Rowe, J. E. *Phys. Rev. B* **1974**, *10*, 2.

(240) Miyamoto, Y.; Oshiyama, A. *Phys. Rev. B* **1991**, *43*, 9287; Uchiyama, T.; Tsukada, N. *Phys. Rev. B* **1996**, *53*, 7917.

(241) Hoshino, T.; Tsuda, T.; Oikawa, S.; Ohdomari, I. *Surf. Sci. Lett.* **1994**, *50*, 14999.

(242) Farman, J. C.; Gardiner, B. G.; Shanklin, J. D. *Nature* **1985**, *315*, 207; Solomon, S. *Nature* **2004**, *427*, 289.

(243) Cheng, H. D.; Landman, U. *Science* **1993**, *1993*, 1304; Svanberg, M.; Markovic, N.; Petersson, J. B. C. *Chem. Phys.* **1997**, *220*, 137; Tomsic, A.; Markovic, N.; Pettersson, J. B. C. *Chem. Phys. Lett.* **2000**, *329*, 200; Christen, W.; Even, U. *Eur. Phys. J. D.* **2001**, *16*, 87.

(244) Even, U.; Schek, I.; Jortner, J. *Chem. Phys. Lett.* **1993**, *202*, 303.

(245) Xu, G. Q.; Bersanek, S. J.; Tully, J. C. *J. Chem. Phys.* **1988**, *88*, 3376.

(246) Engel, T.; Rieder, K. H. *Structural studies of surfaces with atomic and molecular beam diffraction*; Springer: Berlin, 1982.

(247) Vanslow, R.; Howe, R. E. *Chemistry and physics of solid surfaces VII*; Springer: Berlin, 1988.

(248) Christen, W.; Even, U.; Raz, T.; Levine, R. D. *J. Chem. Phys.* **1998**, *108*, 10262.

(249) Raz, T.; Levine, R. D. *J. Phys. Chem.* **1995**, *99*, 7495.

(250) Tully, C. E. *Inelastic ion surface collisions*; Academic: New York, 1977.

(251) Raz, R.; Schek, I.; Ben-Nun, M.; Even, U.; Jortner, J.; Levine, R. D. *J. Chem. Phys.* **1994**, *101*, 8606.

(252) Raz, T.; Levine, R. D. *J. Am. Chem. Soc.* **1994**, *116*, 11167.

(253) Raz, T.; Levine, R. D. *Chem. Phys. Lett.* **1994**, *226*, 47.

(254) Benslimane, M.; Châtelet, M.; Martino, A. D.; Pradère, F.; Vach, H. *J. Chem. Phys.* **1995**, *237*, 223; Menzel, C.; Knoner, A.; Kurtzner, J.; Zacharias, H. *Z. Phys. D* **1996**, *38*, 179; Pradère, F.; Benslimane, M.; Châtelet, M.; Martino, A. D.; Vach, H. *Surf. Sci. Lett.* **1997**, *375*, L375.

(255) Xu, G. Q.; Bersanek, S. J.; Tully, J. C. *J. Chem. Phys.* **1989**, *90*, 3831.

(256) Svanberg, M.; Markovic, N.; Pettersson, J. B. C. *Chem. Phys.* **1995**, *201*, 473.

(257) Wright, J. S.; Buenker, R. J. *J. Chem. Phys.* **1985**, *83*, 4059.

(258) Banerjee, S.; Liu, M.; Johnson, R. *Surf. Sci. Lett.* **1991**, *L504*, 255.

(259) Tennyson, J.; Avoird, A. v. d. *J. Chem. Phys.* **1980**, *77*, 5664; Vigasin, A. A. *J. Mol. Spec.* **2000**, *202*, 59; Avoird, A. v. d.; Brocks, G. *J. Chem. Phys.* **1987**, *87*, 5346.

(260) G. Torchet, Ph. D. Thesis, Université de Paris-Sud, 1978.

(261) Luo, H.; Hoheisel, C. *Phys. Rev. A* **1991**, *43*, 1819.

(262) Vogelsang, R.; Hoheisel, C. *Phys. Chem. Liq.* **1987**, *16*, 189.

(263) Chaabane, N.; Jundt, G.; Vach, H.; Koch, D.; Peslherbe, G. H. *Intern. J. Mass Spectr.* **2002**, *220*, 159.

(264) Dutkiewicz, L.; Johnson, R. E.; Vertes, A.; Pedrys, R. *J. Phys. Chem.* **1999**, *103*, 2925.

(265) Vach, H. *Phys. Rev. B* **2000**, *61*, 2310.

(266) Gear, C. W. *Numerical Initial Value Problems in Ordinary Differential Equations*; Prentice-Hall: Englewood Cliffs, 1971.

(267) Farges, J.; Feraudy, B. d.; Raoult, B.; Torchet, G. *J. Chem. Phys.* **1986**, *84*, 3491.

(268) Becker, E. W.; Gspann, J.; Krieg, G. *Entropy* **1969**, *30*, 59.

(269) Logan, R. M.; Stickney, R. E. *J. Chem. Phys.* **1966**, *44*, 195.

(270) Lambert, J. D. *Vibrational and rotational relaxation in gases*; Clarendon Press: Oxford, 1977.

(271) Vach, H. *Chem. Phys. Lett.* **1990**, *166*, 1.

(272) Smith, I. W. M. *J. Chem. Soc., Far. Trans.* **1997**, *93*, 3741.

(273) Hanson, R. K.; Salimian, S. In *Combustion Chemistry*; W.C. Gardiner, J., Ed.; Springer: Berlin, 1984.

(274) Bradley, J. N. *Shock Waves in Chemistry and Physics;* New York, 1962; Zeldovich, Y. B.; Raizer, Y. P. *Physics of Shock Waves and High-Temperature Hydrodynamics Phenomena;* New York, 1967; Vols. I and II.

(275) Landman, U.; Cleveland, C. L.; Luedtke, W. D. *Physica D* **1993**, *66*, 87.

(276) Born, M.; Oppenheimer, E. *Ann. Phys.* **1927**, *84*, 457.

(277) White, J. D.; Chen, J.; Matsiev, D.; Auerbach, D.; Wodtke, A. M. *Nature* **2005**, *433*, 503.

(278) Huang, Y. H.; Rettner, C. T.; Auerbach, D.; Wodtke, A. M. *Science* **2000**, *290*, 111.

(279) Chao, S. D.; Harich, S. A.; Dai, D. X.; Wang, C. C.; Yang, X.; Skodje, R. T. *J. Chem. Phys.* **2002**, *117*, 8341.

(280) Beckerle, J. D.; Johnson, A. D.; Yang, Q. Y.; Ceyer, S. T. *J. Chem. Phys.* **1989**, *91*, 5756.

(281) Nguyen, T.-N.; Koch, D. M.; Vach, H.; Peslherbe, G. H. *J. Chem. Phys.* **2003**, *119*, 7451.

(282) Clennan, C.; Pace, A. *Tetrahedron* **2005**, *61*, 6665.

(283) Okabe, H. *Photochemistry of small molecules*; John Wiley & Sons: New York, 1978.

(284) Herzberg, G. *Molecular spectra and molecular structure: I. Spectra of diatomic molecules;* Princeton, NJ, 1966.

(285) Siegbahn, P. E.; Almlof, J.; Heiberg, A.; Roos, B. O. *J. Chem. Phys.* **1981**, *74*, 2384.

(286) Werner, H. J.; Knowles, P. J. *J. Chem. Phys.* **1985**, *82*, 5053.

(287) MOLPRO, a package of ab initio programs designed by H.-J. Werner and P. J. Knowles, version 2002.1, R. D. Amos, A. Bernhardsson, A. Berning, P. Celani, D. L. Cooper, M. J. O. Deegan, A. J. Dobbyn, F. Eckert, C. Hampel, G. Hetzer, P. J. Knowles, T. Korona, R. Lindh, A. W. Lloyd, S. J. McNicholas, F. R. Manby, W. Meyer, M. E. Mura, A. Nicklass, P. Palmieri, R. Pitzer, G. Rauhut, M. Schütz, U. Schumann, H. Stoll,

A. J. Stone, R. Tarroni, T. Thorsteinsson, and H.-J. Werner. P. J. Knowles and H.-J. Werner, *Chem. Phys. Lett.* **1985**, 115, 259; Berning, A.; Schweizer, M.; Werner, H.-J.; Knowles, P. J.; Palmieri, P. *Mol. Phys.* **2000**, 98, 1823.

(288) Berning, A.; Schweizer, M.; Werner, H.-J.; Knowles, P. J.; Palmieri, P. *Mol. Phys.* **2000**, *98*, 1823.

(289) Hernandez-Lamoneda, R.; Hernandez, M. I.; Campos-Martinez, J. *Chem. Phys. Lett.* **2003**, *368*, 709.

(290) Bussery-Honvault, B.; Veyret, V. *J. Chem. Phys.* **1998**, *108*, 3243.

(291) Fedorov, D. G.; Koseki, S.; Schmidt, M. W.; Gordon, M. S. *Int. Rev. Phys. Chem.* **2003**, *22*, 551.

(292) Jongma, R. T.; Shi, S.; Wodtke, A. M. *J. Chem. Phys.* **1999**, *111*, 2588.

(293) Lauvergnat, D.; Clary, D. C. *J. Chem. Phys.* **1998**, *108*, 3566.

(294) Dayou, F.; Spielfiedel, A. *J. Chem. Phys.* **2003**, *119*, 4237.

(295) Schek, I.; Jortner, J.; Raz, T.; Levine, R. D. *Chem. Phys. Lett.* **1996**, *257*, 273.

(296) Beckerle, J. D.; Johnson, A. D.; Yang, Q. Y.; Ceyer, S. T. *J. Chem. Phys.* **1987**, *86*, 7236.

(297) Zambuto, M. *Semiconductor devices*; McGraw-Hill: New York, 1989.

(298) Vach, H.; Nguyen, T.-N. V.; Timerghazin, Q. K.; Peslherbe, G. H. *Phys. Rev. Lett.* **2005**, submitted.

(299) Dayou, F.; Hernández, M. I.; Campos-Martínez, J.; Hernández-Lamoneda, R. *J. Chem. Phys.* **2005**, *123*, 074311.

(300) Schweitzer, C.; Schmidt, R. *Chem. Rev.* **2003**, *103*, 1685.

(301) Minaev, B. F.; Ågren, H. *J. Chem. Soc., Faraday Trans.* **1997**, *93*, 2231.

(302) Minaev, B. F.; Lunell, S.; Kobzev, G. I. *J. Mol. Struct. (Theochem)* **1993**, *284*, 1.

(303) Rånby, B. G.; Rabek, J. F. *Singlet oxygen reactions with organic compounds and polymers*; Wiley, 1978.

(304) Li, S. F.; Gong, X. G. *J. Chem. Phys.* **2005**, *122*, 174311.

(305) Peterka, D. S.; Ahmed, M.; Suits, A. G.; Wilson, K. J.; Korkin, A.; Nooijen, N.; Bartlett, R. J. *J. Chem. Phys.* **1999**, *110*, 6095.

(306) Bienner, L.; Romanini, D.; Kachanov, A.; Campargue, A.; Bussery-Honvault, B.; Bacis, R. *J. Chem. Phys.* **2000**, *112*, 6309.

(307) Aquilanti, V.; Bartolomei, M.; Cappelletti, D.; Carmona-Novillo, E.; Pirani, F. *Phys. Chem. Chem. Phys.* **2001**, *3*, 3891.

(308) Dalgaard, E.; Jorgensen, P. *J. Chem. Phys.* **1978**, *69*, 3833; Werner, H. W.; Meyer, W. *J. Chem. Phys.* **1980**, *73*, 2342.

(309) Dunning, T. H., Jr. *J. Chem. Phys.* **1989**, *90*, 1007.

(310) Moss, R. E. *Advanced Molecular Quantum Mechanics*; Chapman & Hall, 1973; Harriman, J. E. *Theoretical Foundations of Electron Spin Resonance*; Academic Press: New York, 1978.

(311) Krishnan, R.; Binkley, J. S.; Seeger, R.; Pople, J. A. *J. Chem. Phys.* **1980**, *72*, 650.

(312) Widmark, P. O.; Malmqvidst, P. A.; Roos, B. O. *Theor. Chim. Acta* **1990**, *77*, 291.

(313) Jellinek, J.; Li, D. H. *Phys. Rev. Lett.* **1989**, *62*, 241.

(314) Fotis, G. C. D. *Physical Review B: Condensed Matter* **1981**, *23*, 4714.

(315) Shaik, S. S.; Epiotis, N. D. *J. Am. Chem. Soc.* **1980**, *102*, 123.

(316) Feynman, R. P. *Statistical Mechanics*; Benjamin, Reading, 1972.

(317) Popelier, P. L. A. *J. Phys. Chem. A* **1998**, *102*, 1873.

(318) Cremer, D.; E, K. *Angew. Chem, Int. Ed. Engl.* **1984**, *23*, 627.

APPENDIX

Table S1. Electronic structure properties of $NaI(CH_3CN)$ from AIM analysis[a]

Property	CIP	SSIP	Hydrogen Bond Criteria[b]
ρ_{BCP}	0.008	0.017	Density at BCP > 0.002
$\nabla^2\rho_{BCP}$	0.019	0.038	$\nabla^2\rho_{BCP}$ > 0.02 for weak/medium bonds
$H_{H\text{-}I}$	0.0007	0.0005	For weak bond H > 0; for medium H < 0
Δq_H	+0.066	+0.129	Hydrogen becomes more positively charged
$\Delta\mu_H$	-0.003	-0.014	Decrease in dipolar polarization of H
Δr_H	0.66	0.68	Mutual penetration of H and I ($\Delta r > 0$)
Δr_I	1.11	1.30	
ΔV_H	-3.2	-10.0	Decrease in atomic volume of H
ΔE_H	+0.037	+0.070	Energetic destabilization of H

a. Atoms-in-Molecules (AIM) analysis of the MP2/6-311+G(d) electron density. ρ_{BCP} is the density, $\nabla^2\rho_{BCP}$ the Laplacian of the density, $\Delta\mu_H$ is the change in the dipolar polarization of the hydrogen atom, Δr_H and Δr_I are the degrees of penetration of both hydrogen and iodine, ΔV_H is the change in the atomic volume of hydrogen, ΔE_H is the change in atomic energy of hydrogen and $H_{H\text{-}I}$ is the energy density. All values are in a.u. Δq_H is the hydrogen atom charge loss, in *e*.
b. As proposed by Popelier in Ref. [317] and Cremer in Ref. [318].

NaI(CH_3CN) – "CIP"

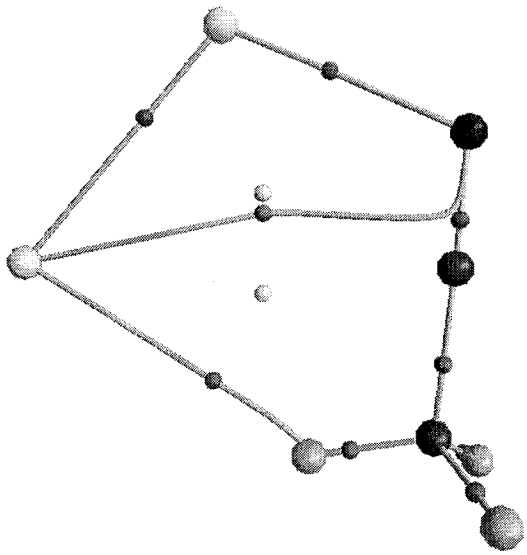

NaI(CH_3CN) – "SSIP"

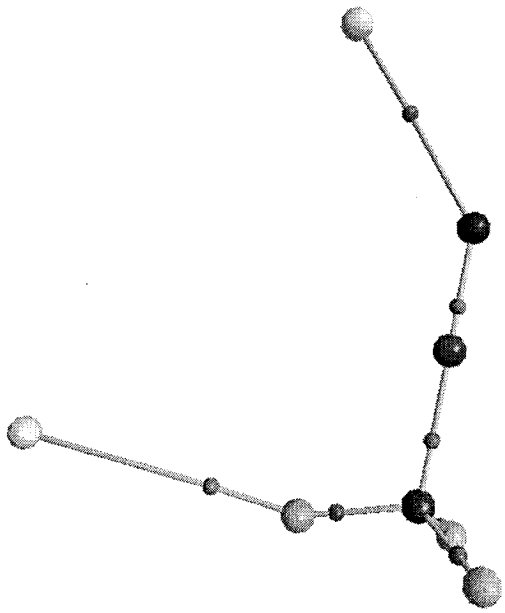

Fig. S1. Bond critical points and interaction lines of the NaI(CH_3CN) CIP and SSIP models from AIM analysis. The orientation is defined in the plane of the NaI ion pair and the donor hydrogen from acetonitrile. (a) CIP global minimum. (b) SSIP model, with r_{NaI} constrained at 5.8 Å.

GLOSSARY

B3LYP	Becke 3 Lee, Yang, Parr
BSSE	Basis Set Superposition Error
CASSCF	Complete Active Space Self-Consistent-Field
CCSD(T)	Coupled-Cluster with Single, Double, and linearized Triple excitations
CIP	Contact Ion Pair
CP	Counterpoise
CTTS	Charge Transfer To Solvent
DZ	Double Zeta
DZS	Dynamic Zone Structure
ECP	Effective Core Potential
ESP	Electrostatic Potential
HF	Hartree-Fock
MP2	Second-Order Moeller-Plesset
NBO	Natural Bond Orbital
PDF	Probability Distribution Fonction
PES	Potential Energy Surface
PMF	Potential of Mean Force
QZ	Quadruple Zeta
SSIP	Solvent Separated Ion Pair
TD-DFT	Time-Dependent Density Functional Theory
TZ	Triple Zeta
ZPE	Zero Point Energy

GLOSSARY

B3LYP	Becke 3 Lee, Yang, Parr
BSSE	Basis Set Superposition Error
CASSCF	Complete Active Space Self-Consistent-Field
CCSD(T)	Coupled-Cluster with Single, Double, and linearized Triple excitations
CIP	Contact Ion Pair
CP	Counterpoise
CTTS	Charge Transfer To Solvent
DZ	Double Zeta
DZS	Dynamic Zone Structure
ECP	Effective Core Potential
ESP	Electrostatic Potential
HF	Hartree-Fock
MP2	Second-Order Moeller-Plesset
NBO	Natural Bond Orbital
PDF	Probability Distribution Fonction
PES	Potential Energy Surface
PMF	Potential of Mean Force
QZ	Quadruple Zeta
SSIP	Solvent Separated Ion Pair
TD-DFT	Time-Dependent Density Functional Theory
TZ	Triple Zeta
ZPE	Zero Point Energy